RÉPUBLIQUE FRANÇAISE
Liberté Égalité Fraternité

Université de Toulouse

Doctorat de l'Université de Toulouse

préparé à l'ISAE-SUPAERO

Développement d'un lidar à haute résolution spectrale pour la caractérisation d'aérosols à courte distance

Thèse présentée et soutenue, le 28 janvier 2026 par

Manuela HOYOS RESTREPO

École doctorale
SDU2E - Sciences de l'Univers, de l'Environnement et de l'Espace

Spécialité
Océan, Atmosphère, Climat

Unité de recherche
ISAE-ONERA PSI Physique Spatiale et Instrumentation

Thèse dirigée par
Romain CEOLATO

Composition du jury
M. Nicolas RIVIERE, Président, ONERA Toulouse
M. Juan Antonio BRAVO ARANDA, Rapporteur, Universidad de Granada
M. Adolfo COMERON TEJERO, Rapporteur, Universitat Politècnica de Catalunya
M. Yoshitaka JIN, Examinateur, National Institute for Environmental Studies, Japan
Mme Cornélia IRIMIEA, Examinatrice, ONERA Palaiseau
M. Romain CEOLATO, Directeur de thèse, ONERA Toulouse

Membres invités
Mme Elena MONTILLA ROSERO, Universidad EAFIT
M. Nobuo SUGIMOTO, National Institute of Environmental Studies, Japan

So remember to look up at the stars and not down at your feet, try to make sense of what you see, and wonder about what makes the universe exist. Be curious. And however difficult life may seem, there is always something you can do and succeed at. It matters that you don't just give up.

Stephen Hawking

La vie n'est facile pour aucun de nous. Mais quoi, il faut avoir de la persévérance, et surtout de la confiance en soi. Il faut croire que l'on est doué pour quelque chose, et que, cette chose, il faut l'atteindre coûte que coûte.

Marie Skłodowska-Curie

Acknowledgements

Tout d'abord, je tiens à remercier l'ONERA pour avoir financé l'intégralité de ma thèse et m'avoir offert l'opportunité de développer mes compétences au sein d'équipes et aux côtés de chercheurs d'une qualité scientifique exceptionnelle, dans un environnement de travail doté des meilleurs moyens techniques et expérimentaux. Je remercie également l'État français qui, par l'intermédiaire de l'Agence Nationale de la Recherche, a financé une partie de mes travaux de recherche dans le cadre du programme Investissements d'avenir, portant la référence EUR TESS N°ANR-18-EURE-0018.

Then, I would like to express my deepest gratitude to the jury members who have accepted to share their expertise with me by evaluating my work. A los profesores Adolfo Comerón Tejero y Juan Antonio Bravo Aranda, muchas gracias por el tiempo dedicado a leer y evaluar mi tesis. Estoy segura de que su experiencia en lidar va a aportar una retroalimentación profundamente valiosa para mi trabajo. Moltes gràcies, Adolfo. Mil gracias, Juan Antonio. Thank you also to Dr. Nobuo Sugimoto and Dr. Yoshitaka Jin for their time and effort in reading and evaluating the thesis. Moreover, thank you to Yoshitaka for sharing all of your HSRL experience and knowledge with me. Enfin, et non des moindres, je remercie le Dr. Cornélia Irimiea pour les nouvelles perspectives que son évaluation apportera à mon travail, grâce à son expertise en optique et en combustion.

Je voudrais également remercier toute l'équipe Lisar et DOTA Toulouse pour m'avoir soutenu pendant ces trois ans et demi que j'ai passés à vos côtés. Merci du fond du cœur à Romain, mon directeur de thèse, qui m'a donné l'opportunité de venir en France et de travailler avec des personnes exceptionnelles comme lui. Merci de m'avoir aidé, même avant mon arrivée à Toulouse, et d'avoir été sincère avec moi dès les premiers instants. Je te serai toujours reconnaissante. Muchas gracias a Andrés por creer en mí y por apoyarme para cumplir mi sueño, incluso antes de conocerme demasiado. Gracias por ser el apoyo colombiano que me hizo falta para sobrevivir en Francia, sin vos no habría sido posible. Merci aussi à Gérald pour toujours être prêt à m'aider, pour toutes les choses que tu m'as apprises, et pour être patient avec mon mauvais français !

A veces ya no sé pa' dónde voy, pero no me olvido de dónde vengo. Muchas gracias a todas y cada una de las personas que me han ayudado a llegar hasta este punto. A todos los

profesores que he tenido a lo largo de mi vida, especialmente a mis profesores de la Universidad EAFIT, a Elena, Daniel y René. A mis excompañeros del grupo de Óptica Aplicada por tantos años de compañía y buenos momentos compartidos. A Ana, que al principio no me caía muy bien y terminó siendo mi mejor amiga desde la maestría. Gracias por todo el apoyo y los buenos momentos (chats sobre todo) que hemos compartido. Sin ti y los videos de gatos que me mandas, creo que habría perdido la cordura durante el proceso. A Jair, Lucho, Hérica, Abraham y Jaime, sin cuya ayuda jamás habría podido terminar ninguno de mis proyectos. Gracias también a todas las maravillosas personas del CEAMA que conocí durante una de las mejores experiencias de mi vida. A Juan Antonio, Juanlu, Pablo, Fátima, Lucas, Juan Andrés, Cristian, Jose, Hasan, Gloria y Alberto. Gracias por su amabilidad y acogida durante mi estancia en Granada, esos siete meses no los olvidaré jamás. A todos aquellos que no menciono, sepan que no por ello los olvido. ¡Gracias totales!

Me gustaría hacer una mención especial a Elena, mi guía, apoyo y referente académico durante todo mi proceso de formación. Eres y siempre serás un modelo a seguir para mí, como mujer, profesora, científica e ingeniera, pero, sobre todo, como persona. Te debo todo lo que sé sobre lidar y a todas las maravillosas personas que he conocido gracias a ello. Sin ti y sin tu apoyo desde aquel café en De Lolita, yo no estaría hoy cumpliendo este sueño. Te quiero muchísimo y te estaré eternamente agradecida.

Por último, y más importante, muchas gracias a mi familia. A mis padres, Diana y Edgar, por su amor y entrega, y enseñarme que el trabajo duro es el único camino al éxito. Espero que la vida me permita devolverles al menos la mitad de todo lo que me han dado. A mi hermana Maria Fernanda, quien siempre fue mi modelo a seguir y me pasaba las medidas cuando las tenía a un metro de distancia, gracias por darme a los dos mejores regalos de mi vida: mis anhelados sobrinos. A mi hermana Paulina, por todas las peleas de pequeñas y por haberme apoyado cuando lo he necesitado. A Benjamin, por alegrar mi vida desde el momento de su concepción, por todas las obras de arte que decoran mi hogar y me hacen sentir en casa, aunque esté tan lejos de ella. A mi ahijado/a, a quien amo con todo mi corazón, aunque, a la fecha, no sabemos ni su sexo. Tía Manu siempre estará a su lado para todo lo que necesiten. Por último, la persona más importante de mi vida: mi novia Camila. Has estado a mi lado desde el primero de mis logros y espero que estés allí hasta el último, pues la vida no tendría ningún tipo de sentido sin ti a mi lado. Gracias por la paciencia y la compañía, a pesar de haber estado separadas durante tanto tiempo. Hoy te menciono porque, como dice Enrique Bunbury: *Ahora puedo decirlo más alto, pero no puedo más claro: todo lo que en el mundo he amado es una canción, un teatro y a ti.*

I have been enormously privileged through my work to be able to contribute to our understanding of the universe, but it would be an empty universe indeed if it were not for the people I love and who love me.

Stephen Hawking

Abstract

In recent years, short-range elastic backscatter lidars (SR-EBLs) have been developed to study the radiative and microphysical properties of particles over short distances for various climate, air quality, and aviation applications. However, the inherently ill-posed nature of the elastic backscatter lidar problem limits SR-EBL's accuracy, particularly for assessing ultrafine particles such as freshly emitted soot. In contrast, high spectral resolution lidars (HSRLs) provide assumption-free, accurate aerosol retrievals but are typically designed for long-range measurements. A thorough literature review found that no time-of-flight-based HSRL has been reported for short-range aerosol studies. In this context, this thesis bridges this gap by developing a short-range HSRL (SR-HSRL) prototype capable of retrieving aerosol properties within the first kilometer of the atmosphere –the blind zone of most HSRLs– with high spectral and spatiotemporal resolution. To this end, a comprehensive methodology for characterizing commercial lasers and optimizing spectral filter configurations was developed. Numerical simulations of the spectral performance of iodine vapor cells and scanning field-widened Michelson interferometers were conducted for different laser linewidths to optimize their performance, followed by laboratory validation using the selected laser sources.

A proof-of-concept SR-HSRL prototype was developed using a 40-cm-long iodine cell and a customized fiber laser (300 MHz linewidth, 50–65 kHz repetition rate). A field validation campaign at the National Institute for Environmental Studies (NIES) in Tsukuba, Japan, demonstrated the prototype's ability to retrieve aerosol and cloud backscattering within the first kilometer of the atmosphere. A dedicated calibration methodology was developed for radiometric and overlap calibration of both channels. The retrieval method, based on the computation of the backscatter ratio from attenuated backscatter coefficients, eliminates the need for lidar ratio assumptions, yielding autocalibrated measurements with high temporal and spatial resolution (6 s and 7.5 m) over an effective measurement range of 50–1000 m. Compared with the only other short-range HSRL reported in the literature, based on the Scheimpflug principle, the pulsed SR-HSRL developed in this thesis is instrumentally more complex but provides constant spatial resolution, real-time, synchronized data acquisition, and an equivalent blind-zone height (50 m). This makes it the first time-of-flight-based short-range HSRL capable of retrieving reliable, autocalibrated aerosol backscattering coefficients close to the ground, opening new perspectives for near-field atmospheric studies and emission monitoring.

Résumé

Au cours des dernières décennies, des lidars à rétrodiffusion élastique à courte portée (*Short-Range Elastic Backscatter Lidars*, SR-EBLs) ont été développés afin d'étudier les propriétés radiatives et microphysiques des particules sur de courtes distances, pour diverses applications liées au climat, à la qualité de l'air et à l'aviation. Cependant, la nature intrinsèquement mal posée du problème de la rétrodiffusion élastique limite la précision des SR-EBL, en particulier pour l'évaluation de particules ultrafines, telles que les suies fraîchement émises. À l'inverse, les lidars à haute résolution spectrale (*High Spectral Resolution Lidars*, HSRLs) permettent une restitution précise et sans hypothèses des propriétés des aérosols, mais sont généralement conçus pour des mesures à longue portée. Une revue approfondie de la littérature a montré qu'aucun lidar HSRL basé sur le principe du temps de vol n'avait encore été rapporté pour des études d'aérosols à courte portée. Dans ce contexte, cette thèse vise à combler cet écart en développant un prototype de HSRL à courte portée (SR-HSRL) capable de restituer les propriétés des aérosols dans le premier kilomètre de l'atmosphère – la zone aveugle de la plupart des systèmes HSRL – avec une haute résolution spectrale, spatiale et temporelle. À cette fin, une méthodologie complète a été élaborée pour la caractérisation de lasers commerciaux et l'optimisation des configurations de filtres spectraux. Des simulations numériques de la performance spectrale de cellules à vapeur d'iode et d'interféromètres de Michelson à élargissement de champ et balayage ont été réalisées pour différentes largeurs de raie laser afin d'optimiser leurs performances, puis validées expérimentalement en laboratoire à l'aide des sources laser sélectionnées.

Un prototype SR-HSRL a été conçu en intégrant une cellule d'iode de 40 cm et un laser à fibre personnalisé (largeur de raie de 300 MHz, fréquence de répétition comprise entre 50 et 65 kHz). Une campagne de validation sur le terrain, menée à l'Institut National d'Études Environnementales (NIES) de Tsukuba, au Japon, a démontré la capacité du prototype à restituer la rétrodiffusion des aérosols et des nuages dans le premier kilomètre de l'atmosphère. Une méthodologie d'étalonnage dédiée a été développée pour l'étalonnage radiométrique et l'étalonnage des recouvrements des deux canaux. La méthode de restitution, fondée sur le calcul du rapport de rétrodiffusion à partir des coefficients de rétrodiffusion atténués, supprime la nécessité d'hypothèses sur le rapport lidar et permet d'obtenir des mesures auto-étalonnées avec une résolution temporelle et spatiale élevée (6 s et 7,5 m), sur une portée de mesure effective comprise entre 50 et 1000 m. Comparé au seul autre lidar

HSRL de courte portée décrit dans la littérature – fondé sur le principe de Scheimpflug –, le lidar SR-HSRL pulsé développé dans cette thèse présente une complexité instrumentale supérieure, mais offre une résolution spatiale constante, une acquisition de données synchronisée en temps réel et une hauteur de zone aveugle équivalente (50 m). Il s'agit ainsi du premier HSRL à courte portée, fondé sur la mesure du temps de vol, capable de restituer de manière fiable et auto-étalonnée les coefficients de rétrodiffusion des aérosols à proximité du sol, ouvrant de nouvelles perspectives pour les études atmosphériques de proche champ et pour la surveillance des émissions à la source.

Contents

Acknowledgements **v**

Abstract **ix**

Résumé **xi**

1 Introduction **1**
1.1 Context 1
1.2 Problem statement 4
1.3 Scientific approach 5
1.4 Outline 7

2 Introduction **11**
2.1 Contexte 11
2.2 Problématique 14
2.3 Démarche scientifique 15
2.4 Organisation du manuscrit 17

3 HSRL fundamentals **21**
3.1 Atmospheric aerosols 22
3.1.1 Microphysical properties 23
3.2 Radiative properties of aerosols 25
3.2.1 Absorption 27
3.2.2 Scattering theory 29
3.3 HSRL theoretical framework 35
3.3.1 Overlap function 39
3.4 Proposed SR-HSRL inversion method 42
3.4.1 Calibration 42
3.4.2 Retrieval of the aerosol backscatter coefficient 44

4 State of the art **47**
4.1 Short-range lidars 47

4.2 High spectral resolution lidars 56
4.2.1 Lasers 61
4.2.2 Spectral filters 64
4.3 Summary 76

5 Design and validation of the SR-HSRL transmitter–spectral subsystems 79
5.1 Characterization of commercial laser sources 80
5.1.1 Keopsys PGFL model 81
5.1.2 Teem Photonics STG model v0 and v1 85
5.2 Numerical simulation of the spectral performance 90
5.2.1 Iodine cell 93
5.2.2 Scanning field-widened Michelson interferometer 97
5.2.3 Summary 104
5.3 Design of two optimized spectral filters 105
5.3.1 20-cm-long iodine cell 105
5.3.2 Scanning FWMI with 200-mm OPD 108
5.4 Validation of the spectral performance 111
5.4.1 Transmission spectra of two iodine cells 111
5.4.2 Transmission of an SFWMI 116
5.5 Summary: Laser - spectral filter configurations for different operational conditions 119

6 Validation campaign: aerosol properties in the first kilometer of the atmosphere 123
6.1 Proof-of-concept campaign overview 123
6.2 SR-HSRL prototype overview 124
6.3 Data preprocessing and calibration 127
6.3.1 Background subtraction and range correction 128
6.3.2 Signal calibration 130
6.4 Determination of the attenuated backscatter signals 135
6.5 Estimation of the aerosol backscatter coefficients 140
6.5.1 Uncertainty analysis of the retrieved aerosol backscattering coefficients 143
6.6 Discussion and summary 145
6.7 Current limitations of the SR-HSRL technique 147
6.7.1 Instrumental limitations 147
6.7.2 Methodological and signal-related limitations 148
6.7.3 Future improvements 148

7 Conclusions and perspectives **151**
7.1 General overview 151
7.2 Synthesis of the main results 154
7.3 Scientific and technical contributions 156
7.3.1 General contributions 156
7.3.2 Contribution to ONERA's methodological competence in short-range aerosol lidar 156
7.4 Perspectives 157

8 Conclusions et perspectives **163**
8.1 Aperçu général 163
8.2 Synthèse des principaux résultats 166
8.3 Contributions scientifiques et techniques 168
8.3.1 Contributions générales 168
8.3.2 Contribution à la compétence méthodologique de l'ONERA en lidar d'aérosols à courte portée 169
8.4 Perspectives 170

Bibliography **175**

List of Figures

3.1 Schematic of size distribution modes, lifetime as well as growing and deposition processes of aerosols. Adapted from [32]. 23
3.2 Schematic of number, surface and volume size distributions related to the nucleation, accumulation and coarse modes. From [2]. 25
3.3 Scattering regimes as a function of radiation wavelength and particle radius. Transition values, given by the value of x, are represented by dotted lines. Taken from [2]. 27
3.4 Rayleigh phase function for different polarization states of the incident radiation: natural light (in black) and linearly polarized parallel (in red) and perpendicular (in blue) to the scattering plane. 29
3.5 Mie phase function for different size parameters ($x = \lambda/3$ on the left, $x = \lambda$ on the right) and polarization states of the incident radiation: natural light (in black) and linearly polarized parallel (in red) and perpendicular (in blue) to the scattering plane. The zoom panel in green shows the minor effect of polarization on larger particles at backward angles. 33
3.6 Working principle of HSRL. Adapted from [50]. 36
3.7 Layout of a typical HSRL system, composed of a laser source, a telescope, collimating optical elements, a beam splitter, spectral filters, and two photodetectors. 37
3.8 Range-dependent lidar overlap function. It represents the gradual coupling between the laser beam and the receiver field of view. 39

4.1 Basic optical diagram of CALs to measure aerosol radiative and microphysical properties in the short range. Adapted from [22]. 50
4.2 Colibri Aerosol Lidar. Picture credits: Romain Ceolato. 50
4.3 Left: Schematic diagram and picture of the NHL developed by Ong et al.[20]. Right: Raymetric's 3D-scanning lidar used by Zhang et al.[67]. 52
4.4 Layout and picture of the P-PML developed by Chen et al. [19]. 52
4.5 Mini MPL (Droplet Measurement Technologies) used by Osibanjo et al. [71]. 53
4.6 Dual-wavelength Scheimpflug lidar developed by Mei et al. [68]. 54

4.7 Left: operation principle of the SLidar technique. Right: SLidar developed by Mei et al. [69]. 55
4.8 Layout of the fused pulsed lidar (Raman + depolarization) and SLidar system developed by Wang et al. [70]. 56
4.9 Left: Layout of the HSRL system developed by Hoffman et al. Right: Schematic and picture of the CFP used as a spectral filter [110]. 66
4.10 Left: Layout of the HSRL system developed by Jin et al. [97]. Right: Schematic diagram of the measurement method. 68
4.11 Picture (left) and diagram (right) of NASA's HSRL-2 355 nm density-tuned FWMI [109]. 69
4.12 Left: mechanical design of NASA's HSRL-2 transmitter and receiver units (upper and middle panels), and a picture of the receiver unit (bottom panel). Credits: Welch Mechanical Design. Right: NASA's airborne HALO instrument, which contains the HSRL-2 system. Credits: NASA Airborne Science Program. 69
4.13 LNG airborne HSRL developed by Bruneau et al. [84]. 70
4.14 Layout (left) and picture (right) of the MZI used as the spectral filter in the airborne LNG [84]. 70
4.15 Layout (left) and CAD design (right) of DLR's airborne WALES system [107]. 73
4.16 Layout (left) and CAD design (right) of DLR's airborne WALES system [49]. 74
4.17 Schematic of the dual-molecular channel HSRL developed by Hair et al. (a) The transmitter system, (b) the Doppler-free frequency monitor, and (c) the receiver with two molecular and one total scattering channels [17]. 75
4.18 Left: Schematic of the short-range HSR-SLidar developed by Chang et al. [27]. Right: The HSR-SLidar during an experiment in 76

5.1 Power stability of Keopsys' laser operating at minimum power. 82
5.2 Power stability of Keopsys' laser operating at maximum power. 83
5.3 Spectral stability of the Keopsys laser for a seed laser temperature of 20.00°C. The top panel shows the linewidth is constant (<400 MHz), and the bottom panel shows the evolution of the air wavelength ($\bar{x}$ = 532.1638 nm). 84
5.4 Output wavelength as a function of the seed laser temperature for the Keopsys laser. 85
5.5 Power stability Teem Photonics laser. 86
5.6 Spectral stability of Teem Photonics' laser v0 for a diode laser temperature of 33.00°C. The constant linewidth value is <400 MHz, the mean wavelength is 532.24155 nm, and the absolute wavelength change is 0.27 pm. 87

5.7 Spectral stability of the improved Teem Photonics laser for a diode laser temperature of 28.50°C. The constant linewidth value is <400 MHz, and the wavelength is 532.23601 nm ± 0.1 pm. 88
5.8 Output wavelength as a function of the crystal temperature for the Teem Photonics v0 and v1 lasers. 89
5.9 Doppler-broadened Rayleigh (in blue), Brillouin (in green), and Rayleigh-Brillouin (in black) backscattering spectra for an atmospheric temperature of 288K and pressure of 1013.25 hPa. 91
5.10 Effect of the laser linewidth on the Doppler-broadened Mie spectral distribution. A narrow linewidth results in a narrow spectral broadening (red curve), while a wide linewidth results in a wider broadening (blue curve). The black curve represents the molecular backscattering spectrum. 92
5.11 Block diagram of the simulation algorithm for estimating the spectral discrimination ratio of two different spectral filters. 93
5.12 Simulated iodine cell spectral performance for various laser linewidths as a function of cell length. The top and middle panels show the effective particle and molecular transmissions, and the bottom panel shows the spectral discrimination ratio. 96
5.13 Setup of a Michelson interferometer using an extended monochromatic source, a non-polarizing beam splitter (NPBS) cube, and two plain, parallel mirrors. The resulting interference pattern are fringes of equal inclination. 98
5.14 Setup of an FWMI inserting a glass rod of length L_g and index of refraction n_g in one of the interferometer's arms. In constructive interference, a single circular fringe is seen on the screen. For destructive interference, the beam is extinguished. 100
5.15 Transmittance functions of an SFWMI when $\delta = 0$ and $\delta = p$. The atmospheric backscattering spectra are shown in black. 101
5.16 Transmittance of the particle (top panel) and molecular (bottom panel) spectra through an SFWMI as a function of its FSR when $\delta(\nu) = \pi$. 102
5.17 Atmospheric visibility as a function of the interferometer's OPD. 102
5.18 Spectral performance of the filter as a function of the FSR for different laser linewidths. 103
5.19 Length-dependent central transmittance of iodine line 1116. 106
5.20 CAD model of the modular spectral unit based on the optimized iodine cell. The isometric view is displayed on the left, while the right shows the module's layout. 107

5.21 Picture of the iodine cell spectral module assembled into the SR-HSRL prototype. 108
5.22 CAD model of the optimized glass rod and beam splitter assembly. 109
5.23 CAD model of the modular spectral unit based on the optimized SFWMI. The isometric view is displayed on the left, while the right shows the interferometer layout. 110
5.24 Picture of the assembled SFWMI spectral module. 110
5.25 Laboratory setup to measure iodine absorption bands in the lasers' wavelength range. L and ∅ stand for cell length and diameter, FS for field stop, NDF for neutral density filter, and IF for interference filter. 111
5.26 Iodine spectrum (10-cm-long cell) in the Keopsys laser wavelength range. Colors represent different measurements performed to validate spectral stability. 112
5.27 Absorption spectrum of a 10-cm-long iodine cell in the Teem Photonics laser v0 wavelength range. 114
5.28 Absorption spectra of a 10-cm-long iodine cell in the Teem Photonics laser v1 wavelength range. 115
5.29 Laboratory setup to measure the transmission of an SFWMI. L and ∅ stand for cell length and diameter, FS for field stop, NDF for neutral density filter, and IF for interference filter. 116
5.30 Validation of the field-widening effect of the designed SFWMI. 117
5.31 Visibility of the interference fringes produced by the SFWMI as a function of seed laser temperature. The visibility remains nearly constant ($\bar{V} = 0.74$) over the measurement range, indicating wavelength-independent minimum and maximum irradiance values. 118
5.32 Transmittance of the scanning-field widening Michelson interferometer for different seed laser temperatures. 119

6.1 Schematic representation of the SR-HSRL developed by ONERA and NIES to study aerosols in the first kilometer of the atmosphere using a compact, high repetition rate, large-linewidth laser. 125
6.2 Temporal evolution of the preprocessed signals for the measurement campaign (11/07/2024 to 12/07/2024). The top panel represents the HSR channel, and the bottom one the total channel. 129
6.3 Color-saturated temporal evolution of the preprocessed signals to emphasize the periodic laser wavelength drift detected in the HSR channel during the validation campaign. 130

6.4 Interchannel calibration parameter calculated as the ratio of the HSR channels outside an iodine band and the total signals. 131
6.5 Half-hour averaged profiles of calibrated (lighter lines) and uncalibrated (darker lines) molecular and total signals. 133
6.6 Temporal evolution of the calibrated signals for the measurement campaign (11/07/2024 to 12/07/2024). The top panel illustrates the Rayleigh channel, and the bottom one represents the corrected total channel. 134
6.7 Color-saturated temporal evolution of the calibrated signals to highlight the reduction in the detected periodic laser wavelength drift in the HSR channel during the validation campaign. 135
6.8 Overlap function of the Rayleigh (blue) and total (red) channels. Optical path differences between the channels cause the differences seen in the incomplete overlap zone (below 550 m). 138
6.9 Temporal evolution of the attenuated backscatter coefficients measured by the SR-HSRL prototype during the field campaign. The top panel presents the molecular channel, and the bottom panel the total channel. 140
6.10 Temporal evolution of the backscatter ratio measured by the SR-HSRL prototype in the first kilometer of the atmosphere during the field campaign. . . 141
6.11 Temporal evolution of β_{aer}^{HSRL} measured by the SR-HSRL prototype in the first 1000 m. It can be noted that all aerosol layers are preserved, as is the strong backscattering from clouds. 142
6.12 Averaged profiles of the backscatter coefficients retrieved in the short range (from 50 m) for aerosol layers and clouds. The gray shadow represents the standard deviation of the averaged profile, with variations due to atmospheric changes over the 30-minute integration time. 146

7.1 CAL-HSR proof-of-concept test to verify Mie suppression in the HSR channel. The top panel displays the HSR channel's RCS, indicating no water-droplet signals. The bottom panel shows the total channel's RCS, where the evolution of the water droplets spray is evident. 159
7.2 CAL-HSR validation test. The panels on the left represent the measurements at $\nu = \nu_{off}$, where the aerosol signals are passed through the iodine cell. The panels on the right show the standard measurements, where the HSR channel clearly shows that the aerosol signals were suppressed. 160
7.3 Mean range-corrected signals measured at the online frequency. It is clear that the Mie component is effectively suppressed in the HSR channel. . . . 161

8.1 Essai de validation du CAL-HSR visant à vérifier la suppression du signal Mie dans le canal HSR. Le panneau supérieur indique le RCS du canal HSR, qui ne présente aucun signal de gouttelettes d'eau. Le panneau inférieur illustre le RCS du canal total, où l'évolution du jet de gouttelettes est clairement visible. 172
8.2 Essai de validation du CAL-HSR. Les panneaux de gauche représentent les mesures à $\nu = \nu_{off}$, où les signaux d'aérosols traversent la cellule d'iode. Les panneaux de droite montrent les mesures standard, où le canal HSR révèle clairement la suppression des signaux d'aérosols. 173
8.3 Signaux moyens corrigés de la portée mesurés à la fréquence en ligne. La suppression de la composante Mie dans le canal HSR est clairement visible. 174

List of Tables

3.1 Types and description of aerosols classified according to their origin process and source [2, 4, 11]. 22

4.1 Short-range lidar (SR-Lidar) systems for aerosol studies developed in the last years 48
4.2 HSRL systems for aerosol studies developed in the last years 58

5.1 Pulse and spectral characteristics of two commercial laser sources 81
5.2 Simulation of the spectral performance of an iodine cell and a scanning FWMI when using two commercial laser sources. 105
5.3 Design specifications of the custom-made 20-cm-long iodine cell. 106
5.4 Iodine absorption bands in the Keopsys wavelength range 113
5.5 Iodine absorption bands in the Teem Photonics laser v0 wavelength range. . 114
5.6 Iodine absorption bands in the Teem Photonics v1 wavelength range 115

6.1 ONERA-NIES SR-HSRL specifications. 126

List of Abbreviations

ACI	Aerosol–Cloud Interaction
ARI	Aerosol–Radiation Interaction
BR	Backscatter Ratio
CFP	Confocal Fabry–Pérot
CW	Continuous Wave
DPSS	Diode-Pumped Solid-State
EBL	Elastic Backscatter Lidar
ERF	Effective Radiative Forcing
FPI	Fabry–Pérot Interferometer
FSR	Free Spectral Range
FWMI	Field-Widened Michelson Interferometer
HSR	High Spectral Resolution
HSRL	High Spectral Resolution Lidar
HSR-SLidar	High Spectral Resolution Scheimpflug Lidar
MPL	Micro Pulse Lidar
NIES	National Institute for Environmental Studies (Japan)
Nd:YAG	Neodymium-Doped Yttrium Aluminum Garnet
ONERA	*Office National d'Études et de Recherches Aérospatiales*
NHL	Near-Horizontal Lidar
NIR	Near Infrared
NPBS	Non-Polarizing Beam Splitter
OPD	Optical Path Difference
PBL	Planetary Boundary Layer
PM	Particulate Matter
RCS	Range-Corrected Signal
RB	Rayleigh–Brillouin
Rb	Rubidium
SFWMI	Scanning Field-Widened Michelson Interferometer
SLidar	Scheimpflug Lidar

List of Symbols

Atmospheric and Optical Properties

A_m	Atmospheric visibility or interferometric constant	Unitless
$\alpha_{aer,mol}(r)$	Aerosol/molecular extinction coefficient	m^{-1}
$\beta_{aer,mol}(r)$	Aerosol/molecular backscatter coefficient	m^{-1} sr^{-1}
I	Irradiance	W/m^2
LR	Lidar ratio (α/β)	sr
N	Particle number concentration	m^{-3}
$N_{\mathrm{mol}}(r)$	Molecular number density profile	m^{-3}
$O_{Ray,tot}(r)$	Overlap function Rayleigh/total channel	Unitless
OD	Optical density	Unitless
OP	Optical path	m
OPD	Optical path difference	m
$P(\Theta)$	Phase function	Unitless
Θ	Scattering angle	rad
γ	Depolarization factor	Unitless
ρ	Air density	$kg{\cdot}m^{-3}$
SDR	Spectral discrimination ratio	
$S_{m,p}$	Doppler-broadened atmospheric backscattering spectra	Hz
T	Transmittance	Unitless
t	temperature	K
$U_{Ray,tot}(r)$	Rayleigh/total channel attenuated backscatter coefficient	m^{-1} sr^{-1}
χ_p	Mie crosstalk parameter	Unitless
x	Size parameter ($2\pi r/\lambda$)	Unitless
$X_{m,p}$	Effective mol./aer. transmittance through an spectral filter	Unitless

Radiometric and Instrumental Parameters

$C(r)$	Interchannel calibration parameter	Unitless
$C_{sca,\ backsca}$	Scattering/backscattering cross section	m^2
$C_{abs,\ ext}$	Absorption/extinction cross section	m^2
$D(n)$	Refractive index proportionality factor	Unitless

$\eta_{hsr,tot}$	Total optical detection efficiency	Unitless
$K_{Ray,tot}$	Radiometric constant (Rayleigh/total channel)	$V{\cdot}m^3{\cdot}sr$
E	Pulse energy	J
f_{rep}	Pulse repetition frequency	Hz
FSR	Free spectral range	Hz
$K_{abs,\ ext}$	Absorption/extinction coefficient constant	m^{-1}
L	Lens focal length	m
P	Pressure	bar
P_{avg}	Average laser pulse power	Watts
$P(r)$	Received optical power at range r	W
$P_{hsr,tot}(r)$	HSR/total channel received power	W
P_0	Transmitted laser power per pulse	W
$Q_{sca,\ backsca}$	Scattering/backscattering efficiency	Unitless
$Q_{abs,\ ext}$	Absorption/extinction efficiency	Unitless
RCS	Range-corrected signal	$V{\cdot}m^2$
Ω	Solid angle of receiver optics	sr

Fundamental Physical Quantities

c	Speed of light in vacuum	$m{\cdot}s^{-1}$
λ	Wavelength	m
ν	Frequency	Hz
ν_0	Laser central frequency	Hz
ν_{off}	Offline iodine line frequency	Hz
ω_0	Angular frequency of emitted radiation	$rad{\cdot}s^{-1}$
τ	Laser pulse length	s
r	Range or distance from lidar	m
σ	Rayleigh extinction cross section	m^2
V	Particle volume	m^3

Chapter 1

Introduction

1.1 Context

The atmosphere is the gaseous envelope that surrounds Earth and allows the existence of life. It generates the pressure that allows liquid water to exist, absorbs harmful ultraviolet (UV) solar radiation, and regulates temperature by controlling the interactions between incoming solar radiation and outgoing terrestrial radiation. Earth's atmosphere is composed of nitrogen (78%), oxygen (21%), argon (0.9%), and trace gases (0.01%) such as water vapor and carbon dioxide [1]. The atmosphere has a thermal vertical structure that depends on the balance between incoming and outgoing radiation, leading to thermal inversions that establish five distinct layers [2]. First, the troposphere (0 to 15 km) has nearly 80% of atmospheric mass and exerts the greatest influence on weather, as it contains 99% of water vapor and aerosols. Second, the stratosphere (15 to 50 km) contains the ozone layer, essential for absorbing harmful UV radiation. Third, the mesosphere (50 to 90 km), characterized by a temperature that decreases with height due to the reduction of ozone heating. Fourth, the thermosphere (90 to 500-1000 km, depending on solar activity) absorbs high-energy solar radiation, and its composition changes with altitude due to molecular diffusive separation. Finally, the exosphere (from 500-1000 km to about 10000 km, about halfway to the moon) is a transition layer between the atmosphere and outer space.

Besides gases, the atmosphere contains aerosols, also called particulate matter (PM). An atmospheric aerosol is any substance, excluding all hydrometeors, present in the atmosphere in a solid or liquid state. Aerosol sources are both natural (desert dust storms, sea salt spray, volcanic eruptions, emissions of smoke, pollen, spores, or bacteria) and anthropogenic (biomass burning from fires, fossil fuel combustion, industrial activities) [3]. As mentioned, the troposphere contains 99% of aerosols, with the remaining 1% in the lower stratosphere.

Throughout history, Earth's climate has naturally changed due to variations in the amount of solar energy received. Yet, since the last century, industrial activities have increased the concentrations of greenhouse gases such as carbon dioxide, methane, and nitrous oxide. Greenhouse gases exert positive radiative forcing, leading to temperature rises [4]. Besides gases, human activities have also increased the tropospheric concentration of atmospheric aerosols through direct emissions of aerosol particles and their precursory gases. Atmospheric aerosols directly influence the climate via aerosol-radiation interactions (ARI), either by scattering or absorbing radiation. Scattering aerosols have a cooling effect, while absorbing aerosols contribute to warming. Aerosols in the atmosphere can both scatter and absorb light, and their overall impact on Earth's energy budget depends on the characteristics of the surface and clouds [5]. Moreover, aerosols indirectly influence climate through aerosol-cloud interactions (ACI), as they serve as condensation nuclei for cloud formation. As a result, aerosols affect the microphysical properties of clouds, consequently influencing precipitation processes [6].

The aviation industry has become one of the primary sources of anthropogenic pollution. Being one of the most important global economic activities in recent decades, the number of commercial aircraft and daily flights has been constantly increasing [7, 8]. The boost in air traffic has raised concerns about the impact of aircraft emissions on local and regional air quality near airports [8]. Aircraft engines emit a variety of gaseous substances –e.g., nitrogen oxides, carbon oxides, sulfur oxides, hydrocarbons– as well as particulate matter –primary soot and sulfate aerosol particles–. These emissions alter Earth's radiative balance through ARI and the microphysics of cirrus clouds via ACI, enhancing the greenhouse effect by forming contrails and contrail-induced cirrus clouds [9, 10]. Current studies indicate that the non-CO2 components of aviation contribute approximately two-thirds of its total effective radiative forcing, with contrail cirrus accounting for the most significant portion—around +57 mW m^{-2} out of an estimated +100 mW m^{-2} in 2018. Using normalization to aviation fuel use, Lee et al. (2021) [7] estimated that the effective radiative forcing (ERF) of the aviation industry accounts for approximately 3.5% of the total anthropogenic ERF. Therefore, understanding aviation's ERF is crucial for accurately quantifying the industry's overall climate impact and for developing effective mitigation strategies.

Different techniques have been developed to study the mechanisms of interaction between atmospheric aerosols and climate, because these uncertainties are a significant limitation on the confidence in climate change projections [11]. Active remote-sensing instruments are a key component for atmospheric research, of which lidar (acronym of LIght Detection And Ranging) is one of the leading techniques, as it allows obtaining information about the

presence [12], nature [13], and spatiotemporal distribution [14] of different atmospheric constituents, covering ranges from the ground to >100 km of altitude.

The most common type of lidar is based on the elastic backscatter technique, in which the wavelength remains unchanged in the scattering process [15]. Based on the time-of-flight principle, laser pulses propagate through the atmosphere, and a photoelectric sensor detects the small percentage of light backscattered by the particles or gas molecules, providing range-resolved measurements of the aerosol distribution [15]. Despite their ability to characterize aerosols with a high or ultra-high spatiotemporal resolution, the elastic backscatter lidar (EBL) is an ill-posed problem as the signal $P(r,\lambda)$ measured at range r and wavelength λ by an EBL is proportional to two physical quantities, the backscatter $\beta(r,\lambda)$ and extinction $\alpha(r,\lambda)$ coefficients. Thus, to solve the EBL equation, one must assume a linear relationship between extinction and backscatter, called lidar ratio (LR) and defined as the ratio of $\alpha(r,\lambda)$ over $\beta(r,\lambda)$. Additionally, it is necessary to have extra atmospheric temperature and pressure profiles to calculate molecular extinction and backscatter. These assumptions limit the accuracy of the EBL technique, making it challenging to assess ultrafine particles with a backscatter coefficient close to the molecular value, such as freshly emitted soot.

Inelastic backscatter lidars using Raman scattering bypass the EBL problem by directly measuring aerosol extinction and backscatter coefficients without relying on assumptions. However, Raman lidar generally requires a long temporal resolution (typically hours) and usually operates under night conditions due to insufficient Raman backscattering intensity. Besides Raman lidar, the high spectral resolution lidar (HSRL) technique also overcomes the ill-posed EBL problem by independently measuring molecular backscattering. HSRL measures the different Doppler shifts induced by molecules and aerosols, which depend on the laser wavelength and linewidth. Depending on the atmospheric temperature and pressure, molecules move at $\sim$300 m/s by random thermal motion, inducing a frequency shift in the order of GHz ($\sim$1 to 4). On the other hand, much more massive aerosols are moved only by the effects of wind ($\sim$10 m/s) and turbulence ($\sim$1 m/s), inducing three orders of magnitude lower Doppler shifts ($\sim$3 to 100 MHz) [16–18]. Thus, the spectral distribution of the backscattered light is composed of a narrow peak near the laser central frequency due to aerosol scattering and a much wider distribution from molecular scattering [16]. HSRL requires narrow-bandwidth spectral filters and ultranarrow linewidth lasers, and the laser and filter central frequencies must be locked to each other.

1.2 Problem statement

In recent years, there has been a growing need to understand and measure the impacts of aerosols near the source for various climate, air quality, and aeronautical applications. Thus, different types of short-range lidars have been developed to determine the radiative and microphysical properties of particles over short ranges. This includes short-range elastic backscatter lidars (SR-EBLs) like micropulse lidars (MPLs) [19], near-horizontal lidars (NHLs) [20], and the Colibri Aerosol Lidars (CALs) [21, 22]. Moreover, in recent years, efforts have been made to implement short-range coherent Doppler wind lidars (CDWL) for aerosol studies [23, 24]. In particular, the CALs developed by ONERA have proven to be excellent tools for measuring particles near the source (from 10 m) with a very high spatiotemporal resolution (<10 cm, 1 ms) [21, 22]. They have introduced new diagnostic capabilities for several aeronautics and environmental applications, such as measuring the pollution emitted by airplane engines [25] and characterizing the atmosphere in the lower planetary boundary layer [26], where long-range lidars are blind. However, the inherently ill-posed EBL problem limits the accuracy of these instruments, as it does for any other elastic lidar. Furthermore, the inversion of the signals requires geometric and radiometric calibrations, as well as a dedicated forward inversion method that does not require knowledge of boundary conditions or a reference zone. Due to these intrinsic limitations, assessing ultrafine particles with a backscatter coefficient close to the molecular value, such as freshly emitted soot, poses a significant challenge for SR-EBLs. Highly precise aerosol retrievals are possible with the well-posed HSRL technique. However, these lidars have mainly been developed for long-range studies. Most existing HSRLs are unable to perform measurements close to the emission source due to two limitations. First, they are often blind for the first hundred meters due to the overlap problem. This is mainly because they emphasize the total measurement range by configuring the system to have a longer full-overlap distance. Second, their spatiotemporal resolution is inadequate for short-range applications as they prioritize spectral performance and signal accuracy by using low-repetition-rate, ultra-narrowband (and therefore long-pulse) lasers.

To the best of our knowledge, only one short-range HSRL has been reported in the literature to date. It is a continuous wave (CW) near-infrared high spectral resolution Scheimpflug lidar (HSR-SLidar) for atmospheric aerosol sensing, developed by Chang et al. [27]. Based on the Scheimpflug principle, this system transmits an intensity-modulated 780 nm CW laser beam into the atmosphere. Then, it obtains the range-resolved atmospheric lidar signal from the pixel intensities of a tilted image sensor that satisfies the Scheimpflug principle. To match the laser wavelength, a temperature-stabilized rubidium cell was used as a spectral filter, achieving a spectral discrimination ratio of up to 10^4. Due to this operational principle,

the HSR-SLidar presents several advantages, including its low cost, low instrumental complexity, and a blind overlap zone of less than 30 m. However, there are also some inherent disadvantages. First, the spatial resolution is range-dependent, decreasing with increasing measurement distance. Second, the pixel-distance relationship must be calibrated by measuring the beam spot from a distant building with a known distance. Additionally, it does not allow continuous, synchronized data acquisition because it requires precise, stepwise wavelength switching of the CW laser. This causes instability in the laser wavelength, requiring a dual-exposure scheme to address it. The first exposure is for waiting for wavelength stabilization, and the second one for performing lidar measurements. This process introduces extended integration periods, resulting in lower temporal resolution to ensure measurement fidelity [27].

To close the gap in highly accurate, highly spatiotemporally resolved aerosol characterization at short ranges, this thesis presents a proof-of-concept of a novel short-range lidar: a short-range high spectral resolution lidar (SR-HSRL). A thorough search of the relevant literature found that no time-of-flight-based HSRL has been reported for short-range aerosol studies due to several technical (e.g., finding the right laser pulse length and linewidth compromise) and scientific (e.g., overlap determination, signal inversion) challenges. This novel instrument offers greater accuracy because the HSRL is a well-posed problem that can be solved without assumptions, enabling a more straightforward inversion of particles' radiometric and microphysical properties.

1.3 Scientific approach

The objective of this thesis is to bridge the gap between short-range elastic backscatter lidars and long-range high spectral resolution lidars, thereby improving the accuracy of aerosol characterization near the source. For this purpose, a short-range high spectral resolution lidar prototype capable of measuring the radiative properties of aerosols with high spatiotemporal and spectral resolution was developed. This new technique would offer a relevant technological solution for numerous applications, ranging from aeronautics (e.g., aviation pollution, engine emissions) to environmental (e.g., measuring the low planetary boundary layer).

First, the prototype design presented an essential technical challenge: finding a laser source that fulfilled several requirements. First, it had to be spectrally fine and stable enough to perform HSRL measurements, while also having a pulse width of a few nanoseconds to enable short-range measurements with good spatiotemporal resolution. Second, it had to be wavelength-tunable to enable the use of vapor cells as spectral filters. Lastly, it had to

be lightweight and compact to be installed in a portable lidar system. Therefore, selecting the right laser required developing a methodology and a laboratory testing bench for the complete characterization of different lasers, as manufacturers do not provide complete spectral and pulse information. The other technical challenges included testing and selecting the appropriate spectral filter, designing and constructing the prototype, validating spectral performance under controlled laboratory conditions, and performing field tests under real atmospheric conditions.

From a scientific perspective, the challenges included developing a dedicated inversion method to retrieve calibrated backscatter profiles without making any assumptions. For this purpose, the general HSRL inversion method was adapted for short-range measurements by developing a methodology to retrieve the overlap functions and radiometric constants for the two lidar channels solely from calibration measurements and corrected signals.

To successfully develop this short-range HSRL prototype, we have set several specific objectives, which are described below.

O.1 Simulation-based design and estimation of the performance: To design a novel short-range high spectral resolution lidar prototype based on a comprehensive review of state-of-the-art short-range elastic backscatter and high spectral resolution lidar systems, and on the development of an end-to-end numerical model to guide the optical and spectral design. This model will be used to simulate and evaluate the spectral performance of candidate filters (a scanning interferometer and a vapor cell), determine key design parameters –such as free spectral range, cavity length, and operating temperature– and estimate the spectral discrimination ratio for different laser linewidths. The combination of the state-of-the-art review and simulation-based analysis will establish the technological feasibility, novelty, and expected performance limitations of the proposed SR-HSRL system.

O.2 Laboratory testing and validation of the performance: To develop a comprehensive methodology for the characterization of the temporal and spectral properties of commercial laser sources, and to perform laboratory validation measurements of the spectral performance of two candidate filters (a scanning interferometer and a vapor cell) for the selected lasers. Based on these results, a first short-range high spectral resolution lidar (SR-HSRL) prototype will be assembled and its performance evaluated under controlled laboratory conditions. Finally, in collaboration with the National Institute for Environmental Studies (NIES) of Japan, the prototype's capability to retrieve aerosol radiative properties with high accuracy and stability will be evaluated during a field campaign.

O.3 Retrieval of calibrated backscattering coefficient profiles: To apply the proposed data inversion methodology on the field-campaign data to retrieve calibrated backscatter coefficient profiles in the short range without relying on lidar ratio assumptions. The proposed methodology will be applied to determine the system's overlap and radiometric calibration constants, derive attenuated backscatter profiles, and retrieve calibrated aerosol backscattering coefficients without assumptions. The retrieved profiles will be compared with those obtained from other reported HSRL systems to assess the consistency and performance of the developed prototype. This comparison aims to highlight the novelty of the SR-HSRL approach, particularly its ability to achieve assumption-free aerosol retrievals over short ranges, an advancement not previously reported in the literature.

1.4 Outline

This dissertation describes the development of a novel short-range high spectral resolution lidar following the outline below.

In Chapter 3, the objective is to present the theoretical framework to understand aerosols and their radiative properties. This is necessary to understand the HSRL working principle, which is described in detail. Special focus is placed on the overlap function, a key parameter for short-range measurements. Then, the data inversion method is described in detail, including signal pre-processing and the methodology for retrieving calibrated aerosol backscatter coefficient profiles from the effective transmittance of the aerosol and molecular spectra through the spectral filter, and the attenuated backscatter coefficient for each channel.

In Chapter 4, the objective is to present a comprehensive review of the current state of the art in short-range lidar and high spectral resolution lidar. The purpose is to identify the novelty, challenges, and potential technological limitations involved in developing a short-range HSRL for aerosol characterization. The chapter first reviews recent advances in short-range lidars for aerosol studies, emphasizing their operating principles (elastic backscatter lidars and Scheimpflug imaging lidars), system architectures, laser specifications, and applications in near-field aerosol studies. Then, it presents existing HSRL systems developed for aerosol applications, their complete laser-source specifications, and spectral discrimination mechanisms. For both lidar techniques, particular attention is given to the technical specifications –such as laser source characteristics, spectral filters, spatial and temporal resolution, and measurement range– as well as to their respective inversion techniques. This analysis

provides the technological and conceptual foundation for the design choices made in the proposed SR-HSRL system.

In Chapter 5, the objective is to present the numerical model developed to optimize the design of the SR-HSRL prototype and to estimate its ability to differentiate Mie and Rayleigh-Brillouin scattering spectra. We evaluate the effects of large laser linewidths in the effective transmission of both scattering terms through two different spectral filters, which is not reported in the literature. To this aim, we implement the equations describing the transmission of the Mie and Rayleigh-Brillouin scattering spectra through the two spectral filters most widely used in the literature, a field-widened scanning Michelson interferometer and an iodine cell. The objective is to develop a numerical model capable of evaluating the spectral discrimination ratio (SDR) for different filter-laser combinations, as there was no reference value for the expected performance of our prototype. This model was developed to obtain SDR vs linewidth results and graphs. The idea behind implementing the numerical model is to identify the laser-spectral filter configuration that maximizes the lidar's capacity to discriminate scattering spectra, thereby enabling an understanding of its limitations and expected performance. Finally, we present the design of an optimized version of both spectral filters to boost lidar spectral performance to the limit set by the laser linewidth. Finally, this chapter presents the laboratory tests and validation of the instrument's spectral performance. For this purpose, a comprehensive methodology is developed to characterize the pulse and spectral characteristics of different laser sources. Eight laser candidates were tested, and the two with the optimal compromise between pulse and spectral features were selected.

In Chapter 6, the objective is to prove the feasibility of short-range implementation of the HSRL technique. This is demonstrated through the development and evaluation of an SR-HSRL prototype that integrates a 40-cm-long iodine vapor cell and a non-conventional, high-repetition-rate diode-based laser with a 300 MHz linewidth and 5 ns pulse duration. To test the SR-HSRL prototype, a validation campaign was performed at NIES (National Institute for Environmental Studies) in Tsukuba, Japan, in July 2024. The proposed data inversion methodology is implemented for this two-day measurement campaign. Accordingly, we present the signal preprocessing, the characterization of the system's overlap function and radiometric constants, and the obtained aerosol backscatter coefficient profiles. We discuss the results and compare the advantages of our prototype with those of the only other short-range HSRL reported in the literature, the HSR Scheimpflug lidar. The results demonstrate that it is possible to perform HSRL measurements with such a wide-linewidth laser, achieving a spectral discrimination ratio of 300, which is sufficient to detect multiple aerosol

layers while maintaining a high range (7.5 m) and temporal (6 s) resolution. It is also shown that, unlike EBLs, the developed SR-HSRL system is effective for investigating clouds and cloud–aerosol interactions, as it enables measurements both within and above clouds.

Finally, in Chapter 7, the purpose is to present the main findings and scientific contributions of this work, along with the design and preliminary results of the ultra-short-range implementation of the developed SR-HSR, a more compact version intended for mobile and airborne applications. The chapter describes the test campaign conducted at ONERA Toulouse, during which the instrument's overlap function and radiometric constant were experimentally determined. The validation of the system's spectral performance is discussed, including an analysis of the stability of the spectral filter's transmission spectrum and the suppression of the Mie component in the molecular channel. Afterwards, the chapter presents preliminary attenuated backscatter coefficient profiles for various aerosols generated under controlled conditions in an aerosol chamber. Finally, the improvements and perspectives of this ultra-short-range HSRL prototype are discussed.

Chapter 2

Introduction

2.1 Contexte

L'atmosphère est l'enveloppe gazeuse qui entoure la Terre et rend possible l'existence de la vie. Elle génère la pression nécessaire à l'existence de l'eau liquide, absorbe le rayonnement solaire ultraviolet (UV) nocif et régule la température en contrôlant les interactions entre le rayonnement solaire incident et le rayonnement terrestre sortant. L'atmosphère terrestre est composée d'azote (78 %), d'oxygène (21 %), d'argon (0,9 %) et de gaz traces (0,01 %) tels que la vapeur d'eau et le dioxyde de carbone [1]. Sa structure verticale thermique dépend du bilan entre le rayonnement entrant et sortant, ce qui conduit à des inversions thermiques définissant cinq couches distinctes [2]. Premièrement, la troposphère (0 à 15 km) contient près de 80 % de la masse atmosphérique et exerce la plus grande influence sur la météorologie, car elle renferme 99 % de la vapeur d'eau et des aérosols. Deuxièmement, la stratosphère (15 à 50 km) abrite la couche d'ozone, essentielle pour l'absorption du rayonnement UV. Troisièmement, la mésosphère (50 à 90 km), caractérisée par une température décroissant avec l'altitude du fait de la diminution du chauffage par l'ozone. Quatrièmement, la thermosphère (90 à 500–1000 km, selon l'activité solaire) absorbe le rayonnement solaire de haute énergie, et sa composition varie avec l'altitude en raison de la séparation diffusive moléculaire. Enfin, l'exosphère (de 500–1000 km jusqu'à environ 10 000 km, soit la moitié de la distance Terre–Lune) constitue la zone de transition entre l'atmosphère et l'espace.

Outre les gaz, l'atmosphère contient des aérosols, également appelés particules (PM). Un aérosol atmosphérique est toute substance, à l'exclusion des hydrométéores, présente dans l'atmosphère à l'état solide ou liquide. Les sources d'aérosols sont à la fois naturelles (tempêtes de poussières désertiques, embruns marins, éruptions volcaniques, émissions de fumées, pollen, spores ou bactéries) et anthropiques (brûlage de biomasse, combustion d'énergies fossiles, activités industrielles) [3]. Comme indiqué, la troposphère contient 99 % des aérosols, le 1 % restant se trouvant dans la basse stratosphère.

Au cours de l'histoire, le climat de la Terre a naturellement varié en raison des changements de l'énergie solaire reçue. Cependant, depuis le siècle dernier, les activités industrielles ont augmenté les concentrations de gaz à effet de serre tels que le dioxyde de carbone, le méthane et le protoxyde d'azote. Les gaz à effet de serre exercent un forçage radiatif positif, entraînant une hausse des températures [4]. Parallèlement aux gaz, les activités humaines ont aussi accru la concentration troposphérique des aérosols atmosphériques via les émissions directes de particules et de leurs précurseurs gazeux. Les aérosols influencent directement le climat par les interactions aérosol–rayonnement (IAR), soit par diffusion, soit par absorption du rayonnement. Les aérosols diffusants tendent à refroidir, tandis que les aérosols absorbants contribuent au réchauffement. Dans l'atmosphère, les aérosols peuvent à la fois diffuser et absorber la lumière, et leur impact net sur le bilan énergétique terrestre dépend des caractéristiques de la surface et des nuages [5]. En outre, les aérosols influencent indirectement le climat via les interactions aérosol–nuage (IAN), en servant de noyaux de condensation pour la formation des nuages. Ils affectent ainsi les propriétés microphysiques des nuages et, par conséquent, les processus de précipitation [6].

Le secteur aérien est devenu l'une des principales sources de pollution anthropique. Activité économique majeure des dernières décennies, le nombre d'aéronefs commerciaux et de vols quotidiens n'a cessé d'augmenter [7, 8]. Cette hausse du trafic aérien a suscité des préoccupations quant à l'impact des émissions aéronautiques sur la qualité de l'air locale et régionale à proximité des aéroports [8]. Les moteurs d'avion émettent diverses espèces gazeuses — p. ex., oxydes d'azote, oxydes de carbone, oxydes de soufre, hydrocarbures — ainsi que des particules — suies primaires et aérosols sulfatés. Ces émissions modifient le bilan radiatif terrestre via les IAR et la microphysique des cirrus au travers des IAN, en renforçant l'effet de serre par la formation de traînées de condensation et de cirrus induits par traînées [9, 10]. Les études actuelles indiquent que les composantes non liées au CO_2 de l'aviation représentent environ les deux tiers de son forçage radiatif effectif total, les cirrus de traînées constituant la part la plus importante — environ +57 mW m^{-2} sur un total estimé à +100 mW m^{-2} en 2018. En normalisant par la consommation de carburant aérien, Lee *et al.* (2021) [7] estiment que le forçage radiatif effectif (ERF) de l'aviation représente environ 3,5 % de l'ERF anthropique total. La compréhension de l'ERF de l'aviation est donc cruciale pour quantifier précisément son impact climatique global et élaborer des stratégies d'atténuation efficaces.

Différentes techniques ont été développées pour étudier les mécanismes d'interaction entre les aérosols atmosphériques et le climat, car ces incertitudes limitent fortement la confiance dans les projections de changement climatique [11]. Les instruments de télédétection active sont des éléments clés de la recherche atmosphérique, parmi lesquels le lidar

(acronyme de *LIght Detection And Ranging*) constitue l'une des techniques de référence, car il permet d'obtenir des informations sur la présence [12], la nature [13] et la distribution spatio-temporelle [14] de différents constituants atmosphériques, sur des portées allant du sol à plus de >100 km d'altitude.

Le type de lidar le plus répandu repose sur la technique de rétrodiffusion élastique, dans laquelle la longueur d'onde demeure inchangée au cours du processus de diffusion [15]. Fondé sur le principe du temps de vol, le lidar émet des impulsions laser qui se propagent dans l'atmosphère, et un capteur photoélectrique détecte le faible pourcentage de lumière rétrodiffusée par les particules ou les molécules, fournissant des mesures résolues en distance de la distribution des aérosols [15]. Malgré leur capacité à caractériser les aérosols avec une résolution spatio-temporelle élevée ou ultra-élevée, les lidars à rétrodiffusion élastique (EBL) posent un problème mal posé, car le signal $P(r,\lambda)$ mesuré à la distance r et à la longueur d'onde λ par un EBL est proportionnel à deux grandeurs physiques, les coefficients de rétrodiffusion $\beta(r,\lambda)$ et d'extinction $\alpha(r,\lambda)$. Pour résoudre l'équation du lidar élastique, il est donc nécessaire de supposer une relation linéaire entre extinction et rétrodiffusion, appelée *rapport lidar* (LR), défini comme le rapport de $\alpha(r,\lambda)$ sur $\beta(r,\lambda)$. De plus, il faut disposer de profils atmosphériques supplémentaires de température et de pression afin de calculer l'extinction et la rétrodiffusion moléculaires. Ces hypothèses limitent la précision de la technique EBL, rendant difficile l'évaluation des particules ultrafines dont le coefficient de rétrodiffusion est proche de la valeur moléculaire, telles que les suies fraîchement émises.

Les lidars à rétrodiffusion inélastique utilisant la diffusion Raman contournent le problème EBL en mesurant directement les coefficients d'extinction et de rétrodiffusion des aérosols sans recourir à des hypothèses. Toutefois, le lidar Raman requiert généralement une résolution temporelle longue (typiquement de l'ordre de l'heure) et fonctionne de préférence de nuit en raison de l'intensité insuffisante de la rétrodiffusion Raman. Outre le lidar Raman, la technique du lidar à haute résolution spectrale (HSRL) permet également de surmonter le caractère mal posé de l'EBL en mesurant indépendamment la rétrodiffusion moléculaire. Le HSRL exploite les décalages Doppler distincts induits par les molécules et les aérosols, qui dépendent de la longueur d'onde et de la largeur de raie du laser. Selon la température et la pression atmosphériques, les molécules se déplacent à $\sim$300 m/s par agitation thermique aléatoire, induisant un décalage fréquentiel de l'ordre du GHz ($\sim$1 à 4). À l'inverse, les aérosols, bien plus massifs, sont animés principalement par le vent ($\sim$10 m/s) et la turbulence ($\sim$1 m/s), induisant des décalages Doppler trois ordres de grandeur plus faibles ($\sim$3 à 100 MHz) [16–18]. Le spectre de la lumière rétrodiffusée est ainsi composé d'un pic étroit proche de la fréquence centrale du laser, dû à la diffusion par les aérosols, et d'une distribution beaucoup plus large, due à la diffusion moléculaire [16]. Le HSRL nécessite des filtres

spectraux à bande passante étroite et des lasers à largeur de raie ultra-étroite, les fréquences centrales du laser et du filtre devant être verrouillées l'une à l'autre.

2.2 Problématique

Ces dernières années, la nécessité de comprendre et de mesurer les impacts des aérosols à proximité des sources s'est accrue pour diverses applications liées au climat, à la qualité de l'air et à l'aéronautique. Différents lidars de courte portée ont donc été développés pour déterminer les propriétés radiatives et microphysiques des particules sur de courtes distances. Cela inclut les lidars élastiques de courte portée (SR-EBL) tels que les lidars micropulsés (MPL) [19], les lidars quasi-horizontaux (NHL) [20] et les Colibri Aerosol Lidars (CAL) [21, 22]. Par ailleurs, des efforts récents ont visé la mise en œuvre de lidars Doppler cohérents de courte portée (CDWL) pour l'étude des aérosols [23, 24]. En particulier, les CAL développés à l'ONERA se sont révélés des outils d'excellence pour mesurer les particules à proximité de la source (à partir de 10 m) avec une très haute résolution spatio-temporelle (<10 cm, 1 ms) [21, 22]. Ils ont ouvert de nouvelles capacités de diagnostic pour plusieurs applications aéronautiques et environnementales, comme la mesure de la pollution émise par les moteurs d'avion [25] et la caractérisation de l'atmosphère dans la basse couche limite planétaire [26], là où les lidars longue portée sont aveugles. Cependant, le caractère intrinsèquement mal posé de l'EBL limite la précision de ces instruments, comme pour tout lidar élastique. De plus, l'inversion des signaux requiert des calibrations géométriques et radiométriques, ainsi qu'une méthode d'inversion directe dédiée ne nécessitant ni conditions aux limites ni zone de référence. En raison de ces limitations intrinsèques, l'évaluation des particules ultrafines présentant un coefficient de rétrodiffusion proche de la valeur moléculaire, telles que les suies fraîchement émises, constitue un défi majeur pour les SR-EBL. Des restitutions d'aérosols très précises sont possibles avec la technique HSRL, qui est un problème bien posé. Néanmoins, ces lidars ont principalement été conçus pour des études de longue portée. La plupart des HSRL existants ne peuvent pas mesurer au plus près de la source d'émission pour deux raisons. Premièrement, ils sont souvent aveugles sur les premières centaines de mètres en raison du problème de recouvrement, car la configuration privilégie une grande portée au prix d'une distance de plein recouvrement plus longue. Deuxièmement, leur résolution spatio-temporelle est insuffisante pour les applications de courte portée, car ils privilégient la performance spectrale et la précision du signal, recourant à des lasers à très faible fréquence de répétition, ultra-étroits en bande (et donc à impulsions longues).

À notre connaissance, un seul HSRL de courte portée a été rapporté à ce jour dans la littérature. Il s'agit d'un lidar à haute résolution spectrale proche infrarouge continu (CW) fondé sur le principe de Scheimpflug (HSR-SLidar) pour la détection des aérosols atmosphériques, développé par Chang *et al*. [27]. Basé sur le principe de Scheimpflug, ce système transmet un faisceau laser continu à 780 nm modulé en intensité dans l'atmosphère. Le signal lidar résolu en distance est ensuite obtenu à partir des intensités de pixels d'un capteur d'image incliné satisfaisant le principe de Scheimpflug. Pour accorder la longueur d'onde laser, une cellule au rubidium thermostabilisée a été utilisée comme filtre spectral, atteignant un taux de discrimination spectrale allant jusqu'à 10^4. En raison de ce principe de fonctionnement, le HSR-SLidar présente plusieurs avantages, dont un coût réduit, une faible complexité instrumentale et une zone aveugle de recouvrement inférieure à 30 m. Il présente néanmoins des inconvénients intrinsèques. D'abord, la résolution spatiale dépend de la distance, décroissant avec l'augmentation de la portée. Ensuite, la relation pixel–distance doit être calibrée en mesurant l'empreinte du faisceau sur un bâtiment lointain de distance connue. De plus, il n'autorise pas une acquisition continue et synchronisée des données, car il requiert un balayage par paliers précis de la longueur d'onde du laser CW. Cela induit une instabilité de la longueur d'onde laser, nécessitant un schéma à double exposition : la première pour l'attente de stabilisation, la seconde pour la mesure lidar. Ce procédé impose des temps d'intégration allongés, ce qui dégrade la résolution temporelle afin de préserver la fidélité des mesures [28].

Pour combler le déficit en caractérisation d'aérosols à courte portée à la fois très précise et à haute résolution spatio-temporelle, cette thèse présente la preuve de concept d'un lidar inédit : un lidar à haute résolution spectrale de courte portée (SR-HSRL). Une revue approfondie de la littérature pertinente n'a identifié aucun HSRL fondé sur le temps de vol pour des études d'aérosols à courte portée, en raison de difficultés techniques (p. ex., compromis longueur d'impulsion/largeur de raie) et scientifiques (p. ex., détermination du recouvrement, inversion du signal). Cet instrument novateur offre une précision accrue, le problème HSRL étant bien posé et se résolvant sans hypothèses, ce qui permet une inversion plus directe des propriétés radiométriques et microphysiques des particules.

2.3 Démarche scientifique

L'objectif de cette thèse est de réduire l'écart entre les lidars élastiques de courte portée et les lidars à haute résolution spectrale de longue portée, afin d'améliorer la précision de la caractérisation des aérosols au voisinage des sources. À cette fin, un prototype de HSRL de courte portée, capable de mesurer les propriétés radiatives des aérosols avec une haute

résolution spatio-temporelle et spectrale, a été développé. Cette nouvelle approche constitue une solution technologique pertinente pour de nombreuses applications, de l'aéronautique (p. ex., pollution aérienne, émissions moteurs) à l'environnement (p. ex., mesure de la basse couche limite planétaire).

La conception du prototype posait un défi technique central : identifier une source laser satisfaisant plusieurs exigences. D'une part, elle devait être suffisamment fine et stable spectr al e pour réaliser des mesures HSRL, tout en présentant une largeur d'impulsion de quelques nanosecondes afin de permettre des mesures à courte portée avec une bonne résolution spatio-temporelle. D'autre part, elle devait être accordable en longueur d'onde pour permettre l'utilisation de cellules à vapeur comme filtres spectraux. Enfin, elle devait être légère et compacte pour une intégration dans un lidar portable. Le choix du laser a donc nécessité l'élaboration d'une méthodologie et d'un banc d'essais de laboratoire pour la caractérisation complète de différentes sources, les fabricants ne fournissant pas toutes les informations temporelles et spectrales pertinentes. Les autres défis techniques incluaient l'essai et la sélection du filtre spectral approprié, la conception et la réalisation du prototype, la validation des performances spectrales en conditions contrôlées, puis les essais sur le terrain en conditions atmosphériques réelles.

Du point de vue scientifique, les défis comprenaient le développement d'une méthode d'inversion dédiée pour restituer des profils de rétrodiffusion calibrés sans recourir à des hypothèses. À cette fin, la méthode d'inversion HSRL classique a été adaptée à la courte portée en établissant une méthodologie pour déterminer les fonctions de recouvrement et les constantes radiométriques des deux canaux du lidar à partir des seules mesures de calibration et des signaux corrigés.

Afin de mener à bien le développement de ce prototype SR-HSRL, nous avons défini plusieurs objectifs spécifiques, détaillés ci-dessous.

O.1 Conception fondée sur la simulation et estimation des performances : concevoir un prototype de HSRL de courte portée à partir d'une revue exhaustive de l'état de l'art des lidars élastiques de courte portée et des HSRL, et du développement d'un modèle numérique de bout en bout pour guider la conception optique et spectrale. Ce modèle sera utilisé pour simuler et évaluer les performances spectrales de filtres candidats (un interféromètre à balayage et une cellule à vapeur), déterminer des paramètres clés de conception — tels que l'intervalle spectral libre, la longueur de cavité et la température de fonctionnement — et estimer le taux de discrimination spectrale pour différentes largeurs de raie laser. La combinaison de l'état de l'art et de l'analyse par

simulation établira la faisabilité technologique, la nouveauté et les limites de performance attendues du système SR-HSRL proposé.

O.2 Essais en laboratoire et validation des performances : développer une méthodologie complète pour la caractérisation des propriétés temporelles et spectrales de sources laser commerciales, et réaliser des validations expérimentales en laboratoire des performances spectrales de deux filtres candidats (interféromètre à balayage et cellule à vapeur) pour les lasers retenus. Sur cette base, assembler un premier prototype SR-HSRL de courte portée et évaluer ses performances en conditions contrôlées. Enfin, en collaboration avec le National Institute for Environmental Studies (NIES, Japon), évaluer la capacité du prototype à restituer avec précision et stabilité les propriétés radiatives des aérosols lors d'une campagne de terrain.

O.3 Restitution de profils calibrés du coefficient de rétrodiffusion : appliquer la méthodologie d'inversion proposée aux données de la campagne de terrain afin d'obtenir des profils calibrés du coefficient de rétrodiffusion à courte portée, sans hypothèses sur le rapport lidar. La méthodologie sera utilisée pour déterminer la fonction de recouvrement et les constantes de calibration radiométrique du système, dériver les profils de rétrodiffusion atténuée et restituer les coefficients de rétrodiffusion des aérosols calibrés sans hypothèses. Les profils obtenus seront comparés à ceux d'autres systèmes HSRL rapportés dans la littérature pour évaluer la cohérence et les performances du prototype développé. Cette comparaison vise à mettre en évidence la nouveauté de l'approche SR-HSRL, en particulier sa capacité à fournir des restitutions d'aérosols sans hypothèses sur de courtes distances, ce qui n'avait pas été rapporté auparavant.

2.4 Organisation du manuscrit

Cette dissertation décrit le développement d'un nouveau lidar HSRL de courte portée selon la structure suivante.

Le Chapitre 3 présente le cadre théorique nécessaire à la compréhension des aérosols et de leurs propriétés radiatives. Il introduit en détail le principe de fonctionnement du HSRL, avec un accent particulier sur la fonction de recouvrement, paramètre clé pour les mesures à courte portée. La méthode d'inversion des données est ensuite exposée en détail, incluant le prétraitement des signaux et la méthodologie de restitution des profils calibrés du coefficient de rétrodiffusion des aérosols à partir de la transmittance effective des spectres aérosol et moléculaire à travers le filtre spectral, ainsi que du coefficient de rétrodiffusion atténuée

pour chaque canal.

Le Chapitre 4 propose une revue exhaustive de l'état de l'art des lidars de courte portée et des HSRL. L'objectif est d'identifier la nouveauté, les défis et les limitations technologiques potentielles associés au développement d'un HSRL de courte portée pour la caractérisation des aérosols. Le chapitre commence par un bilan des avancées récentes des lidars de courte portée dédiés aux aérosols, en insistant sur leurs principes de fonctionnement (lidars à rétrodiffusion élastique et lidars d'imagerie Scheimpflug), leurs architectures système, les spécifications laser et leurs applications en proche champ. Il présente ensuite les systèmes HSRL existants développés pour l'étude des aérosols, leurs spécifications complètes de source laser et leurs mécanismes de discrimination spectrale. Pour les deux techniques lidar, une attention particulière est portée aux spécifications techniques — caractéristiques des sources laser, filtres spectraux, résolutions spatiale et temporelle, et plage de mesure — ainsi qu'aux méthodes d'inversion associées. Cette analyse fournit les bases technologiques et conceptuelles des choix de conception retenus pour le système SR-HSRL proposé.

Le Chapitre 5 décrit le modèle numérique développé pour optimiser la conception du prototype SR-HSRL et estimer sa capacité à distinguer les spectres de diffusion de Mie et de Rayleigh–Brillouin. Nous évaluons l'effet de grandes largeurs de raie laser sur la transmission effective des deux composantes de diffusion au travers de deux filtres spectraux, ce qui n'est pas rapporté dans la littérature. À cette fin, nous implémentons les équations décrivant la transmission des spectres de diffusion de Mie et de Rayleigh–Brillouin à travers les deux filtres les plus utilisés dans la littérature : un interféromètre de Michelson à élargissement de champ et balayage, et une cellule à iode. L'objectif est de disposer d'un modèle numérique capable d'évaluer le *spectral discrimination ratio* (SDR) pour différentes combinaisons filtre–laser, en l'absence de valeur de référence des performances attendues de notre prototype. Ce modèle a été développé pour obtenir des résultats et des graphes SDR en fonction de la largeur de raie. L'idée est d'identifier la configuration laser–filtre spectral maximisant la capacité du lidar à discriminer les spectres de diffusion, afin d'en cerner les limites et les performances attendues. Enfin, nous présentons la conception d'une version optimisée des deux filtres spectraux afin de pousser les performances spectrales du lidar vers la limite imposée par la largeur de raie laser. Enfin, ce chapitre présente les essais de laboratoire et la validation des performances spectrales de l'instrument. À cette fin, une méthodologie complète est proposée pour caractériser les propriétés impulsionnelles et spectrales de différentes sources laser. Huit lasers candidats ont été testés, et les deux présentant le meilleur compromis entre caractéristiques impulsionnelles et spectrales ont été sélectionnés.

Le Chapitre 6 a pour objectif de démontrer la faisabilité d'une mise en œuvre à courte portée de la technique HSRL. Cela est montré au moyen du développement et de l'évaluation d'un prototype SR-HSRL intégrant une cellule à vapeur d'iode de 40 cm et un laser à diode non conventionnel, à haute fréquence de répétition, de largeur de raie 300 MHz et de durée d'impulsion 5 ns. Pour tester le prototype, une campagne de validation a été menée au NIES (National Institute for Environmental Studies), à Tsukuba (Japon), en juillet 2024. La méthodologie d'inversion proposée est appliquée à ces deux journées de mesures. Nous présentons le prétraitement des signaux, la caractérisation de la fonction de recouvrement et des constantes radiométriques du système, ainsi que les profils obtenus du coefficient de rétrodiffusion des aérosols. Les résultats sont discutés et les avantages de notre prototype sont comparés à ceux du seul autre HSRL de courte portée rapporté dans la littérature, le lidar Scheimpflug HSR. Les résultats montrent qu'il est possible d'effectuer des mesures HSRL avec un laser à largeur de raie aussi grande, en atteignant un taux de discrimination spectrale d'environ 300, suffisant pour détecter plusieurs couches d'aérosols tout en conservant une haute résolution en distance (7,5 m) et temporelle (6 s). Il est également montré que, contrairement aux EBL, le SR-HSRL développé est pertinent pour l'étude des nuages et des interactions nuage–aérosol, car il permet des mesures à l'intérieur et au-dessus des nuages.

Enfin, le Chapitre 7 présente les principaux résultats et contributions scientifiques de ce travail, ainsi que la conception et les premiers résultats de l'implémentation ultra-courte portée du SR-HSRL développé, une version plus compacte destinée aux applications mobiles et aéroportées. Le chapitre décrit la campagne d'essais conduite à l'ONERA Toulouse, au cours de laquelle la fonction de recouvrement et la constante radiométrique de l'instrument ont été déterminées expérimentalement. La validation des performances spectrales du système est discutée, incluant une analyse de la stabilité du spectre de transmission du filtre spectral et de la suppression de la composante Mie dans le canal moléculaire. Sont ensuite présentés des profils préliminaires du coefficient de rétrodiffusion atténuée pour divers aérosols générés en conditions contrôlées dans une chambre à aérosols. Enfin, les améliorations et perspectives de ce prototype HSRL ultra-courte portée sont discutées.

Chapter 3

HSRL fundamentals

Aerosols interact with radiation through scattering and absorption processes, with scattering dominating absorption in the visible wavelengths. Aerosols that scatter solar radiation have a cooling effect, while those that absorb solar radiation have a warming effect. In the atmosphere, a mixture of scattering and absorbing aerosols exists, and their net effect on Earth's energy budget depends on surface and cloud characteristics [5]. Thus, to understand the net effect of aerosols on climate, it is necessary to assess their effective radiative forcing (ERF). As stated by the Sixth Assessment Report of the Intergovernmental Panel on Climate Change (IPCC) [29], "aerosol ERF uncertainty was assessed as the largest contributor to the overall ERF uncertainty since 1750". In climate change projections, the most significant uncertainties are related to aerosol-radiation interactions, where ERF = –0.3 ± 0.3 Wm^{-2} (medium confidence), and aerosol-cloud interactions, where the ERF is –1.0 ± 0.7 Wm^{-2} (medium confidence) [30]. To mitigate these uncertainties, it is crucial to investigate the radiative properties of aerosols, particularly their interaction with radiation through absorption or scattering. Characterizing these parameters is crucial for evaluating aerosol radiative forcing, constraining climate models, and enhancing future projections.

In this chapter, the bases of aerosol science are discussed, including the microphysical and radiative properties. The primary focus is on absorption and scattering, the physical principles of the lidar technique. Then, we propose a dedicated SR-HSRL inversion method. It is based on the absolute calibration of the system via the interchannel calibration parameter, obtained from offline measurements. From this parameter, the total signal is corrected. Then, Mie crosstalk is assessed and removed from the HSR channel, yielding a purely molecular signal. This allows determining the overlap functions and radiometric constants of both channels. Then, the backscatter ratio is calculated from attenuated backscatter and the filter's characterization measurements, enabling an assumption-free retrieval of aerosol backscatter coefficients.

3.1 Atmospheric aerosols

As mentioned earlier, the term atmospheric aerosol refers to any substance present in the atmosphere in solid or liquid state by natural or anthropogenic sources, except for all hydrometeors (cloud droplets, ice crystals, raindrops, snowflakes, and graupel) [3]. 99% of aerosols are suspended in the troposphere, with the remaining 1% being situated in the low stratosphere. The heterogeneous nature of aerosol sources, combined with their relatively short residence time, leads to highly variable spatial and temporal concentrations. Moreover, due to their widespread size distributions, it is usually preferable to study aerosol populations rather than individual particles [2]. The main characteristics of an aerosol population are its chemical composition, particle size distribution, and shape.

Aerosols can be classified according to their size distribution, their source or origin process. Table 3.1 presents a summary of the last two categories.

Classification	**Description**	**Aerosol types**
Origin process		
Primary	Emitted as particles	Black carbon, dust, biomass burning, sea salt, fuels, etc.
Secondary	Formed by condensation of gas-phase species	Sulfur, nitrogen, plus carbonaceous and organic materials
Source		
Biological	Released from living organisms or viruses	Seeds, pollen, spores, bacteria, protozoa, algae, viruses
Marine	Unleashed from the oceans	Sea salt and other forms of chlorides and sulfates
Mineral	Transfered from continental surfaces	Desert dust, urban ash, soil particles
Biomass	Produced by burning organic materials	Organic and brown carbon
Anthropogenic	Resulting from any human activity	Road dust, industrial processes, biomass burning, wind erosion of tilled land, fuel combustion, mining, etc.

TABLE 3.1: Types and description of aerosols classified according to their origin process and source [2, 4, 11].

3.1.1 Microphysical properties

Atmospheric aerosols are usually classified into three modes according to their size [31], as summarized in Fig. 3.1.

- **Nucleation mode:** Clusters the smallest aerosols ($\leq$ 50 nm), which have been newly formed either by vapor condensation processes or by chemical reactions of their precursory gases. These particles have a short residence time since they easily grow and become part of the accumulation mode and are also quickly deposited to the surface due to their highly diffusive nature –a result of their low individual mass and high tendency to undergo Brownian motion–.

- **Accumulation mode:** Groups particles whose diameters range from 50 nm to 1 μm, being too small to settle under gravity and too large to tend to rapid Brownian motion. They grow only through coalescence because they do not coagulate as rapidly as fine and coarse particles do, and there are diffusion barriers to their growth by condensation. Therefore, these particles have the longest atmospheric lifetime (days to even a month), and their deposition is primarily determined by rain. Aerosols resulting from anthropogenic emissions belong to this mode, which is why their polluting and climate effects are so severe.

- **Coarse mode:** Gathers those aerosols with diameters greater than 1 μm, which are normally generated mechanically through coalescence. Dust, wind-blown soil, sea spray, and particles resulting from industrial operations belong to this mode. Their atmospheric lifetime is significant but much shorter than that of the previous mode, because their size allows for appreciable gravitational settling velocities. They are therefore deposited through sedimentation.

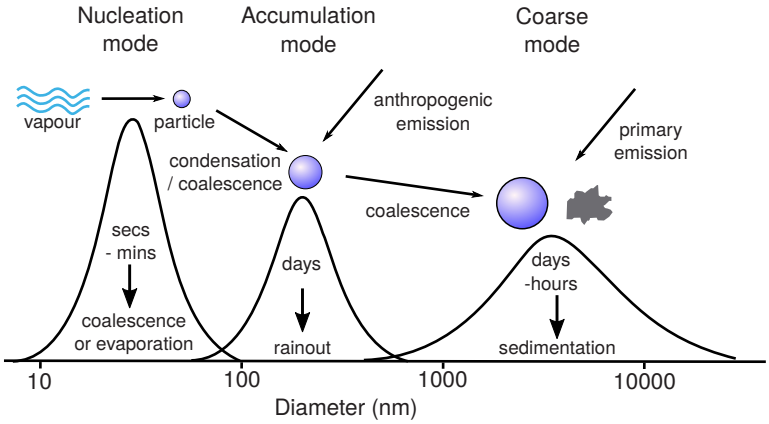

FIGURE 3.1: Schematic of size distribution modes, lifetime as well as growing and deposition processes of aerosols. Adapted from [32].

The physical system composed of the atmosphere and the aerosols suspended in it can be described in terms of particle shape, size, and total content. Nevertheless, to obtain an accurate description, it is necessary to consider the different size distributions, defined as the number, mass, and volume of aerosols present in the atmosphere according to a given size range.

Considering spherical particles with radii in a closed interval $[\ln r, \ln r + \mathrm{d}r]$, the total number of particles is $\mathrm{d}N$ and their total mass $\mathrm{d}M$. The number size distribution is $n(r) = \mathrm{d}N/\mathrm{d}\ln r$, and the mass size distribution $m(r) = \mathrm{d}M/\mathrm{d}\ln r$. The volume size distribution, defined as the volume of aerosols in an air parcel of unitary cross section, is $v(r) = \mathrm{d}V/\mathrm{d}\ln r$. Thus, the total mass, volume, and number of particles are obtained by integrating the corresponding size distribution over the radii interval [4].

The following expression relates the volume and number size distributions:

$$v(r) = \frac{4\pi}{3} r^3 \frac{\mathrm{d}N}{\mathrm{d}\ln r} \tag{3.1}$$

In the same way, mass and number size distributions can be related if considering constant density for particles, as follows:

$$m(r) = \frac{4\pi}{3} \rho r^3 \frac{\mathrm{d}N}{\mathrm{d}\ln r} \tag{3.2}$$

Various analytical expressions have been proposed to represent aerosol size distributions. The Junge law satisfactorily explains the spectral dependence of aerosol light scattering for larger particles (coarse mode); however, it does not capture small particles (nucleation and Aitken modes) nor account for multimodal size distributions [33]. The Gamma distribution (and its modifications) describes many real-size distributions, but it has a large number of fitting parameters, which is inconvenient for practical applications. Finally, the log-normal distribution is the most used because it provides a simple yet accurate representation of observed aerosol size distributions over several orders of magnitude in particle size. It is entirely determined by choosing a characteristic or modal radius r_m and a measure of the dispersion of the given distribution $\ln \sigma_g$ [2].

The log-normal law for the number size distribution per unit logarithmic radius interval is given by Eq. (3.3), where N is the total aerosol concentration and $n(r)\mathrm{d}\ln r$ is the number of particles per unit volume for which the logarithm of the radius lays between $[\ln r, \ln r + \mathrm{d}r]$. Homologous functions describe mass and volume size distributions [2, 34].

$$n(r) = \frac{\mathrm{d}N}{\mathrm{d}\ln r} = \frac{N}{\ln\sigma_g\sqrt{2\pi}} \exp\left(-\frac{1}{2}\left(\frac{\ln\left(r/r_m\right)}{\ln\sigma_g}\right)^2\right) \tag{3.3}$$

The different size distributions can be represented as the sum of the three size distribution modes (nucleation, accumulation, and coarse), as shown in Fig. 3.2. The nucleation mode dominates the aerosol number distribution, the accumulation mode is predominant in the surface distribution, while the coarse mode is more pronounced in the volume distribution. For the illustration, three log-normal distributions with mean geometric number radius r_g of 0.01, 0.1, and 1 μm, geometric standard deviation σ_g of 2, and with total concentrations of 1000, 200, and 1 cm^{-3}, respectively, were supposed [2].

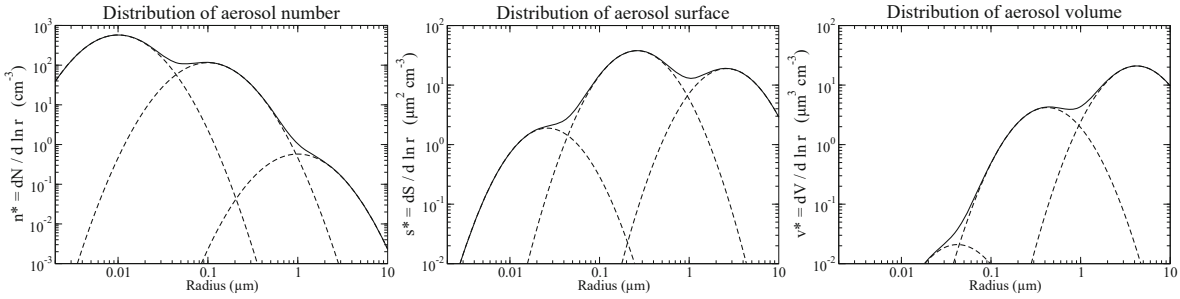

FIGURE 3.2: Schematic of number, surface and volume size distributions related to the nucleation, accumulation and coarse modes. From [2].

Furthermore, particle shape can be directly determined only through microscopy, which becomes a convoluted task due to the need for highly technological equipment and the vast range of different particle shapes and sizes suspended in the atmosphere, many of which cannot be collected. The depolarization lidar technique enables the indirect determination of the effective aerosol shape based on the particle's depolarization capability, making it a key tool for retrieving aerosol physical properties.

3.2 Radiative properties of aerosols

Aerosols either scatter or absorb radiation, and the sum of absorption and scattering in all directions is called extinction. The energy absorbed is radiated at longer wavelengths, a process that is negligible at optical wavelengths, known as emission. To understand the optical properties of atmospheric particles, it is necessary to introduce three parameters used to define and calculate them: scattering and absorption cross sections, and size parameter.

Absorption and scattering cross sections [35]: The scattering and absorption cross-sections C_{sca}, C_{abs} are defined by electromagnetic theory assuming a perfectly spherical particle interacting with a plane electromagnetic wave. The absorption cross-section is defined in terms

of the volume of the particles V, the wavenumber of the scattered light k, the electric vectors inside the particle $\mathbf{E}$ and of the incident wave $\mathbf{E_0}$, and the dielectric permittivity $\varepsilon^{''} = 2n\chi$ as in Eq. (3.4).

$$C_{abs} = \frac{k}{|\mathbf{E_0}|^2} \int_V |\mathbf{E}|^2 \, \varepsilon^{"} \mathrm{d}V \tag{3.4}$$

C_{abs} vanishes if the imaginary part (χ) of the complex refractive index (m) equals zero. For the vast majority of aerosols, except for soot, χ is a small number for visible wavelengths, which explains the small absorption effects of light-aerosol interactions. Moreover, the scattering cross-section measures the surface of the particle that interacts with the plane wave, *i.e.*, the degree of interaction in square meters. Mathematically,

$$C_{sca} = \frac{1}{I_0} \int_S I_{sca} \mathrm{d}S \tag{3.5}$$

Where I_0 and I_{sca} represent the intensities of the incident and scattered light, respectively, and S is the particle surface.

Phase function: To characterize the interaction between radiation and particles better, it is necessary to understand the directional characteristics of the scattering process. The phase function is defined as the probability for an incident photon to be scattered in a certain direction. For a spherical particle, it is dependent only on the angle Θ between the directions of propagation of the incident and scattered beams, which ranges between 0 and π, or on its cosine μ, where $\mu = \cos\Theta$. Mathematically,

$$\int_0^{\pi} P(\Theta) \sin\Theta \mathrm{d}\Theta = \int_{-1}^{1} P(\mu) \, \mathrm{d}\mu = 2 \tag{3.6}$$

In a more general case, the incident and scattered directions s_i and s_d are referenced by their zenith and azimuthal angles θ_i, φ_i and θ_s, φ_s. It depends only on the scattering direction relative to the incident direction. The more general description of the phase function is given by Eq. (3.7).

$$\int_{\omega} P(\omega) \, \mathrm{d}\omega = \int_0^{2\pi} \int_0^{\pi} P(\theta_s, \varphi_s) \sin\theta_s \mathrm{d}\theta_s \mathrm{d}\varphi_s = 4\pi \tag{3.7}$$

The most usual parameter used to describe the shape and properties of the phase function is called the asymmetry factor g, a measure of the degree of forward–backward symmetry of the phase function, described by Eq. (3.8). When $g = 1$, all radiation is scattered in the forward direction; if $g = -1$, the radiation is completely backscattered; in the case $g = 0$, the radiation is equally scattered in the forward and backward directions [36].

$$g = \int_{-1}^{1} P(\mu) \, \mu \mathrm{d}\mu \tag{3.8}$$

Size parameter: Defined as the ratio of the characteristic dimension of a particle (r) and the wavelength of the incident radiation (λ), as stated in Eq. (3.9).

$$x = \frac{2\pi r}{\lambda} \tag{3.9}$$

As illustrated in Fig. 3.3, particles whose $x \gg 1$ scatter radiation according to their scattering cross section C_{sca}, acting like geometric shapes. When $x \approx 1$, scattering is described by Mie theory, so interference effects appear due to phase changes over the particle's surface. Finally, if the particle is much smaller than the incident wavelength, *i.e.* $x \ll 1$, its whole surface re-radiates with the same phase in a process known as Rayleigh scattering.

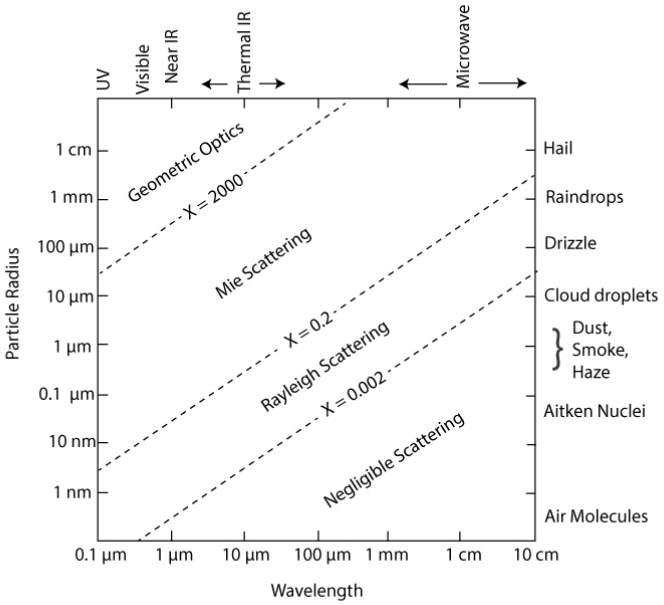

FIGURE 3.3: Scattering regimes as a function of radiation wavelength and particle radius. Transition values, given by the value of x, are represented by dotted lines. Taken from [2].

3.2.1 Absorption

As aforementioned, light absorption by atmospheric particles is small at visible wavelengths. The ratio of absorption (spectral aerosol absorption coefficient) $K_{abs} = N\overline{C}_{abs}$, is less than 10% and even 1% of the extinction coefficient $K_{ext} = N\overline{C}_{ext}$ for remote clean areas. In these coefficients, N is the number of particles in a unit volume, and the overbar on the cross-sections means averaging with respect to the aerosol size distribution. The probability of photon absorption $\Gamma = K_{abs}/K_{ext}$ varies substantially from zero only if soot is present in great amounts, as it is the primary atmospheric absorber [37]. There are several *in situ* techniques used to study aerosol absorption, some of which are: filter methods, polarimetric techniques,

techniques based on the measurement of differences between light extinction and scattering for a given atmospheric volume, optical acoustic spectrometry, the diffuse transmittance method as well as the radiative transfer retrieval approach based on the measurements of the aerosol optical thickness, small-angle scattering, and diffuse light transmission by a sunphotometer. This diversity of techniques is an indicator that there is no a single reliable method, leading to massive uncertainties in the estimations of aerosol radiative forcing. Despite this, substantial attempts have been undertaken in order to determine the spatial distribution of K_{abs} and also of single-scattering albedo $\overline{\omega}_o = 1 - \beta$ [38].

Aerosol absorption coefficients can be analytically calculated for spherical particles as long as their size and refractive index are known. These calculations serve as a base for identifying possible spectral dependencies that might be found in corresponding measurements. The spectral absorption coefficient is defined as

$$K_{abs}(r,\lambda) = \sum_j N_j(r) \frac{\mathrm{d}C_{j,abs}}{\mathrm{d}\Omega}(r,\lambda) \tag{3.10}$$

where N_j is the concentration of absorbing particles of type j in the volume, and $\mathrm{d}C_{j,abs}/\mathrm{d}\Omega$ is the particle's differential absorption cross section at wavelength λ. It has the units of m^{-1}.

For absorbing particles with radii much smaller than the wavelength, C_{abs} can be approximated as described in Eq. (3.11), where V is the volume of particles, a the bulk absorption coefficient $a = 4\pi\chi/\lambda$, and $D(n)$ the proportionality constant defined in Eq. (3.12) [39]. For particles of arbitrary shapes, $D \to 1$ if the real part of the refractive index $n \to 1$.

$$C_{abs} = aVD \tag{3.11}$$

$$D(n) = \frac{9n}{\left(n^2+2-\chi^2\right)^2 + 4n^2\chi^2} = \frac{9n}{(n^2+2)} \quad (\text{if } \chi \ll n) \tag{3.12}$$

In the case of large absorbing aerosols, both spherical and nonspherical, the Eq. (3.13) can be applied to estimate the absorption cross section. It is assumed that the size parameter $x = 2\pi r/\lambda \gg 1$ and that the bulk absorption coefficient $a \gg 1$.

$$C_{abs} = (1-\rho)S \tag{3.13}$$

Where S is the geometrical cross-section of the particle and ρ the reflection coefficient. The value of ρ for such particles can be found using the Fresnel reflection coefficients R_i.

3.2.2 Scattering theory

When an electromagnetic wave finds an obstacle in its path, the electric charges of which the obstacle's matter is composed are set into oscillatory motion by the electric field of the incident radiation. After being accelerated, electric charges re-radiate electromagnetic energy in all directions, a process known as scattering. Scattering can be classified according to the frequency of the re-radiated energy as elastic if the frequency (and therefore the wavelength) of the incident radiation is conserved and only its direction is changed, and as inelastic if the interaction of the incident radiation with the obstacle leads to the Raman effect.

Rayleigh scattering: The predominant form of elastic scattering is called Rayleigh scattering, where particles interact with radiation whose wavelength is much larger than their size. This phenomenon is an outcome of the electric polarizability (α) of the particles: when their electric charges are driven to oscillate at the same frequency as the incident radiation's electric field, the particles become small radiating dipoles, with the radiation constituting the scattered energy. The simplification introduced by the small size of the particles is that they may be considered to be placed in a homogeneous electric field $\mathbf{E}$, thus their own electric field –caused by their electric polarization– modifies this field both inside and near the particle, and the oscillating dipole radiates in all directions. For scattering angles other than 0 and π, Rayleigh scattering intensity is strongly dependent on the polarization state of the incident radiation, as illustrated in the figure below.

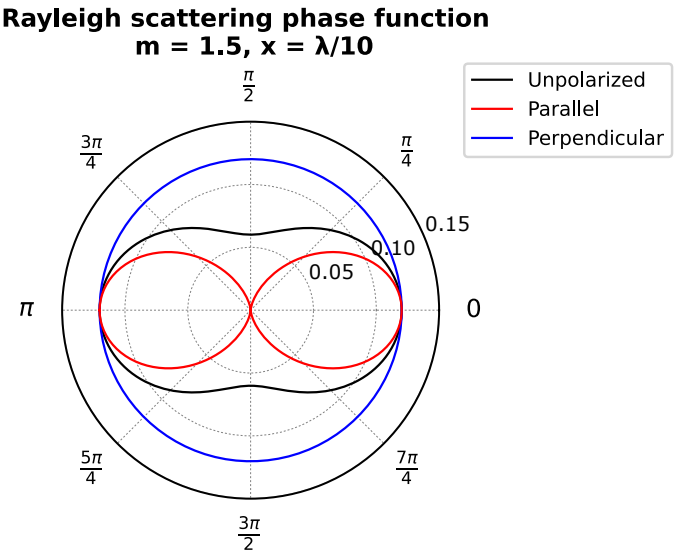

FIGURE 3.4: Rayleigh phase function for different polarization states of the incident radiation: natural light (in black) and linearly polarized parallel (in red) and perpendicular (in blue) to the scattering plane.

The figure shows that, for randomly polarized (natural) light, the scattered radiation intensity exhibits azimuthal symmetry around the direction of incidence. For linearly polarized light, the scattering intensity is null for the axial direction and maximum on a plane normal to it. Furthermore, Rayleigh's phase function is independent of the size parameter x and the refractive index m [40]. It depends only on the polarization state of the incoming radiation and the scattering angle.

Suppose the frequency of the incident radiation is well below the resonance frequency of the scatterer. In that case, the intensity of the scattered radiation is inversely proportional to the fourth power of the wavelength, $I \propto 1/\lambda^4$, and to $1+\cos^2\Theta$. Thus, forward $(\Theta = 0)$ and backward $(\Theta = \pi)$ scattering are equally strong, as depicted in Fig. 3.4. The intensity of light scattered by small particles is described by Eq. (3.14) [34].

$$I = I_0 \frac{1+\cos^2\Theta}{2R^2} \left(\frac{2\pi}{\lambda}\right)^4 \left(\frac{m^2-1}{m^2+2}\right)^2 \left(\frac{r}{2}\right)^6 \tag{3.14}$$

Where I_0 is the intensity of the incident beam, R is the distance to a particle of radius r, m is the complex refractive index, and Θ is the scattering angle. If Eq. (3.14) is averaged over all angles, the Rayleigh scattering cross section (Eq. (3.15)) is obtained [41, 42].

$$\sigma_{sca} = \frac{2\pi^5}{3} \frac{r^6}{\lambda^4} \left(\frac{m_r^2-1}{m_r^2+2}\right)^2 \tag{3.15}$$

Where $m_r = m/m_{med}$ is the ratio of the complex refractive index of the particle to that of the surrounding medium. The Rayleigh backscattering coefficient $\beta(r,\lambda)$ describes the intensity of light that is backscattered, i.e., $\Theta = \pi$, by small particles. Mathematically,

$$\beta(r,\lambda) = \sum_j N_j(r) \frac{\mathrm{d}\sigma_{j,sca}}{\mathrm{d}\Omega}(\pi,\lambda) \tag{3.16}$$

Where N_j is the concentration of scattering particles of type j in the scattering volume, and $\mathrm{d}\sigma_{j,sca}/\mathrm{d}\Omega$ is the particle's Rayleigh differential scattering cross section for the backward direction at wavelength λ. It has the units of $\mathrm{m}^{-1}\mathrm{sr}^{-1}$. For molecules, Eq. (3.14) can be simplified taking into account the dependence of m on the molecular polarizability α, which is proportional to the dipole moment induced by the electric field of the light. Thus, the Rayleigh scattering intensity for a single particle (in CGS units) is

$$I_{mol} = I_0 \frac{8\pi^4\alpha^2}{\lambda^4 R^2} \left(1+\cos^2\Theta\right) \tag{3.17}$$

Mie scattering: In 1908, Gustav Mie proposed a more general theory for elastic scattering based on continuum electromagnetic theory and on illumination by a plane wave infinite

in lateral extent [43]. Mie theory is usually applied to particles whose diameter is larger than the wavelength of the incident radiation. Although there is no defined boundary between Mie and Rayleigh, it is said that the Mie scattering model applies if the particle size is larger than ∼10% of the wavelength of the incident radiation (see Fig. 3.3).

Briefly, Mie's solution to the problem of scattering by an arbitrary homogeneous sphere is obtained by expanding the incident, scattered, and internal fields in a series of vector-spherical harmonics, choosing the coefficients of these expansion functions a_n and b_n so that the tangential components of the electric and magnetic fields are continuous across the surface of the sphere. Riccati-Bessel functions Ψ_n and ξ_n, and the logarithmic derivative $D_n(x) = \frac{\mathrm{d}}{\mathrm{d}x} \ln \Psi_n(x)$ can be used to define the scattering coefficients if the permeability of the sphere and its surroundings is the same [44], i.e.,

$$a_n = \frac{\left[D_n(m_r x)/m_r + n/x\right]\Psi_n(x) - \Psi_{n-1}(x)}{\left[D_n(m_r x)/m_r + n/x\right]\xi_n(x) - \xi_{n-1}(x)} \tag{3.18}$$

$$b_n = \frac{\left[m_r D_n(m_r x) + n/x\right]\Psi_n(x) - \Psi_{n-1}(x)}{\left[m_r D_n(m_r x) + n/x\right]\xi_n(x) - \xi_{n-1}(x)} \tag{3.19}$$

Using the scattering coefficients a_n and b_n, the extinction and scattering cross sections are defined as [36]:

$$C_{ext} = \frac{2\pi}{k^2}\sum_{n=1}^{\infty}(2n+1)\,\mathrm{Re}\{a_n + b_n\} \tag{3.20}$$

$$C_{sca} = \frac{2\pi}{k^2}\sum_{n=1}^{\infty}(2n+1)\left(|a_n|^2 + |b_n|^2\right) \tag{3.21}$$

For the backward direction ($\Theta = \pi$), the scattering cross section, referred to as the backscattering cross section, is defined as [36]

$$C_{\mathrm{backsca}} = \frac{2}{k^2}\left|\sum_{n=1}^{\infty}(-1)^n \frac{2n+1}{n(n+1)}(a_n - b_n)\right|^2 \tag{3.22}$$

For a small x and $|m|$, an approximation for the scattering, backscattering, and extinction efficiencies is given by:

$$Q_{ext} = 4x\mathrm{Im}\left\{\frac{m_r^2-1}{m_r^2+2}\right\} \tag{3.23}$$

$$Q_{sca} = \frac{8}{3}x^4\left|\frac{m_r^2-1}{m_r^2+2}\right|^2 \tag{3.24}$$

$$Q_{backsca} = 2x^4\left|\frac{m_r^2-1}{m_r^2+2}\right|^2 \tag{3.25}$$

Mie scattering differs from Rayleigh scattering in several aspects. First, it is roughly independent of wavelength. Second, its phase function is steeply inclined to the forward direction: the greater the particle size, the more pronounced the forward scattering. Third, the Mie phase function is indeed dependent on the particle size and its index of refraction. Fourth, for larger particle sizes, the phase function and scattering intensity are independent of the polarization state of the incident radiation, having only negligible effects for backward scattering directions (Θ between $\pi/2$ and $3\pi/2$). For smaller particle sizes, which are close to Rayleigh scattering since there is no defined limit between these regimes, Mie intensity and phase function are polarization-dependent.

The dependency of Mie scattering on the particle size and polarization state of the incident radiation is illustrated in Fig. 3.5 for a non-absorbing particle of an index of refraction $m = 1.5$. The left panel presents a particle with a size parameter $x = \lambda/3$, close to the Rayleigh limit. The right panel represents a particle three times larger, with a size parameter equal to the incident wavelength. For both cases, there is clearly a preferential forward scattering, although a minor component remains in the backward direction for the smaller particle. The polarization dependency is explicit for small particles, exhibiting the same behavior as Rayleigh scattering, but with the characteristic steeply forward-scattering intensity of the Mie regime. On the other hand, the right panel depicts the independence of Mie scattering on the polarization state of the incident radiation for large particles. The zoom on the lower-right corner illustrates that there is only a small effect for the backward scattering angles (Θ between $\pi/2$ and $3\pi/2$).

Mie scattering intensity $I(\Theta)$ is defined as in Eq. (3.26), where $i_1(\Theta)$, $i_2(\Theta)$ are the intensities in the orthogonal polarization states. $i_1(\Theta)$ is the intensity of the perpendicular component of the scattered radiation electric vector, while $i_2(\Theta)$ is parallel to the scattering plane.

$$I(\Theta) = I_0\frac{\lambda^2}{8\pi^2 r^2}\left[i_1(\Theta)+i_2(\Theta)\right] \tag{3.26}$$

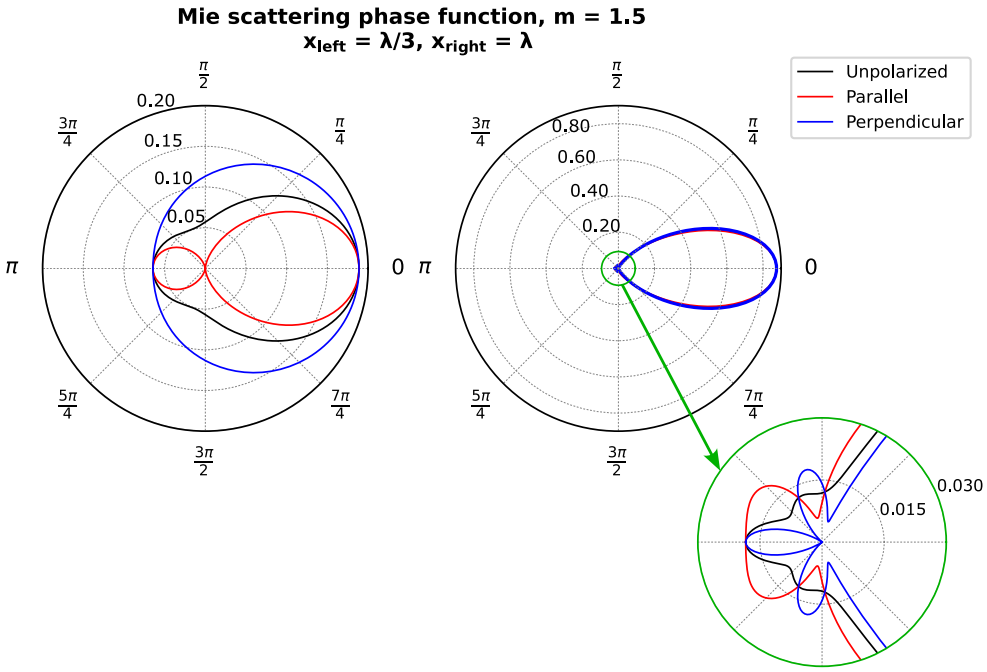

FIGURE 3.5: Mie phase function for different size parameters ($x = \lambda/3$ on the left, $x = \lambda$ on the right) and polarization states of the incident radiation: natural light (in black) and linearly polarized parallel (in red) and perpendicular (in blue) to the scattering plane. The zoom panel in green shows the minor effect of polarization on larger particles at backward angles.

The orthogonal scattering intensities $i_1(\Theta)$ and $i_2(\Theta)$ are defined as the square of their respective amplitude-scattering matrix elements S_{11} and S_{22}, which, for isotropic and homogeneous spherical particles, are represented by the scattering coefficients a_n and b_n as:

$$S_{11} = \sum_n \frac{2n+1}{n(n+1)} (a_n \tau_n + b_n \pi_n) \tag{3.27}$$

$$S_{22} = \sum_n \frac{2n+1}{n(n+1)} (a_n \pi_n + b_n \tau_n) \tag{3.28}$$

Where π_n and τ_n are the associated Legendre polynomials of the first kind, defined as $\pi_n = \frac{P_n^1}{\sin\Theta}, \tau_n = \frac{dP_n^1}{d\Theta}$. Note that for spherical particles, $S_{21} = S_{12} = 0$ [45]. Thus, the polarization states of the incident and scattered radiations are the same, a consequence of the sphere's symmetry [44].

In a more general case, the intensity of the scattered radiation can also be defined in terms of the amplitude function of a single particle of arbitrary shape and composition in an arbitrary orientation illuminated by a plane electromagnetic wave. Consider the reference frame L described by Mishchenko *et. al.* [46], *i.e.*, a right-handed Cartesian coordinate system with

orientation fixed in space, having its origin inside the particle. The direction of propagation of a transverse electromagnetic wave is specified by a unit vector $\hat{\mathbf{n}} = \hat{\theta} \times \hat{\varphi}$ where $\phi \in [0, \pi]$ is the zenith angle measured from the positive z axis, and $\varphi \in [0, 2\pi]$ is the azimuth angle measured from the positive x axis in the clockwise sense. The θ and φ components of the electric field are $\mathbf{E}_\theta = E_\theta \hat{\theta}$, which lies in the meridional plane (plane through the beam and the z axis), and $\mathbf{E}_\varphi = E_\varphi \hat{\varphi}$ is perpendicular to this plane. To specify the orientation of the particle with respect to the reference frame L, the authors Mishchenko *et. al.* [46] introduce another right-handed coordinate system P fixed on the particle having the same origin as L. They specify the orientation of the particle with respect to the reference frame L by the three Euler angles of rotation $\alpha \in [0, 2\pi], \beta \in [0, \pi], \gamma \in [0, 2\pi]$ that transform $L\{x, y, z\}$ into $P\{x', y', z'\}$.

Now, consider a plane monochromatic electromagnetic wave incident upon a nonspherical particle in a direction $\hat{\mathbf{n}}^{inc}$. The electric field vectors of the plane incident wave and the spherical scattered wave (in the fard field region, where $kR \gg 1, R = |\mathbf{R}|$) are given by

$$\mathbf{E}^{inc}(\mathbf{R}) = \left(E_{\theta 0}^{inc} \hat{\theta}^{inc} + E_{\varphi 0}^{inc} \hat{\varphi}^{inc}\right) \exp\left(ik\hat{\mathbf{n}}^{inc}\mathbf{R} - i\omega t\right) = E_\theta^{inc} \hat{\theta}^{inc} + E_\varphi^{inc} \hat{\varphi}^{inc} \tag{3.29}$$

$$\mathbf{E}^{sca}(\mathbf{R}) = E_\theta^{sca}(R, \hat{\mathbf{n}}^{sca}) \hat{\theta}^{sca} + E_\varphi^{sca}(R, \hat{\mathbf{n}}^{sca}) \hat{\varphi}^{inc} \quad , \quad \hat{n}^{sca} = \frac{\mathbf{R}}{R} \tag{3.30}$$

where k is the free-space wavenumber and $\mathbf{R}$ is the radius vector with its origin at the origin of the reference coordinate system. From now on, for brevity we suppress the time factor $\exp(-i\omega t)$. Because of the linearity of Maxwell's equations and boundary conditions, it must always be possible to linearly relate the electric field vector components of the incident wave to those of the scattered wave by means of a 2x2 amplitude scattering matrix (**S** matrix) as

$$\begin{pmatrix} E_\theta^{sca} \\ E_\varphi^{sca} \end{pmatrix} = \frac{\exp(ikR)}{R} \mathbf{S}\left(\hat{\mathbf{n}}^{sca}, \hat{\mathbf{n}}^{inc}, \alpha, \beta, \gamma\right) \begin{pmatrix} E_{\theta 0}^{inc} \\ E_{\varphi 0}^{inc} \end{pmatrix} \tag{3.31}$$

$$= \frac{\exp(ikR)}{R} \begin{pmatrix} S_{11} & S_{12} \\ S_{21} & S_{22} \end{pmatrix} \begin{pmatrix} E_{\theta 0}^{inc} \\ E_{\varphi 0}^{inc} \end{pmatrix} \tag{3.32}$$

The amplitude matrix depends on the directions of incidence and scattering; on the size, morphology, and composition of the scatterer; and on its orientation with respect to the reference frame as specified by α, β and γ. For spherical particles, the off-diagonal elements of the amplitude-scattering matrix vanish, *i.e*, $S_{12} = S_{21} = 0$, because the polarization states of the incident and scattered waves are the same, a consequence of the sphere's symmetry [44].

A fundamental property of the amplitude matrix is the reciprocity relation [45, 46] (see Eq. (3.33)), a manifestation of the symmetry of the light-scattering process with respect to an inversion of time. The reciprocity principle states that, when an incident wave gets scattered on an object, the scattering amplitude would not change if the incident and scattered waves are interchanged [47]. It follows directly from Maxwell's equations and holds for any particle in an arbitrary orientation; the only requirement is that the dielectric, permeability, and conductive tensors of the incident beam should be symmetric.

$$\mathbf{S}\left(-\hat{\mathbf{n}}',-\hat{\mathbf{n}},\alpha,\beta,\gamma\right)=\begin{pmatrix} S_{11}\left(\hat{\mathbf{n}},\hat{\mathbf{n}}',\alpha,\beta,\gamma\right) & -S_{21}\left(\hat{\mathbf{n}},\hat{\mathbf{n}}',\alpha,\beta,\gamma\right) \\ -S_{12}\left(\hat{\mathbf{n}},\hat{\mathbf{n}}',\alpha,\beta,\gamma\right) & S_{22}\left(\hat{\mathbf{n}},\hat{\mathbf{n}}',\alpha,\beta,\gamma\right) \end{pmatrix} \tag{3.33}$$

A consequence of reciprocity is the backscattering theorem, which states that "the scattering matrix of an arbitrary particle referred to an arbitrary plane of reference has for $\Theta=\pi$ the property $S_{12}+S_{21}=0$" [45], i.e.,

$$S_{21}\left(-\hat{\mathbf{n}},\hat{\mathbf{n}},\alpha,\beta,\gamma\right)=-S_{12}\left(-\hat{\mathbf{n}},\hat{\mathbf{n}},\alpha,\beta,\gamma\right) \tag{3.34}$$

3.3 HSRL theoretical framework

The atmospheric backscattered signal is a superposition of molecular (Rayleigh-Brillouin) and aerosol (Mie) scattering. To retrieve aerosol radiative properties from measured atmospheric backscattering, EBL requires an assumed lidar ratio value, which introduces significant uncertainties into the retrieved aerosol properties. To solve this problem, HSRL considers the spectral distribution of the two scattering processes, a consequence of the different Doppler broadening induced. Depending on air temperature and pressure, air molecules undergo random thermal motion, with velocities of $\sim$300 m/s. As a result, the molecular Rayleigh-Brillouin scattering produces a Doppler broadening of the ultra-narrowband incident laser radiation on the order of several gigahertz (up to 4). In contrast, heavier aerosol particles move only by the effects of wind and atmospheric turbulence at velocities commonly ranging from 1 to 10 m/s [16–18]. Thus, for ultra-narrowband lasers, Mie backscattering is essentially unbroadened and spectrally coincident with the narrowband transmitted laser line. However, as the laser linewidth increases, Mie Doppler broadening becomes appreciable.

The fundamental principle of HSRL is illustrated in Fig. 3.6. In short, the spectral distribution of light backscattered by the atmosphere is composed of a narrow peak corresponding to the lower frequency shift of aerosol scattering and a wide distribution from molecular

scattering, as shown in the lower-left plot. This signal is split into two channels. One unchanged portion is directed to the total channel detector, essentially serving as an EBL signal (lower-right graph). In the other channel, a high-resolution spectral filter –such as an interferometer or a vapor cell, depicted in red– allows for cutting the frequencies corresponding to Mie backscattering, yielding a second signal primarily due to molecular backscattering, as displayed in the upper-right chart. By measuring two different signals for the two atmospheric variables at each height, the HSRL problem becomes well-posed. Performing a precise yet simple calibration of the HSRL signals enables the straightforward retrieval of aerosol backscatter and extinction coefficients, eliminating the need for an assumed lidar ratio [16, 48].

The HSRL technique provides precise range-resolved measurements of aerosol optical depth, lidar ratio, and single-scattering albedo, which are essential parameters for constraining radiative transfer models and evaluating the role of aerosols in climate change. Different types of HSRL systems have demonstrated high accuracy in profiling aerosols, playing a critical role in field campaigns targeting aerosol transport, boundary layer processes, and pollution events [49]. The combination of molecular-aerosol separation and absolute calibration makes HSRL uniquely capable among lidar techniques for characterizing the microphysical and radiative impacts of atmospheric aerosols.

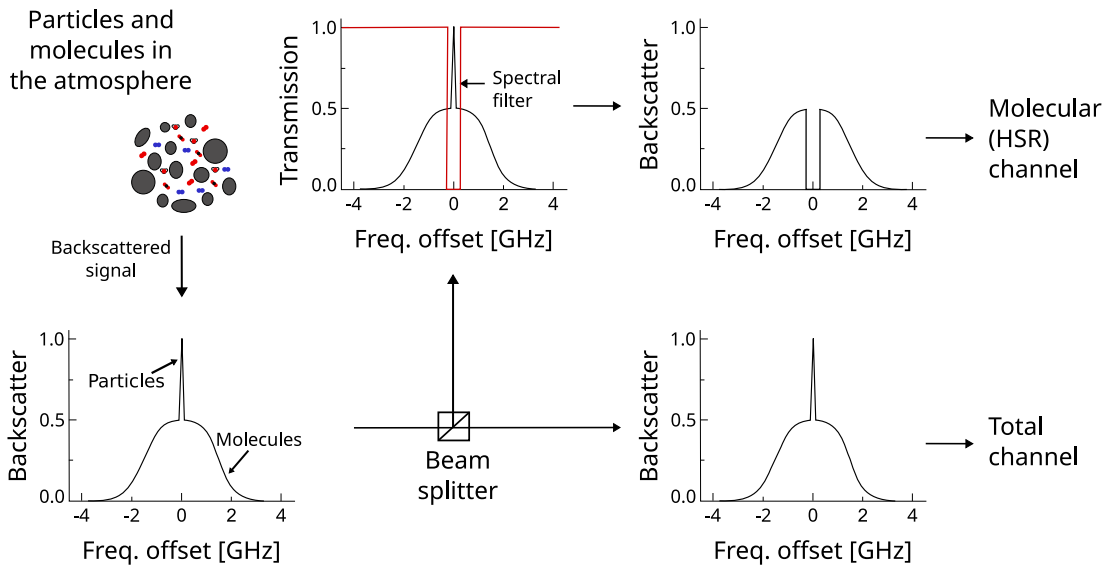

FIGURE 3.6: Working principle of HSRL. Adapted from [50].

A layout of a typical HSRL system is presented in Fig. 3.7. A narrowband laser (commonly a frequency-doubled Nd:YAG at 532 nm or tripled Nd:YAG at 355 nm) is emitted into the atmosphere, where it interacts with the particles and molecules present. In the receiver part, a telescope collects the backscattered light, which, as described, contains both

Mie and Rayleigh-Brillouin scattering components. The received beam is then collimated, for example, by placing a field stop in the telescope's back focal plane and using a lens. Then, a narrow interference filter is placed to select only the wavelengths corresponding to the emitted laser and to eliminate background noise signals. Thereafter, a non-polarizing beam splitter separates the signals into two distinct components. One unchanged part, which contains both aerosol and molecular scattering, passes through a lens that focuses it onto the photodetector (PD) of the total channel. The other part is directed towards the spectral filter (typically an interferometer or a vapor cell), which then cuts the Mie scattering signals to obtain a mostly pure molecular signal on the other channel. Before the high-spectral-resolution channel photodetector, it is common to place an additional interference filter to block potential fluorescence. After proper absolute calibration, i.e., radiometric calibration and overlap correction, the recorded signals $P_{hsr}(r)$ and $P_{tot}(r)$ enable the direct and independent retrieval of aerosol backscatter and extinction coefficients, as well as derived products such as the lidar ratio and aerosol optical depth.

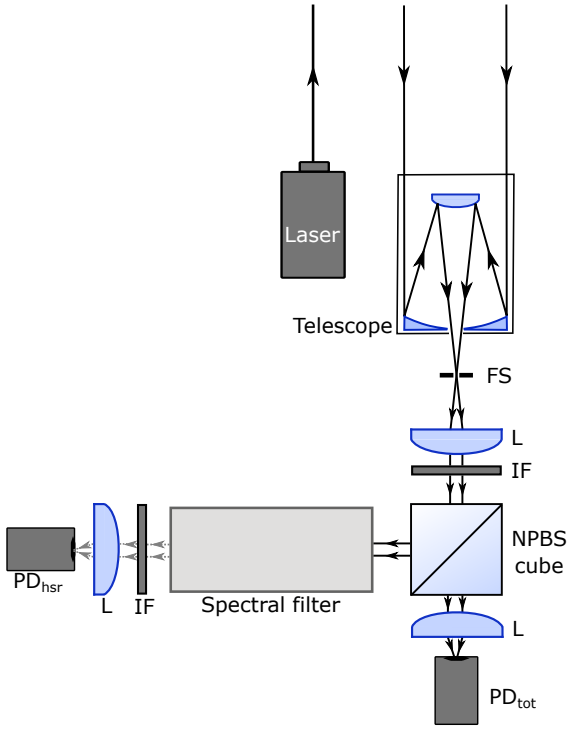

FIGURE 3.7: Layout of a typical HSRL system, composed of a laser source, a telescope, collimating optical elements, a beam splitter, spectral filters, and two photodetectors.

Dropping the wavelength dependence for simplicity, the signals $P_{hsr}(r)$ and $P_{tot}(r)$ measured by the HSR and total channels are described by Eqs. (3.35) and (3.36) [51], respectively.

$$P_{hsr}(r) = K_{hsr}\frac{O_{hsr}(r)}{r^2}\left[X_m\beta_{mol}(r) + X_p\beta_{aer}(r)\right]\exp\left[-2\int_0^r\left[\alpha_{mol}(r') + \alpha_{aer}(r')\right]dr'\right] \tag{3.35}$$

$$P_{tot}(r) = K_{tot}\frac{O_{tot}(r)}{r^2}\left[\beta_{mol}(r) + \beta_{aer}(r)\right]\exp\left[-2\int_0^r\left[\alpha_{mol}(r') + \alpha_{aer}(r')\right]dr'\right] \tag{3.36}$$

Where $K_{hsr,tot} = P_0 A\frac{c\tau}{2}\eta_{hsr,tot}$ is the performance factor of each channel, given by the average power of the laser pulses P_0, the effective spatial pulse length $c\tau/2$, the area of the receiving telescope A, and $\eta_{hsr,tot}$ the overall channel efficiency. The geometric factor includes the overlap function of each channel $O_{hsr,tot}(r)$ and the quadratic decrease of the signal intensity with distance r^{-2} as the light waves propagate throughout the atmosphere. Considering that the spectral filter is not ideal and that some parasitic aerosol signal will be transmitted through the molecular channel, its equation accounts for the spectral filter's transmittance functions at both molecular and aerosol frequencies, X_m and X_p.

The molecular backscatter and extinction coefficients $\beta_{mol}(r)$ and $\alpha_{mol}(r)$ can be estimated using Rayleigh's scattering theory and additional atmospheric temperature and pressure profiles, as in Equations (3.37) and (3.38) [51].

$$\alpha_{mol}(r) = N_{mol}(r)\,\sigma \tag{3.37}$$

$$\beta_{mol}(r) = \frac{\alpha_{mol}(r)}{8\pi/3} \tag{3.38}$$

The Rayleigh extinction cross-section σ for standard air (P_s = 1013.25 mb, T_s = 288.15 K, 300 ppm CO_2) and the range-dependent number density of molecules $N_{mol}(r)$ are defined as in Eqs. (3.39) and (3.40), respectively [52].

$$\sigma = \frac{24\pi^3\left(m_s^2 - 1\right)^2}{\lambda^4 N_s^2\left(m_s^2 + 2\right)^2}\frac{6 + 3\gamma}{6 - 7\gamma} \tag{3.39}$$

$$N_{mol}(r) = N_s\frac{T_s}{P_s}\frac{P(r)}{T(r)} \tag{3.40}$$

Where m_s is the refractive index for standard air at the given wavelength, $N_s = 2.546899 \times 10^{19}$ cm^{-3} is the molecular number density for standard air [53], and γ is the wavelength-dependent depolarization factor that describes the effect of molecular anisotropy [52].

3.3.1 Overlap function

The accurate retrieval of aerosol optical properties using HSRL critically depends on the proper treatment of the overlap function $O(r)$, which represents the effective collection efficiency of the lidar receiver as a function of range. The overlap function accounts for the gradual spatial coupling between the transmitted laser beam and the receiver field of view, as displayed for a monostatic biaxial lidar in Fig. 6.8. For a lidar with an infinite telescope aperture and perfect alignment, the overlap function would be unity at all ranges. In practice, however, the finite geometry of the transmitter and receiver introduces a partial-illumination regime in the near-field, during which the overlap gradually increases from zero to one.

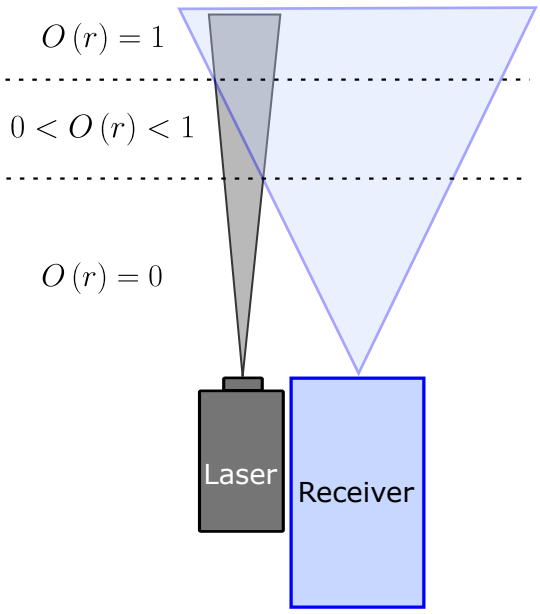

FIGURE 3.8: Range-dependent lidar overlap function. It represents the gradual coupling between the laser beam and the receiver field of view.

It is particularly important to emphasize that, in contrast to long-range lidar systems where overlap can often be approximated as unity beyond a certain altitude, this simplification is not valid in the near-field for HSRL measurements. Within the first several hundred meters of range –typically up to about 1000 m, depending on the specific transmitter–receiver geometry—- the overlap function varies significantly from zero to one. Neglecting this effect in the short-range region leads to systematic underestimation of the signal power, as part of the return is geometrically excluded from the receiver aperture. Such losses manifest as distortions in the attenuated backscatter profiles and can propagate into retrievals of the backscatter ratio if not properly corrected. For this reason, the accurate determination and

application of the overlap correction are crucial to ensure that the retrieved properties accurately represent the measured particles.

Short-range lidars are based on a low full-overlap distance, which enables them to measure close to the ground or the particle source for horizontal or near-horizontal lidars. A low full-overlap range is achieved by the optomechanical alignment of the system, for example, by varying the angle between the laser and the receiver axes, as described by Ceolato et. al. [21]. As has been previously reported [54, 55], even small misalignments between the laser beam path and the receiver optical axis can significantly affect the overlap function at short ranges. Moreover, in the incomplete overlap zone, the overlap function differs between the two channels due to the different optical paths resulting from the use of different optical elements. Firstly, the beam splitter cube that splits the received atmospheric backscattering into the two channels can slightly modify the beam profile and divergence, leading to channel-dependent overlap. Moreover, the narrowband spectral filter used in the molecular channel introduces additional differences in the optical path, alignment, and field of view of this channel relative to the total channel, thereby affecting the overlap function. Furthermore, the optical axes of the detectors in each channel are not identically positioned relative to the laser beam. Finally, coatings on the spectral and interference filters may preferentially transmit different angular components of the incoming light, again modifying the near-field overlap [28].

Determination of the overlap function

The accurate treatment of the overlap function is essential for precise lidar retrievals in the near-field region (typically below 1 km). In an ideal system, $O(r) = 1$ for all ranges, but in practice the overlap gradually increases from 0 to 1 in the near-field due to finite receiver geometry, divergence of the laser beam, and imperfect alignment. Neglecting this effect leads to significant signal loss and biases in the attenuated backscatter profiles, which in turn propagate into errors in the backscatter ratio (BR) and the aerosol backscatter coefficient $\beta_{aer}(r)$.

Several strategies have been proposed in the literature to determine the overlap function. Some of them are described below.

- **Experimental measurement**: For ultra-short-range lidars, where no free-aerosol region exists, the overlap function can be experimentally determined by performing a series of lidar measurements on a calibrated low-reflectance Lambertian surface at different ranges, as reported by Ceolato et al. [21]. Then, an analytical function [56] is used to fit the measurements using the lidar parameters. The advantage of this method is that it does not rely on the usual assumption of a homogeneous atmosphere.

- **Molecular channel-assisted methods:** Using elastic and molecular channels simultaneously, it is possible to derive explicit non-iterative formulas for $O(r)$ that depend only on measured signals. Comerón et al. [57] demonstrated this approach in an aerosol lidar with both elastic and Raman N_2 and/or O_2 channels used for independent measurements of aerosol backscatter and extinction coefficients. Their method requires only the measured, range-corrected elastic and the corresponding Raman signals, plus an assumed lidar ratio. Hoyos-Restrepo et al. [28] developed a method for estimating the overlap function of a short-range HSRL based on the interchannel calibration parameter $C(r)$, the purely molecular (corrected HSR) signal, and the effective transmittance of the Rayleigh-Brillouin signals through the spectral filter. Their approach allowed them to determine the different overlap functions for both channels from the ground to 1000 m, highlighting the importance of geometric correction for HSRL retrieval in the first 100 m.

- **Dual field-of-view configurations:** Dual field-of-view (FOV) lidar systems can exploit the ratio of signals from different fields of view to constrain $O(r)$ without strong assumptions about atmospheric homogeneity [58]. Eloranta [59] presented a methodology to characterize the overlap function of the University of Wisconsin HSRL system based on placing a second molecular channel using a wide field-of-view (WFOV) receiver mounted behind the secondary mirror of the main telescope. This second molecular channel duplicates the molecular signal of the main HSRL with a 10x larger FOV and a full-overlap range of 375 m. By doing the ratio of the signals in the wide and narrow FOV molecular channels, they retrieve the overlap function of the HSRL from $\sim$ 400 m to 6 km, where the narrow FOV channel reaches the full overlap. Correcting the overlap below 400 m is only possible for cases with a well-mixed boundary that extends above 400 m, where it is possible to measure both the extinction and the backscatter cross-section accurately.

- **Analytical modeling:** Halldorsson et al. [60] proposed a theoretical method to calculate the overlap function of a lidar considering the effects of the telescope's FOV, laser beam divergence, and misalignment of the transmitter axis. This geometrical-optics model has been widely used to model the lidar overlap function in subsequent works. Povey et al. [61] proposed retrieving the overlap function of a Raman channel via nonlinear regression using Halldorsson's model and a simple extinction profile model, constrained by aerosol optical thickness. The method reduced the RMS error between the attenuated backscatter coefficient measured by the calibrated instrument and a commercial instrument by a factor of 1.4 to 2.0, even under non-ideal conditions.

Shen et al. [62] proposed using Halldorsson's model in an iterative-based general determination (IGD) method to determine the overlap function of a HSRL. The basic idea of the IGD method is to calculate the overlap function from the difference of backscatter coefficients from HSRL (not affected by the overlap) and those from the Fernald algorithm. Through an iterative optimization, the particulate backscatter coefficients calculated by the Fernald algorithm approach the exact HSRL values. Therefore, the signals in the last iteration can be considered as the overlap-corrected combined signals.

- **Cross-instrument comparison:** Overlap functions can also be determined by comparison with a reference instrument of known overlap performance, such as a well-calibrated lidar or ceilometer, as shown by Sicard et al. [55]. The authors reported that the error of the retrieved overlap function when it reaches 1 is usually less than 7%. Moreover, they report that the temporal variability of $O(r)$ estimated over 1.5 years is less than 11% in the first 1.5 km, with a maximum of 18% at heights between 1.7 and 2.4 km. The authors also studied the implication of using an inappropriate overlap function to retrieve aerosol optical properties, finding up to 60% error in the backscatter coefficient in the first 0.5 km and up to 20% above. Mei et al. [63] presented a new experimental approach to calibrate the overlap factor of a pulsed elastic lidar system using a collocated Scheimpflug lidar (SLidar) system. The obtained overlap function was also validated through horizontal comparison measurements with the assumption of homogeneous atmospheric conditions. The authors found that the median overlap factor obtained by the proposed SLidar method agreed well with that from the horizontal-measurement approach, with discrepancies generally less than 10%. Their SLidar-based method extended the measurement range of the time-of-flight-based lidar by gluing the lidar curves measured by the two systems. As a result, they retrieved the aerosol extinction coefficient from the near-surface ($\sim$90 m) to 28 km in a slant geometry during nighttime.

3.4 Proposed SR-HSRL inversion method

3.4.1 Calibration

The first step in retrieving calibrated aerosol radiative properties from HSRL measurements is data pre-processing, during which background removal and range correction are applied to eliminate systematic offsets and ensure that the measured backscatter signals are properly normalized across range. This step is essential, as any uncorrected bias would directly propagate into the subsequent calibration procedure and compromise the accuracy of the retrievals.

Once the data are pre-processed, the next objective is to calibrate the signals. For the total channel, the correction involves multiplying by the interchannel calibration parameter $C(r)$, which serves as a scaling factor to represent the total signal within the framework of the HSR channel. This calibration step is critical for enabling a consistent comparison between the two channels.

The interchannel calibration parameter $C(r)$ is derived from calibration measurements conducted outside the filter's absorption band, at a frequency $\nu = \nu_{\text{off}}$ where both Mie and Rayleigh-Brillouin scattering are transmitted. At this frequency, the effective transmittance of both components can be approximated as unity ($X_m \approx X_p \approx 1$). As a consequence, the attenuated backscatter coefficients $U_{hsr,tot}(r)$ are equal, but not the measured signals $P_{hsr,tot}(r)$. The differences are due to dissimilarities in their respective overlap functions and radiometric constants. Thus, based on the fact that if $\nu = \nu$off the attenuated backscatter coefficients are equal, the interchannel calibration parameter is derived as

$$\begin{aligned} U_{tot}(r) &= U_{hsr}(r, \nu = \nu_{\text{off}}) \\ \frac{P_{tot}(r)\, r^2}{K_{tot} O_{tot}(r)} &= \frac{P_{hsr}(r, \nu = \nu_{\text{off}})\, r^2}{K_{hsr} O_{hsr}(r)} \\ \frac{P_{hsr}(r, \nu = \nu_{\text{off}})}{P_{tot}(r)} &= \frac{K_{hsr} O_{hsr}(r)}{K_{tot} O_{tot}(r)} = C(r) \end{aligned} \tag{3.41}$$

Consequently, by taking the ratio of the offline HSR signal to the corresponding total channel signal, the interchannel calibration parameter is obtained, as formalized in Eq. (3.41). This procedure establishes the foundation for all subsequent corrections and ensures the internal consistency of the dual-channel HSRL system. The corrected total signal $P_{tot,corr}(r)$, i.e., the total signal scaled onto the framework of the HSR channel, is retrieved as

$$P_{tot,corr}(r) = C(r)\, P_{tot}(r) \tag{3.42}$$

Once $C(r)$ has been determined and the total channel signal has been corrected, the subsequent step is to correct the HSR signal. For this, it is necessary to quantify the Mie scattering crosstalk into the molecular channel. This undesired effect is characterized by the parameter χ_p, which represents the fraction of the aerosol signals that are improperly transmitted through the spectral filter. Accurate determination of χ_p is of critical importance, as even a small degree of aerosol contamination can bias the molecular signal, thereby affecting retrievals of aerosol optical properties. To estimate χ_p, atmospheric regions dominated by strong aerosol or cloud layers detected by the HSR channel are analyzed. Ideally, this channel should be insensitive to Mie signals, since its spectral filter is designed to reject aerosol contributions. Therefore, any signal observed in the molecular channel under these

conditions can be attributed to undesired crosstalk from the Mie component. The crosstalk parameter should be optimized to minimize the aerosol contributions in the molecular channel, leaving only the pure Rayleigh-Brillouin signal.

By multiplying the corrected total channel signals by the crosstalk parameter, one gets the amount of signal that must be subtracted from the measured HSR signal, as expressed in Eq. (3.43). This correction ensures that the molecular channel is adequately isolated from aerosol contamination, thereby providing a reliable foundation for the subsequent inversion algorithms and the quantitative retrieval of atmospheric optical parameters.

$$P_{Ray}(r) = P_{hsr}(r) - \chi_p P_{tot,corr}(r) \tag{3.43}$$

3.4.2 Retrieval of the aerosol backscatter coefficient

With the corrected signals $P_{Ray}(r)$ and $P_{tot,corr}(r)$ established, the decomposition of the atmospheric backscattering into its fundamental molecular and particulate components is complete. The calibration stage is essential, as it homogenizes the signal's frameworks and removes contamination from Mie crosstalk, thereby ensuring that the molecular and aerosol contributions are physically consistent with the true atmospheric scattering processes. By separating the Mie and Rayleigh-Brillouin components, HSRL becomes a well-posed problem, achieving one of its most significant advantages: the capability to retrieve calibrated aerosol backscatter coefficients directly from the measured signals, without requiring prior assumptions about the lidar ratio. The explicit formulation of β_{aer} is given by the ratio of Eq. (3.36) to Eq. (3.35), as shown in Eq. (3.44) [64].

$$\beta_{aer}(r) = \left[BR(r) - 1\right] \beta_{mol}(r) \tag{3.44}$$

Where $\beta_{mol}(r)$ is the molecular backscatter coefficient, calculated from radiosonde data using Eq. (3.38), and $BR(r)$ is the backscatter ratio, defined as the ratio of the total backscatter coefficient to the molecular backscatter coefficient. Mathematically,

$$BR(r) = \frac{\beta_{aer}(r) + \beta_{mol}(r)}{\beta_{mol}(r)} \tag{3.45}$$

In long-range HSRLs, the backscatter ratio is estimated from the ratio of the signals and the radiometric constants as displayed in Eq. (3.46) [16], where the ratio of the radiometric constants K_{hsr}/K_{tot} corresponds to the interchannel calibration constant K. This is because long-range lidars operate only in full overlap zones; therefore, when calculating the signal ratio, this term is canceled. Moreover, traditional long-range HSRLs use ultra-narrowband lasers where the Doppler broadening of Mie scattering is small, and the effective transmission of aerosol signals through the spectral filter is then negligible, meaning $X_p \approx 0$.

$$BR(r) = \frac{K_{hsr} P_{tot}(r)}{K_{tot} P_{hsr}(r)} = K \frac{P_{tot}(r)}{P_{hsr}(r)} \tag{3.46}$$

In a more general context where the overlap function can not be assumed to be unity, or where the overlap of both channels is not equal, the computation of $BR(r)$ requires calculating the attenuated backscatter profiles $U_{Ray}(r)$ and $U_{tot}(r)$ of the Rayleigh-Brillouin (corrected molecular) and corrected total channels, respectively. In general, the attenuated backscatter is defined as the product of the backscattering coefficient and the transmission term, i.e.,

$$U(r) = \beta(r) \exp\left[-2\int_0^r \alpha(r')\,\mathrm{d}r'\right] \tag{3.47}$$

Therefore, in the most general HSRL case, the attenuated backscatter profiles are defined as shown in Eqs. (3.48) and (3.49). The radiometric constants $K_{Ray,tot}$ can be either calculated if all the involved instrumental parameters are known, estimated from the measurements on a calibrated hard target [21], or estimated from the molecular signal and the interchannel calibration parameter [28], as will be explained in Chapter 6. The overlap function can also be measured using a hard target [21], modeled from geometrical optics calculations or analytical methods [62, 65], using dual-FOV lidar measurements [58], or determined using pure molecular channels [28, 57], as detailed in Section 3.3.1 and as demonstrated in Chapter 6.

$$\begin{aligned} U_{Ray}(r) &= \left[X_m \beta_{mol}(r) + X_p \beta_{aer}(r)\right] \exp\left[-2\int_0^r \left[\alpha_{mol}(r') + \alpha_{aer}(r')\right] \mathrm{d}r'\right] \\ &= \frac{P_{Ray}(r)\ r^2}{K_{Ray} O_{Ray}(r)} \end{aligned} \tag{3.48}$$

$$\begin{aligned} U_{tot}(r) &= \left[\beta_{mol}(r) + \beta_{aer}(r)\right] \exp\left[-2\int_0^r \left[\alpha_{mol}(r') + \alpha_{aer}(r')\right] \mathrm{d}r'\right] \\ &= \frac{P_{tot}(r)\ r^2}{K_{tot} O_{tot}(r)} \end{aligned} \tag{3.49}$$

Solving Eqs. (3.35) and (3.36), $BR(r)$ is calculated from the ratio of U_{Ray} and U_{tot}, and the molecular and particle backscattering transmittance through the iodine cell X_m and X_p, as described in Eq. (3.50) [66]. The transmittance terms $X_{m,p}$ are determined from laboratory calibration measurements, as will be detailed in Chapter 5, or by gauging a reference signal from the laser.

$$BR(r) = \frac{\left(X_m - X_p\right)^{U_{tot}/U_{Ray}}}{1 - X_p^{U_{tot}/U_{Ray}}} \tag{3.50}$$

Chapter 4

State of the art

In this chapter, we review the current state of the art to identify the novelty, challenges, and potential technological limitations associated with the development of an SR-HSRL for aerosol studies. The review is structured in two parts. The first section is dedicated to recent advances in short-range lidars for aerosol characterization, focusing on their operating principles, design strategies, and performance (spatiotemporal resolution, measurement range). The second part presents the high spectral resolution lidars developed over the last 25 years for studying atmospheric aerosols, emphasizing the technical specifications (laser and spectral filters) most relevant to the system's performance and accuracy. Together, these analyses provide the conceptual and technological context for the design and implementation of the SR-HSRL proposed in this work.

4.1 Short-range lidars

In recent years, there has been a growing need to understand and measure the impacts of aerosols near the source for various climate, air quality, and aeronautical applications. Thus, different types of short-range lidars (SR-Ls) have recently been developed to determine the radiative and microphysical properties of particles near the source. These SR-Ls differ primarily in their laser source and operating principle. There are two main types of short-range lidars for aerosol studies: elastic backscatter lidars and Scheimpflug lidars. To the best of our knowledge, there is only one short-range high spectral resolution lidar, and it is based on the Scheimpflug principle. This system will be presented in Section 4.2, along with other state-of-the-art HSRLs. Ten short-range lidar systems developed over the last seven years are discussed, discussing their technical specifications –regarding the laser used–, capabilities –spatiotemporal resolution, measurement range–, and the inversion method used. Pictures of the lidar's configuration or the system itself will be presented, if available. Table 4.1 presents a summary of the systems' specifications.

TABLE 4.1: Short-range lidar (SR-Lidar) systems for aerosol studies developed in the last years

Short-range lidar characteristics																
Country	**Lab**	**Author Year**	**SR-Lidar type**	**Inversion method**	Reference	Laser Type	λ (nm)	f_{rep} (Hz)	E (mJ)	τ (ns)	Θ (mrad)	**Resolution** Temporal (s)	Spatial (m)	**Measurem. range** (m)	**Full overlap** (m)
France	ONERA	Ceolato 2020 [21]	CAL EBL	Dedicated forward Fernald	N.R.	Freq. doubl. Nd:YAG	532	1000	0.020	0.08	0.5	1e-3	<0.10	0 - 60	25
		Ceolato 2022 [22]			N.R.	Freq. doubl. Nd:YAG	532.8	1000	0.025	0.6	0.5	4e-3	0.05	0 - 30	<8
		Bedoya-V. 2024 [26]			N.R.	Freq. doubl. Nd:YAG	532	1000	0.025	<2	1.8	1e-3	1	0 - 150	32.4
Japan	Chiba Univ.	Ong 2020 [20]	Near-horizontal EBL	Backward Klett	SpectraPhysics Explorer 349	Diode-pumped Nd:YLF	349	1000	0.060	<5	3.2	300	7.5	0 - 5000	200
Germany	Karlsruhe Instit. of Technology	Zhang 2024 [67]	Near-horiz. scanning EBL	Backward Klett-Fernald	N.R.	DPSS Nd:YAG	355	20	32.1	N.R.	<0.15	>60	5	200 - 60000	200
China	Dalian University	Mei 2018 [68]	Dual wav. SLidar	Backward Fernald	Ushio, HL40033G N.R.	MM laser diodes	407 808	–	1 W 4 W	–	194 80	45	3	80 - 10000	80
		Mei 2019 [69]	SLidar	Backward Fernald	N.R.	MM laser diode	520	–	1 W	–	0.1	45	1.5 - 300	80 - 10000	80
		Wang 2025 [70]	SLidar	Backward Fernald	SpitLight 600	Freq. doubl. Nd:YAG	532.07	10	50	10	<0.1	N.R.	15	60 - 1000	60
	Ocean University	Chen 2021 [19]	Polarized MPL	Forward Fernald	N.R.	DPSS Nd:YAG	532	7000	0.06	5	0.2	60	37.5	100 - 20000	400
USA	University of Houston	Osibanjo 2022 [71]	Mini MPL	N.R.	N.R.	DPSS Nd:YAG	532	2500	0.03	5	0.2	60-900	5 - 75	120 - 20000	N.R.

Elastic backscatter lidars

The most common type of lidar is based on the elastic backscatter technique, in which the wavelength remains unchanged during the scattering process [15]. Based on the time-of-flight principle, laser pulses propagate through the atmosphere, and a photoelectric sensor detects the small percentage of light backscattered by the particles or gas molecules, providing range-resolved measurements of the aerosol distribution [15]. Short-Range Elastic Backscatter Lidars (SR-EBLs) have received growing attention from the scientific community, with early advances often relying on rethinking lidar geometry. In 2020, Ceolato et al. [21] presented a novel bi-static, multi-axial short-range elastic backscatter lidar (SR-EBL), named Colibri Aerosol Lidar (CAL), which is lightweight, compact, and suitable for mobile platforms. It can operate in vertical or horizontal mode and was specifically designed to characterize aerosol plumes with up to 1 ms temporal resolution and <10 cm range resolution within the first hundredth meters (from 10 m). They employ a compact, air-cooled, frequency-doubled Nd:YAG laser that emits 800-ps light pulses of 20 μJ with a repetition rate of 1 kHz and a divergence of 0.5 mrad. A scanning aluminum mirror allows controlling the bi-static angle between the laser and telescope, enabling full control of the overlap function. For short-range measurements, where scattering volumes can cause defocus problems, the lidar focal plane is adjusted by mounting the optical reception system on a translation stage.

According to Ceolato et al. [21], retrieving the radiative and microphysical properties of aerosol plumes in the short range –where no reference molecular zone is available– from SR-EBLs measurements requires a different methodology than usual long-range EBL systems. Thus, the authors developed a specific forward Fernald inversion method without boundary conditions. This method involved performing geometric calibrations to determine the lidar's overlap function –a critical parameter at short range, where it cannot be assumed to be 1– and radiometric calibrations, required to retrieve attenuated backscatter profiles using dedicated inversion methods without a reference zone. Building on the Colibri SR-EBL and the dedicated forward Fernald inversion method, in 2022, Ceolato et.al. [22] estimated the aerosol number and mass concentration of soot fractal aggregates at 8 to 10 m from the source using another version of the Colibri micro-lidar. For this study, they employed a compact, air-cooled Nd:YAG laser with a 600 ps pulse length, 25 μJ pulse energy, 532.8 nm wavelength, 1 kHz repetition rate, and 0.5 mrad beam divergence. The high spatio-temporal resolution of this SR-EBL allowed the retrieval of the microphysical properties of this rapid and turbulent phenomenon, i.e., freshly emitted black carbon plumes, at a range of 9 m from the lidar with a range resolution of 5 cm and a time resolution of 4 ms.

Moreover, in 2024, Bedoya-Velásquez et al. [26] presented a study combining SR-EBL with in-situ aerosol measurements to fill the gap in understanding near-surface aerosol processes related to aerosol radiative properties and their connections with the atmospheric boundary layer (ABL), focusing on the residual layer and the ABL transition periods. Using the Colibri Aerosol Lidar, they corrected near-field retrievals (2-150 m) by benchmarking against ground-based sensors, thereby improving profile consistency during transition periods in the atmospheric boundary layer. This synergy approach emphasizes the importance of integrating remote sensing with direct sampling to resolve near-surface aerosol dynamics. This CAL version employed a frequency-doubled Nd:YAG laser with 532 nm wavelength, <2 ns pulse length, 25 μJ pulse energy, 1 kHz repetition rate, 1.8 mrad beam divergence, and a bi-static angle from 1 to 5 mrad. All the CALs share a similar configuration, differing in size, laser used, and telescope diameter. The schematic of the CALs is presented in Fig. 4.1, while a picture of the lidar is displayed in Fig. 4.2.

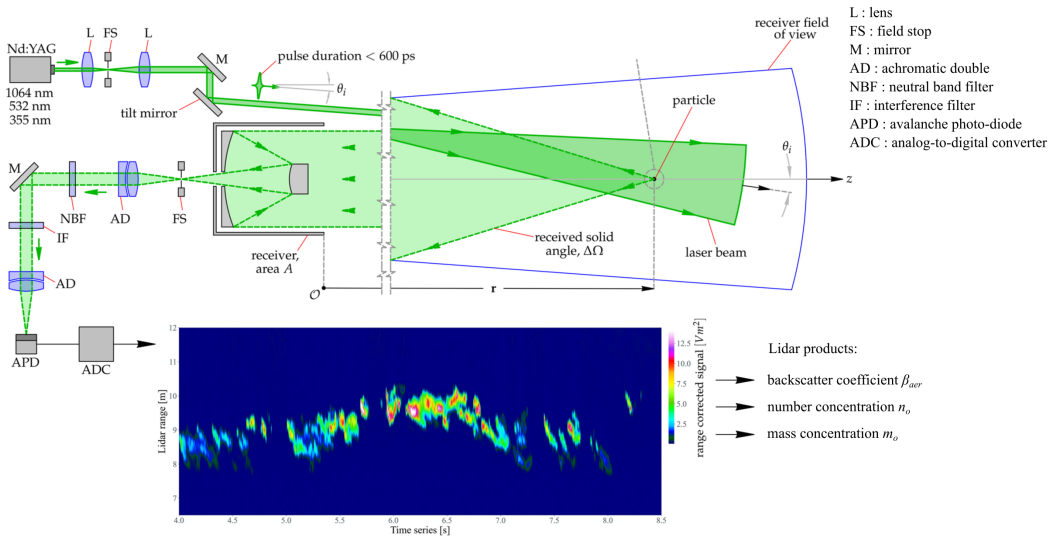

FIGURE 4.1: Basic optical diagram of CALs to measure aerosol radiative and microphysical properties in the short range. Adapted from [22].

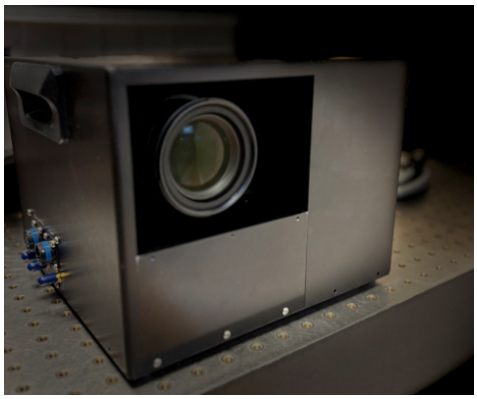

FIGURE 4.2: Colibri Aerosol Lidar. Picture credits: Romain Ceolato.

Near-horizontal lidars (NHLs) are another type of SR-EBLs, configured to have full overlap at a few hundred meters above the ground, making them appropriate for short-range aerosol studies. Ong et al. [20] presented in 2020 an NHL to detect diurnal changes in atmospheric aerosol extinction near the ground and to characterize the diurnal response of the aerosol extinction coefficient with respect to relative humidity. The NHL used in this work has an elevation angle of 4°, i.e., an observable range of ∼200 to 5000 m, equivalent to an altitude of approximately 350 m. The employed light source is a SpectraPhysics diode-laser pumped Nd:YLF laser emitting <5 ns-long light pulses of 60±7 μJ energy at 1 kHz pulse repetition rate at a wavelength of 349 nm. The lidar records the backscattered signal with a 5 min time resolution and a 7.5 m range resolution. To derive the aerosol extinction coefficient from lidar data, the authors used the well-established Klett and adaptive-slope methods. The schematic diagram and a picture of this NHL are presented in the left panel of Fig. 4.3.

Similarly, Zhang et al. [67] recently presented a comparison study of scanning aerosol lidar and in situ measurements of aerosol physical properties and boundary layer heights. The lidar system used in this work is the 3D-scanning lidar developed by Raymetrics, which avoids the overlap problem by performing low-elevation horizontal scanning. The lidar operates at 355 nm and has an overlap height of 200 m. It can retrieve aerosol profiles at altitudes as low as 25–50 m above ground level when scanning at a zenith angle of 5°. This commercial lidar employs a laser with a pulse energy of 32.1 mJ and a repetition rate of 20 Hz. The laser, a 200 mm telescope, and the signal detection units are mounted on a 3D rotating platform. Comparison with in-situ measurements confirmed the scanning aerosol lidar's accuracy, highlighting scanning as an operationally straightforward strategy for near-field to stratospheric retrievals of aerosol particle distributions and profiles, with a resolution (1 s, 5 m) similar to that of in-situ sensors. The commercial lidar used in this work is displayed in the right panel of Fig. 4.3.

Another common type of elastic lidar for short-range studies is the micropulse lidar (MPL), a small-form-factor, low-power, commercially available elastic backscatter lidar designed for continuous operation to determine cloud altitude and detect atmospheric aerosols. In 2021, Chen et al. [19] presented the polarized micropulse lidar (P-MPL) developed by the Institute of Oceanographic Instrumentation, Qilu University of Technology, which is illustrated in Fig. 4.4. The P-PML enabled continuous monitoring of spatiotemporal variations in aerosols and clouds, including the aerosol extinction coefficient and depolarization ratio, as well as the structure of the planetary boundary layer (PBL). The detection range of the P-MPL is 0.1 to 20 km, with a complete overlap at ∼400 m. It employs a 532 nm diode-pumped solid state (DPSS) Nd:YAG pulsed laser emitting a Gaussian laser beam with a

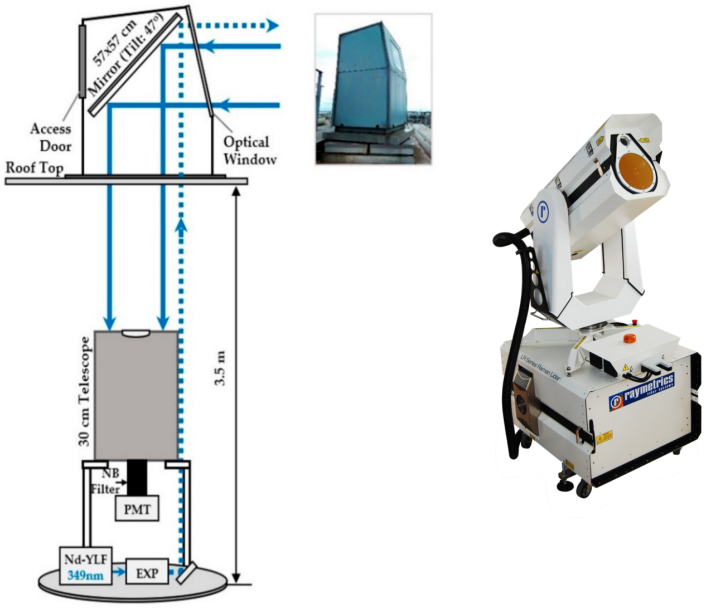

FIGURE 4.3: Left: Schematic diagram and picture of the NHL developed by Ong et al.[20]. Right: Raymetric's 3D-scanning lidar used by Zhang et al.[67].

single laser energy of 60 µJ, pulse length of 5 ns, and repetition frequency of 7 kHz. The spatial and temporal resolutions of the P-MPL are 37.5 m and 1 minute, respectively. Later in 2022, Osibanjo et al. [71] used a commercial mini-MPL –developed by Sigma Space, now Droplet Measurement Technologies, displayed in Fig. 4.5– to retrieve the PBL height over Mexico City. The mini MPL employed in this study operates at 532 nm, with a pulse repetition frequency of 2.5 kHz and a pulse energy of 3–4 µJ. It is ground-based, pointing upward, and provides aerosol backscatter from ∼120 m up to ∼20 km agl. The temporal resolution is 1 minute, and the range resolution is programmable (5, 15, 30, 75 m).

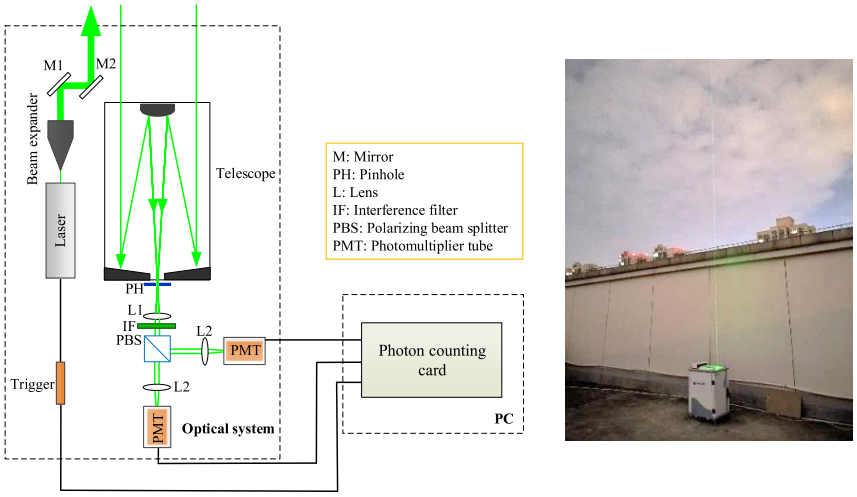

FIGURE 4.4: Layout and picture of the P-PML developed by Chen et al. [19].



FIGURE 4.5: Mini MPL (Droplet Measurement Technologies) used by Osibanjo et al. [71].

Despite being excellent tools for characterizing aerosols close to the source at high or ultra-high spatiotemporal resolution, the inherently ill-posed EBL problem limits the accuracy of short-range elastic backscatter lidars. This limitation comes as the signal $P(r,\lambda)$ measured at range r and wavelength λ by an EBL is proportional to two physical quantities, the backscatter $\beta(r,\lambda)$ and extinction $\alpha(r,\lambda)$ coefficients. Thus, to solve the EBL equation, one must assume a linear relationship between extinction and backscatter, called lidar ratio (LR) and defined as $LR = {}^{\alpha(r,\lambda)}/_{\beta(r,\lambda)}$. In addition, it is necessary to have extra atmospheric temperature and pressure profiles to calculate molecular extinction and backscatter. Due to these assumptions, assessing ultra-fine particles with a backscatter coefficient close to the molecular value, such as freshly emitted soot, poses a significant challenge for elastic lidars.

Scheimpflug imaging lidars

To overcome the overlap limitations of time-of-flight-based lidar techniques, the Scheimpflug lidar (SLidar) technique has recently been developed. The Scheimpflug principle states that light backscattered from different ranges can be sharply focused onto different pixels of an image sensor with infinite depth of field (DOF) when employing a large-aperture receiving telescope, provided that the planes of the image sensor, the telescope lens, and the laser beam intersect. The operation principle of the SLidar technique is illustrated in the left panel of Fig. 4.7. The atmospheric backscattering coefficients are retrieved from pixel intensities, and the range information is determined from the pixels' angles of incidence rather than their time of arrival. Thanks to this unique imaging principle, SLidars utilize continuous-wave (CW) high-power laser diodes as light sources and highly integrated image sensors as detectors [69].

Over the last years, SLidars operating at different diode wavelengths have been developed for aerosol sensing. In 2018, Mei et al. [68] introduced a dual-wavelength Scheimpflug lidar system designed to study aerosol extinction coefficients and Ångström exponents. This SLidar employed two temperature-controlled multimode laser diodes (1 W at 407 nm and 4 W at 808 nm) as light sources, along with two CMOS sensors as detectors. To eliminate the sunlight background, the two laser diodes were intensity-modulated. The architecture of this dual-wavelength SLidar is displayed in Fig. 4.6. The measurement range was 80 m to 10 km, and the range-dependent spatial resolution was set to 3 m to improve signal-to-noise ratio (SNR). A two-week continuous measurement campaign in near-horizontal mode was performed to validate the system performance. The authors studied the correlations between aerosol extinction coefficients and particle concentrations, relative humidity, and Ångström exponents, as well as between Ångström exponents and the concentration fraction and size distribution of aerosol particles.

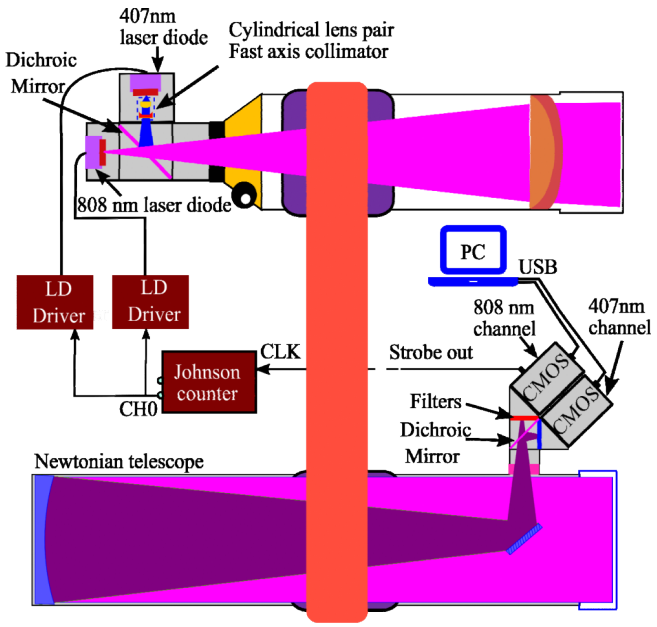

FIGURE 4.6: Dual-wavelength Scheimpflug lidar developed by Mei et al. [68].

In 2019, Mei et al. [69] compared the retrievals of a 520-nm Scheimpflug lidar system and a 532-nm pulsed lidar by measuring in near-horizontal mode (3.3° elevation angle) and on a slant direction with an elevation angle of 30°. The SLidar system employed a CW 1-W laser diode with 0.1 mrad divergence in the Scheimpflug plane. A CMOS image sensor tilted 45° from the optical axis of the Newtonian telescope was employed to measure the backscattered signals. The separation between the optical axes of the laser beam and the receiver was about 806 nm to satisfy the Scheimpflug principle. The SLidar used in this study is presented in Fig. 4.7. The authors found that the spatiotemporal variations in atmospheric backscattering measured by the two lidars generally agreed well, and that the

median extinction coefficients showed a correlation coefficient of 0.99. The extinction root-mean-square errors (RMSEs) were about 11% in homogeneous atmospheric conditions for the near-horizontal measurements and <5% for the slant direction. Finally, the authors report that errors increased with range due to the SLidar's reduced range resolution.

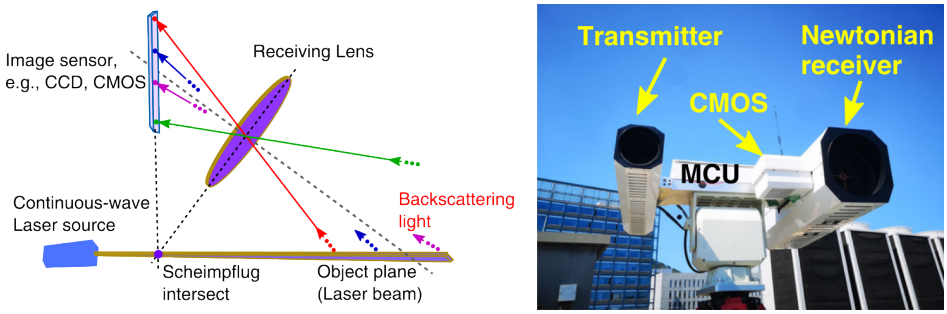

FIGURE 4.7: Left: operation principle of the SLidar technique. Right: SLidar developed by Mei et al. [69].

More recently, Wang et al. [70] proposed a novel low-blind-range lidar by combining a Raman-Mie lidar and a Scheimpflug lidar. The layout of this fused lidar system is presented in Fig. 4.8. The fused lidar is based on a SpitLight 600 frequency-doubled Nd:YAG laser (532.07 nm) with 10 ns pulse length, 10 Hz repetition rate, 50 mJ output power, and <0.1 mrad divergence. The configuration of the SLidar (including the tilt angle, baseline, and telescope focal length) determines its spatial resolution and blind range. The authors calibrated the overlap function by determining the ratio of Mie to Scheimpflug lidar signals in a region where the spatial resolutions were similar. The signals measured by both lidars matched with a small standard deviation from 60 m to 1 km, at a 15 m spatial resolution. Since the SLidar's range resolution decreases with the square of the detection range, the SNR at far ranges deteriorates, especially when there is a heavy aerosol load near the ground. To allow daytime measurements with the SLidar, the authors set a short exposure time for the image sensor and acquired images in "on-signal minus off-signal" mode, using the laser trigger signal to control the exposure.

Due to their operational principle, the SLidars offer several inherent advantages, including low cost, low instrumental complexity, and a short blind overlap range (usually <100 m). Moreover, the SNR does not decrease with the square of the measurement distance, as in pulsed lidar techniques [68]. However, there are also some inherent disadvantages. First, the spatial resolution is inversely proportional to the square of the measurement distance, leading to centimeter-level range resolution in the near range and significantly larger range resolution in the far range [68]. Second, the pixel-distance relationship must be calibrated by measuring the beam spot from a distant building with a known distance [27, 69]. Third, image sensors can be saturated during the daytime if the background is bright, potentially

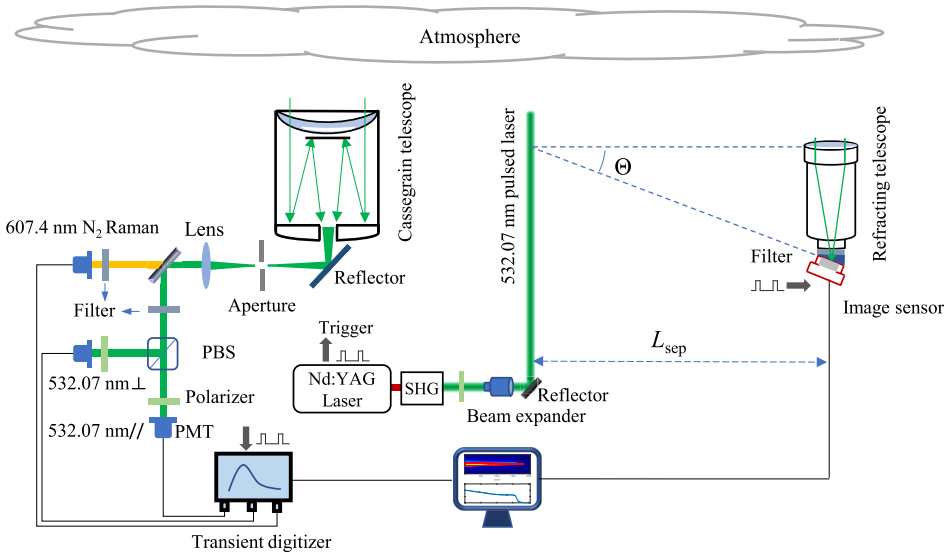

FIGURE 4.8: Layout of the fused pulsed lidar (Raman + depolarization) and SLidar system developed by Wang et al. [70].

limiting measurements to nighttime if ultra-narrowband interference filters are not used [69]. Furthermore, high-power laser diodes or large-aperture telescopes are needed to enhance the SNR [68]. Additionally, they do not allow continuous, synchronized data acquisition, as it requires precise, step-wise wavelength switching of the CW laser. This causes instability in the laser wavelength, requiring a dual-exposure scheme to address it. The first exposure is for waiting for wavelength stabilization, and the second one for performing lidar measurements. This process introduces extended integration periods, resulting in lower temporal resolution to ensure measurement fidelity [27, 69].

4.2 High spectral resolution lidars

The operating principle of HSRL was described and demonstrated in 1968 by Fiocco and DeWolf [72], who performed preliminary laboratory experiments using a pressure-scanned Fabry-Perot interferometer to determine the aerosol content of air. After this successful non-ranging demonstration of separating aerosol and molecular backscattering, the University of Wisconsin (UW) lidar group [48, 73] coined the name and described the HSRL technique in the early 80s. They used a narrowband optically pumped oscillator-amplifier dye laser and a two-channel Fabry-Perot polyetalon interferometer to separate atmospheric backscattering into its Doppler-broadened molecular and elastically scattered aerosol components, enabling measurement of the extinction cross-section and the aerosol-to-molecular backscatter ratio. In several subsequent works, the UW lidar group demonstrated the potential of HSRL to derive, without assumptions, profiles of aerosol [74] and cirrus clouds [64, 75, 76] optical properties –optical depth, extinction and backscatter cross sections, and backscatter phase

function–. Other studies suggested that, because the molecular Doppler shift depends on atmospheric state parameters, HSRL could be used to determine atmospheric temperature and pressure. Schwiesow and Lading [77] proposed measuring atmospheric temperature profiles using HSRL via two stabilized Michelson interferometers.

To improve the sensitivity and reliability of HSRL, the Colorado State University lidar group proposed using tunable lasers and atomic vapor cells as blocking filters due to their higher and wider dynamic-range aerosol-scattering rejection ratio, stability in absorption characteristics, and ease of use and alignment [78, 79]. Later on, She et al. [80] used a barium atomic absorption filter and an Argon-ion CW dye laser to retrieve the first simultaneous HSRL vertical profiles of atmospheric temperature, pressure, and density, as well as aerosol backscatter ratio, extinction coefficient, and backscatter phase function. Afterward, Piironen and Eloranta [81] presented the first results of HSRL measurements using an iodine cell as the spectral filter, which allowed the use of narrow-bandwidth, frequency-doubled Nd:YAG lasers instead of Argon-ion CW dye lasers. This allowed obtaining strong absorption using a shorter cell at room temperature, resulting in better performance and improved accuracy of the technique. Ever since, the HSRL technique has evolved to new and diverse atmospheric applications, like stratospheric temperature [82, 83] and wind-velocity retrieval [82, 84], aerosol classification [85, 86]. But it has also proved to be a useful tool in other fields like ocean sciences to investigate the marine atmospheric boundary layer [87] or to retrieve the seawater volume scattering function [88] and depth-resolved optical properties [89]. Moreover, technical improvements have allowed lower costs and more durable and accurate systems, including using different laser sources like multimode [90–92], diode [93] and fiber lasers [94] besides different spectral filters like rubidium cells [93], Fizeau interferometers [83], and Mach-Zender interferometers [90, 95].

In this section, we examine the HSRL systems developed over the last few years, discussing their technical specifications –laser source and spectral filter– and capabilities –temporal and spatial resolution–. The systems under discussion are summarized in Table 4.2, and some relevant layouts or figures are presented where appropriate. We report 27 different HSRLs from Japan, China, the European Union, and the United States; these are ground-based, airborne, shipborne, or spaceborne systems. The oldest is from 1999, and the latest is from 2025. Most use the second (532 nm) or third (355 nm) harmonics of Nd:YAG lasers. The spectral filters used are vapor cells (iodine and rubidium) and interferometers (Michelson, Fabry-Pérot, Fizeau, Mach-Zehnder) in various configurations (field-widened, density-tuned, scanning, confocal, and self-tuning). The technical specifications most relevant to HSRL's performance and accuracy will be discussed.

TABLE 4.2: HSRL systems for aerosol studies developed in the last years

HSRL characteristics															
			Laser							Spectral filter				Resolution	
Country	**Lab**	**Author Year**	Reference	Type	λ (nm)	f_{rep} (Hz)	E (mJ)	τ (ns)	Δυ (MHz)	Type	Scanning range and frequency	Vapor filter temperature or pressure	FSR (GHz)	Temporal (min)	Spatial (m)
Japan	NIES	Liu 1999 [96]	Continuum Powerlight 7010	Injection seeded Nd:YAG	532	10	400	5 – 7	90	40 cm long iodine cell	–	N.R.	N.R.	15	>7.5
		Jin 2017 [90]	Continuum Surelite I	Multimode Nd:YAG	532	10	200	4 – 6	116	Scanning Mach–Zehnder interferometer	255 MHz 1 Hz	–	0.255	15	1.5
		Jin 2020 [18]	Continuum SL I-10	Injection seeded, Q-switched Nd:YAG	355	10	100	4 – 6	173	Field-widened scanning Michelson interferometer	1 fringe 1 Hz	–	2.4	15	90
		Jin 2022 [97]	Continuum SL I-10	Injection seeded, Q-switched Nd:YAG	355 532	10	100	4 – 6	173 116	Field-widened scanning Michelson interferometer	1.5 fringes (355 nm) 1 fringe (532 nm), 1 Hz	–	2.4	15	90
China	Ocean University	Li 2008 [87]	Continuum Powerlite 7000	Injection seeded Nd:YAG	532	10	80	10	100	Iodine cell	–	N.R.	N.R.	N.R.	37.5
		Liu 2009 [98]	N.R.	N.R.	532	2800	1.79	20	99% SP	10 cm long iodine cell	–	65°C	–	45	100
	AIOFM	Zhao 2015 [99]	N.R.	Injection seeded Nd:YAG	532	30	150	8	<90	20 cm long iodine cell	N.R.	60°C	2.0	5	7.5
	Zhejiang University	Liu 2016 [100]	N.R.	Injection seeded Nd:YAG	532	N.R.	270	N.R.	100	Field-widened Michelson interferometer	–	–	3.0	N.R.	7.5
		Liu 2019 [66]	N.R.	N.R.	532	40	150	N.R.	N.R.	10 cm long iodine cell	–	39°C	N.R.	N.R.	480

		Wang 2021 [101]	Continuum	Injection seeded, Q-switched Nd:YAG	532	10	100	10	N.R.	Iodine cell	–	N.R.	N.R.	2	75
		Wang 2022 [92]	Self developed	Passive Q-switched few-LM laser	532	20	1.5	15	N.R.	Field-widened Michelson interferometer	–	–	3.0	5	15
		Ke 2022 [102]	N.R.	N.R.	532	30	21	15	<10	10 cm long iodine cell	–	39°C	N.R.	N.R.	24
	Xi'an University of Technol.	Liu 2006 [103]	N.R.	Injection seeded Nd:YAG	354.7	20	200	N.R.	N.R.	Fabry-Pérot etalon	–	–	2.5	4	30
		Gao 2023 [95]	N.R.	Multi-mode Nd:YAG	532	10	150	N.R.	N.R.	Self-tunning Mach–Zehnder interferometer	–	–	0.3	0.5	1.5
	Yancheng Teachers University	Shen 2018 [104]	N.R.	Injection seeded Nd:YAG	355	50	350	N.R.	90	Triple Fabry–Pérot etalon	–	–	8	5	30
	Huazhong University of Science & Technol.	Xu 2021 [83]	InnoLas SpitLight DPSS 250-100	Diode-pumped Nd:YAG	532	100	120	N.R.	N.R.	Fizeau interferometer	–	–	8.4	5	300
	Dalian University of Technol.	Chang 2025 [27]	Self developed	CW distributed Bragg reflector	780	–	2 W	–	1	50 mm long rubidium cell	–	60°C 1.2 mPa	N.R.	1	0.2-80
EU China	CNIM BRIT	Sannino 2019 [105]	Custom Bright Solutions Srl	Injection seeded Nd:YAG	532	20	100	N.R.	N.R.	Confocal Fabry-Pérot interferometer	–	–	N.R.	N.R.	1000
European Union	DLR	Esselborn 2008 [106]	Custom	Nd:YAG freq.doub. by KTP crystal	532	100	110	N.R.	N.R.	19 cm long iodine cell	–	53-159 Pa	2.0	∼0.18	15

		Wirth 2009 [107]	Custom	Injection seeded KTP OPO pumped by Nd:YAG	532	100	100	7.5	<150	40 cm long iodine cell	–	53-159 Pa	2.0	∼0.18	15
	LATMOS	Bruneau 2015 [84]	Quantel YG980	Injection seeded Nd:YAG	355	20	50	7	70	Field-widened Mach-Zehnder interfer., four channels in phase quadrat.	–	–	1.5	N.R.	60
United States	Colorado State University	Hair 2001 [17]	Spectra-Physics DCR-3A	Injection seeded Nd:YAG	532	20	300	5	74	15.24 cm long iodine cells (2)	–	57°C 82°C	3.0 4.3	3	75
	NASA	Hair 2008 [49]	Custom Fibertek	Injection seeded Nd:YAG	532	200	2.5	15	38	38 × 10 cm iodine cell	–	65°C	2.0	∼0.17	60
		Burton 2015 [108] & Burton 2018 [109]	N.R.	Injection seeded Nd:YAG	355	200	11	N.R.	N.R.	Field-widened Michelson interferometer	–	–	2.0	12	15
					532					38 × 10 cm iodine cell	–	65°C	2.0		
	Montana State University	Hoffman 2012 [110]	Continuum Surelite I-10	Injection seeded Nd:YAG	532	10	160	6	<150	Confocal Fabry–Pérot interferometer	–	–	7.5	1	45
	NCAR	Hayman 2017 [93]	Photodigm PH780DB-R120T8	Distributed Bragg reflector laser	780	7e3	5e-3	1e3	77	1.9 x 7.5 cm rubidium 87 cell	–	65°C	N.R.	1	150
	University of Wisconsin-Madison	Razenkov 2018 [111]	Photonics Ind. Inc. DS10-532/1064 SLM	Injection seeded diode pumped Nd:YAG	532	4e3	5e-2	2.7e5	<50	10 cm long iodine cell	–	N.R.	1.8	N.R.	N.R.

4.2.1 Lasers

For performing HSRL measurements, the narrower the laser bandwidth, the better. However, its choice depends on the type of spectral filter used, as vapor filters have specific absorption lines, and the laser wavelength must be tuned to one of them. Almost all the papers (21/27) report the use of Nd:YAG lasers, as they are stable, have a narrow bandwidth, offer higher energy output, and support Q-switched and variable repetition rates. Only Hayman and Spuler [93] and Chang et al. [27] use a different, lower-cost light source: a diode (distributed Bragg reflector) laser. The vast majority of HSRLs are based on the time-of-flight principle and thus operate with pulsed lasers. Only the HSRL based on the Scheimpflug principle (HSR-SLidar), developed by Chang et al. [27], operates with a continuous-wave (CW) laser.

Manufacturers

Of the 27 HSRLs presented in Table 4.2, 14 report using commercially available lasers, 2 use commercial but customized lasers, 2 use a self-developed laser, and the remaining 9 do not present any information on the laser reference. The most common manufacturer is Continuum Inc., being the SL I-10 model the most used [18, 90, 97, 110]. The other manufacturers are InnoLas, Bright Solutions, Quantel, Spectra-Physics, Photodigm, and Photonics Ind. The self-developed laser reported by Want et al. [92] is a passively Q-switched few-longitudinal-mode (less than 3) laser. Some advantages reported for this novel laser source include its good match to the HSR filter's periodic spectral function, leading to a stable, highly precise spectral discrimination effect. Moreover, the laser is compact and has a relatively lower development cost, which benefits the miniaturization and extensive application of the HSRL system. Lastly, the laser used by Chang et al. [27] in their HSR-SLidar is based on a tunable CW butterfly distributed Bragg reflector(DBR) laser diode operating at 780 nm, which is used as the seed source for a semiconductor optical amplifier (SOA). The advantage of this CW DBR laser diode is that it is not fundamentally constrained by the Fourier-transform limit associated with pulsed operation, allowing a FWHM of typically 1 MHz with a side-mode suppression of around 50 dB.

Wavelength

Selecting the operating wavelength of an HSRL system depends on the laser source and multiple parameters, including the application, the chosen spectral filter, and its performance. Since most systems use Nd:YAG lasers, the most used wavelengths are its second (532 nm, 19/27 papers) and third (355 nm, 4/27 papers) harmonics, or both (2/27 papers). These two wavelengths are well-established in the aerosol lidar community, making it easy to find related studies for validating and comparing the results obtained. It is noteworthy that other

technologies, such as diode-based lasers, are being evaluated for use in lidar systems, as reported by Hayman and Spuler [93] and Chang et al. [27]. Operating at 780 nm, they found a midpoint between system deployability, encompassing factors such as cost, simplicity, safety, reliability, and transportability, and the accuracy of optical products. This represents an advantage over Nd:YAG lasers, which are larger and more expensive. As a drawback, molecular backscatter intensity decreases with wavelength, so the measured signals must be denoised to improve measurement accuracy. Furthermore, it is difficult to find other lidar systems operating at diode wavelengths for comparison and validation of the results of such studies. However, other remote sensing instruments, such as sunphotometers, which operate at multiple wavelengths, could be used for validation.

Repetition rate and energy

The pulse repetition rate and energy determine the potential sampling rate (and thus the temporal resolution) of an HSRL system, which is ultimately limited by the bandwidth of the data-acquisition system. Higher pulse repetition rates enable faster data acquisition and/or higher spatial resolution. The pulse energy also determines the system's effective measurement range and its SNR. Since the vast majority of HSRLs are used for long-range studies, the main focus is on improving the measurement range rather than the effective temporal resolution, resulting mostly in lasers with low repetition rates (10 to 200 Hz) and high-energy pulses (1.5 to 400 mJ). There are only three systems [93, 98, 111] reporting repetition rates in the order of kHz. Hayman and Spuler's [93] diode-laser-based HSRL instrument operates at 7 kHz with low-pulse energies of 5 μJ, which results in a low SNR that decreases the spatiotemporal resolution of the system. Liu et al. [98] HSRL's laser has a repetition rate of 2.8 kHz with a pulse energy of 1.79 mJ, resulting in a spatial resolution of 100 m for a measurement range of only 16 km (only 160 points per profile). Finally, Razenkov and Eloranta [111] system uses a laser with a frequency of 4 kHz and a pulse energy of 50 μJ. However, their paper only describes the lidar system and does not report the resolution or the measurement range.

In contrast to the works described above, our short-range, high-spectral-resolution lidar focuses on effective temporal resolution rather than measurement range. To achieve this, our laser source was chosen to have a high pulse repetition rate, on the order of kilohertz, while maintaining a lower pulse energy of around ten microjoules. This setup will enable us to investigate a range of complex, rapidly changing atmospheric and industrial processes, including new particle formation and aerosol dynamics within the atmospheric boundary layer, as well as the characterization of emission sources in the industrial and aeronautics sectors [21].

Temporal and spectral width

The temporal τ and spectral $\Delta\upsilon$ widths of an electromagnetic pulse are inversely proportional and linearly dependent, as stated by Fourier theory. Thus, a short pulse in the time domain will have a broad spectrum, and vice versa. There is a minimum time-bandwidth product defined as

$$\Delta\upsilon\Delta t \geq K \tag{4.1}$$

Where Δt is proportional to τ and K is a constant, both depending on the shape of the power spectrum of the laser pulse. For Gaussian pulses, $\Delta t = 2\sqrt{2}\tau, K = 0.441$ and for Lorentzian pulses $\Delta t = 1.287\tau, K = 0.142$ [112]. When the equality holds, the pulses are unmodulated or unchirped and are called bandwidth-limited, Fourier-limited, or transform-limited. Another important consideration related to the temporal width of the pulses is that it defines the theoretical resolution of a lidar system, which equals its effective spatial pulse length, i.e., $\Delta R = c\tau/2$. However, the bandwidth and frequency of the sensing and signal-acquisition systems will limit the actual spatial resolution.

The long-range atmospheric HSRL systems listed in Table 4.2 prioritize spectral width over pulse duration, as their main priority is spectral discrimination rather than spatial resolution. According to Eloranta [16], HSRL requires a laser with an ultra-narrow linewidth of less than 100 MHz to achieve accurate spectral discrimination. Most systems adhere to this guideline [17, 27, 49, 84, 93, 96, 99, 103–105, 111], with linewidth values as short as 1 MHz for the HSR-SLidar reported by Chang et al. [27]. For the pulsed-laser HSRL systems, the linewidth ranges from 38 MHz (corresponding to a pulse duration of 15 ns) for NASA's airborne HSRL-2 [49] to 100 MHz (10 ns) for Chinese shipborne [87] and ground-based [100] systems. Other authors have reported larger linewidth values. The three HSRL systems developed by Jin et al. [18, 90, 97] operate at 116 MHz at 532 nm and 173 MHz at 355 nm (both with pulse durations of 4–6 ns). DLR's multilidar airborne system [107] conducts HSRL measurements at 532 nm using light pulses with linewidths of less than 150 MHz (7.5 ns), as noted by Hoffman et al. [110] (6 ns). The remaining nine papers did not report the linewidth of their lasers.

For short-range HSRL measurements, it is essential to consider both laser spectral width and pulse duration, as spatiotemporal resolution is just as critical as spectral discrimination. Using laser sources designed for long-range HSRL systems is not suitable, as their spatial resolution is inadequate for short-range measurements. For instance, if the pulse duration is 15 ns, the spectral width would be greater than or equal to 29.4 MHz, ideal for HSRL measurements. However, the spatial resolution would exceed 2.25 m, which is insufficient

for short-range applications. Conversely, a shorter laser source, such as the picosecond laser (less than 800 ps) used in the short-range elastic backscatter lidar developed by Ceolato et al. [21], which allows for an effective spatial resolution of less than 10 cm, would not be appropriate for HSRL. This is because the spectral width of such pulses would exceed 551.25 MHz, surpassing by far any values reported in the literature and leading to extensive Mie frequency shifts, and thus, an insufficient spectral discrimination. Therefore, implementing the HSRL technique at short ranges requires finding the right balance between the laser spectral width and pulse duration, along with other parameters such as temporal and spectral stability, and a high pulse repetition rate.

4.2.2 Spectral filters

The spectral filter is the core of an HSRL system, allowing the separation of the molecular and aerosol backscattering signals. Throughout history, these filters have varied and evolved. Initially, early HSRLs used Fabry-Pérot interferometers. Then, to enhance spectral sensitivity, atomic filters were introduced, but this required locking the laser wavelength to specific atomic lines, along with controlling pressure and temperature. As a result, amplitude-splitting interferometers (e.g., Michelson and Mach-Zehnder) and multiple-beam interferometers (like Fizeau) began to be used. The following subsections will outline the advantages and disadvantages of each of these techniques, drawing from the findings reported by various authors in Table 4.2.

Interferometers

- **Fabry-Pérot interferometers**

  The Fabry-Pérot (FP) or multiple-beam interferometer, developed by Charles Fabry and Alfred Pérot in 1897, is a high-resolution spectroscopic device consisting of two plane, parallel, highly reflecting surfaces separated by some distance d. When one of the mirrors moves, it is called a Fabry-Pérot interferometer. If the mirrors are fixed and adjusted for parallelism, the system is referred to as a Fabry-Pérot etalon [113]. Light waves entering the FP will travel many round-trips between the two mirrors, interfering constructively or destructively. Constructive interference occurs when d equals an integer multiple q of half the input wavelength, i.e., $q\lambda/2$. All other wavelengths destructively interfere. The transmission spectrum of an FP consists only of TEM_{00} modes that differ by different values of the parameter q. The distance between two consecutive TEM_{00} modes is called the free spectral range (FSR) of the FP and is given by $FSR = c/2d$.

The FP performance depends mainly on mirror reflectivity: high-reflectivity mirrors yield narrower transmission peaks and vice versa. Thus, reflectivity is a crucial parameter for the interferometer's resolution, i.e., its ability to distinguish closely spaced transmission peaks [114]. Thus, by varying d or the mirror reflectivity, an FP can be used to transmit or block certain wavelengths, making it a suitable spectroscopic device for filtering Mie scattering in HSRL applications. However, its performance is limited by its finesse (mirror reflectivity), and its spectral separation performance may decay rapidly with increasing incidence angle [81, 115], thus requiring great effort in beam collimation and alignment. On the other hand, FP interferometers achieve high molecular transmittance, thereby improving SNR [115].

The confocal Fabry-Pérot (CFP) configuration, based on two equally curved mirrors separated by their respective radii of curvature, offers several advantages over a conventional FPI. First, it has a common resonance condition among the multiple spatial modes associated with the HSRL receiver, making it insensitive to angular misalignment [110]. Second, if the cavity spacing and mirror reflectance are carefully chosen, the spectral response of the CFP can potentially be used anywhere in the UV to NIR spectral region, allowing for the development of multiwavelength CFP-based HSRL [110]. Third, the CFP enables overcoming problems related to the spectral stability of the laser source [105]. A drawback of a confocal configuration is that the FSR (CFSR) is halved since both the even and odd spatial modes of atmospheric backscattering are simultaneously resonant. Consequently, the maximum transmission through the CFP is limited to 50% [110]. Also, the distance between the two mirrors must be precisely controlled to enable the CFPI to filter backscattered aerosol [105].

Although widely used in the early years of the HSRL technique, FP interferometers have been less used recently. Only Liu et al. [103], Shen et al. [104], Sannino et al. [105], and Hoffman et al. [110] report using this type of filter. The first two use the fixed configuration (FP etalons), while the latter use CFP interferometers. Those using etalons operate at 355 nm because it enhances daytime measurement capability and enables eye-safe operation. Liu et al. [103] made the FPI resonant at a high-frequency line of the Rayleigh spectrum (354.7 nm), avoiding interference from longer-wavelength fluorescence. Their FSR is 2.5 GHz, and the resolution is 500 MHz. With this setup, they achieve a measurement range of up to 15 km. However, because the peak transmission is low (60%), they require a high-energy pulse (200 mJ) with a low temporal resolution (4 min integration time) to improve the SNR. On the other hand, the system developed by Shen et al. [104] is based on a triple FP etalon with an

FSR of 8 GHz and a resolution of 1 GHz per etalon. It allows wind, temperature, and aerosol measurements from 0.2 to 35 km altitude. Based on simulations, the authors showed that their system has an accuracy of the aerosol backscattering ratio better than 2.5×10^{-3} at night and 3.4×10^{-3} during the day. The high accuracy implies a low resolution, both temporal (5 min integration time) and spatial (30 m at 0.2–10 km, 100 m at 10–20 km, and 200 m at 20–35 km).

To implement their CFP-based HSRL (illustrated in the left panel of Fig. 4.9), Hoffman et al. [110] used mirrors with a radius of curvature of 1 cm (CFSR = 7.5 GHz) and reflectances of 94% at 532 nm and 99% at 1064 nm (finesse of ∼25.38 and ∼156.29, respectively). Thus, the interferometer resolution is ∼300 MHz, twice the laser linewidth at 532 nm, and three times wider than the potential laser frequency jitter. The CFP diagram and picture are displayed on the right side of Fig. 4.9. Additionally, an interesting observation reported by the authors of the second CFP-based HSRL study [105] is the estimated relative errors in signal retrieval due to deviations and fluctuations in CFP transmission at low, medium, and high pollution levels. For deviations in CFP transmission, the estimated errors for aerosol (molecular) signals are as follows: 0.08% (0.09%) for low pollution, 0.04% (0.24%) for medium pollution, and 0.04% (0.44%) for high pollution. Regarding fluctuations in CFP transmission, the estimated errors are 0.87% (1.10%) for low pollution, 0.58% (3.70%) for medium pollution, and 0.60% (7.60%) for high pollution. This shows that deviations and fluctuations from theoretical performance are negligible error sources, and that CFP interferometers are well-suited for HSRL.

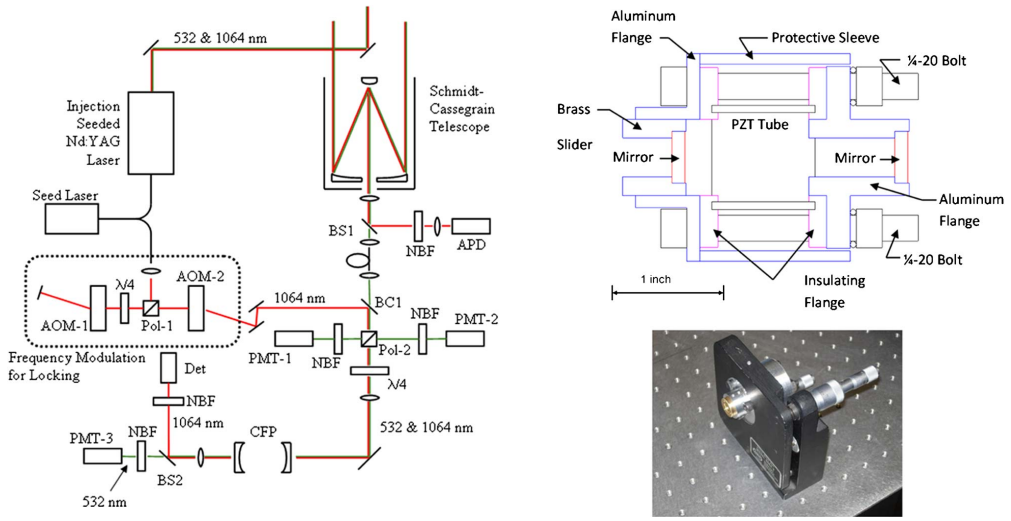

FIGURE 4.9: Left: Layout of the HSRL system developed by Hoffman et al. Right: Schematic and picture of the CFP used as a spectral filter [110].

- **Michelson interferometers**

  Michelson interferometers (MIs) are the best-known and most widely used type of amplitude-splitting interferometer, named for their ability to split the incident beam into two lower-amplitude rays [113]. A basic MI configuration includes a 50/50 beam splitter and a mirror at the end of each arm. Analogously to Fabry-Pérot interferometers, MIs can filter any frequency range by adjusting the optical path difference (OPD) [115], making them suitable spectral filters for HSRL applications. While an ideal MI with zero OPD yields an interference signal that is independent of the incident beam's angle, it provides no useful information about the incident radiation because its free spectral range, defined for MIs as $FSR = c/OPD$, would be infinite. For effective filtering, the OPD must align with the input signal spectrum [116]. To solve the angular dependency problem, a glass block is inserted in one of the interferometer's arms, resulting in a field-widened Michelson interferometer (FWMI). A proper combination of the glass and air arm's length compensates the field displacement of the two diverged beams due to the OPD, therefore reducing the angular dependence [18]. The performance of FWMIs is degraded by many external factors, such as the surface flatness of the optical elements, the anti-reflection (AR) coating quality, the frequency drift of the interferometer due to ambient vibration [117], alignment imperfections, parallelism between the two arms, and dimensions of the components in the system [116].

  FWMIs are used as spectral filters in five HSRL systems reported in Table 4.2. Those developed by Jin et al. [18, 97] and Wang et al. [92] scan one of the interferometer's arms. This approach allows correcting phase shifts due to laser wavelength instability in every scan using reference signals from the transmitted laser to create constructive and destructive interference in the molecular channel signal. Thus, the systems do not require a wavelength control system. Some disadvantages reported for this approach [18] are: i) the scanning FWMI is less efficient and has a lower temporal resolution because the interference contrast is determined after the scan, and ii) the system requires a wider dynamic range because the signal intensity can vary during the scan. Another critical aspect of the Japanese single-wavelength [18] and dual-wavelength [97] systems is that they use part of the transmitted beam as a reference to calibrate the interference contrast for Mie scattering, being less affected by contrast degradation due to possible misalignments of the interferometer. The left panel of Fig. 4.10 shows the layout of the DW-HSRL developed by Jin et al. [97], which is based on a scanning FWMI. The right side shows the schematic diagram of the measurement method using the laser reference signal.

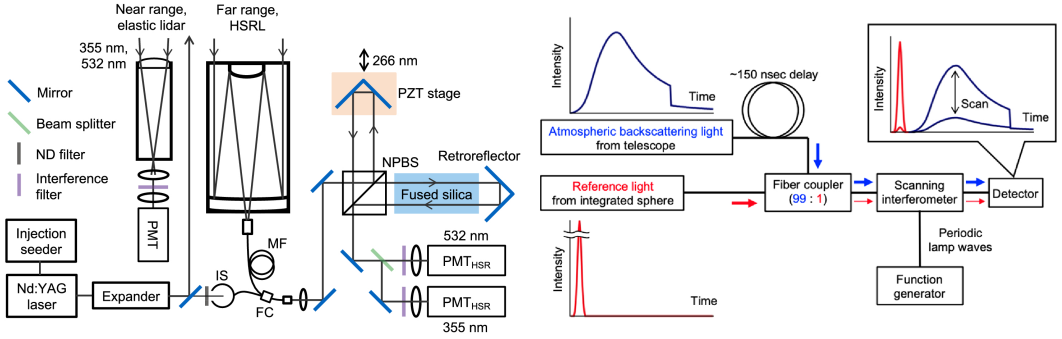

FIGURE 4.10: Left: Layout of the HSRL system developed by Jin et al. [97]. Right: Schematic diagram of the measurement method.

Based on simulations, the Japanese authors [18, 97] selected an OPD of 125 mm (FSR = 2.4 GHz), which maximizes the contrast for Mie scattering, while Rayleigh scattering is small enough to be ignored. They used an 80 mm-long fused silica glass block to achieve field-widening. Having temporal and spatial resolutions of 5 min and 30 m, the errors reported in the backscatter and extinction coefficients are 8.5×10^{-6} $km^{-1}sr^{1}$ and 3.3×10^{-2} km^{-1} at heights between 2.5 and 3.0 km. At lower heights (0.5 to 1.0 km), the error in extinction is 1.9×10^{-2} km^{-1} [18]. On the other hand, the Chinese authors [92] chose an FSR of 3 GHz, matching the laser's longitudinal mode spacing. They also quantitatively evaluated the spectral rejection using a strong backscattering signal (detected over a range of 2 to 3 km) to calculate the ratio of the maximum to minimum signal in the molecular channel during interferometer scanning. Optimum spectral rejection was achieved when the ratio stabilized.

NASA Langley's HSRL-2 described by Burton et al. [108, 109], uses the density-tuned FWMI displayed in Fig. 4.11 for HSR measurements at 355 nm. For HSR measurements at 532 nm, it uses a 38-cm-long iodine cell. The mechanical design and a picture of HSRL-2 are presented in Fig. 4.12. To ensure proper airborne operation, more stable conditions are needed. Thus, the FWMI is continuously and automatically locked to the target frequency (355 nm) using the Pound–Drever–Hall locking technique. The optimal FSR that evenly distributes the molecular signal across the different operational temperatures is 2.0 GHz. To optimize the contrast ratio (the interferometer's ability to distinguish particulate and molecular backscattered light) in flight, the air density inside the sealed air arm is adjusted using a bellows to pump air in or out, thereby fine-tuning the index of refraction and, hence, the optical path length of the air arm. Finally, Liu et al. [100] use a conventional FWMI with an FSR of 3 GHz, and its 37.876 mm long glass block is made of H-ZF52 in the Chengdu glass category (CDGM glass). The reported length of the air arm is 20.3821 mm. This setup

increases the field of view (FOV) of the interferometer up to 3.5 degrees, causing an OPD variation of only 0.12λ.

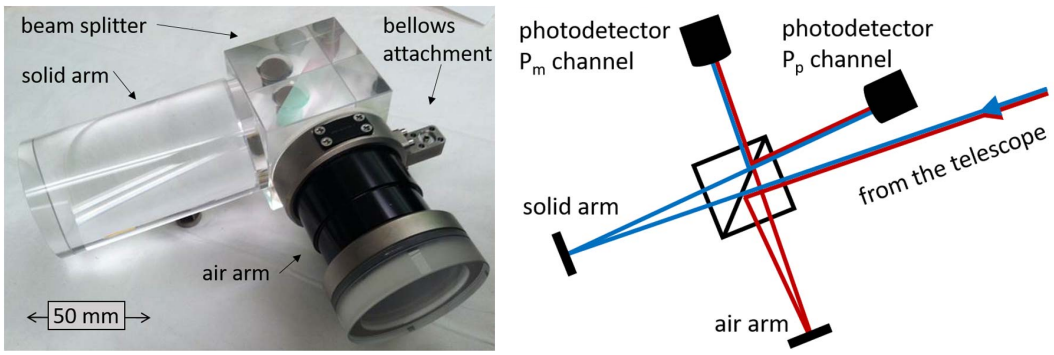

FIGURE 4.11: Picture (left) and diagram (right) of NASA's HSRL-2 355 nm density-tuned FWMI [109].

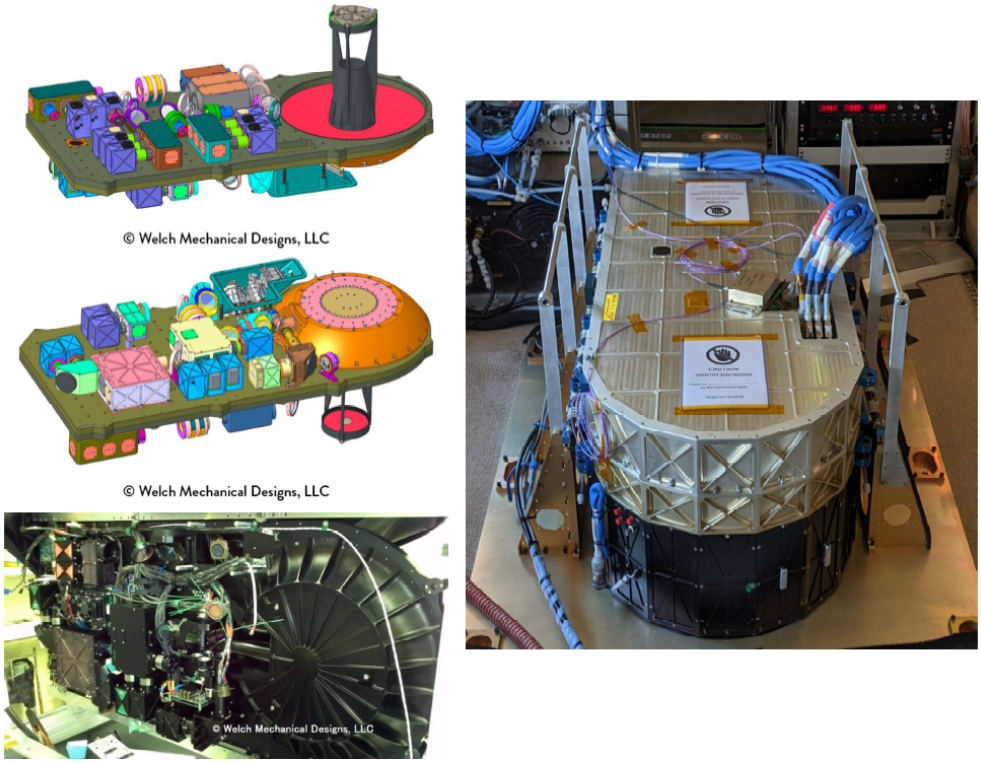

FIGURE 4.12: Left: mechanical design of NASA's HSRL-2 transmitter and receiver units (upper and middle panels), and a picture of the receiver unit (bottom panel). Credits: Welch Mechanical Design. Right: NASA's airborne HALO instrument, which contains the HSRL-2 system. Credits: NASA Airborne Science Program.

- **Mach-Zender interferometers**

  The Mach–Zehnder interferometer (MZI) is another amplitude-splitting device that uses two totally reflecting mirrors and two beam splitters: one for splitting the beams

and the other for recombining them. Hence, the light beams travel along separate paths, which makes the MZI more difficult to align than the MI [113]. This kind of interferometer was used as a spectral filter by Bruneau et al. [84], Jin et al. [90], and Gao et al. [95]. The first to develop an MZI-based HSRL were Bruneau et al. [84] for their LNG airborne multichannel lidar system, which is displayed in Fig. 4.13.

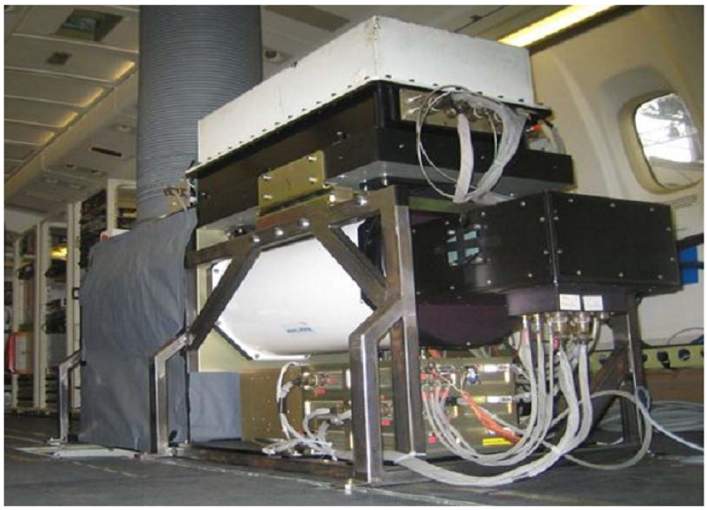

FIGURE 4.13: LNG airborne HSRL developed by Bruneau et al. [84].

Their MZI-based HSRL method measured the contrast ratio, related to the backscatter ratio, using fused-silica prisms and air gaps with a quarter-wave plate to create an MZI that provides four output signals in phase quadrature, with an OPD of 20 cm. The layout and a picture of the MZI are displayed in Fig. 4.14. This approach was independent of the laser spectral position relative to the MZI transmission function. As a result, they designed a system that did not require frequency stabilization for either the laser or the MZI. The configuration allowed them to obtain backscatter and extinction coefficients at 355 nm with a relative precision of 10% and vertical resolutions of 60 m (for β) and 240 m (for α) in aerosol layers of $\beta = 10^{-6}$ m^{-1} sr^{-1}.

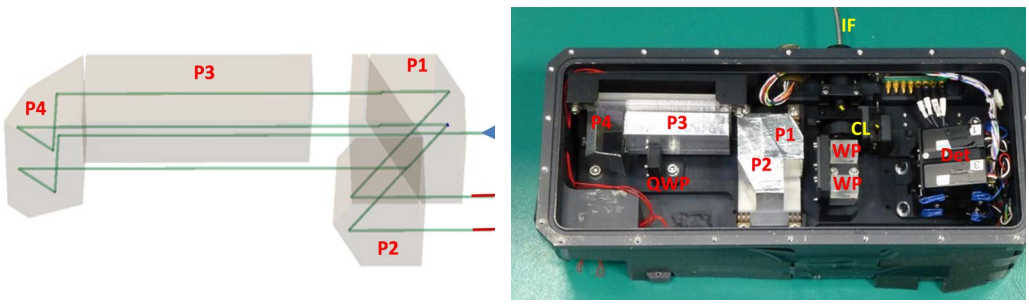

FIGURE 4.14: Layout (left) and picture (right) of the MZI used as the spectral filter in the airborne LNG [84].

Jin et al. [90] developed an HSRL based on a multilongitudinal mode (MLM) laser and a scanning MZI with the same mode spacing as the laser (255 MHz), which does not require any feedback for laser wavelength control. The interferometer length (59 cm) was optimized by maximizing the contrast of the reference light. However, such a large MZI lowers the spectral performance (Mie-scattering rejection rate) due to the narrow FOV of the receiver system. In consequence, the authors report large errors and low SNR in the extinction coefficient above the planetary boundary layer. In lower layers, where the SNR is greater, the temporal resolution is as low as 15 min. However, this work reports the best range resolution, 1.5 m.

Finally, using an MLM laser, Gao et al. [95] optimized the spectral performance of their MZI, ensuring a stable match between the MZI's FSR and the MLM's mode interval (300 MHz). This optimization employs a self-tuning technique that dynamically adjusts the MZI's OPD of 100 cm to maximize the contrast ratio. The self-tuning technique ensures that the relative error in the effective transmittance of the Mie channel, used to detect aerosol-scattering signals, remains below 10%. As a result, the retrieval outcomes are reliable and achieve the best-reported spatial and temporal resolutions (0.5 min and 1.5 m). However, a drawback of the OPD self-tuning technique is that it takes about 15 min in real measurements to determine the optimal value.

Atomic filters

Atomic cells were proposed as blocking filters to improve the sensitivity and reliability of the HSRL technique, as they are simpler, more stable, and offer higher spectral resolution and a higher intensity rejection ratio than interferometers [79]. In the early stages, barium cells were used [79, 80] since their absorption lines were suitable for Argon-ion dye lasers. Iodine cells then became the most widely used because they enable the use of narrow-band, frequency-doubled Nd:YAG lasers. However, these are not the only atoms suitable for the technique; rubidium (Rb), cesium (Cs), and lead (Pb) have also been reported as suitable blocking filter materials. Of the 27 HSRLs reported in Table 4.2, 14 use atomic cells: 12 use iodine cells, and 2 use a different atom (rubidium 87).

- **Iodine cells**

  Iodine cells were proposed as HSRL blocking filters by Piironen and Eloranta [81], who compared the performance of iodine cells vs FP etalons and found that the molecular transmissions are similar. However, iodine cells are more sensitive to air temperature because of their broader absorption linewidth. The signal separation was found

to be 2:1 for the etalon compared to 1000:1 for an iodine cell operated at 27°C, resulting in an effective aerosol rejection ratio of approximately 1:5000. This significant potential of iodine cells as spectral filters for HSRL led to their widespread use in the field. These authors also stated that of the several iodine absorption peaks, eight (1106 to 1113) can be readily accessed by thermal tuning of a frequency-doubled Nd:YAG laser. Therefore, the choice of iodine absorption line depends on the lidar design and the seed laser used. One limitation of iodine cells is their range dependency, since their sensitivity depends on the product of the Cabannes–Brillouin Scattering (CBS) spectrum and the FWHM of the chosen iodine absorption line. At altitudes of elevated temperatures, the CBS spectrum can be broader than the FWHM of the absorption line. Conversely, as temperature decreases, the CBS spectrum becomes narrower. Maximum sensitivity occurs when the CBS spectrum and the absorption line have equal widths [98]. Additionally, the molecular transmission of iodine cells is affected by laser frequency jitter. Even frequency instabilities as small as $\pm$15 MHz increase the molecular transmission uncertainty $\sim$0.6% at 200 K temperature and $\sim$0.3% at 300 K [106]. As a consequence, active laser frequency locking to the iodine absorption line is required [107].

Below, we describe the 12 articles reported in Table 4.2 that use iodine cells, categorizing them into four groups based on the iodine absorption line used. Group 1 includes those systems based on line 1109, the most used [87, 98, 101, 106, 107, 111]. Group 2 corresponds to line 1111, the second-most used [49, 96, 99, 109]. Group 3 features two systems that use line 1110 [66, 102]. Finally, Group 4 corresponds to an overlap region of lines 1107 and 1108, an implementation from NASA's HSRL-1 [17].

- Group 1 - Iodine absorption line 1109

  To remove the error introduced by the absorption spectrum difference, both molecular and total signals pass through Liu et al. [98] 10-cm-long iodine cell operating at 65°C. The molecular signal passes once, while the total signal passes twice, effectively doubling the optical path length. This reduces the cell's length, achieving stronger Mie absorption without increasing the vapor pressure/temperature, reducing self-pressure broadening of the iodine absorption line, and enhancing Rayleigh transmission [106]. The HSRL systems reported by Esselborn et al. [106] and Wirth et al. [107] also double the molecular signal path through their 19- and 40-cm long cells operated from 53 to 159 Pa. Molecular transmission through the small cell was calculated to be 0.430, while aerosol transmission was estimated in orders of 10^{-6} to 10^{-5}. The longer cell enhances Mie scattering suppression to values better than 10^{4}. Similarly, the system reported by

Razenkov and Eloranta [111] doubles the molecular path length but using two separate cells with different FWHMs. The aerosol signal is rejected by a first 10-cm-long iodine cell with an FWHM of 1.8 GHz. Then, a portion of that signal is reflected to a detector (the molecular signal), and the remaining portion passes through a second cell of the same length, filled with iodine and argon buffer. The argon vapor increases the iodine absorption linewidth by pressure broadening to 2.85 GHz, enabling atmospheric-temperature measurements. Fig. 4.15 presents the optical layout and CAD design of DLR's multi-wavelength WALES airborne lidar, which uses a 40-cm-long I_2 cell as the HSR blocking filter.

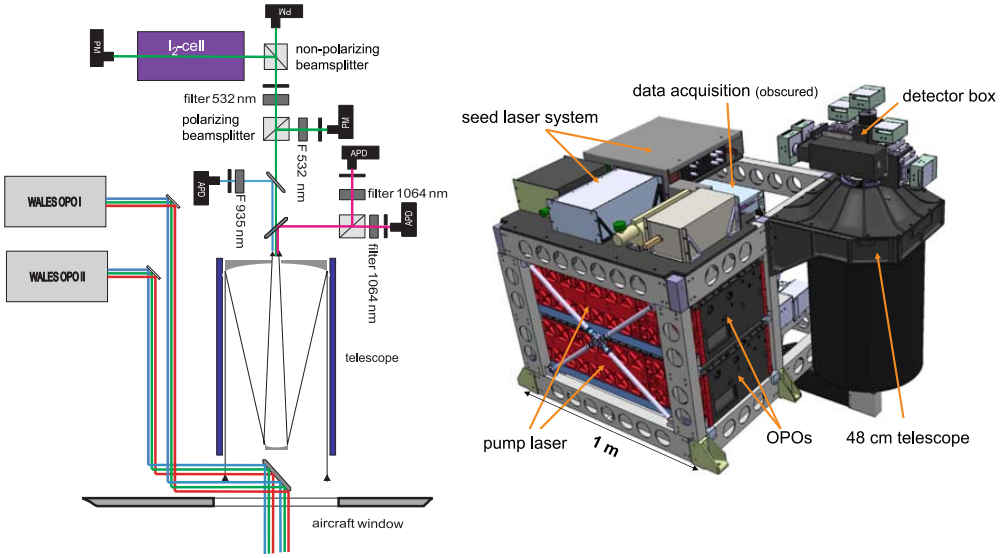

FIGURE 4.15: Layout (left) and CAD design (right) of DLR's airborne WALES system [107].

▲ Group 2 - Iodine absorption line 1111

Some researchers prefer this line for its stronger absorption compared to line 1109. However, it is closer to line 1110, necessitating larger or hotter cells for effective operation. Zhao et al. [99] used a 20-cm-long cell operating at 60°C with high aerosol rejection (up to 10^4) and ∼2 GHz linewidth broadening. Hair et al. [49] and Burton et al. [109] used a 3.8 × 10 cm cell operating at 65°C, achieving less temperature sensitivity in molecular transmission (0.36%/K), low Mie aerosol transmission (<10^{-6}), and excellent long-term stability (absolute change <0.3%). Fig. 4.16 displays the mechanical design (left) and the layout of the molecular channel (right) of NASA's HSRL-1 spaceborn system. On the other hand, Liu et al. [96] operated at room temperature but had to use a longer cell (40 cm) to use line 1111.

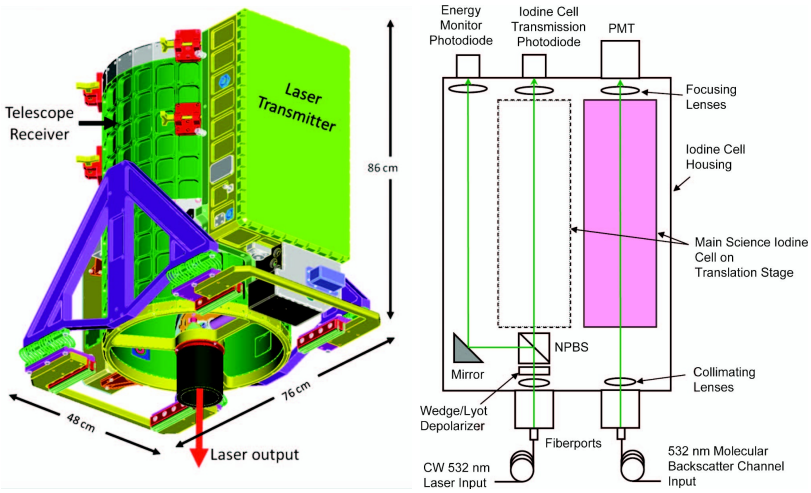

FIGURE 4.16: Layout (left) and CAD design (right) of DLR's airborne WALES system [49].

▲ Group 3 - Iodine absorption line 1110

Based on a bi-objective optimization model [118], Liu et al. [66] reported that line 1110 outperforms line 1109 with 22% more efficiency, and has more stable transmittance characteristics than lines 1109 and 1111. Moreover, based on a study of the transmittance through different absorption lines at different cell and finger temperatures [119], they found that the optimal cell and finger temperatures are 39°C and 37°C, respectively. This allowed them to use a 10-cm-long saturated cell with negligible Mie scattering transmission (10^{-6} to 10^{-4}) and an efficiency of 0.375, being the low SNR the main source of uncertainty. As an airborne prototype of China's first spaceborne HSRL described by Liu et al. [66], the HSRL described by Ke et al. performed validation tests using an identical iodine cell setup.

▲ Group 4 - Superposition of iodine absorption lines 1107 and 1108

Hair et al. [17] chose to lock their lasers' frequency near the center of the overlapping absorption of lines 1107 and 1108 to increase filter width and thus enhance Mie scattering suppression while keeping cell temperatures low to avoid losing molecular signal. Their HSRL, whose schematic diagram is presented in Fig. 4.17, featured two molecular channels with 15.24-cm-long iodine cells operating at 82.19 and 56.18°C, achieving FWHMs of 3.0 and 4.3 GHz, respectively. The cells have different transmission spectra, yielding two independently filtered molecular-scattering signals that allow precise temperature and aerosol property measurements. The hot cell achieved a measurement sensitivity of 0.42%/K to atmospheric temperature changes while passing at least 1% of the Cabannes-scattered signal. Even with such low molecular signal transmission, the authors

reported uncertainties in aerosol backscatter ratios at 1 and 5 km of 0.97% and 1.7%, respectively.

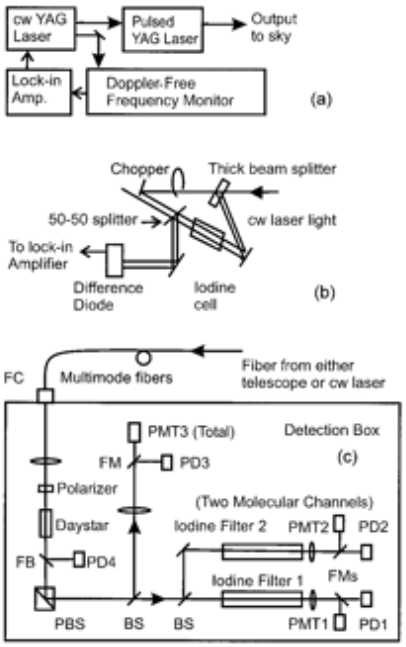

FIGURE 4.17: Schematic of the dual-molecular channel HSRL developed by Hair et al. (a) The transmitter system, (b) the Doppler-free frequency monitor, and (c) the receiver with two molecular and one total scattering channels [17].

- **Rubidium cells**

  Rubidium cells have been used in HSRL systems operating in the infrared, where cost-competitive diode lasers are available. Hayman and Spuler [93] opted for a distributed Bragg reflector diode laser operating at 780 nm because it is reliable, cost-effective, and meets HSRL requirements on frequency stability and linewidth. The wavelength was chosen because it matches the rubidium D2, F=2 absorption line. Thus, as a spectral filter, they used a 7.5-cm-long cell containing isotopic rubidium-87, controlled to approximately 65°C. This spectrally narrow notch has a high optical depth, enabling attenuation of aerosol backscatter by more than 4 orders of magnitude. Since molecular backscattering intensity can be low when operating at such large wavelengths (the authors reported less than 10^2 photon counts), the molecular signal measured must be denoised to increase the SNR and increase the precision of backscatter coefficient retrievals in layers of low aerosol loading in the free troposphere and high altitude clouds during daytime.

  Recently, Chang et al. [27] developed a CW near-infrared high spectral resolution Scheimpflug lidar (HSR-SLidar) for atmospheric aerosol sensing in the short range.

Based on the Scheimpflug principle, this system employs a 780-nm laser diode and a tapered semiconductor optical amplifier to build a CW tunable laser source. Employing a ^{87}Rb cell, the authors created a wavelength stabilization unit that locks the laser wavelength to the center of the rubidium absorption line with an accuracy of $\pm$72 MHz ($\pm$0.15 pm). This wavelength-stabilization unit enables real-time switching between on- and off-resonance wavelengths, as required by the SLidar processing method. Then, it obtains the range-resolved atmospheric lidar signal from the pixel intensities of a tilted image sensor that satisfies the Scheimpflug principle. To match the laser wavelength, a 25-mm-diameter, 50-mm-long temperature-stabilized rubidium cell mounted directly on the telescope was utilized as the spectral filter. It operates at 60° and 0.0012 Pa, achieving a spectral discrimination ratio up to 10^4. The measurement range is 0-5000 m, and the full overlap is reached at 30 m. The layout and a picture of the HSR-SLidar are presented in Fig. 4.18.

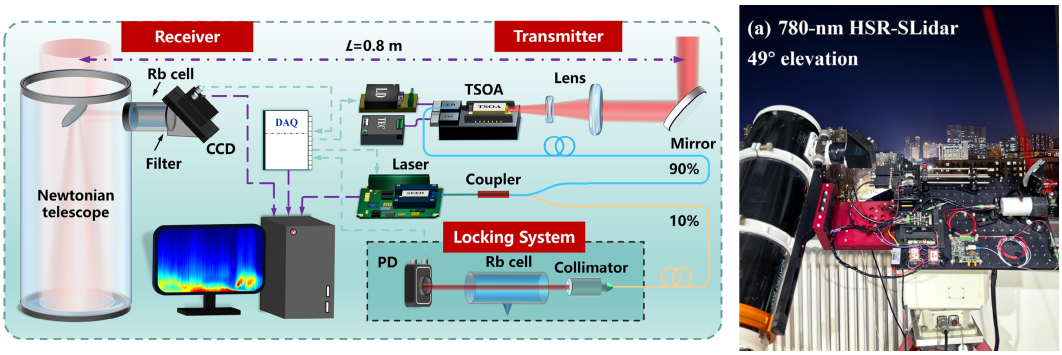

FIGURE 4.18: Left: Schematic of the short-range HSR-SLidar developed by Chang et al. [27]. Right: The HSR-SLidar during an experiment in

4.3 Summary

The comprehensive state-of-the-art review presented in this chapter has indicated that there are currently no time-of-flight-based, short-range, high-spectral-resolution lidar systems. Therefore, to identify the novelty, challenges, and potential technological limitations associated with the development of an SR-HSRL for aerosol studies, the literature review was divided into two parts. The first part describes ten short-range lidars used for aerosol studies, categorized into two main types based on their operating principles: short-range elastic backscatter lidars (SR-EBLs) and Scheimpflug lidars (SLidars). The second part presents 27 ground-based, airborne, shipborne, or spaceborne HSRLs developed in the last 25 years, discussing their technical specifications (laser source and spectral filter) and capabilities (temporal and spatial resolution).

Short-range elastic backscatter lidars operate on the time-of-flight principle, utilizing pulsed lasers. SR-EBLs include Colibri Aerosol Lidars [21, 22, 26], Micro Pulse Lidars [19, 71], near-horizontal lidars [20], and scanning lidars [67]. Colibri Aerosol Lidars use either picosecond or less than 2 ns laser pulses, enabling them to achieve ultra-high spatial resolutions (from centimeters to 1 meter) and temporal resolutions (milliseconds). By varying the bistatic angle, these lidars can control both the full-overlap height and the measurement range. The authors have developed a dedicated forward Fernald method for aerosol retrieval, which allows for the determination of aerosol backscatter coefficients as well as the number and mass concentrations at distances as close as 8 meters from the source. Micro Pulse Lidars and near-horizontal lidars are commercially available and useful for short- to medium-range aerosol studies, with a measurement range of approximately 100 meters to 20 kilometers and full overlap at around 200-400 meters from the lidar. NHLs can retrieve aerosol properties at short heights above ground level (25-50 m) by measuring at low elevation angles. However, these two types of EBLs require a longer integration time (greater than 1 minute) and have lower spatial resolutions (5 to 75 meters). For inversion, they use the classic forward Fernald method, which relies on an assumed lidar ratio value.

Although they can measure aerosols near the source at high or ultra-high spatiotemporal resolution, the inherently ill-posed EBL problem limits the accuracy of all SR-EBLs. Consequently, assessing ultrafine particles—such as freshly emitted soot—with a backscatter coefficient close to the molecular value remains a significant challenge for elastic lidars. To circumvent the inherent EBL problem, Scheimpflug-based lidars have been proposed for short-range studies. Their measurement principle allows for a full overlap range as low as 60 meters while still measuring the entire troposphere (approximately 10 kilometers). However, there are some disadvantages associated with the Scheimpflug principle: the spatial resolution is range-dependent, the pixel-distance relationship requires calibration by measuring the beam spot at a known distance, and extended integration periods are necessary, resulting in lower temporal resolution to ensure measurement accuracy.

Highly accurate, calibrated aerosol radiative and microphysical properties can be retrieved using other lidar techniques, such as Raman or HSRL, which bypass the EBL problem by directly measuring molecular backscattering. This way, Raman and HSRL are both well-posed problems that allow for the retrieval of aerosol extinction and backscatter coefficients without relying on assumptions. Twenty-seven HSRLs developed in the last 25 years were analyzed, highlighting their technical specifications and capabilities. Twenty-six of these lidars are based on the time-of-flight principle; therefore, they use pulsed lasers. Most of them use the second or third harmonics of Nd:YAG lasers, although a couple of them report

using NIR diode lasers. Different types of interferometers and vapor cells are reported as spectral filters. Twenty-six of these systems were designed for far-range aerosol studies, and thus prioritize measurement range and spectral discrimination. As a consequence, they use low-repetition-rate, ultra-narrow-linewidth lasers, which imply long-pulse lasers and, thus, low spatial resolution. Only one of the twenty-seven HSRLs reported is able to measure in the short range. It is a CW near-infrared, high-spectral-resolution Scheimpflug lidar. Being a SLidar, it inherits the advantages and disadvantages of this operating principle.

After this literature review, it is safe to say that developing a time-of-flight-based SR-HSRL is a contribution to lidar remote sensing that will help close the gap in highly accurate, high-spatiotemporal-resolution aerosol characterization at short ranges (the blind zone of long-range elastic and high-spectral-resolution lidars). This contribution represents a significant step forward for short-range lidars by introducing a well-posed variant of the technique that avoids assumptions, thereby increasing the accuracy of retrievals. The identified technical and scientific requirements for developing an SR-HSRL are:

- The optomechanical alignment must be configurable to control the full overlap of the system, enabling measurements at short distances.
- Both laser linewidth and pulse duration must be considered, as spatiotemporal resolution is just as critical as spectral discrimination and overlap range. This implies searching for a laser source that strikes the right balance between spectral and pulse features, along with other parameters such as temporal and spectral stability, pulse repetition rate, and size.
- As a consequence of the laser source, there will be limitations in the spectral performance of the system. These must be addressed via numerical simulations.
- From numerical simulations and laboratory validation measurements, choose the correct spectral filter-laser configuration to optimize the system's performance.
- Be compact, lightweight, and transportable to carry out field measurements at different locations.

Chapter 5

Design and validation of the SR-HSRL transmitter–spectral subsystems

As previously discussed, developing a short-range HSRL presented a key technical challenge: finding a laser source that met the demanding requirements of short-range and high-spectral-resolution measurements. The proper laser had to exhibit narrow, stable spectral characteristics suitable for HSRL operation, while delivering few-nanosecond pulses to ensure high spatial and temporal resolution at near ranges. It also had to be wavelength-tunable to enable the use of vapor cells as spectral filters, as well as lightweight and compact enough for integration into a portable lidar platform. In addition, a further challenge was the selection of an appropriate spectral filter capable of maintaining a high spectral discrimination ratio even when operating with relatively broad laser linewidths.

This chapter describes the design and development methodology of the SR-HSRL prototype transmitter and spectral filtering units. It begins by describing the developed characterization methodology for commercial laser sources, which allowed the identification of three suitable candidates for the SR-HSRL implementation. Then, the numerical simulations performed to predict the spectral performance and limitations of two candidate spectral filters identified from the state-of-the-art review —-a scanning field-widened Michelson interferometer and an iodine vapor cell—- are presented. These simulations guide the optimization of design parameters to maximize the spectral discrimination performance for different laser linewidths. Afterward, the laboratory validation of the spectral performance of the combined laser–filter configurations is presented. Finally, based on the laboratory characterization and validation measurements, the most appropriate laser/spectral filter combinations for different operational conditions are identified and discussed.

This chapter establishes the foundation for the prototype implementation, ensuring that the transmitter and spectral filtering units meet the necessary performance requirements for SR-HSRL operation. Chapter 6 builds on this work by presenting and analyzing the results obtained during a field campaign with the fully integrated SR-HSRL prototype.

5.1 Characterization of commercial laser sources

To perform HSRL measurements in the short range, a proper balance between spatiotemporal resolution (crucial for short-range measurements) and spectral performance (for accurate HSRL retrievals) must be found. To identify a suitable laser source for the SR-HSRL prototype, a comprehensive methodology for characterizing the pulse and spectral properties of various laser sources was developed. The pulse characteristics measured were the pulse width, repetition rate, average power (and stability), and divergence. The spectral features included the linewidth and wavelength (with their stability), and the laser wavelength tuning as a function of temperature, an indispensable feature for coupling with iodine cells. Eight laser candidates were tested, and the three that offered the right compromise between pulse and spectral features were selected and the results represented in this chapter.

The first laser is a custom Keopsys PGFL model, a compact, wavelength-tunable commercial fiber laser with a high repetition rate (50-65 kHz). It enables short-range measurements due to its temporal pulse length of 4.96 ns, corresponding to a theoretical spatial resolution of $\Delta R < 80$ cm. However, it must be considered that the bandwidth and frequency of the sensors and the signal-acquisition system define the actual resolution. A Fourier-limited Gaussian laser with such a pulse length would have a linewidth >90 MHz. In reality, the laser linewidth is by design 300 MHz, so, based on the simulations, a spectral discrimination ratio of $\sim$300 and $\sim$3330 was expected for the 10-cm- and 20-cm-long iodine cells, and of 3 for the SFWMI. As shown in the literature review (Chapter 4), most HSRL systems employ lasers with much narrower linewidths, achieving higher spectral performance at the expense of spatial resolution. This laser source was selected for testing the SR-HSRL prototype because, for this application, it offers a satisfactory compromise between the two characteristics. Additionally, the laser housing measures 270 x 270 x 40 mm and weighs only 2.9 kg, making it ideal for integration into a portable HSRL system.

On the other hand, Teem Photonics' STG-3PW-000 is a new laser prototype co-developed with the company to meet the SR-HSRL requirements. It is a compact, lightweight frequency-doubled Nd:YAG laser with a 1 kHz repetition rate and an average pulse power of 7.68 mW. The output wavelength can be tuned by adjusting the crystal temperature, featuring a temperature-regulation system to ensure power and spectral stability. The pulse width is 3.72 ns, corresponding to a theoretical spatial resolution of $\Delta R < 60$ cm, making it ideal for short-range measurements. The linewidth is 196 MHz, close to some values previously reported in the literature [18, 90, 97, 107], as discussed in Chapter 4. The expected spectral discrimination ratios are around 2800, 650000, and 6 for the short and large I_2 cells and the interferometer, respectively. The short temporal pulse length and the correct linewidth make

this laser a suitable candidate for an SR-HSRL system. Yet, due to its low pulse energy, it would only be feasible for ultra-short studies (a few hundred meters). Due to temperature-regulation-related wavelength instability detected during characterization, the company produced an improved version of the prototype. It features an improved temperature-regulation system that provides greater power and spectral stability. Since it is the same laser prototype, only the stability-related features were measured for this updated version.

Table 5.1 presents the complete specifications of both lasers. The characterization measurements performed will be described in detail below.

TABLE 5.1: Pulse and spectral characteristics of two commercial laser sources

			Keopsys		**Teem Photonics**	
Parameters	**Units**	**Expected value**	**Measured**	**Datasheet**	**Measured**	**Datasheet**
Repetition rate	kHz		50 to 65	50 to 1000	1	1
Pulse energy	µJ	5 to 10	0.9006 to 11.2962	11	7.68	8.2
Average power	mW		45.03 to 564.81	555	7.68	8.2
Power stability	%	<5	3.53 to 1.65	0.6	2.01	
Peak power	kW		0.182 to 2.28	2.20	2.06	2.65
Pulse width	ns	<10	4.96	5	3.72	3.1
Linewidth	MHz	<= 300	<400	300	<400	196
Linewidth stability	MHz	<50	<400		<400	
Wavelength	nm		532.11357 to 532.20615	532.139	532.21396 to 532.26460	532
Wavelength stability	pm	<0.1	<0.1		<0.1	

5.1.1 Keopsys PGFL model

As mentioned previously, Keopsys' PGFLL-E01-010-010-050-0532-PG08D-C1 model was selected for its compact size, moderate linewidth, and high repetition rate, which together offer a promising compromise among spatial resolution, spectral discrimination, and signal-to-noise ratio. The developed experimental setup enabled the measurement of both pulse and spectral parameters under controlled laboratory conditions. The pulse characterization included determining the temporal width, repetition rate, and output power (with stability).

For spectral characterization, the temporal evolution of wavelength and linewidth was measured using a commercial wavelength meter (HighFinesse WS/6-200 VIS/IR-II), which has an estimation accuracy of 400 MHz for the linewidth and 100 MHz for the wavelength. The temperature-dependent wavelength variation was determined by measuring the full seed laser temperature range (19.00 to 21.50°) in 0.05° increments to assess wavelength tunability linearity and stability across temperatures. These measurements allowed validation of the spectral discrimination ratios predicted by the simulations.

Pulse characterization

The pulse performance of the Keopsys laser was characterized to assess its suitability for short-range lidar operation, where pulse duration is critical for spatial resolution, and repetition rate and power are critical for achieving high temporal resolution. The measurements focused on determining the pulse width, repetition rate, average output power, and power stability under steady operating conditions.

- **Repetition rate:** The manufacturer reported in the laser's datasheet that the pulse repetition frequency varied between 50 and 65 kHz. This was confirmed using a PicoScope 6824E oscilloscope, with a bandwidth of 500 MHz and a resolution of 8/10/12 bits. The photodetector used was the APD210 model by MenloSystems.

- **Average power:** The averaged output pulse power can be changed by varying the seed laser current from 0 to 3.4 A. Consequently, the laser pulse average power ranges from 45.03±1.59 mW to 564.81±9.34 mW. It was measured using Thorlabs' power meter sensor model S415C. When operating at minimum power, the stability is 3.53% over a 16-hour measurement, as illustrated in Fig. 5.1.

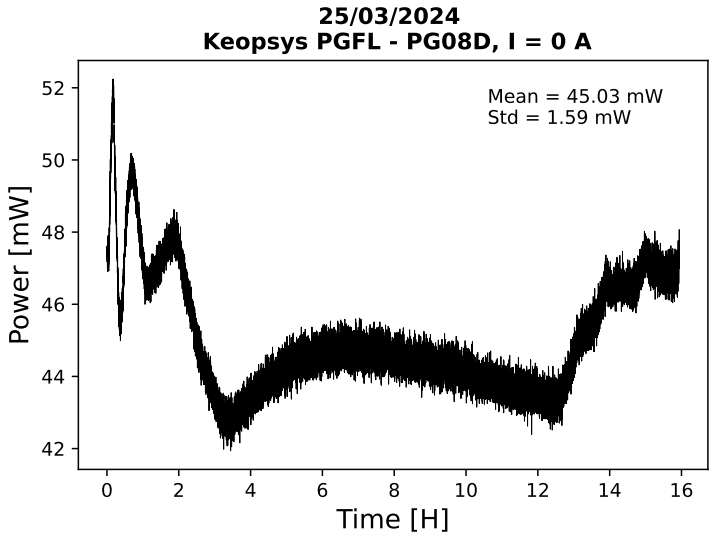

FIGURE 5.1: Power stability of Keopsys' laser operating at minimum power.

However, increasing the power to the maximum improves the stability to 1.65%, as shown in Fig. 5.2. This measurement was performed over 30 minutes due to the high laser energy.

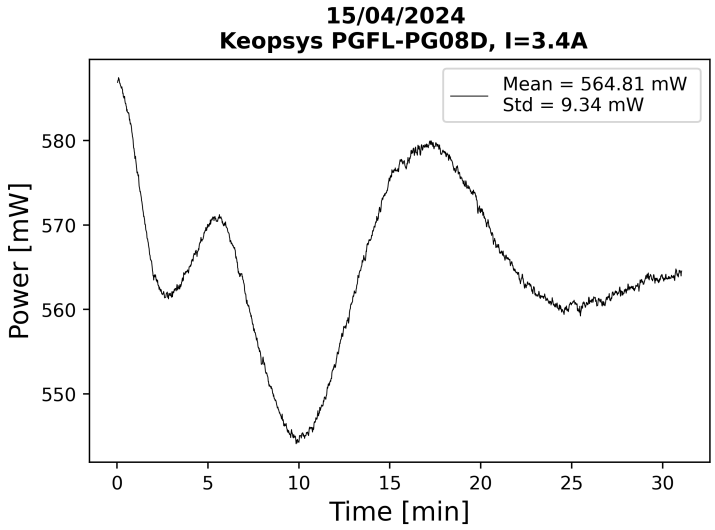

FIGURE 5.2: Power stability of Keopsys' laser operating at maximum power.

- **Energy:** Accordingly to the average power variation, the pulse energy ranges from 0.69 μJ (at 0 A, 65 kHz) to 11.30 μJ (at 3.4 A, 50 kHz).

- **Pulse width:** The pulse duration was measured using Lecroy's HDO4104 oscilloscope and Femto's HSA-X-S-1G4-SI-FS ultra-high-speed Si-PIN photodiode. A Gaussian pulse with a FWHM of 4.96 ns was found. This pulse length τ corresponds to a theoretical lidar spatial resolution $\Delta R = c\tau/2 = 74.35$ cm, ideal for performing short-range measurements. However, it should be noted that the finite bandwidth of the detection electronics and the data-acquisition system may degrade the actual resolution.

Spectral characterization

As previously discussed, the spectral features of a laser are critical for the performance of an HSRL. The linewidth influences the Doppler-broadened atmospheric backscattering spectra, so most HSRL systems reported in the literature use lasers with a spectral width of <100 MHz to maximize performance. The main challenge of this thesis was to demonstrate that it is possible to implement an HSRL with a laser as wide as the Keopsys model (300 MHz) that also enables short-range measurements. Thus, characterizing the laser linewidth and its stability was vital to determine whether a laser had the right compromise between linewidth and pulse width for our application. Moreover, using an iodine cell as the spectral filter required a tunable, stable laser wavelength that could be locked to one of iodine's absorption bands.

A commercial wavelength meter was used to measure the laser linewidth and wavelength, with resolutions of 400 MHz for the linewidth and 0.1 pm for the wavelength.

- **Linewidth and wavelength stability:** The linewidth and wavelength stability of the Keopsys laser were monitored continuously over 18 hours, and the results are shown in Fig. 5.3. The linewidth and wavelength stability were measured over 18 hours for the Keopsys laser, and the results are presented in Fig. 5.3. The top panel shows the temporal evolution of the linewidth, which remained constant and below the instrument's resolution of <400 MHz. This is consistent with the manufacturer's expected design value of 300 MHz. The bottom panel portrays the temporal evolution of the emission wavelength in air for a seed laser temperature of 20.00°. It can be extracted from the measurement that after an initial half-hour stabilization period, the long-term wavelength drift remained below the instrumental resolution limit (0.1 pm or 100 MHz). It can be concluded that Keopsys' laser exhibits excellent spectral stability after a 30-minute warm-up.

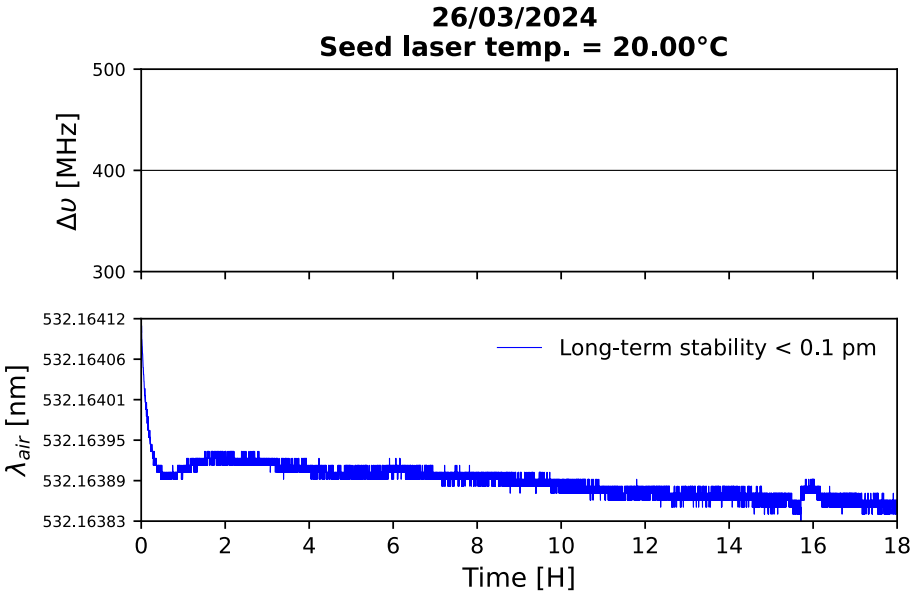

FIGURE 5.3: Spectral stability of the Keopsys laser for a seed laser temperature of 20.00°C. The top panel shows the linewidth is constant (<400 MHz), and the bottom panel shows the evolution of the air wavelength ($\bar{x}$ = 532.1638 nm).

- **Wavelength tunability:** Slightly varying the wavelength was an indispensable requisite for choosing the laser, since this was mandatory for coupling with the iodine cell in the lidar. For this laser, the wavelength can be adjusted by varying the crystal temperature with a 0.01°C resolution. To assess the linearity and repeatability of the tuning process, the entire temperature range was scanned with a resolution of 0.05°C

to determine the wavelength dependence on the crystal temperature. The resulting $\lambda(T)$ curve is presented in Fig. 5.4. The wavelength rate of change is 37 pm/0.01°C, and the wavelength in nanometers can be estimated for any temperature value using the equation $\lambda(T) = 0.03704\ T + 531.40979$ nm. Moreover, we found that the wavelength tuning is linear ($R^2 = 1$), which ensures repeatability when scanning the iodine spectral bands to find the ideal transmittance–FWHM combination to optimize the cell performance.

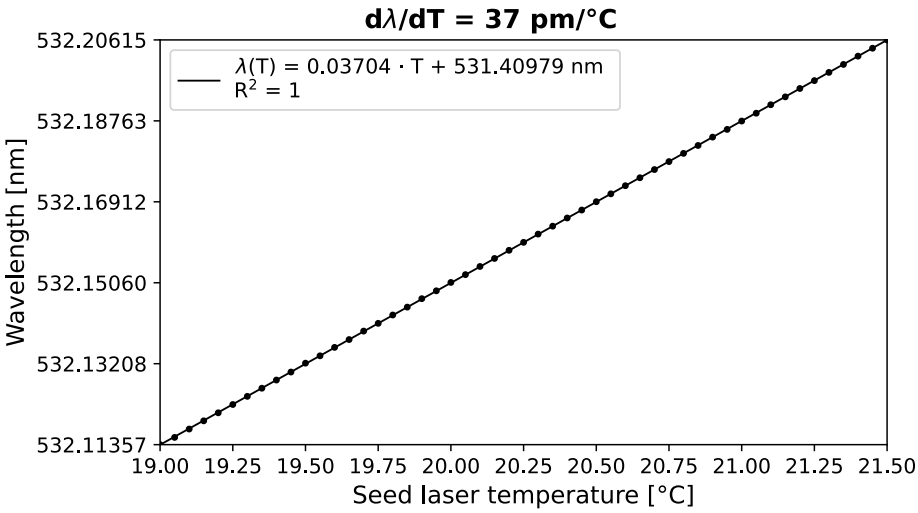

FIGURE 5.4: Output wavelength as a function of the seed laser temperature for the Keopsys laser.

5.1.2 Teem Photonics STG model v0 and v1

The second laser source selected for the SR-HSRL prototype was co-developed with Teem Photonics. Following all the given specifications about compactness, pulse requirements (high repetition rate and <10 ns pulse length), wavelength (range, tunability, and stability), and linewidth, they developed the model STG-3PW-000 prototype. The short temporal pulse length and the linewidth value –close to values reported in the literature–, made this laser a suitable candidate for an SR-HSRL system. Yet, due to its low pulse energy, it would only be feasible for ultra-short studies (a few hundred meters). As mentioned above, the first prototype (v0) exhibited some wavelength instability related to temperature regulation. Thus, the manufacturer developed a second version (v1) with an improved temperature regulation system. The results presented below apply to both laser versions, and specifications are provided as needed.

Pulse characterization Following the characterization of the Keopsys laser, the temporal performance of the Teem Photonics laser was assessed to evaluate its suitability for short-range operation, given its 3.72 ns pulse width. However, its low energy (7.68 μJ) limits its use for ultra-short measurement ranges to maintain an acceptable SNR. The measured parameters are described below.

- **Repetition rate:** The STG-3PW model has a fixed repetition frequency of 1 kHz, which was measured with the same oscilloscope and photodetector as for the Keopsys laser to guarantee measurement fidelity.
- **Average power:** The average output power is also fixed. Using the same power meter sensor and console, the mean measured value was 7.68 mW. The power stability was assessed over a 4-hour measurement period and was 2.01%. The results are displayed in Fig. 5.5.

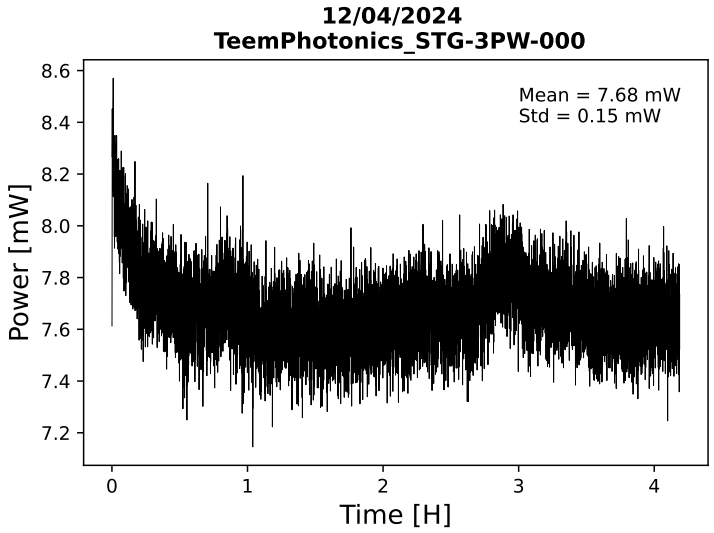

FIGURE 5.5: Power stability Teem Photonics laser.

- **Energy:** From the average power P_{avg} and the repetition rate f_{rep}, the pulse energy of Teem Photonics lasers is

$$E = \frac{P_{avg}}{f_{rep}} = \frac{7.68 \text{ mW}}{1 \text{ kHz}} = 7.68 \ \mu\text{J}$$

  The low pulse energy makes this laser suitable only for ultra-short-range measurements (a few hundred meters) to guarantee a proper signal-to-noise ratio.

- **Pulse width:** Using the same setup as for the previous laser, the temporal length of the pulse was determined from the FWHM of the Gaussian pulse measured. A value

of 3.72 ns was found, corresponding to a theoretical lidar spatial resolution of 55.76 cm, ideal for short-range measurements.

Spectral characterization Following the determination of Keopsys' laser's spectral properties, the same methodology was used to assess Teem Photonics' laser's performance. These measurements revealed a significant wavelength instability in version v0 of the laser prototype, prompting the development of an improved diode-temperature regulation system in version v1. The linewidth, wavelength, and wavelength tunability are described below.

- **Linewidth and wavelength stability:** For the laser v0, the manufacturer measured the linewidth using a Fabry-Pérot interferometer. The value reported is 196 MHz, which is relatively close to some of the papers reported in the literature review (e.g., Hoffman et al. [110] report a linewidth <150 MHz, and Jin et al. [18, 90, 97] use a laser with a linewidth of 173 MHz at 355 nm). The spectral stability measurements were performed at different diode temperatures (and thus laser output wavelengths), finding different wavelength stability values. These values ranged from 0.1 to 0.5 pm, and required using a temperature-controlled breadboard for improved performance. As an example, Fig. 5.6 shows the measurements performed at a diode temperature of 33.00°. It can be observed that, between minutes 14 and 17, there is a sudden wavelength upshift, and the mean value after is ≈ 0.57 pm greater than before. These types of stability problems were detected in this laser version and attributed to issues with diode temperature regulation.

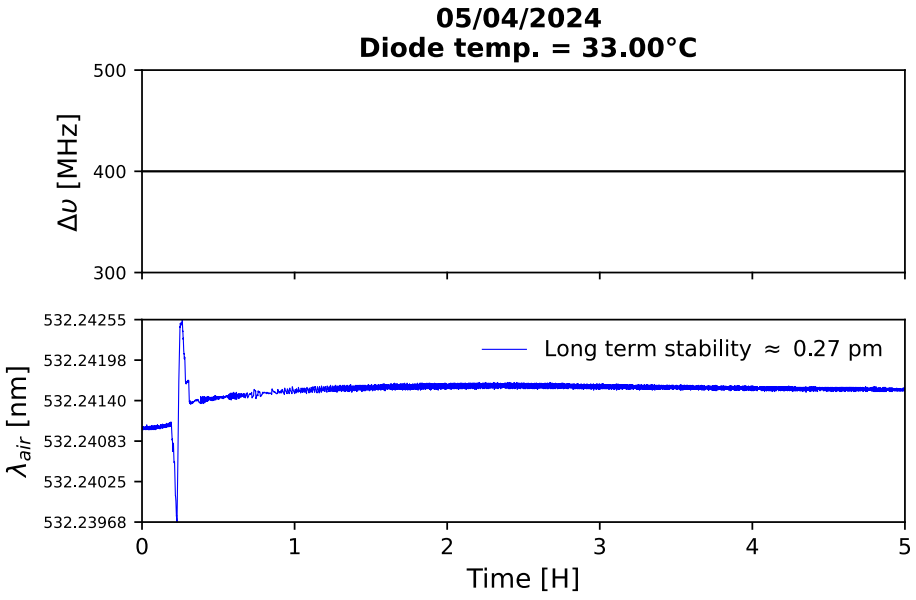

FIGURE 5.6: Spectral stability of Teem Photonics' laser v0 for a diode laser temperature of 33.00°C. The constant linewidth value is <400 MHz, the mean wavelength is 532.24155 nm, and the absolute wavelength change is 0.27 pm.

The detected stability issues led to the development of the laser version v1. The stability measurements were then repeated to check the improvement. The measurements were carried out during 35 hours at a diode temperature of 28.50°C. The results are shown in Fig. 5.7. There is a pronounced wavelength drift of 0.4 pm, but over 10-hour periods, the stability is 0.1 pm, an acceptable value for the HSRL.

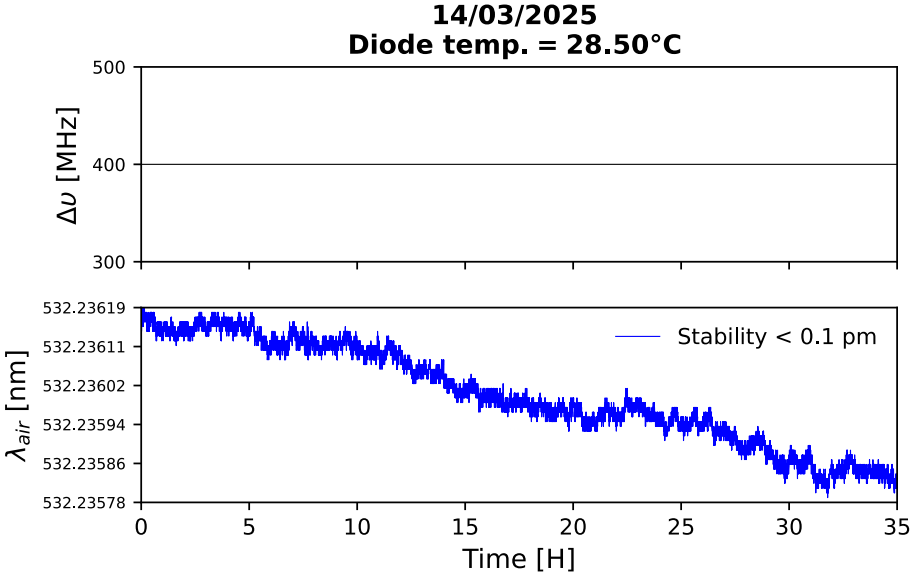

FIGURE 5.7: Spectral stability of the improved Teem Photonics laser for a diode laser temperature of 28.50°C. The constant linewidth value is <400 MHz, and the wavelength is 532.23601 nm ± 0.1 pm.

- **Wavelength tunability:** For these lasers, the wavelength variation was achieved via crystal-temperature regulation. We scanned the diode laser temperature from 31.00 to 35.00° C in 0.10°C steps to determine the relationship between crystal temperature and output wavelength. The resulting $\lambda(T)$ curves are presented in Fig. 5.8, where the blue curve represents the laser v0, and the black one the laser v1. It can be seen that, for both laser versions, the wavelength is a piecewise function of the crystal temperature. The functions and corresponding R^2 values are presented in Eq. (5.1) for the laser v0 and Eq. (5.2) for the laser v1.

$$\lambda_{v0}(T) = \begin{cases} 532.91828 - 0.02215 \cdot T, R^2 = 1.00000, & \text{if } 31.00 \leq T \leq 31.50 \\ 531.82004 + 0.01271 \cdot T, R^2 = 0.99927, & \text{if } 31.50 < T \leq 33.50 \\ 533.03960 - 0.02371 \cdot T, R^2 = 1.00000, & \text{if } 33.50 < T \leq 34.00 \\ 531.78558 + 0.01317 \cdot T, R^2 = 0.99991, & \text{if } 34.00 < T \leq 35.00 \end{cases} \tag{5.1}$$

$$\lambda_{v1}(T) = \begin{cases} 532.12075 + 0.00405 \cdot T, R^2 = 0.99982, & \text{if } 31.00 \leq T \leq 31.80 \\ 543.88292 - 0.36583 \cdot T, R^2 = 1.00000, & \text{if } 31.80 < T \leq 31.90 \\ 532.08679 + 0.00395 \cdot T, R^2 = 0.99964, & \text{if } 31.90 < T \leq 33.90 \\ 525.90836 + 0.18621 \cdot T, R^2 = 1.00000, & \text{if } 33.90 < T \leq 34.00 \\ 532.11144 + 0.00376 \cdot T, R^2 = 0.99994, & \text{if } 34.00 < T \leq 35.00 \end{cases} \quad (5.2)$$

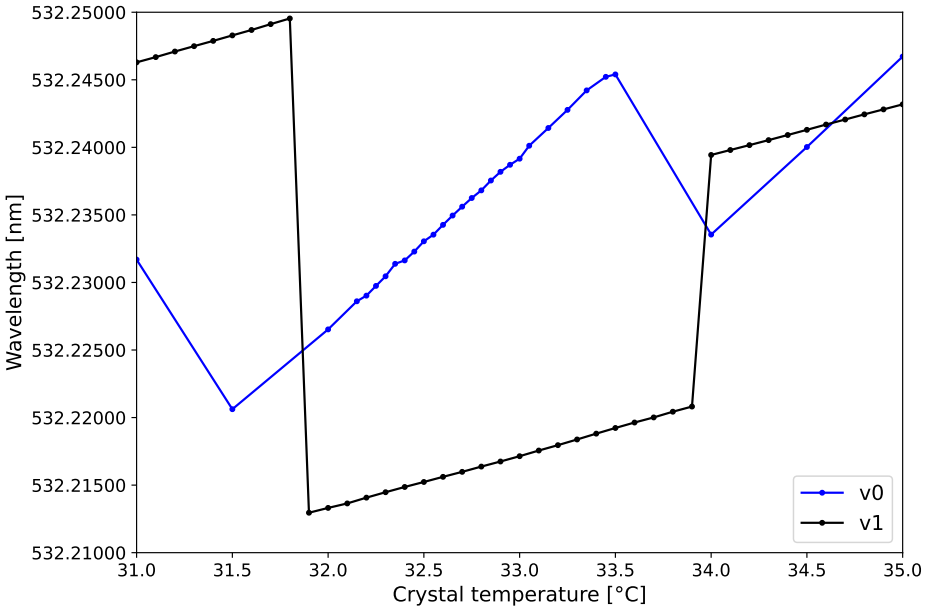

FIGURE 5.8: Output wavelength as a function of the crystal temperature for the Teem Photonics v0 and v1 lasers.

Summary

These two laser sources were selected for the SR-HSRL prototype because they strike a proper balance between their pulse and spectral characteristics. The Keopsys laser has greater pulse power, making it suitable for short- to medium-range HSRL applications. Additionally, its output wavelength shows excellent stability across the entire wavelength range, and its wavelength tunability is linear, ensuring repeatability. Its disadvantages over the Teem Photonics laser are that the linewidth has not been precisely determined –it was only estimated by the design characteristics–, and that its pulse width is larger. On the other hand, the Teem Photonics laser has an excellent combination of pulse length (3.72 ns) and linewidth (196 MHz). Wavelength stability was an issue detected in v0 and corrected in version v1. Its disadvantage compared to Keopsys' laser is its low power, which limits it to ultra-short applications to guarantee a correct SNR.

5.2 Numerical simulation of the spectral performance

As mentioned in Chapter 3, a high spectral resolution lidar has two main components: the emitter and the receiver. The emitter is primarily composed of a narrowband laser source. The receiver contains the collection and collimation optics, as well as the spectral filter that separates the Mie and Rayleigh-Brillouin backscattering spectra. The spectral performance of an HSRL is determined by its filter's ability to minimize the transmission of aerosol (Mie) backscattered signals while maximizing the pass of the molecular (Rayleigh-Brillouin) backscattered spectrum, a parameter called spectral discrimination ratio (SDR) which, for conventional HSRLs, ranges typically between 10^3 to 10^6. Mathematically, it is defined as the ratio of the effective transmittance of the Rayleigh-Brillouin backscattering spectrum X_m to the effective transmittance of the Mie backscattering spectrum X_p, i.e.,

$$SDR = \frac{X_m}{X_p} \tag{5.3}$$

The effective transmittance of the backscattering spectra $X_{m,p}$ is defined in terms of the Doppler-broadened Rayleigh-Brillouin or Mie backscattering spectrum $S_{m,p}$ and the filter spectral function F, as in Eq. (5.4), where $\omega = \nu' - \nu$ is the frequency shift from the laser central frequency ν.

$$X_{m,p} = \frac{\int_{-\infty}^{\infty} S_{m,p}(\omega) F(\omega) d\omega}{\int_{-\infty}^{\infty} S_{m,p}(\omega) d\omega} \tag{5.4}$$

Air molecules undergo random thermal motion, moving at high velocities that cause GHz Doppler broadening. The molecular backscattering spectrum S_m, described by Eq. (5.5), is a superposition of Rayleigh and Brillouin scattering. It consists of a central Gaussian peak from Rayleigh scattering, superposed on two shifted, lower-intensity Gaussian Brillouin peaks corresponding to Stokes and anti-Stokes interactions, as illustrated in Fig. 5.9.

$$\begin{aligned} S_m(x,y) = & \frac{A}{\sqrt{2\pi}\sigma_R} \exp\left[-\frac{1}{2}\left(\frac{x}{\sigma_R}\right)^2\right] \\ & + \frac{1-A}{2\sqrt{2\pi}\sigma_B} \exp\left[-\frac{1}{2}\left(\frac{x+x_B}{\sigma_B}\right)^2\right] \\ & + \frac{1-A}{2\sqrt{2\pi}\sigma_B} \exp\left[-\frac{1}{2}\left(\frac{x-x_B}{\sigma_B}\right)^2\right] \end{aligned} \tag{5.5}$$

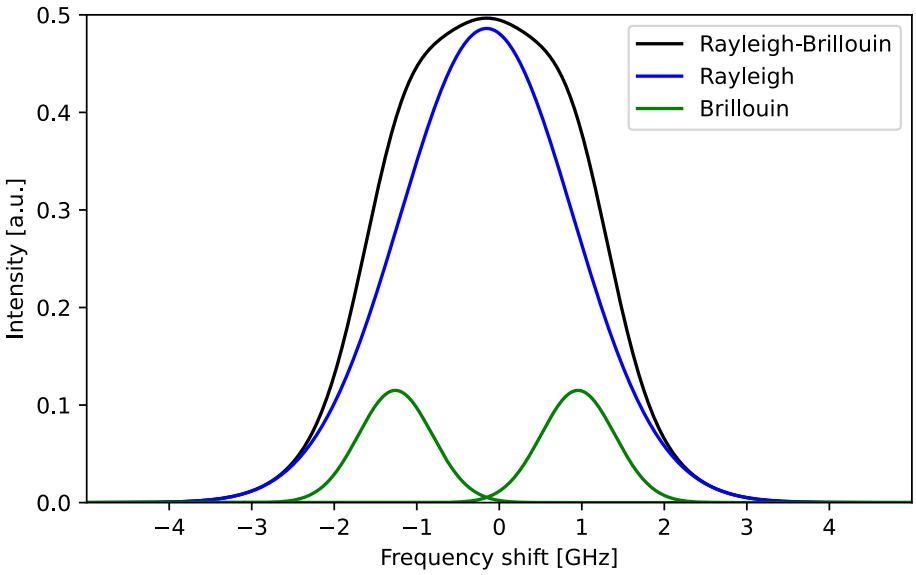

FIGURE 5.9: Doppler-broadened Rayleigh (in blue), Brillouin (in green), and Rayleigh-Brillouin (in black) backscattering spectra for an atmospheric temperature of 288K and pressure of 1013.25 hPa.

Where x and y are two non-dimensional parameters defined by Eq. (5.6) [120]. The optical frequency shift is represented by x, and the collision frequency by y. From the equation, it can be seen that Rayleigh-Brillouin scattering is primarily dependent on atmospheric temperature and particle speed and is relatively insensitive to the laser linewidth.

$$x = \frac{\omega}{\sqrt{2}kV_{th}}, \quad y = \frac{P}{\sqrt{2}k\eta V_{th}} \tag{5.6}$$

Where $k = 4\pi\lambda^{-1}\sin\left(\Theta/2\right)$ is the magnitude of the scattering vector, $V_{th} = \sqrt{k_B t/m}$ is the thermal speed at temperature t, P is the air pressure at each range, $\eta = 1.846 \times 10^{-5}$ kg m^{-1} s^{-1} is the shear viscosity of air, k_B is Boltzmann's constant, and $m = 4.808 \times 10^{-26}$ kg is the average mass of an atmospheric molecule [120]. Moreover, the parameters A (integrated intensity of Rayleigh's peak), $\sigma_{R,B}$ (the standard deviation of Rayleigh and Brillouin distributions), and x_B (Brillouin frequency shift) are defined in terms of y as described in Eqs. (5.7) to (5.10) [120].

$$A(y) = 0.18526\exp\left(-1.31255y\right) + 0.07103\exp\left(-18.26117y\right) + 0.74421 \tag{5.7}$$

$$\sigma_R(y) = 0.70813 - 0.16366y^2 + 0.19132y^3 - 0.07217y^4 \tag{5.8}$$

$$\sigma_B(y) = 0.07845\exp\left(-4.88663y\right) + 0.80400\exp\left(-0.15003y\right) - 0.45142 \tag{5.9}$$

$$x_B(y) = 0.80893 - 0.30208 \times 0.10898^y \tag{5.10}$$

On the other hand, aerosol backscattering is governed by Mie scattering. The spectral function of the Doppler-broadened Mie backscattering component, defined in Eq. (5.11), is

characterized by the half-width at 1/e of the Mie spectral distribution, denoted as γ_p. Because particles move at relatively low speeds, their Doppler-broadened spectral distribution is strongly influenced by the laser linewidth, as shown in Eq. (5.12), where γ_{laser} represents the laser linewidth and γ_{Ds} is the Doppler broadening induced by the particles moving at a relative speed V_p due to wind or turbulence [121].

$$S_p(\omega) = \frac{1}{\sqrt{\pi}\gamma_p} \exp\left[-\frac{\omega^2}{\gamma_p^2}\right] \tag{5.11}$$

$$\gamma_p = \sqrt{\gamma_{laser}^2 + \gamma_{Ds}^2}, \quad \gamma_{Ds} = \frac{2V_p}{c}\nu \tag{5.12}$$

Fig. 5.10 illustrates the dependence of the particle spectral function on the laser linewidth. In this figure, the wide spectral distribution shown in black corresponds to the Rayleigh-Brillouin spectrum at an atmospheric temperature of 288 K and pressure of 1013.25 hPa. The Mie spectral distribution for particles moving at 10 m/s is displayed for two different laser linewidths. An ultra-narrow linewidth (30 MHz) produces a correspondingly narrow aerosol Doppler broadening (represented by the red curve). On the other hand, a broader laser linewidth (300 MHz) results in a significantly wider aerosol Doppler broadening, as illustrated by the blue curve.

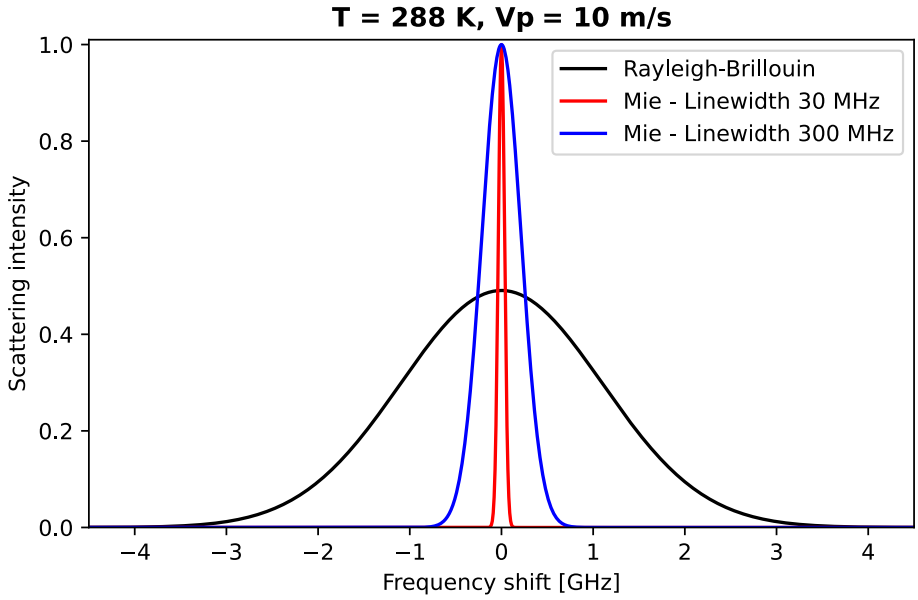

FIGURE 5.10: Effect of the laser linewidth on the Doppler-broadened Mie spectral distribution. A narrow linewidth results in a narrow spectral broadening (red curve), while a wide linewidth results in a wider broadening (blue curve). The black curve represents the molecular backscattering spectrum.

As discussed previously, the effective transmittance of the atmospheric spectral components, defined in Eq. (5.4), depends directly on the spectral response of the filter $F(\omega)$.

Numerical simulations of the spectral response for several laser linewidths were conducted for the two spectral filters selected from the literature review: an iodine vapor cell and a scanning field-widened Michelson interferometer. The block diagram of the simulation algorithm is presented in Fig. 5.11. These simulations were used to evaluate the spectral discrimination capabilities of each filter and to determine the optimal design parameters influencing their performance, such as free spectral range, length, and operating temperature. The simulations were later compared to the laboratory validations, helping select the laser-spectral filter configuration that maximized the performance of the SR-HSRL prototype.

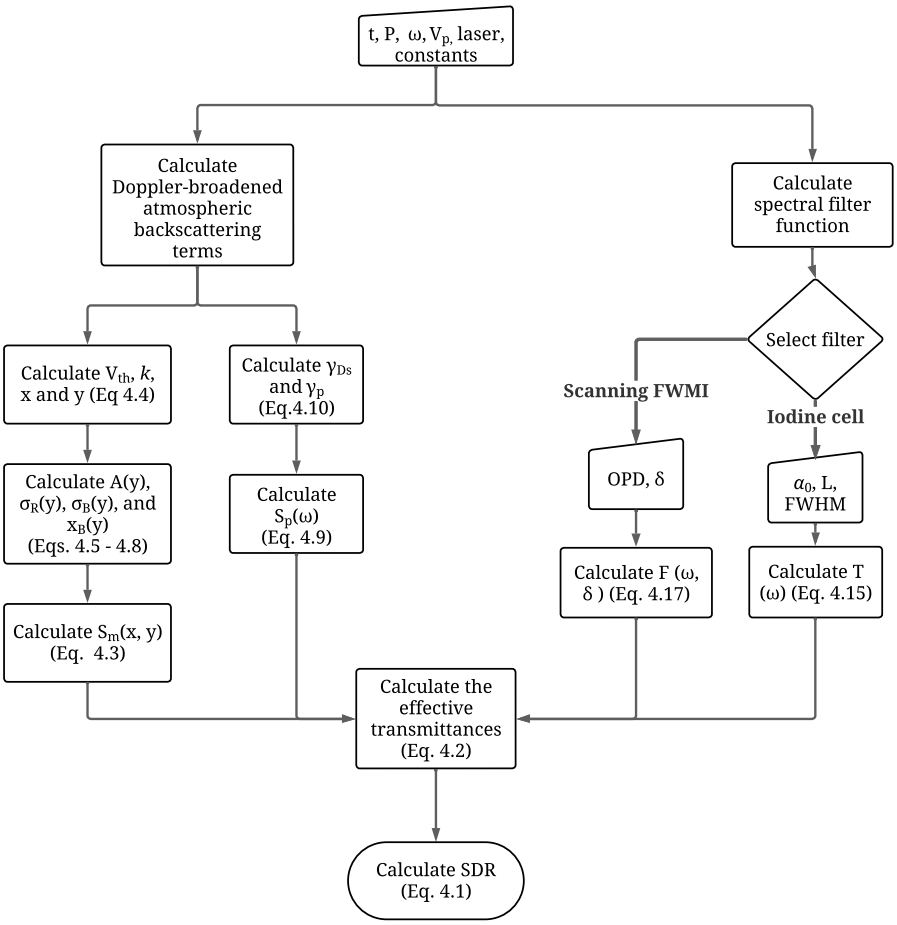

FIGURE 5.11: Block diagram of the simulation algorithm for estimating the spectral discrimination ratio of two different spectral filters.

5.2.1 Iodine cell

The transmission of iodine absorption bands depends on the convolution of Doppler- and pressure-broadening effects [118, 122, 123]. Doppler broadening, caused by the thermal motion of iodine molecules, produces a Gaussian profile. On the other hand, pressure or collisional broadening caused by molecular collisions and interactions with the cell walls

or a buffer gas produces a Lorentzian profile. For low-pressure iodine cells where collision effects are negligible, Doppler broadening dominates, and a Gaussian profile can accurately describe the transmission [118]. When higher pressures are employed (>20 Torr), i.e., if a buffer gas is injected into the cell, pressure broadening becomes significant, and a Voigt profile (the convolution of Gaussian and Lorentzian components) is required for accurate modeling [118]. In the design of the SR-HSRL prototype, iodine transmission was modeled using a Gaussian line shape because of the low operating pressure. This simplification provided a reliable, computationally efficient method for predicting the cell's spectral performance and optimizing its parameters, such as cell length and temperature.

The transmittance of an iodine absorption band depends on its pressure P and full-width at half-maximum (FWHM). The cell pressure is related to the heating temperature t, as shown in Eq. (5.13), where P is the vapor pressure in bar, t is the heating temperature in Kelvin, and A, B, and C are dimensionless parameters whose values are 3.36429, 1039.159, and -146.589, respectively [124].

$$\log_{10} P = A - \frac{B}{t + C} \tag{5.13}$$

To ensure iodine line transmission, it is necessary to calculate the iodine saturation pressure by calculating the mass of iodine to be added to the cell. This is done using the ideal gas law (see Eq. (5.14), which relates the mass m to the molar mass M [g/mol], the pressure P [kPa], the volume [cm^3], the ideal gas constant $R = 8.314 \times 10^3$ [kPa cm3/mol·K], and the temperature t [K].

$$PV = n \cdot R \cdot t = \frac{m}{M} R \cdot t \quad \therefore \quad m = \frac{M \cdot P \cdot V}{R \cdot t} \tag{5.14}$$

Finally, the Beer-Bouguer-Lambert law is used to estimate the frequency-dependent transmission $T(\omega)$ of an iodine absorption line at frequency ν' relating it to the cell length L [cm] –which defines the optical path length–, and the absorption coefficient $\alpha(\omega)$ [cm^{-1}] of the given absorption line, as described in the equation below.

$$T(\omega) = \exp\left[-\alpha(\omega) L\right] \tag{5.15}$$

Considering only Doppler-broadening for the iodine line, the absorption coefficient is approximated by a Gaussian profile as shown in Eq. (5.16), where σ is the standard deviation of the Gaussian line, related to its FWHM as FWHM $= 2\sigma\sqrt{2\ln 2}$.

$$\alpha(\omega) = \alpha_0 \exp\left[-\frac{1}{2}\left(\frac{\omega}{\sigma}\right)^2\right] \tag{5.16}$$

Substituting Eq. (5.16) into Eq. (5.15) yields the line transmission as a function of the central frequency and length:

$$T(\omega) = \exp\left\{-\alpha_0 L \exp\left[-\frac{1}{2}\left(\frac{\omega}{\sigma}\right)^2\right]\right\} \tag{5.17}$$

Based on Eq. (5.17), the simulation algorithm illustrated in Fig. 5.11 was implemented to evaluate the spectral performance and optimize the design parameters of an iodine cell. For laser linewidths in a range from 100 to 600 MHz, the Doppler-broadened atmospheric backscattering terms $S_m(x,y)$ and $S_p(\omega)$ using Eqs. (5.5) and (5.11), respectively. The transmission was then calculated for different cell lengths L, considering an absorption band with central transmittance $T_0 = 1 \times 10^{-4}$ and an FWHM of 1.8 GHz, according to Eq. (5.17). The central transmittance and FWHM values were chosen from the ranges typically reported in the literature (1.5–2.0 GHz for the FWHM and $10^{-3} - 10^{-5}$ for iodine's T_0). Subsequently, the effective transmittance of each backscattering term was obtained from Eq. (5.4), allowing for a direct assessment of the filter's spectral discrimination using Eq. (5.3). The simulations of the spectral performance of such an iodine cell are presented in Fig. 5.12. The top panel shows the simulated Mie transmission through the cell, and the middle panel portrays the transmission of the Rayleigh-Brillouin spectrum. The bottom panel displays the resulting spectral discrimination ratio.

The results presented in the figure provided valuable insights for optimizing the iodine cell design. They indicate that the SDR improves with cell length and decreases with increasing laser linewidth, as expected. A longer cell implies a longer optical path length, which, according to the Beer-Lambert law, results in a smaller transmission. Moreover, broader laser linewidths lead to a wider Mie spectrum, as predicted by Eq. (5.11), allowing a larger fraction of aerosol backscatter to pass through the filter and thereby reducing spectral discrimination. The simulation outcomes guided the selection of the laser source and the design of the iodine cell for the SR-HSRL prototype, ensuring a balance between compactness, spectral performance, and signal throughput.

Due to the short-range operation of the HSRL prototype developed in this thesis, additional optimization of the cell length was required, as increasing it boosts optical losses from beam divergence. In short-range lidar systems, where the transmitter and receiver units are closely spaced in a bi-static configuration, the received backscattered light originates from scattering volumes that subtend relatively large solid angles with respect to the optical axis. As a result, the collected beam is not perfectly collimated but slightly convergent or divergent, depending on the telescope's focus setting and the overlap function [125, 126].

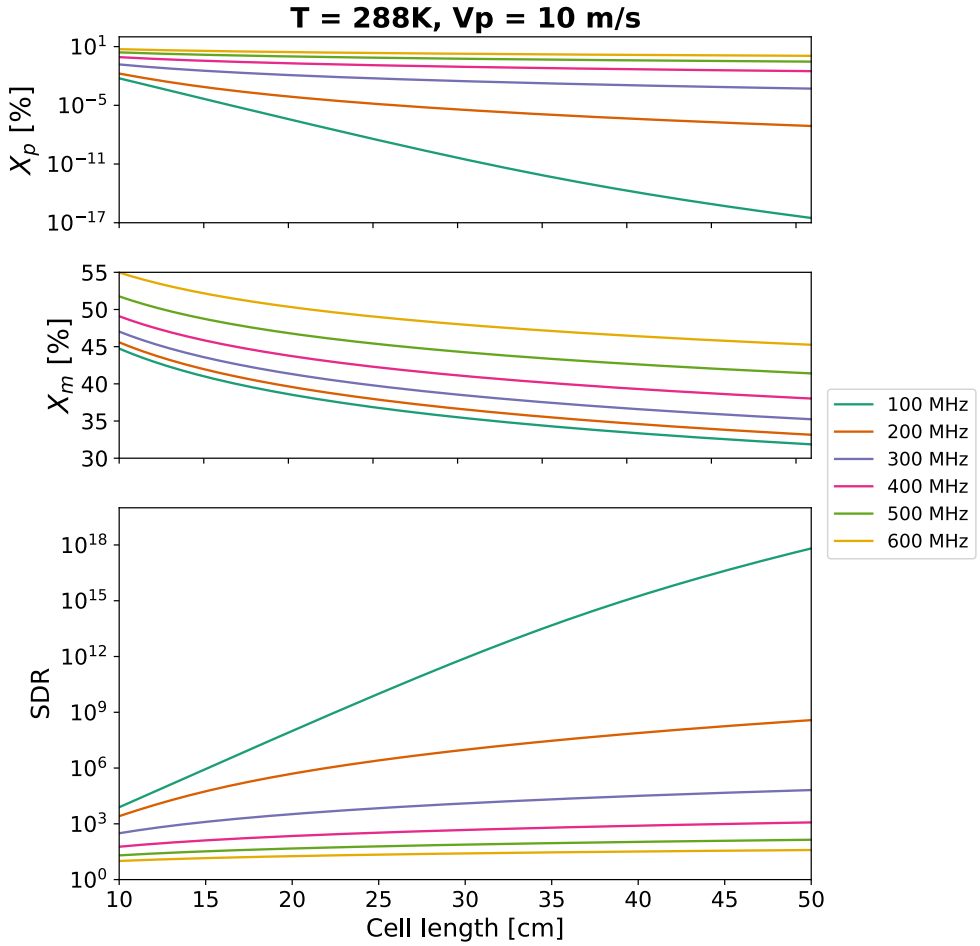

FIGURE 5.12: Simulated iodine cell spectral performance for various laser linewidths as a function of cell length. The top and middle panels show the effective particle and molecular transmissions, and the bottom panel shows the spectral discrimination ratio.

Due to these intrinsic geometric factors, the collected beam has short spatial coherence, resulting in a short collimation distance [127]. The beam diverges with distance z following the relationship $D(z) = D_0 + 2\theta \cdot z$, where D_0 is the beam waist and θ the divergence half-angle [128]. Divergence causes signal loss due to geometrical truncation, as parts of the diverging beam may fall outside the cell's clear aperture. Consequently, although increasing the iodine cell length enhances molecular absorption and spectral discrimination, it also increases beam–divergence–related losses and reduces the overall SNR. Therefore, an optimal compromise had to be found between transmission efficiency and spectral discrimination, depending on the measurement range and the beam divergence. For ultra-short ranges (<50 m), shorter cell lengths ($\sim$10 cm) were preferred if the diameter is 25 mm or less, to avoid geometrical truncation. For longer ranges, larger cells can be employed, preferably of larger apertures (>50 mm).

5.2.2 Scanning field-widened Michelson interferometer

Having explored the spectral performance of iodine cells as a function of length and laser linewidth, the next step was to evaluate the alternative filtering approach selected from the literature review: the scanning field-widened Michelson interferometer (SFWMI). Unlike the absorption-based iodine cell, which relies on frequency-related molecular absorption to achieve spectral discrimination, the SFWMI uses interference effects to separate the atmospheric Doppler-broadened backscattering components. In this section, we present numerical simulations of the spectral performance of an SFWMI as a function of the optical path difference for the same range of laser linewidths. These results were used to guide the final design of the SFWMI for the SR-HSRL prototype, ensuring it provided maximum spectral discrimination while maintaining sufficient SNR for short-range measurements.

Michelson interferometers (MIs) are the most well-known and important type of amplitude-splitting interferometers. In a basic MI configuration, a light source emits a beam towards a beam splitter, which reflects one part of the wavefront to a mirror M_1 and transmits the other to a second mirror M_2. The waves are then recombined to produce an interference pattern [129] that depends on the original wavefront. For an extended (divergent) source, the interference pattern consists of a series of concentric circular bands centered on the perpendicular drawn from the eye to the film. The fringes in this interference pattern are called of equal inclination. The existence of fringes of equal inclination depends on the incident light being reflected by two parallel mirrors, and the angle of incidence θ determines the changes in the OPD [129]. On the other hand, a point (collimated) source produces fringes of equal thickness. It also holds if the mirrors are not parallel. In these cases, the interference pattern consists of equispaced parallel fringes for which the optical thickness is the dominant parameter rather than θ [113]. A schematic of a Michelson interferometer is presented in Fig. 5.13 for an extended monochromatic source.

The quality of the fringes produced by an interferometer is described by the visibility V, which relates the maximum and adjacent minimum irradiances in the fringe system [113]. Mathematically,

$$V = \frac{I_{max} - I_{min}}{I_{max} + I_{min}} \tag{5.18}$$

Where the irradiance at any point is described from the irradiances of each arm I_1 and I_2 as shown in Eq. (5.19), where δ is the phase difference between the two waves, defined in Eq. (5.20). The irradiance is maximal when δ is an even integer multiple of π and minimal if δ is an odd integer multiple of π.

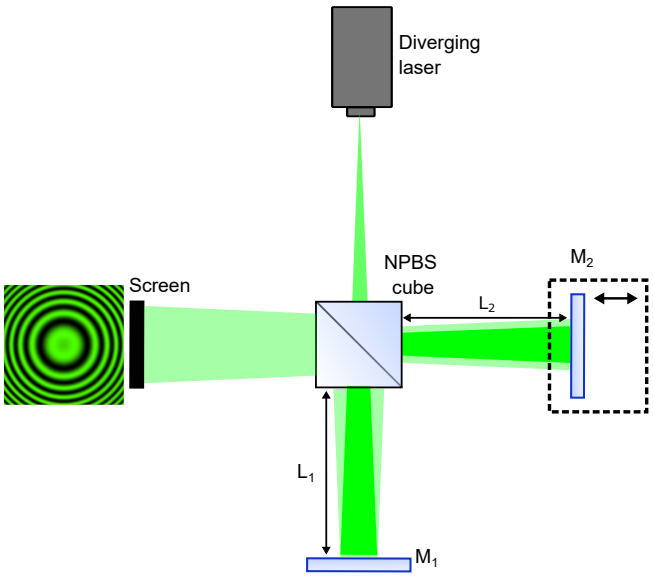

FIGURE 5.13: Setup of a Michelson interferometer using an extended monochromatic source, a non-polarizing beam splitter (NPBS) cube, and two plain, parallel mirrors. The resulting interference pattern are fringes of equal inclination.

$$I = I_1 + I_2 + 2\sqrt{I_1 I_2}\cos\delta \tag{5.19}$$

$$\delta = \frac{2\pi}{\lambda} OPD \tag{5.20}$$

An essential parameter governing the performance of a Michelson interferometer is the OPD, defined as the round-trip difference in the optical paths of the two waves, $OP_1(n_1, \theta_1)$ and $OP_2(n_2, \theta_2)$, where $\theta_{1,2}$ are the angles of incidence of the rays on the mirrors and $n_{1,2}$ is the refractive index at each arm [113]. The angle-dependent OPD can be expressed as:

$$OPD(\theta) = 2\left[OP_2(\theta_2) - P_1(\theta_1)\right] = 2\left[n_2 L_2 \cos\theta_2 - n_1 L_1 \cos\theta_1\right] \tag{5.21}$$

For small incidence angles ($\theta \ll 1$ rad) and considering a symmetric configuration ($L_1 \approx L_2$), the cosine term can be expanded as $\cos\theta \approx 1 - \theta^2/2$, leading to the simplified expression of the angle-dependent OPD shown in Eq. (5.22). In this equation, the first term represents the on-axis optical path difference, while the second term indicates that the OPD decreases quadratically with increasing field angle, producing fringe curvature and spectral broadening, and reducing the fringes' visibility [129].

$$OPD(\theta) \approx 2(n_2 L_2 - n_1 L_1) - (n_1 L_1 + n_2 L_2)\theta^2 \tag{5.22}$$

Field widening requires that the second-order angular term in Eq. (5.22) cancels out. In that case, the OPD remains nearly constant with angle to second order. This is achieved when $n_1 L_1 = n_2 L_2$. To satisfy the field-widening condition, a compensator, such as a glass

rod of length L_g and index of refraction n_g, is added to one of the arms. In that case, the field-widening condition is $n_1L_1 + n_gL_g = n_2L_2$. The difference in the refractive index of the glass rod helps compensate for light rays traveling slightly longer geometric paths in the other arm at off-axis angles. The OPD then becomes insensitive to field angle (to first order), keeping the interference fringes straight for point sources or eliminating the concentric rings for expanded sources, and maintaining high contrast over a wide field of view.

The output signal is also independent of the incident angle of the input beam if the OPD of a conventional MI is zero. In that case, however, the MI provides no useful information about the incident radiation. To use an MI as a spectral filter, the OPD should be matched to the input signal's spectrum. A stable spectral filter requires a fixed OPD, as the OPD determines the spectral filter's free spectral range (FSR) [116] as shown in Eq. (5.23) for a double-pass MI. The FSR determines the spacing between consecutive interference fringes in the output spectrum, determining the range of frequencies that can be analyzed before fringes overlap.

$$OPD(\theta) = \frac{c}{FSR(\theta)} \tag{5.23}$$

The angular dependency of MIs is particularly significant in wide-field-of-view lidar receivers. When implemented as the spectral filters of HSRLs, it limits the instrument's spectral discrimination performance. To mitigate this dependence, it is common to implement a field-widening MI configuration. Field-widened Michelson interferometers (FWMI) introduce a glass rod into one of the arms to reduce the angle dependency of the OPD [97, 116], as portrayed in Fig. 5.14.

When the field-widening condition is satisfied, the angular dependence of OPD is largely canceled, and the residual path difference can be approximated by Eq. (5.24), where L_g and n_g are the length and refractive index of the glass rod. Liu et al. [116] analyzed the changes in the OPD as a function of the incident angle for an FWMI and a conventional MI. They demonstrate that, even for angles as small as 1°, the OPD of a conventional MI changes more than 60λ. For the same angle of incidence, the OPD of the FWMI is nearly constant, with a change of only 0.068λ. This confirms that FWMIs are suitable spectral filters for HSRL, providing high spectral discrimination over a wider acceptance angle.

$$OPD = 2\left[OP_2 - \left(OP_1 + OP_g\right)\right] = 2\left[L_2 - L_1 - n_gL_g\right] \tag{5.24}$$

Jin et al. [18, 97] reported that introducing a scanning in one of the FWMI arms results in a spectral filter with some advantages over vapor cells. They allow multi-wavelength acquisitions; the laser wavelength does not need to be controlled, and only one detector is needed

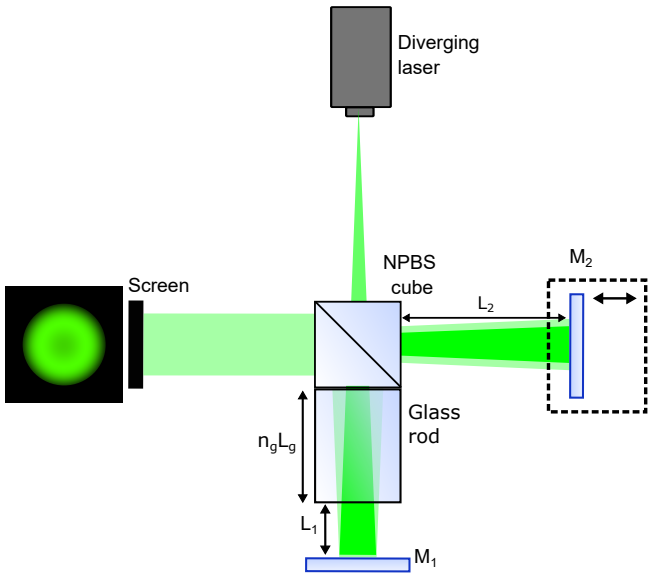

FIGURE 5.14: Setup of an FWMI inserting a glass rod of length L_g and index of refraction n_g in one of the interferometer's arms. In constructive interference, a single circular fringe is seen on the screen. For destructive interference, the beam is extinguished.

to measure both the Mie and the total backscattering signals at each wavelength. The main disadvantages are that they have lower SNR because the measured signals are distributed across multiple phases of an interference fringe to obtain the scan data, and that the SDRs are lower than for iodine cells because the transmittance of the Mie spectrum is higher [97].

The spectral function of a scanning FWMI (SFWMI) is described by Eq. (5.25), where $\delta = (2n+1)\pi$ is the phase shift introduced by the scanning, and $2\pi OPD\omega/c$ is the phase variation caused by frequency deviation from the laser central frequency ν.

$$F(\omega,\delta) = \frac{1}{2}\left[1+\cos\left(\frac{2\pi OPD}{c}\omega+\delta\right)\right] \tag{5.25}$$

Scanning introduces a phase shift δ that modifies the interferometer's spectral function. To select the optimal FSR, one must consider a half-wavelength scan, i.e., $\delta = 0$ and $\delta = \pi$, that allows measuring the total signal (when $\delta = 0$) and filtering out the Mie component to obtain the HSR signal (when $\delta = \pi$). This is illustrated in Fig. 5.15, where the Doppler-broadened Mie and Rayleigh-Brillouin backscattering spectra are displayed in black, and the filter transmittance curves in red. The continuous red curve $(\delta = 0)$ displays the interferometer acting as a spectral filter, whereas the red dotted curve $(\delta = \pi)$ is when it enables registering the total signal. This illustrates that both the HSR and total signals needed for HSRL retrievals could be registered in a single channel.

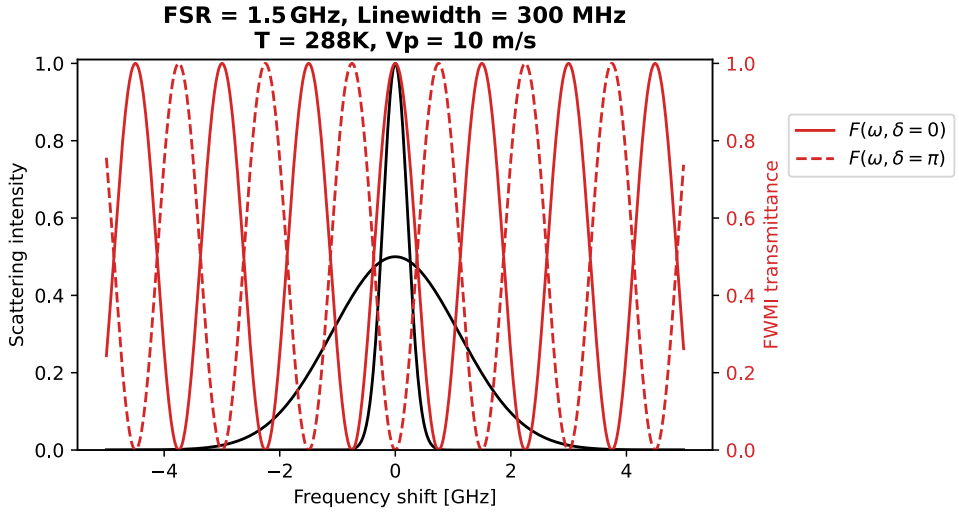

FIGURE 5.15: Transmittance functions of an SFWMI when $\delta = 0$ and $\delta = p$. The atmospheric backscattering spectra are shown in black.

The data processing for an SFWMI-based HSRL is founded on the calculation of the interferometric contrast or atmospheric visibility A_m, which is defined at both scanning points as shown in Eq. (5.26). To optimize filter performance, A_m should be set to zero, meaning the Mie backscattering signals are fully filtered [97].

$$A_m(OPD) = \frac{X_m(0, OPD) - X_m(\pi, OPD)}{X_m(0, OPD) + X_m(\pi, OPD)} \tag{5.26}$$

The simulation algorithm illustrated in Fig. 5.11 was also implemented to evaluate the spectral performance and optimize the design parameters of the scanning field-widened Michelson interferometer. Like in the case of the iodine cell simulations, the Doppler-broadened atmospheric backscattering terms $S_m(x,y)$ and $S_p(\omega)$ were calculated for laser linewidths from 100 to 600 MHz using Eqs. (5.5) and (5.11), respectively. The effective transmission of the SFWMI was then calculated using Eq. (5.25) for FSRs ranging from 0 to 11 GHz. The simulated parameters are the same as those for the iodine cell ($X_{m,p}$ and the SDR), along with the atmospheric visibility A_m. The simulations were used to define the optimal OPD, which is related to the FSR, and to estimate the filter's performance for different laser linewidths. Fig. 5.16 presents the simulated values of X_p and X_m as a function of the FSR for linewidth values ranging from 100 to 600 MHz.

The SFWMI design optimization thus involved selecting the optimal FSR to maximize X_m while minimizing X_p. To do so, the molecular interference contrast was used to determine the OPD (and thus FSR) that maximized the transmission of the Rayleigh-Brillouin spectrum at both scanning positions, making $X_m(0, OPD) = X_m(\pi, OPD)$. This ensures no molecular signals are lost during the scanning and that the interferometer filters only the Mie scattering

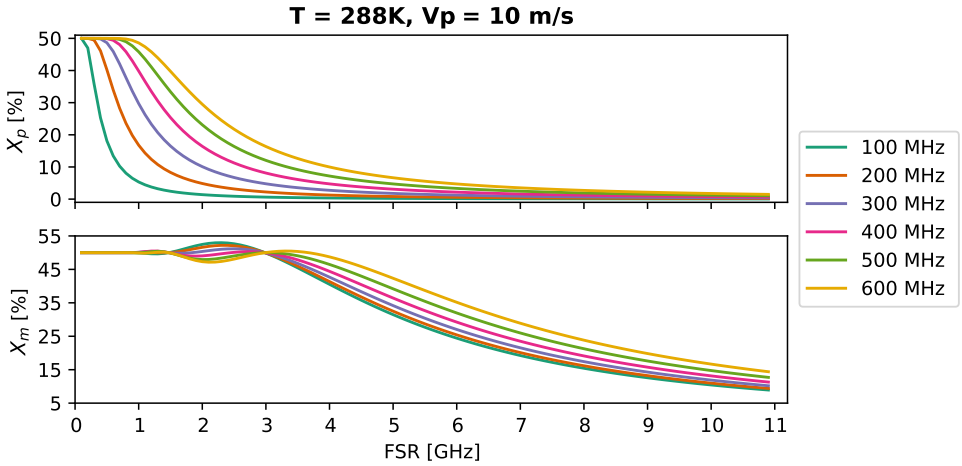

FIGURE 5.16: Transmittance of the particle (top panel) and molecular (bottom panel) spectra through an SFWMI as a function of its FSR when $\delta(\nu) = \pi$.

component. The results of the atmospheric visibility simulations are presented in Fig. 5.17. It can be seen that for OPD values between 100 and 200 mm, the phase of the scan signals is inverted, leading to negative oscillations in the interference visibility when the linewidth is small and positive ones when the linewidth is large. This is an undesired effect inherent to the form of the Rayleigh-Brillouin spectrum. Thus, even though at an OPD of 100 mm the atmospheric visibility is zero, it is an unstable point, as any minor misalignment could increase the interferometric contrast. Moreover, the shorter the OPD, the larger the FSR, resulting in a lower spectral resolution of the filter. Thus, the optimal OPD value was chosen to be 200 mm, at which the interferometric contrast stabilizes at nearly 0 regardless of laser linewidth, as desired. This corresponds to an FSR of 1.5 GHz.

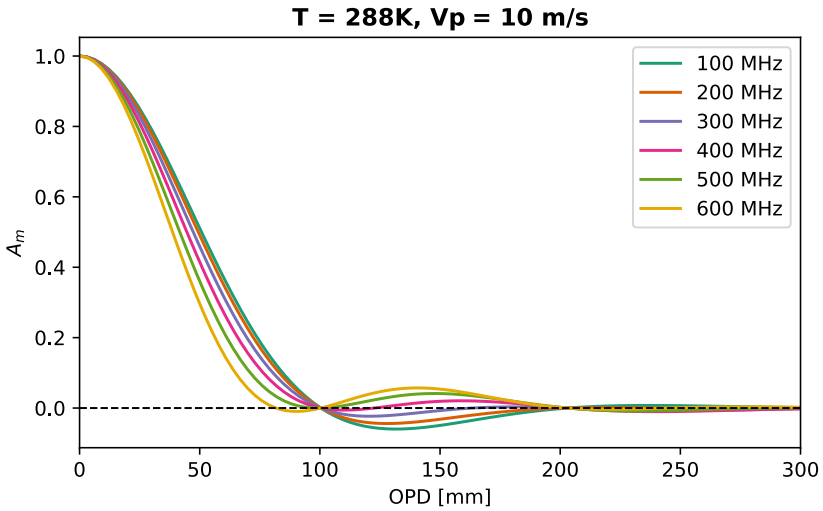

FIGURE 5.17: Atmospheric visibility as a function of the interferometer's OPD.

Finally, Fig. 5.18 presents the simulated values of the interferometer's spectral discrimination ratio. As discussed previously, higher FSR values yield larger SDR values due to reduced particle transmission, but at the expense of lower molecular transmission, which implies a poor SNR. It can also be noted that, as expected, performance increases with shorter laser linewidths, with negligible change for values > 400 MHz.

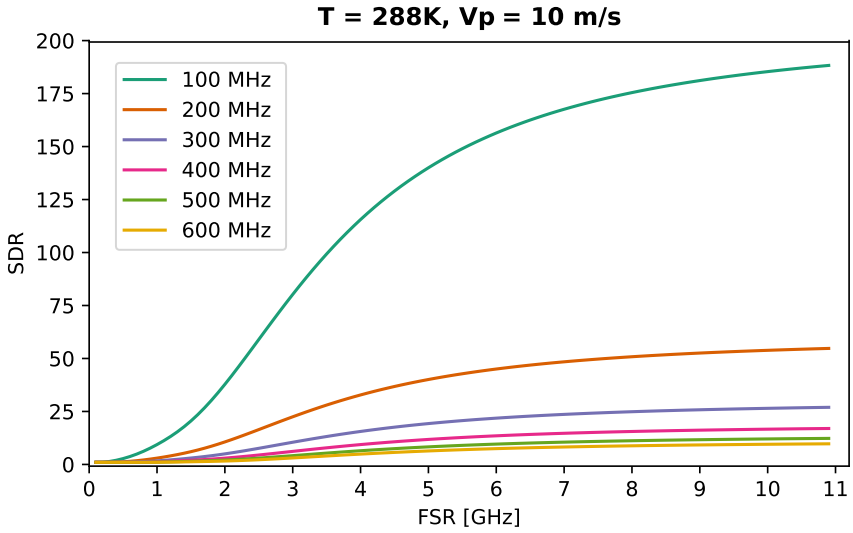

FIGURE 5.18: Spectral performance of the filter as a function of the FSR for different laser linewidths.

The simulation results provided critical insight into the optimal configuration of the SFWMI for the SR-HSRL system. The molecular and particle transmission terms (X_m and X_p) were used to analyze the interferometer's spectral discrimination capacity as a function of the FSR. Selecting the optimal FSR implied maximizing the transmission of the Doppler-broadened Rayleigh-Brillouin component to ensure a correct SNR. For this, the molecular interference contrast was simulated for OPDs ranging from 0 to 300 mm. The results show that for A_m >200 mm, A_m approaches zero, ensuring that no molecular signals are lost during scanning, i.e., that the interferometer filters only the Mie scattering component. The SDR curves revealed a clear difference for a linewidth of 100 MHz compared to the other five values. This expected behavior, also observed in the iodine cell simulations, is why most HSRLs reported in the state of the art employ ultranarrowband lasers. The difference between 200 and 300 MHz is shorter, and negligible between 400, 500, and 600 MHz. The curves at 400 to 600 MHz also showed that the SDR is quasi-independent of the FSR for values greater than ∼3 GHz. Based on these results, the optimal OPD (200 mm) and the corresponding FSR (1.5 GHz) were selected to maximize the SDR while maintaining sufficient molecular transmission.

5.2.3 Summary

The simulation results provided essential insights into the limitations of HSRL spectral performance when using lasers with broad linewidths. Understanding the expected spectral response enabled the identification of the optimal trade-off between spectral resolution and range performance, guiding the selection of the most suitable laser source. To that end, eight commercial lasers were characterized in the laboratory; since manufacturers typically do not provide complete spectral information, a comprehensive characterization of all HSRL- and short-range lidar-related specifications was performed. This included measuring pulse parameters such as power (and stability), repetition rate, and pulse width. The spectral features measured included the linewidth and wavelength (and their stability) as well as wavelength tuning for coupling with iodine cells. In addition to meeting all spectral and pulse requirements, the laser had to be compact and lightweight to ensure compatibility with prospective airborne applications. Because no commercial laser met all these criteria, three custom lasers were developed in collaboration with Keopsys (a Lumibird company) and Teem Photonics. The first is a custom version of Keopsys PGFL model [130] that meets our requirements. The second was co-developed with Teem-Photonics, resulting in the custom-made STG-3PW-000 model. Since the characterization measurements revealed a significant spectral instability due to temperature-regulation issues in this model, the company developed an improved, more stable model, which was also tested. Section **??** describes the laboratory characterization measurements of the three laser sources, and Section 5.4 presents the validation of the spectral performance of the laser-spectral filters configurations.

Table 5.2 summarizes the simulated spectral performance of both spectral filters for the selected laser sources. The lasers developed by Teem Photonics have a linewidth of 196 MHz, while the Keopsys one has a linewidth of 300 MHz. The simulations were performed for 10-cm-long and 20-cm-long iodine cells, and a scanning FWMI with an FSR of 1.5 GHz. The results show that the iodine cells provide significantly higher SDRs, particularly for the longer cell with the narrower-linewidth laser. The effective Rayleigh-Brillouin transmittance remains nearly constant with linewidth, but decreases with the cell's length, as expected since X_m is poorly dependent on the laser linewidth and the cell's length directly influences the filter function. On the other hand, effective Mie transmittance decreases by nearly an order of magnitude for the short cell and two orders of magnitude for the long cell when considering the narrower linewidth. For the short cell, the SDR values are 2790 (196 MHz) and 311 (300 MHz). For the longer cell, the results are 6.49×10^5 (196 MHz) and 3333 (300 MHz). Regarding the interferometer, the performance is low for both lasers: the SDRs are 6 and 3 for the Teem Photonics and Keopsys lasers, respectively.

TABLE 5.2: Simulation of the spectral performance of an iodine cell and a scanning FWMI when using two commercial laser sources.

Laser (Linewidth)	**Simulated parameter**	**Iodine cell 10 cm long**	**Iodine cell 20 cm long**	**Scanning FWMI FSR 1.5 GHz**
Teem Photonics (196 MHz)	X_m	0.46	0.39	0.50
	X_p	1.63×10^{-4}	6.10×10^{-7}	8.02×10^{-2}
	SDR	2790	6.49×10^{5}	6
Keopsys (300 MHz)	X_m	0.47	0.41	0.50
	X_p	1.51×10^{-3}	1.24×10^{-4}	1.7×10^{-1}
	SDR	311	3333	3

The outcomes of these simulations established the design parameters for both spectral filters, defining the required optical path difference (and corresponding FSR) for the Michelson interferometer and the optimal cell length and temperature for the iodine filter. The following section describes the optical and mechanical design of these two filters before proceeding to the experimental laser characterization and validation of their combined spectral performance.

5.3 Design of two optimized spectral filters

5.3.1 20-cm-long iodine cell

The design of the iodine cell involved finding the optimal length that guarantees the desired Mie transmission value. As previously discussed, the first step is to estimate the saturation pressure P. For this, the heating temperature t was set to 80°C from laboratory characterization measurements performed on the commercial 10-cm-long cell. Applying Eq. (5.13), the saturation temperature is $P = 0.0216$ bar $= 2.16$ kPa. The mass of iodine needed to exert the desired pressure at that temperature, calculated using Eq. (5.14) for a cell diameter of 2.5 cm, is $m = 9.16\times10^{-4}\ L$, where L is the cell length. Finally, the Beer-Bouger-Lambert law was used to determine the transmittance as a function of L. From laboratory measurements with the Keopsys laser and the 10-cm-long I_2 cell, the iodine absorption line 1116 was found to be a suitable line for operation. The value of the central transmission measured at 80°C was $T_0 = 4.66\times10^{-3}$. From Eq. 5.15, the central absorption coefficient is:

$$\alpha_0 = \frac{-\ln(T_0)}{10\text{ cm}} = 5.37\times10^{-1}\text{ cm}^{-1} \tag{5.27}$$

Therefore, the transmission of line 1116 can be related to any length using the relationship $T_0 = \exp\left(-5.37\times10^{-1}\ L\right)$, as illustrated in Fig. 5.19.

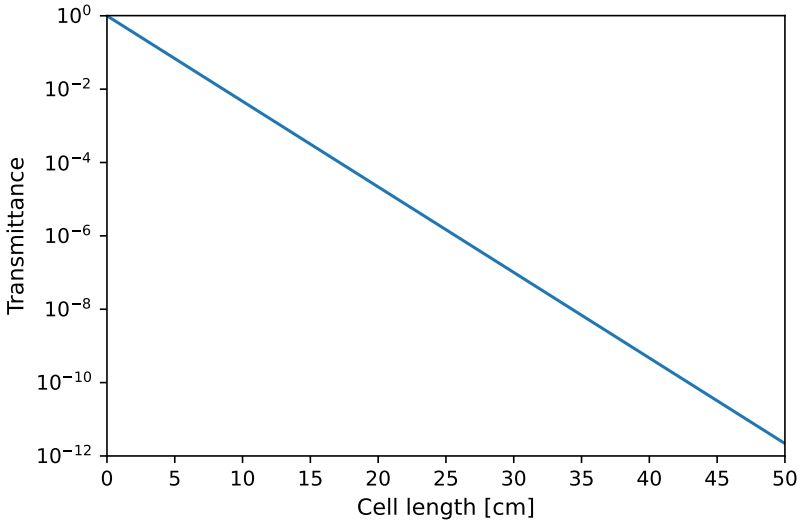

FIGURE 5.19: Length-dependent central transmittance of iodine line 1116.

To optimize both the spectral discrimination and the transmission efficiency, the cell length was set to 20 cm. This length provides a good suppression of Mie backscattering ($T_0 = 2.17 \times 10^{-5}$) while being a reasonable distance to minimize beam-divergence-related loss of irradiance. Based on the simulations and calculations, a custom iodine absorption cell was fabricated by Photonics Technologies in accordance with the geometrical and optical quality specifications summarized in Table 5.3. The main requests were a length of 200 mm, a diameter of 25 mm, an iodine mass of 18.40 mg, and AR-coated windows with wave flatness of $\lambda/10$ and scratch/dig quality of 10/5.

TABLE 5.3: Design specifications of the custom-made 20-cm-long iodine cell.

Fill material	Excess iodine
Cell	Material: Quartz
	L: 200 m, ∅: 25 mm
Windows	2° wedge, attached 11° angle
	532 nm AR-coated (both faces)
	Wave flatness: $\lambda/10$ wave flatness
	Scratch/dig quality: 10/5

All the requirements were met, except for the iodine mass. The manufacturer stated that accurately controlling the iodine mass introduced into the cell is technically complex. This is because it was nearly impossible to transfer an aliquot of solid iodine, pre-measured under vacuum conditions, into the sealed cell without losses, as any exposure to air leads to oxidation, and any residual pressure causes partial sublimation during the filling process. Consequently, the company could not guarantee the exact requested iodine mass. Instead, they adopted a well-established approach in iodine cell production: introducing an excess quantity of iodine to ensure that a small fraction remains in the solid phase at room temperature.

This secures sufficient vapor pressure to achieve the desired absorption when combined with the 20 cm path length, even without active heating. In practice, the cell's effective transmittance can later be fine-tuned by controlling the heating temperature, which adjusts the vapor pressure according to the iodine pressure–temperature relationship described in Eq. (5.13). This allows compensation for uncertainty in iodine mass and ensures the desired optical absorption during both laboratory calibration and lidar operation.

Using the custom-made iodine cell, a dedicated spectral filtering subsystem was designed for straightforward integration into the SR-HSRL prototype. The subsystem was conceived as a modular unit, enabling the exchange of spectral filters without requiring major optical realignment. The modular design allows both the iodine cell and the scanning FWMI to be easily installed, tested, or operated as interchangeable spectral filters. The configuration ensures precise, stable alignment with the lidar's reception optics while facilitating maintenance and future system upgrades. In addition, the module has a closed design that effectively shields the spectral unit and detectors from background light, improving signal-to-noise performance. The CAD model of the I_2 cell spectral filter subsystem final layout is shown in Fig. 5.20, which depicts the iodine cell mount, optical path, and mechanical housing used in the SR-HSRL prototype. In the figure, IF represents the interference filter, BS the 90:10 beam splitter, and MA the mirror for aligning the beam towards the HSR channel focusing lens. The cell is heated using two Thorlabs glass-cell heaters. Fig. 5.21 presents the iodine cell spectral module assembled into the SR-HSRL prototype.

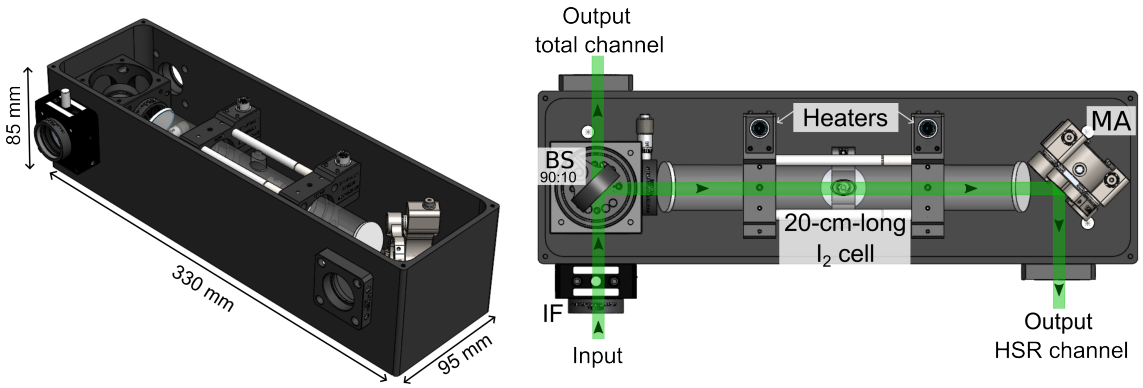

FIGURE 5.20: CAD model of the modular spectral unit based on the optimized iodine cell. The isometric view is displayed on the left, while the right shows the module's layout.

Once the spectral filtering subsystem was assembled, it was integrated into the SR-HSRL receiver, as depicted in the figure above. Particular attention was given to ensuring the cell's optical and thermal stability and to minimizing misalignment between the filter unit and the collection optics. Mechanical mounts were designed to maintain the optical axis aligned with the receiver's axis to avoid signal loss from misalignment or defocus. The optical path was

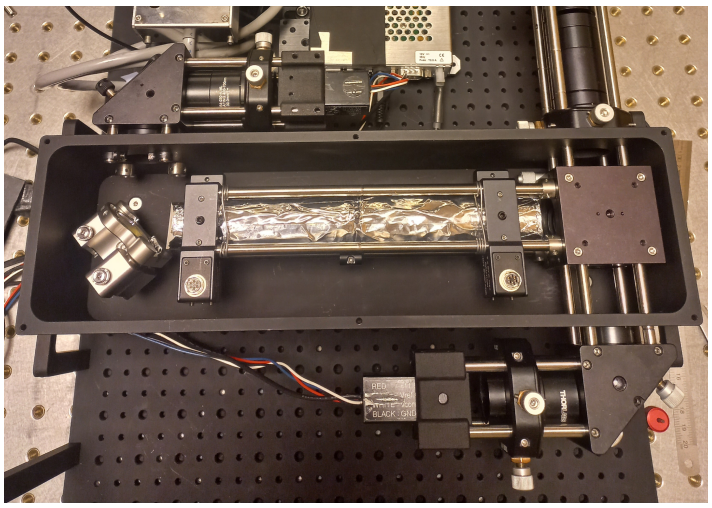

FIGURE 5.21: Picture of the iodine cell spectral module assembled into the SR-HSRL prototype.

verified during alignment tests to confirm beam collinearity through the receiver telescope, spectral unit, and detection optics. Another critical consideration was to ensure uniform cell heating to prevent iodine condensation at the cell windows. For this reason, the cell was covered with aluminum foil, which provides thermal isolation and uniformity. This modular, precisely aligned filter configuration enabled a straightforward transition from laboratory tests to field deployment, providing a stable platform for the spectral performance validation and atmospheric measurements presented later.

5.3.2 Scanning FWMI with 200-mm OPD

As discussed in Section 5.2.2, since the SFWMI spectral filter depends on the scanning phase shift δ, both scanning positions must be considered to select the optimal OPD value. To account for this, the atmospheric visibility A_m is defined; optimal performance is achieved when A_m approaches zero. If this condition is met, the transmission of the Rayleigh-Brillouin spectrum is nearly identical at both half-wavelength scanning positions. Thus, molecular signals are not filtered by the scanning; the interferometer blocks only the Mie component, thereby improving the SNR. The optimal OPD and FSR were determined to be 200 mm and 1.5 GHz, respectively. To ensure the selected OPD is independent of the incident angle, a field-widened glass rod was incorporated and permanently glued to a custom beam splitter cube. This assembly is bonded to a robust optomechanical support that was designed to minimize vibrations and external perturbations. This configuration preserves the interferometer's alignment and spectral fidelity, preventing misalignments that could degrade its performance. These design measures directly enhance the reliability and reproducibility of experimental

measurements under varying environmental conditions. The designed glass rod assembly is presented in Fig. 5.22.

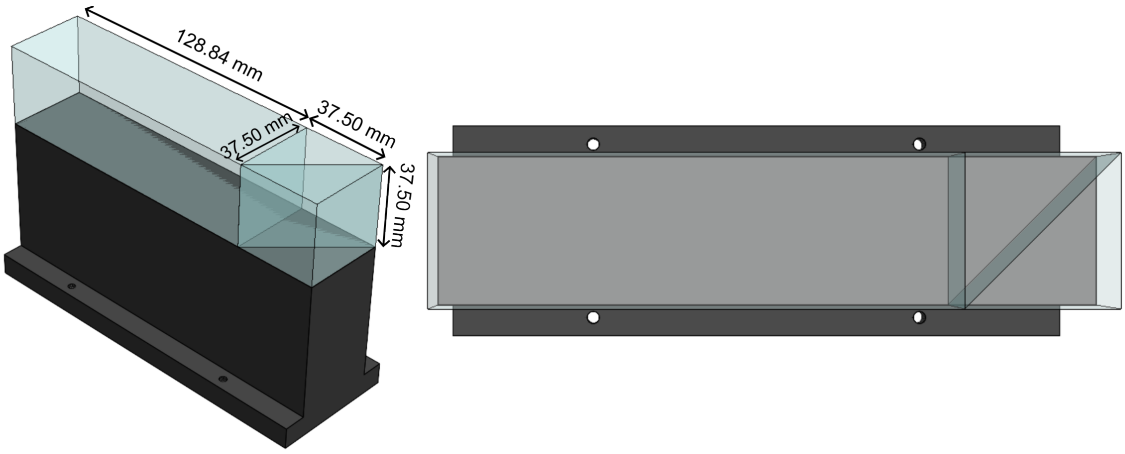

FIGURE 5.22: CAD model of the optimized glass rod and beam splitter assembly.

The beam splitter is a cube with a length of 37.50 mm, while the glass rod has a length of $L_g = 128.84$ mm. The glass-rod length was calculated so that the field-widening condition $OPD = 2\left[L_2 - L_1 - n_g L_g\right] = 200$ mm was met, where $n_g = 1.4607$ is the real refractive index of fused silica, the glass rod material. Fused silica was selected as the material for the field-widening glass rod due to its advantageous optical and thermal properties that minimize changes in the optical path difference induced by thermal fluctuations, thereby securing interferometric stability. Thermal stability is guaranteed by its low coefficient of thermal expansion (CTE $\approx 5.5 \times 10^{-7}$ K^{-1}); while the field-widening properties remain unaffected with temperature variations since fused silica's refractive index has a low rate of change with temperature (its thermo-optic coefficient $\mathrm{d}n/\mathrm{d}T$ is about $1.0 \times 10^{-5} K^{-1}$ at 532 nm). In addition, its low optical dispersion (Abbe number ≈ 67) and high optical transmission (> 90% from 200 nm to 2 μm) preserve the spectral integrity of the Rayleigh–Brillouin signal.

Like for the iodine cell, a modular spectral filtering subsystem was designed for the SFWMI. It is another compact, stable, modular spectral unit that can be straightforwardly integrated into the SR-HSRL prototype, ensuring precise, stable alignment with the lidar's reception optics. It also ensures the alignment and stability of the SFWMI, preventing vibration-induced interference degradation. The closed-module design preserves the quality of the interference pattern, preventing background noise contamination and degradation of the interference contrast. The CAD model of the final layout of the SFWMI spectral filter subsystem is shown in Fig. 5.23, which depicts the glass rod and beam splitter, the retroreflecting mirrors used, the optical path, and the mechanical housing.

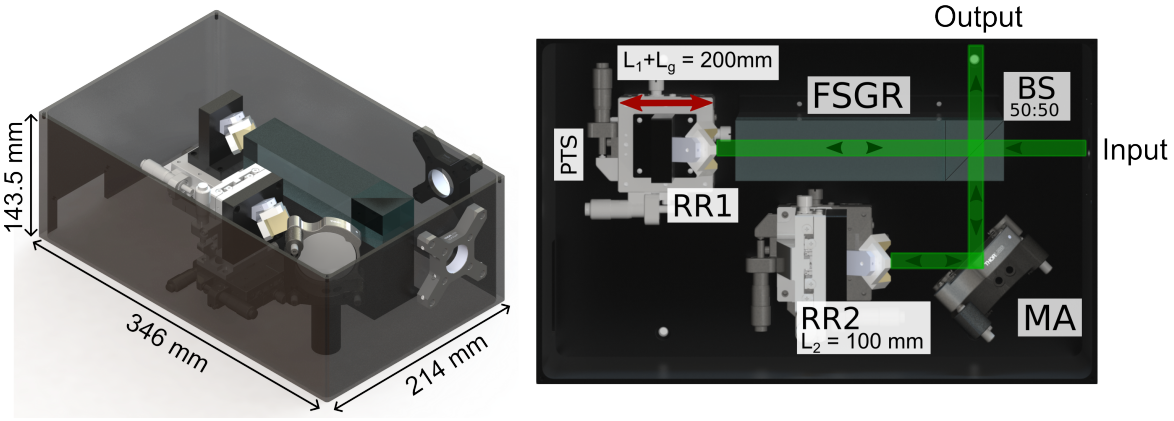

FIGURE 5.23: CAD model of the modular spectral unit based on the optimized SFWMI. The isometric view is displayed on the left, while the right shows the interferometer layout.

In the figure, BS represents the 50:50 beam splitter, FSGR the fused silica glass rod, $RR_{1,2}$ the retroreflecting mirror of each arm, PTS the piezoelectric translation stage used for the half-wavelength scanning, and MA the mirror for aligning the beam towards the retroreflector of the air arm. The red arrow presents the direction of the scanning. Fig. 5.24 presents the SFWMI spectral module final assembly.

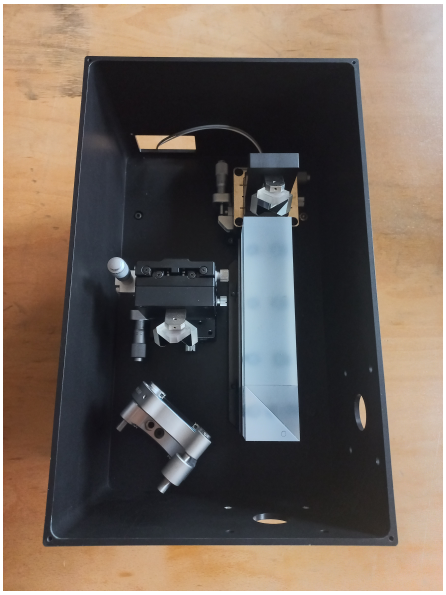

FIGURE 5.24: Picture of the assembled SFWMI spectral module.

After having simulated, designed, and assembled both spectral filters –the 20-cm-long iodine cell and the scanning field-widened Michelson interferometer with an FSR of 1.5 GHz-—, the subsequent stage involved finding the right laser source for the SR-HSRL prototype. As discussed earlier, a laser characterization methodology was developed to measure the complete pulse and spectral features of commercial laser sources. Eight lasers were

tested, with three being selected as possible candidates for the SR-HSRL prototype. Consequently, after constructing the optimized spectral filters and identifying the laser sources, the filters' performance was experimentally validated. The following section describes the experimental procedures and results of the laser characterization. Finally, Section 5.4 presents the spectral performance validation of the two filters using the selected lasers.

5.4 Validation of the spectral performance

After developing the optimized spectral filters and characterizing the two laser sources, the last step was to verify that the laser–spectral filter configurations were suitable for implementing a high spectral resolution lidar. To do so, laboratory measurements were performed to verify the iodine absorption bands within the wavelength range of each laser, and to confirm the field-widening of the interferometer and its transmission of Mie scattering. The results are described below.

5.4.1 Transmission spectra of two iodine cells

To validate the spectral discrimination of iodine, both a commercial 10-cm-long cell with a 19 mm diameter and the designed 20-cm-long, 25 mm diameter cell were analyzed. To maximize performance and keep comparable conditions, the operating temperature was set to 80°C. The setup for the laboratory characterization of iodine transmission is depicted in Fig. 5.25. The laser is injected into the iodine cell of length L and diameter$\varnothing$ after passing through a neutral density filter (NDF). After passing through the cell, the beam is directed through an interference filter (IF) to block background light and potential fluorescence effects. Then, a power sensor records the intensity. To record the iodine spectrum, the complete wavelength range of each laser was scanned. The measurements were repeated if needed to ensure stability and repeatability.

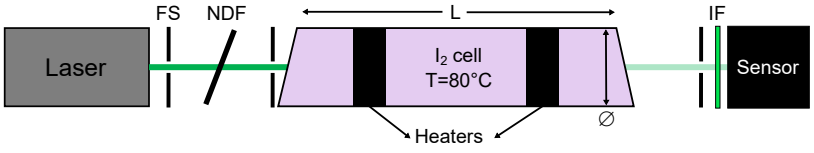

FIGURE 5.25: Laboratory setup to measure iodine absorption bands in the lasers' wavelength range. L and ∅ stand for cell length and diameter, FS for field stop, NDF for neutral density filter, and IF for interference filter.

The results of the transmission spectrum of the 10-cm-long iodine cell in the Keopsys wavelength range are presented in Fig. 5.26. The seed laser temperature was scanned from 19.00 to 21.50°C in steps of 0.01°C. For each temperature value, the power was recorded 20

times for 1 second to avoid potential laser instabilities, and the values were averaged. The process was carried out 7 times to assess repeatability, the invariance of the absorption band positions, and differences in transmittance values.

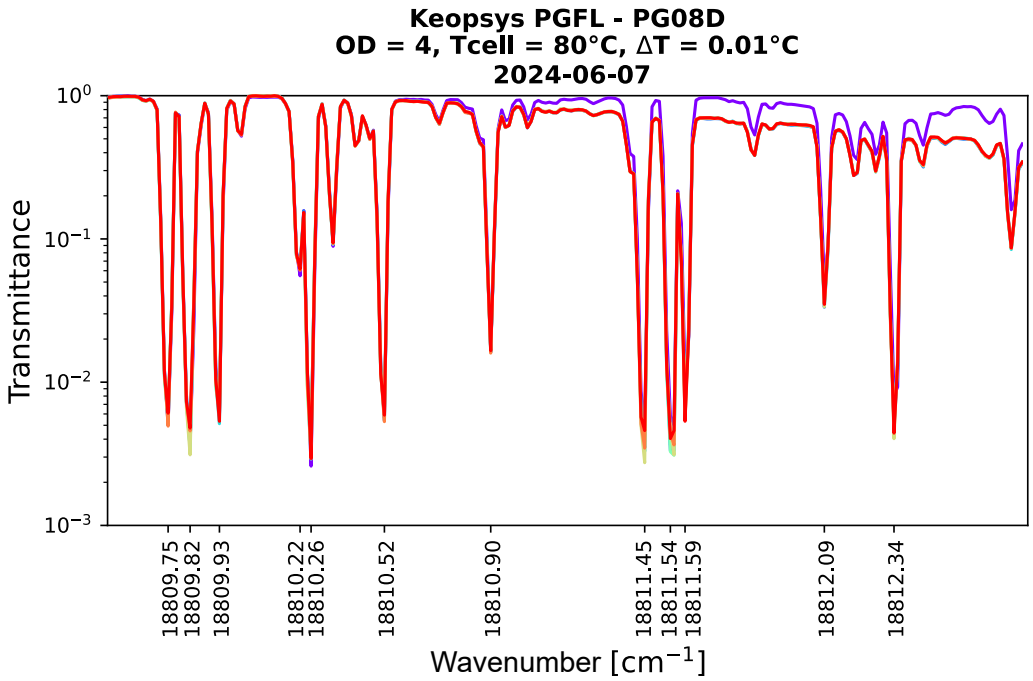

FIGURE 5.26: Iodine spectrum (10-cm-long cell) in the Keopsys laser wavelength range. Colors represent different measurements performed to validate spectral stability.

Twelve iodine absorption bands were found in the laser wavelength range (532.11357 to 532.20615 nm). The central wavenumbers range from 18809.75 cm^{-1} to 18812.34 cm^{-1}. The transmission values are between 6.15×10^{-2} to 2.93×10^{-3}, and the FWHMs between 630.22 MHz and 3169.44 MHz. The absorption band chosen for HSRL operation was 18809.82 cm^{-1}. The decision was based on the FWHM value (1985.16 MHz) –which allowed filtering wide Doppler-broadened aerosol signals resulting from the broad laser linewidth–, the low transmittance (4.77×10^{-3}), and the sufficient separation from the adjacent bands. The combination of low transmission and moderate FWHM maximizes the spectral discrimination ratio. From the measurements, the effective transmittances of the molecular and aerosol spectra through this iodine band for the Keopsys laser were determined to be $X_m = 0.43$ and $Xp = 8.25 \times 10^{-4}$, resulting in an SDR of 516. A summary of each absorption band's wavenumber, wavelength, transmission, and FWHM is presented in Table 5.4.

TABLE 5.4: Iodine absorption bands in the Keopsys wavelength range

Wavenumber [cm^{-1}]	**Frequency [MHz]**	**Transmission**	**FWHM [MHz]**
18809.75	563745024.78	6.07×10^{-3}	1514.63
18809.82	563747379.20	4.78×10^{-3}	1985.16
18809.93	563750518.42	5.33×10^{-3}	1536.30
18810.22	563759151.28	6.15×10^{-2}	630.22
18810.26	563760328.49	2.93×10^{-3}	2705.45
18810.52	563768176.54	5.89×10^{-3}	1656.12
18810.90	563779556.22	1.66×10^{-2}	1441.65
18811.45	563796037.13	4.59×10^{-3}	2229.98
18811.54	563798783.95	4.04×10^{-3}	3169.44
18811.59	563800353.56	5.33×10^{-3}	966.50
18812.09	563815264.87	3.49×10^{-2}	1256.40
18812.34	563822720.52	4.41×10^{-3}	1345.51

Following a similar procedure, the iodine spectrum in the wavelength range of the Teem Photonics lasers was characterized to determine the corresponding absorption bands and transmission values. First, the laser version v0 was used with the smaller cell to find the I_2 absorption bands in this wavelength range. The laser diode temperature was scanned from 31.00 to 35.00°C in steps of 0.01°C, with 10 measurements of 1 second each at each temperature step. The results are displayed in Fig. 5.27 and the summarized information is presented in Table 5.5. In this wavelength range, only 7 absorption bands were found, of which 3 had significant absorption, i.e., transmittance values lower than 10^{-1}. These bands are at 18807.53, 18808.33, and 18809.00 cm^{-1}. The transmittance (FWHMs in MHz) values are 7.77×10^{-5} (1945.81), 1.01×10^{-2} (1439.99), and 7.39×10^{-3} (1457.82), respectively. For this laser-iodine cell configuration, the iodine band chosen is the first one (centered at 18807.53 cm^{-1}) due to its significantly low transmission value. From the FWHM and transmittance value of this band, the effective transmissions of the Doppler-broadened backscattering terms were determined to be $X_m = 0.42$ and $Xp = 1.26\times10^{-4}$, resulting in an SDR of 3325. A summary of each absorption band's wavenumber, wavelength, transmission, and FWHM is presented in Table 5.4.

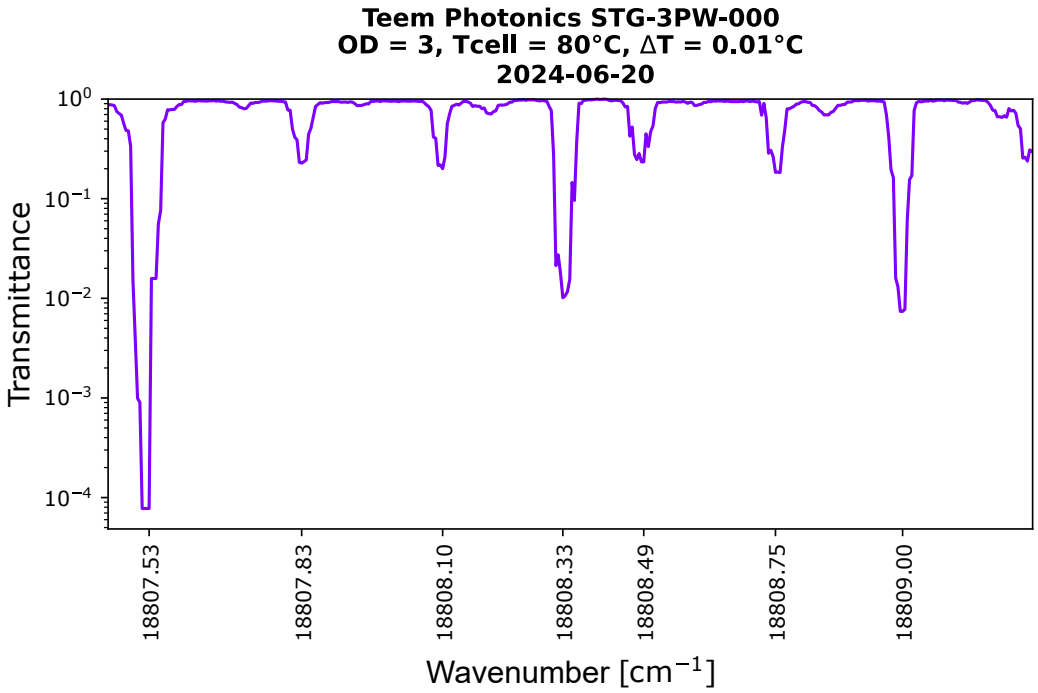

FIGURE 5.27: Absorption spectrum of a 10-cm-long iodine cell in the Teem Photonics laser v0 wavelength range.

TABLE 5.5: Iodine absorption bands in the Teem Photonics laser v0 wavelength range.

Wavenumber [cm^{-1}]	**Frequency [MHz]**	**Transmission**	**FWHM [MHz]**
18807.53	563678444.79	7.77×10^{-5}	1945.81
18807.83	563687477.89	2.28×10^{-1}	1201.90
18808.10	563695702.06	2.00×10^{-1}	893.42
18808.33	563702712.83	1.01×10^{-2}	1439.99
18808.46	563707431.61	2.34×10^{-1}	1434.24
18808.76	563715386.14	1.83×10^{-1}	1092.79
18809.00	563722531.73	7.39×10^{-3}	1457.82

Then, the process was repeated for the improved laser version because, as shown in Fig. 5.8, the output wavelength ranges are different. The laser crystal temperature was scanned from 31.00 to 3(.00°C in steps of 0.01°C, with 10 measurements of 1 second each at each temperature step. The scanning process was repeated several times to assess repeatability, the invariance of the absorption band positions, and differences in transmittance values. The results are displayed on Fig. 5.28, while Table 5.6 presents the information on each absorption band.

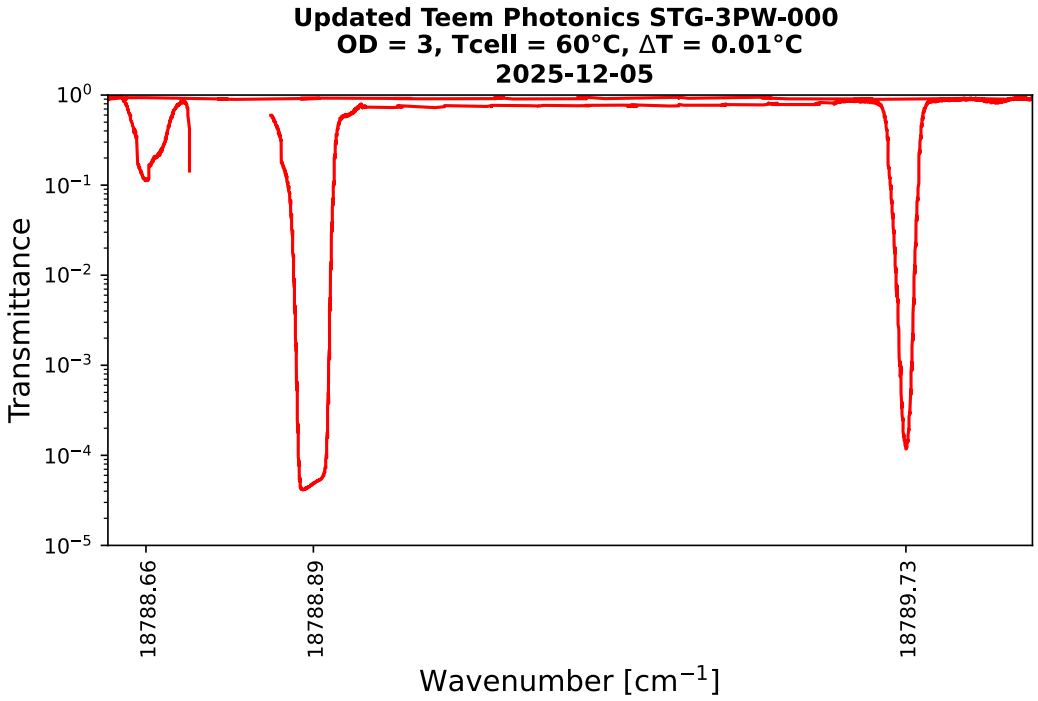

FIGURE 5.28: Absorption spectra of a 10-cm-long iodine cell in the Teem Photonics laser v1 wavelength range.

TABLE 5.6: Iodine absorption bands in the Teem Photonics v1 wavelength range

Wavenumber [cm^{-1}]	**Frequency [MHz]**	**Transmission**	**FWHM [MHz]**
18788.89	563276751.62	4.90×10^{-5}	2710.16
18789.73	563301934.19	1.17×10^{-4}	707.59

From the figure and table, it can be seen that there are only two significant absorption bands in this wavelength range. The first one (at 18788.89 cm^{-1}) has a low central transmission (4.90×10^{-5}) but a FWHM (2710.16 MHz) that is too broad to achieve a reasonable SNR, since most of the molecular signals would be filtered out. The second one has a slightly higher central transmission (1.17×10^{-4}) and a FWHM (707.59 MHz) that is too narrow to efficiently discriminate between Rayleigh-Brillouin and Mie spectra, because most of the particle signals would pass through. However, since the FWHM of an iodine absorption band is proportional to the square root of the cell temperature, it has been determined that the first band can be used if the cell temperature is reduced, as this would yield a lower FWHM. On the other hand, to use the second band, one would have to increase the cell temperature until its FWHM is broad enough for HSRL operation.

5.4.2 Transmission of an SFWMI

To validate the performance of the designed scanning field-widening Michelson interferometer, the first step was to validate the field-widening effect of the fused-silica glass rod. The setup for the laboratory characterization of the SFWMI transmission is depicted in Fig. 5.29. The laser is injected into the interferometer after passing through a neutral density filter (NDF). A non-polarizing beam splitter (NPBS) cube divides the irradiance into two halves. One is directed into the air arm, and the other passes through the fused-silica glass rod (FSGR). An alignment mirror (MA) is used in the air arm to reduce the interferometer's size by making the retroreflector and glass rod axes parallel. Retroreflectors (RR) are used to reflect each beam, which are then recombined to produce the interference pattern. A camera or a power meter were used to record the field-widened interference pattern.

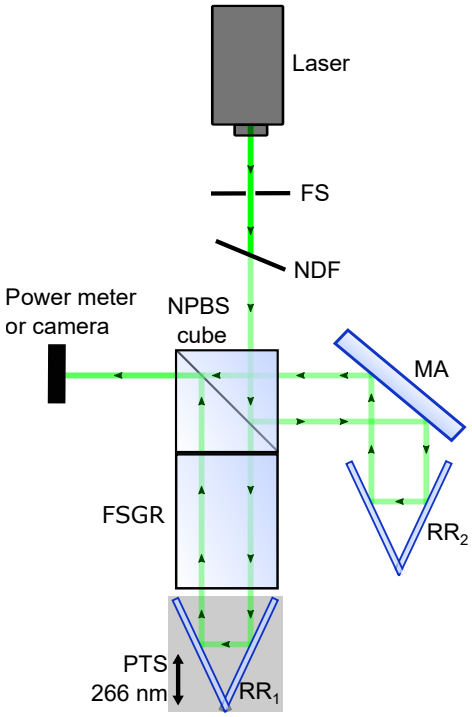

FIGURE 5.29: Laboratory setup to measure the transmission of an SFWMI. L and ∅ stand for cell length and diameter, FS for field stop, NDF for neutral density filter, and IF for interference filter.

As previously discussed, optimal performance and field widening in the interferometer was achieved when the OPD condition described in Eq. (5.28) was satisfied, where $L_2 =$ 100 mm was the optical path length of the air arm, $L_g = 128.84$ mm the length of the FSGR, L_1 the air gap between RR1 and the surface of the glass rod, and $n_g = 1.4607$ the refractive index of fused silica at 532 nm.

$$OPD = 2\left[L_2 - L_1 - n_g L_g\right] = 200 \text{ mm} \tag{5.28}$$

To test the interferometer's performance, Keopsys laser was used as the laser source. When the OPD deviated significantly from this condition, the interferometer was strongly dependent on the incidence angle. As a result, the interference pattern recorded by the camera consisted of fringes of equal inclination, observed as a series of concentric circular bands (left panel of Fig. 5.30). On the other hand, when the field-widening condition was satisfied and the phase shift between the interfering beams was $\delta = 0$, the interferometer became insensitive to the incidence angle, therefore the interference pattern collapsed into a single circular fringe (center panel). Finally, when the condition was met and $\delta = \pi$, destructive interference occurred at the laser wavelength, and the SFWMI functions as a spectral filter that attenuates the laser signal (right panel). A residual signal was still detected due to the relatively high Mie transmittance of the interferometer ($T \sim 1 \times 10^{-1}$).

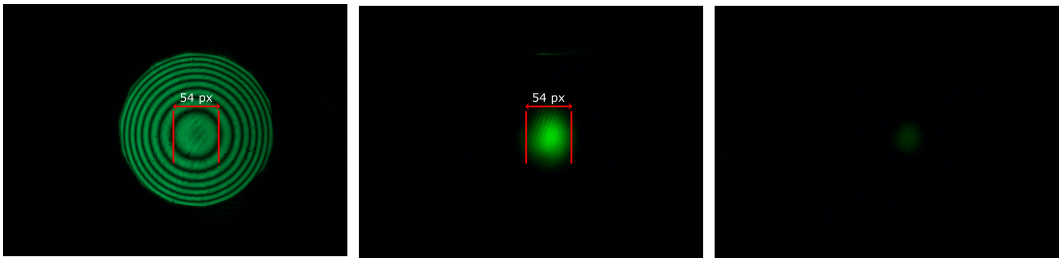

FIGURE 5.30: Validation of the field-widening effect of the designed SFWMI.

To verify the quality of the fringes produced by the constructed SFWMI and their wavelength dependency, the visibility V, described by Eq. (5.18), was evaluated for seed laser temperatures ranging from 19.00 to 20.00°. The results are presented in Fig. 5.31, where it is evident that the SFWMI fringes remained essentially constant across the tested temperature range. The mean value is $V = 0.74$, and the standard deviation is 6.6×10^{-3}. The stability of the interference visibility indicates that small wavelength changes associated with laser temperature tuning do not degrade the interference contrast. In contrast, the half-wavelength scanning must be precise and accurate to guarantee the phase shift values $\delta = 0$ and $\delta = \pi$ always correspond to the maximum and minimum positions of the fringes. The few appreciable errors in the visibility likely arise from transient perturbations affecting the recorded interferograms (mechanical vibrations, background noise, or brief laser intensity fluctuations) rather than from any change in the interferometer's operating point. Overall, the data demonstrate that the constructed SFWMI maintains stable, wavelength-independent fringe visibility, supporting its use as a stable spectral filter for the SR-HSRL prototype. As a consequence, for a SR-HSRL whose spectral filter is an SFWMI, the wavelength stability of a laser is not a crucial parameter for the spectral performance of the system as long as the filter operates under stable background and mechanical conditions.

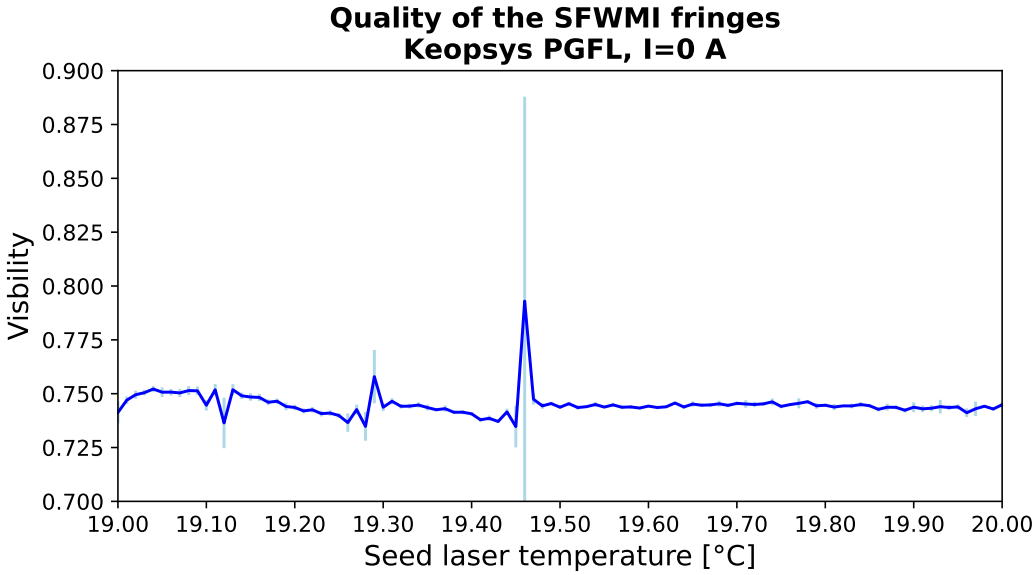

FIGURE 5.31: Visibility of the interference fringes produced by the SFWMI as a function of seed laser temperature. The visibility remains nearly constant ($\bar{V} = 0.74$) over the measurement range, indicating wavelength-independent minimum and maximum irradiance values.

The stability of the interference visibility V confirmed that the SFWMI maintains high fringe contrast over small wavelength variations, demonstrating that the optical alignment, field-widening condition, and half-wavelength scanning phase conditions remained stable as the laser wavelength changed. Stable visibility was a prerequisite for steady spectral filtering performance, as a stable interference pattern ensures that the half-wavelength scanning phase conditions, $\delta = 0, \pi$, accurately correspond to the transmission maxima and minima. Building upon this result, the SFWMI transmittance was then evaluated to directly assess its spectral filtering response as a function of laser wavelength. To this aim, Mie scattering transmittance was evaluated by performing half-wavelength scans, as previously discussed in Section 5.2.2. The transmittance was expected to remain constant across minor wavelength variations, provided that the phase shift conditions ($\delta = 0, \pi$) are maintained. To verify this, several half-wavelength scans were carried out for the same seed laser temperature range. The results presented in Fig. 5.32 show the mean transmittance for each wavelength, with error bars representing the corresponding standard deviations. For most laser output wavelengths, the standard deviation was negligible, indicating that the interferometer maintained stable transmission characteristics between the scans. Where larger standard deviations were observed, the errors can be associated to distortions in the interferograms, probably caused by background noise or mechanical vibrations perturbing the interference pattern. Overall, these results confirm the expected SWFMI behavior: for stable conditions, the transmittance is independent of the laser wavelength. The mean transmittance was $1.47 \times 10^{-1} \pm 1.71 \times 10^{-2}$.

This value agrees well with simulation results and demonstrates that the interferometer behaves as a stable spectral filter over the operating wavelength range of the Keopsys laser.

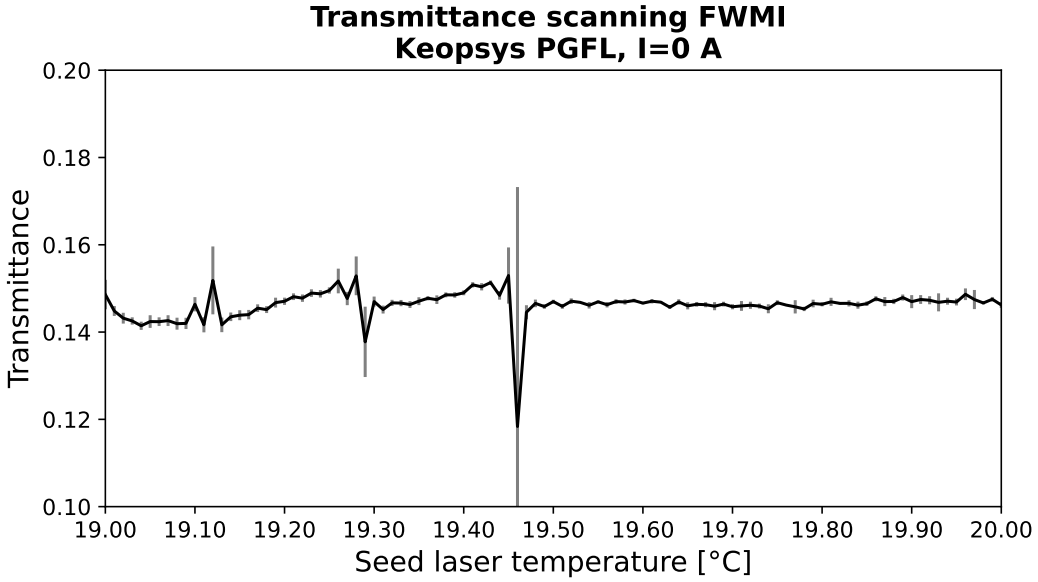

FIGURE 5.32: Transmittance of the scanning-field widening Michelson interferometer for different seed laser temperatures.

5.5 Summary: Laser - spectral filter configurations for different operational conditions

The simulations, laser characterization, and validation measurements presented in this chapter have demonstrated that the SR-HSRL prototype performance strongly depends on the combination of laser source and spectral filter used. It is concluded that no single configuration simultaneously optimizes all critical parameters –SDR, SNR, spatial and temporal resolution, and measurement range–. Considering this, two compact laser sources were chosen, and two spectral filters were designed as modular units to allow the prototype to be adapted to specific scientific objectives. By selecting the most appropriate laser-spectral filter combination, the SR-HSRL can be adapted for different operational conditions and measurement ranges. This section summarizes the recommended configurations for the two main operational regimes of the SR-HSRL prototype: ultra-short range and short- to medium-range.

Ultra-short range measurements ($\sim$<500 m) For measurements at very near ranges (a few hundred meters, typically below 300 m), the priority is achieving the highest possible spectral discrimination ratio, even at the expense of a low SNR. In this regime, the most suitable combination is the Teem Photonics v1 laser with the 20 cm iodine cell, provided the

received laser beam is well collimated so that divergence does not cause signal loss due to geometrical truncation. If this is the case, the 10 cm iodine cell should be used, at the expense of reduced spectral performance. This laser is chosen for its narrow linewidth –which allows for effective aerosol-molecular separation–, short pulse duration –which enhances spatial resolution–, and the presence of adequate iodine absorption lines –low transmission and adequate FWHM– within its wavelength range at the optimal cell temperature. Although its relatively low pulse energy limits the achievable SNR and restricts the system's applicability to very short ranges, this limitation is acceptable when high spectral and spatial resolutions are the primary objectives. Under these conditions, the iodine absorption bands provide strong suppression of Mie scattering while retaining sufficient molecular transmission, making this configuration particularly well-suited for boundary-layer profiling and aerosol studies close to the lidar.

Short- to medium-range measurements (<2-3 km) For distances up to approximately 1 to 3 km, the system requirements shift toward a balanced compromise between SDR, SNR, and spatiotemporal resolution. Under these requirements, the Keopsys laser is the preferred source due to its significantly higher pulse power and repetition rate, which enhance detection sensitivity and extend the prototype's operational range. Two spectral filtering options were identified as suitable for this range:

- Keopsys + 40 cm iodine cell: This configuration offers high spectral discrimination while maintaining strong molecular signal returns, making it appropriate for profiling the low troposphere. Other advantages are its wavelength stability and that several suitable iodine absorption bands were found in this wavelength range. This configuration was used to test the first SR-HSRL prototype in a field campaign performed at NIES (National Institute for Environmental Studies) in Tsukuba, Japan. The results of this validation campaign are presented in Chapter 6. It is worth noting that the 40 cm cell used for these measurements was provided by NIES and was not part of the thesis design effort.

- Keopsys + SFWMI: While the spectral discrimination achieved by the interferometer is significantly lower than that of iodine cells, this configuration presents distinct advantages. Its transmission is largely insensitive to small wavelength drifts, relaxing the requirements on laser wavelength stability. Furthermore, its broader spectral response makes it especially useful for future multi-wavelength implementations of the SR-HSRL. It would allow the use of multimode laser sources, for which iodine cells are not suitable. The main disadvantage is the reduced spectral performance –which comes from the low molecular–aerosol separation capability– compared with the iodine-based configuration.

The systematic design, optimization, and laboratory validation of the SR-HSRL transmitter and spectral filtering units presented in this chapter established a robust foundation for implementing a functional SR-HSRL prototype. It has been demonstrated that, through careful selection of laser–filter configurations, the system can be tailored to meet the requirements of specific measurement scenarios, from high-resolution ultra-short-range studies to flexible short-range atmospheric profiling. With these components integrated into a fully assembled lidar system, the next step was to evaluate its performance under real atmospheric conditions. The following chapter presents the results of a dedicated field campaign conducted at NIES, during which the SR-HSRL prototype was deployed to assess its operational capabilities, validate its spectral discrimination performance in situ, and demonstrate its potential for atmospheric remote sensing applications.

Chapter 6

Validation campaign: aerosol properties in the first kilometer of the atmosphere

Building upon the design and characterization of the transmitter and spectral units of an SR-HSRL prototype developed in the previous chapter, the next logical step was to integrate these components into a fully operational lidar system to evaluate its performance under real atmospheric conditions. To this end, a short- to medium-range HSRL prototype based on the Keopsys laser and a 40-cm-long iodine cell was developed in collaboration between ONERA and NIES, the National Institute of Environmental Studies of Japan. This chapter presents the field validation campaign conducted in Tsukuba, Japan, in July 2024 to test the SR-HSRL method. The main objective was to evaluate its ability to retrieve aerosol optical properties in the first kilometer of the atmosphere under real-world conditions. The vast majority of HSRLs reported in the literature review are limited by a near-field blind zone, typically extending to 1-2 km, which prevents them from probing aerosol properties near the emission source. The SR-HSRL prototype developed in this work was explicitly designed to overcome this limitation and bridge the observational gap between short-range elastic backscatter lidars and conventional HSRLs. This chapter details the proof-of-concept campaign, signal preprocessing and calibration procedures, retrieval of aerosol backscatter profiles, and comparison with other HSRL systems. It concludes by discussing the implications of these results for future developments and applications.

6.1 Proof-of-concept campaign overview

To validate the SR-HSRL prototype, a proof-of-concept field campaign was conducted on July 11–12, 2024, at NIES in Tsukuba, Japan. This research center is well known for state-of-the-art atmospheric research, including elastic, inelastic, and high spectral resolution lidar techniques. Moreover, the city of Tsukuba provides diverse aerosol conditions influenced by both urban emissions and natural sources, offering an ideal environment to test the system's capabilities. The primary objective of the campaign was to demonstrate that it was possible

to retrieve aerosol optical properties, including attenuated and calibrated aerosol backscatter coefficients, within the first kilometer of the atmosphere —-the blind region of conventional HSRL systems–. The SR-HSRL prototype was installed in the lab and configured in a vertical, bistatic, multiaxial configuration to optimize the overlap function in the short range. The system used the Keopsys laser in the transmitter unit and employed a custom-designed 40-cm-long iodine absorption cell provided by NIES as a spectral filter.

The field campaign had four main goals:

1. Demonstrate that it is feasible to implement the HSRL technique in the short range using a broad linewidth, compact laser source.
2. Develop a methodology to experimentally determine the overlap functions and radiometric constants to convert raw signals into attenuated backscatter profiles.
3. Validate the performance of the SR-HSRL prototype, focusing on the stability and spectral discrimination of the iodine absorption cell under real atmospheric conditions.
4. Retrieve and analyze calibrated aerosol backscatter profiles in the short range and evaluate the instrument's capability to resolve aerosol layers within the first kilometer of the atmosphere.

This campaign represents the first demonstration of a short-range HSRL designed to fill the near-field blind zone of conventional systems and to provide detailed, accurate aerosol characterization close to the source.

6.2 SR-HSRL prototype overview

The proof-of-concept lidar system described in Fig. 6.1 is a novel Short-Range High Spectral Resolution Lidar (SR-HSRL) prototype developed in this thesis. This system was conceived through a collaboration between ONERA — the French Aerospace Lab and NIES, the National Institute for Environmental Studies of Japan. This partnership aimed to combine ONERA's expertise in ultra-highly spatiotemporally resolved short-range elastic backscatter lidars with NIES's experience in developing state-of-the-art, highly accurate, high-spectral-resolution lidar systems. The goal was to develop a novel time-of-flight-based, short-range, high-spectral-resolution lidar to bridge the gap in precise aerosol characterization in the lower troposphere —-the blind zone of conventional HSRLs.

The primary goal of this proof-of-concept prototype was to demonstrate that the HSRL technique could be implemented with sufficiently high spectral discrimination performance

even when employing a relatively broad-linewidth laser. The demonstration was made by separately measuring aerosol (Mie) and molecular (Rayleigh-Brillouin) backscattering signals in the planetary boundary layer (PBL), extending up to the first thousand meters of the atmosphere. The lidar prototype was designed with high range resolution (7.5 meters) and high time resolution (6 seconds), limited by the bandwidth and resolution of the detectors and signal acquisition system. While the laser has the capability for much higher spatiotemporal resolution, the primary focus of this proof-of-concept campaign was on spectral discrimination rather than studying fine atmospheric structures or rapid processes. Detailed specifications of the SR-HSRL prototype can be found in Table 6.1.

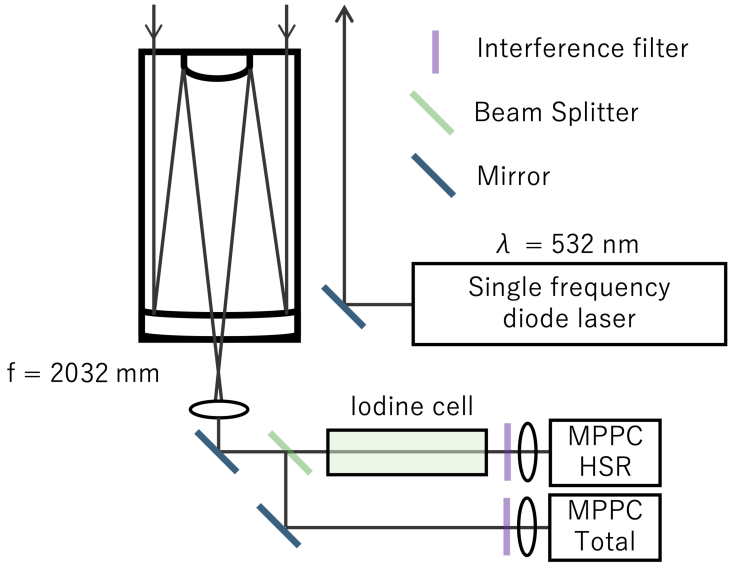

FIGURE 6.1: Schematic representation of the SR-HSRL developed by ONERA and NIES to study aerosols in the first kilometer of the atmosphere using a compact, high repetition rate, large-linewidth laser.

The primary innovation of the SR-HSRL prototype lay in its laser source, which, along with the system's bi-static, multi-axial optical configuration, enabled high-spectral-resolution measurements at short ranges, a region corresponding to the blind zone of most HSRL systems reported in the literature. Unlike traditional HSRL instruments that utilize injection-seeded Q-switched Nd:YAG lasers, which emit high-energy pulses (several millijoules) at low repetition rates (typically several tens of Hertz), the SR-HSRL prototype presented here used the amplified fiber laser customized by Keopsys that was described and characterized in Chapter 5. Its wavelength is tunable near 532 nm with low-energy pulses ($\sim$8 μJ) and a high repetition rate (50-65 kHz). This configuration provided pulses with sufficient energy for an operational range of up to 1 km, while the pulse temporal length and spectral width were adequate to enable high-spectral-resolution retrievals in the near field. Inspired by previous short-range EBL works [21, 22, 26], the overlap function was controlled by an aluminum

TABLE 6.1: ONERA-NIES SR-HSRL specifications.

Laser	Wavelength	532.11357 to 532.20615 nm
	Wavelength stability	< 0.1 pm
	Linewidth	< 400 MHz
	Linewidth stability	< 400 MHz
	Pulse duration	4.96 ns
	Pulse repetition rate	50 to 65 kHz
	Pulse energy	0.90 to 11.30 μJ
	Divergence angle	1.5 mrad
	Beam diameter (1/e)	1 mm
	Beam quality	M^2 = 1.3
	Dimensions	270 x 270 x 40 mm
	Weight	2.9 kg
Spectral filter	Type	Iodine cell
	Diameter	2 in
	Length	400 mm
	Absorption band wavenumber	18809.82 cm^{-1}
	Absorption band FWHM	1958.16 MHz
	Cell temperature	40 °C
Receiver	Type	Schmidt-Cassegrain
	Diameter	203.2 mm
	Focal length	2032 mm
	F-number	10
Sensors	Type	Hamamatsu MPPC
	Reference	C13366
	Bandwidth	5 MHz
	Active area	9 mm^2

mirror at the laser exit that allowed changing the bi-static angle, i.e., the angle subtended between the laser and receiver optical axes. This approach enabled optimization of the overlap range and facilitated the retrieval of aerosol backscatter coefficient profiles within the first kilometer of the atmosphere.

In the receiver subsystem, the backscattered signal was divided into two detection paths to separately measure the Mie and Rayleigh-Brillouin components of the backscattered light. To this end, a 10:90 non-polarizing beam splitter reflected 10% of the received signal toward the total channel, which recorded the full atmospheric backscattering. The remaining 90% was transmitted to the HSR channel, where a 40 cm-long iodine vapor cell heated at 40° was used as a narrowband spectral filter to suppress the Mie component and obtain a second signal composed mainly of molecular backscattering. To achieve the greatest possible suppression of Mie signals, the laser emission wavelength was precisely matched to the

center of the selected iodine absorption line (18809.82 cm^{-1}, FWHM = 1985.16 MHz) by temperature-tuning the laser diode, as described in the previous chapter. This spectral filter unit configuration ensured an optimal balance between optical throughput and spectral discrimination. The use of the long-path iodine cell provided strong molecular selectivity while maintaining sufficient transmission of the molecular component for adequate SNR. However, as discussed before, such a large optical path length could lead to potential signal loss due to geometric truncation of the diverging beam. This effect is especially noticeable within the first hundred meters of measurement. To mitigate these divergence-related losses, the iodine cell had a 2-inch diameter, ensuring that most of the collected beam remains within the optical path even under near-field conditions. Consequently, the cell design achieved a suitable compromise between spectral selectivity and transmission efficiency, allowing for high signal-to-noise ratios even in the first few hundred meters of the atmosphere.

Finally, the signals transmitted from both channels were detected by two thermoelectrically cooled silicon photomultiplier (SiPM) Multi-Pixel Photon Counters (MPPCs), which provided high sensitivity and low dark noise, making them suitable for low-light conditions and short-range measurements. The analog output of each detector was digitized using a fast analog-to-digital converter (ADC) operating at up to 160 MHz, ensuring sufficient temporal sampling for resolving the rapid return signals associated with near-field scattering. With this configuration, the achievable signal-to-noise ratio (SNR) reached 203 for the HSR channel and 471 for the total channel at a temporal resolution of 6 s, confirming the system's high stability and sensitivity. The spatiotemporal resolution, limited by the acquisition system and detectors, is 7.5 m and 6 s. This proof-of-concept test did not require a finer spatiotemporal resolution, as the primary goal was to demonstrate that the compact, high-repetition-rate fiber laser used, despite having a linewidth of 300 MHz, had a satisfactory spectral performance to suppress Mie scattering in the HSR channel and is suitable for a future implementation of an SR-HSRL with a higher spatiotemporal resolution.

6.3 Data preprocessing and calibration

To retrieve calibrated aerosol optical properties from the SR-HSRL signals, the raw data must undergo several pre-processing and calibration steps to remove noise and instrument effects. The pre-processing included background subtraction and range correction, while the calibration included removing Mie crosstalk and finding the interchannel calibration parameter to represent the total signal in the HSR channel framework. The pre-processing and calibration of the data measured during the validation campaign are described below.

6.3.1 Background subtraction and range correction

In lidar, the total signal detected by the sensors includes not only atmospheric backscattered radiation but also background counts from sunlight, stray light, and the detector's intrinsic electronic noise. To reduce background noise, narrowband interference filters were placed in front of the detectors. Other reported solutions include reducing the telescope's FOV, but this is not feasible in HSRL because it would reduce the detected molecular signal and, consequently, the SNR. Therefore, to completely isolate the true atmospheric return, the first preprocessing step was to remove the remaining background and dark noise contributions. This was done by averaging the signals at far ranges –in regions beyond the maximum measurement range–, where atmospheric backscatter is negligible, and then subtracting this average from the entire profile. Background correction significantly improves SNR, particularly for daytime measurements or for weak signals such as the molecular return expected in the HSR channel. Accurate background correction is particularly critical in HSRL or molecular-detection lidar systems because the molecular return signal can become comparable to (or even lower than) ambient or detector-dark noise [131], the signal-to-noise ratio degrades rapidly, and small changes in the background can dominate the measurement error.

Once the background contribution was removed, the next preprocessing step was to correct the signals for range dependence. This correction compensates for the geometric decrease in signal intensity with distance, allowing the backscattered power to be directly related to the atmospheric backscatter coefficient [125]. Since the detected lidar power decreases inversely to the square of the range (see Eqs. (3.35) and (3.36)), the correction is applied to obtain the range-corrected signals (RCS) by multiplying the background-corrected signals $P_{hsr,tot}(r)$ by the square of the range, i.e., $RCS_{hsr,tot} = P_{hsr,tot}(r) \cdot r^2$. This correction normalizes the geometric spreading of the laser beam, enabling a more direct comparison of signal amplitudes at different distances. [125, 126]. For short-range lidars, such as the SR-HSRL developed in this work, range correction is particularly important because overlap effects and near-field geometry can significantly distort the raw signal in the first few hundred meters. Applying range correction allows the retrieval of meaningful profiles even in regions where the overlap function is still evolving.

The temporal evolution of the preprocessed lidar signals acquired during part of the validation campaign, from July 11th at 18:00 to July 12th at 05:00 local time (UTC+9), is shown in Fig. 6.2. The top panel corresponds to the RCS of the HSR channel, while the bottom panel represents the total channel. In both datasets, invalid measurements (negative values) are masked in gray for clarity. In the HSR channel, it can be seen that the aerosol component is effectively suppressed from the molecular return in aerosol-only layers, demonstrating the

correct functioning of the spectral discrimination unit. However, some residual Mie crosstalk is visible in regions affected by cloud backscattering. In contrast, the total channel reveals the vertical distribution and temporal evolution of several aerosol layers extending from approximately 150 m up to 900–1500 m, with their mean altitude gradually increasing throughout the night, particularly after 23:00. Intermittent low-level clouds (300-40 m) are also visible, occasionally dominating the backscattered signal and temporarily masking aerosol features. Overall, these observations confirm the system's ability to resolve fine-scale temporal and vertical structures in the aerosol and cloud distributions, validating the prototype's performance under real atmospheric conditions.

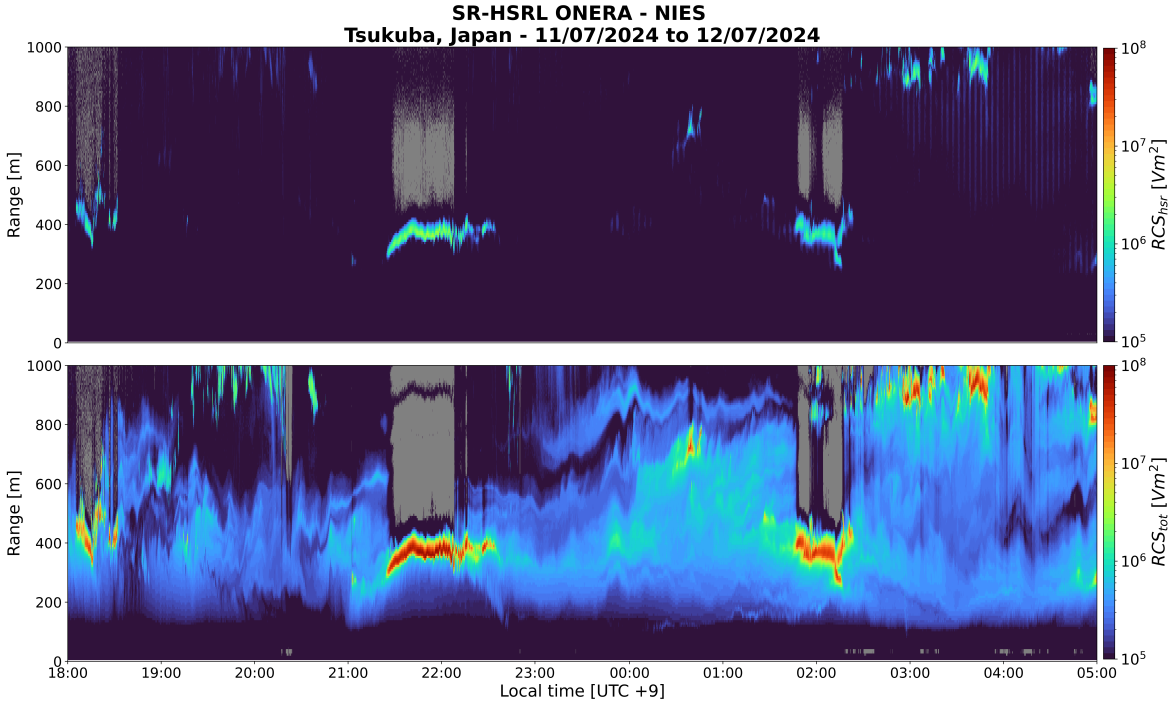

FIGURE 6.2: Temporal evolution of the preprocessed signals for the measurement campaign (11/07/2024 to 12/07/2024). The top panel represents the HSR channel, and the bottom one the total channel.

A noticeable stripe-like periodic pattern appears in the upper-right portion of the HSR panel, which was likely caused by minor, periodic variations in the seed laser wavelength due to temperature-control instabilities, as determined during the laser characterization measurements presented in Section 5.1.1. Such wavelength drifts cause a slight mismatch between the laser emission and the iodine absorption line, altering the effective transmission of the Mie spectrum and resulting in the observed stripe structure. Fig. 6.3 presents a color-saturated version of Fig. 6.2 for a better visualization of this stripe-like periodic wavelength drift. This undesired effect was corrected by applying a low-pass filter and performing the signal calibration described below.

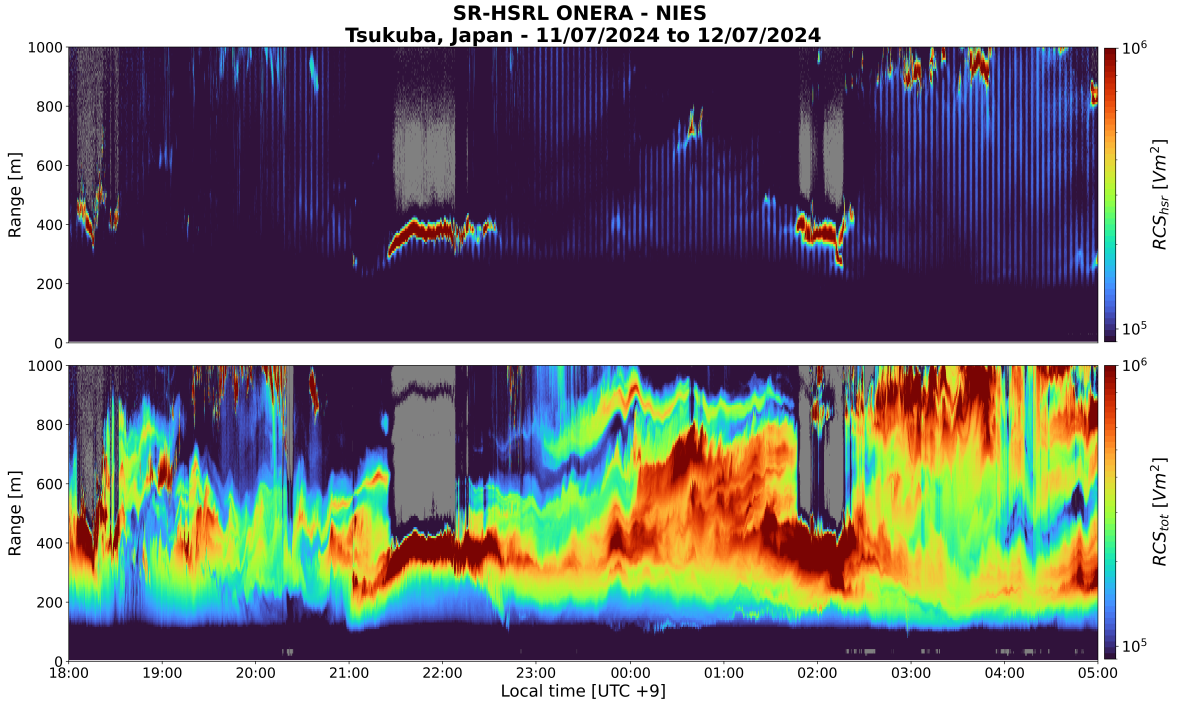

FIGURE 6.3: Color-saturated temporal evolution of the preprocessed signals to emphasize the periodic laser wavelength drift detected in the HSR channel during the validation campaign.

6.3.2 Signal calibration

As discussed in Section 3.4, once the data are pre-processed, the next objective is to calibrate the signals. For the total channel, the correction involves multiplying the signals by the inter-channel calibration parameter $C(r)$, which encompasses the ratio of both channels' overlap and radiometric constants, as described in Eq. (3.41). This parameter serves as a scaling factor that allows the total signal to be expressed within the HSR channel framework, thereby ensuring a consistent, physically meaningful comparison between the two channels. The interchannel calibration parameter $C(r)$ was derived from calibration measurements conducted outside an iodine absorption band ($\nu = \nu_{\text{off}}$) where both Mie and Rayleigh-Brillouin scattering are transmitted by the cell. At this off-line frequency, the effective transmittance of both components is equal and can be approximated as unity ($X_m \approx X_p \approx 1$). Therefore, any differences between the signals arise solely from disparities in their overlap functions and radiometric constants. The interchannel calibration parameter was calculated as

$$C(r) = \frac{P_{hsr}(r, \nu = \nu_{\text{off}})}{P_{tot}(r)}$$

The resulting calibration parameter for the SR-HSRL prototype deployed during the validation campaign is shown in Fig. 6.4. Then, the total channel was calibrated by multiplying the background-corrected signals by $C(r)$ as

$$P_{tot,corr}(r) = C(r)\,P_{tot}(r)$$

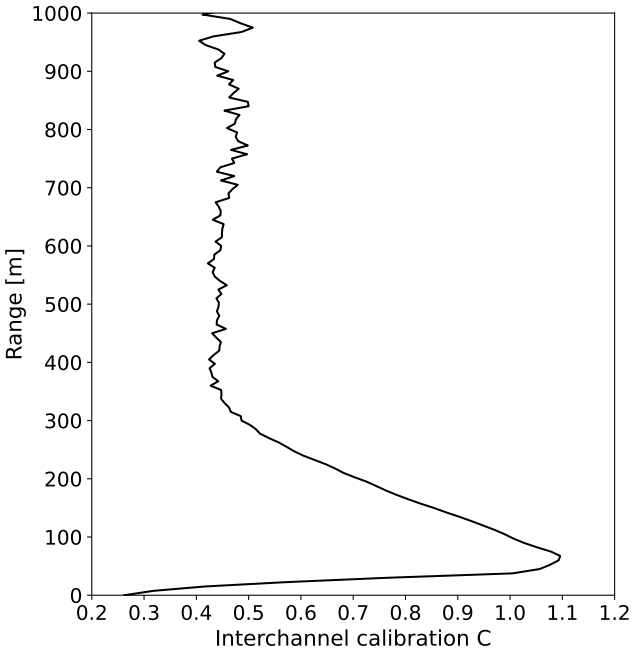

FIGURE 6.4: Interchannel calibration parameter calculated as the ratio of the HSR channels outside an iodine band and the total signals.

Once the interchannel calibration was applied to align both detection paths and correct the total channel signals, the HSR channel calibration required accounting for and removing Mie crosstalk. This correction ensured that the molecular signal measured through the iodine cell was not contaminated by the residual aerosol backscatter component, which could partially pass through the spectral filter due to its finite spectral discrimination ratio. To perform this correction, the crosstalk parameter χ_p was determined and optimized from the experimental data. The analysis was carried out using 2-minute-averaged HSR profiles, corresponding to the frequency of the wavelength drift observed in the raw measurements. For each averaged profile, a linear regression was performed in regions where crosstalk was evident –typically those dominated by clouds or intense aerosol backscatter– between the expected molecular signal (approximated by a straight line within the selected region) and the corrected HSR signal, expressed as

$$P_{Ray,n}(r) = P_{hsr}(r) - \chi_{p,n}\,P_{tot,corr}(r)$$

Several candidate values $\chi_{p,n}$ (with n representing the nth tested value) were evaluated for each averaged profile using an optimization algorithm, and the value $\chi_{p,n}$ that maximized the coefficient of determination (R^2) of the fitted curve was selected as the optimal parameter. The resulting optimal χ_p values ranged from 2×10^{-3} to 8.9×10^{-2}, with most averaged

profiles indicating approximately 8.9% Mie crosstalk. Once the optimal parameters were obtained, the entire HSR signal was corrected by subtracting the corresponding residual Mie contribution from the measured HSR signal, as shown in the equation below. It is important to note that the temporal resolution of the signals remained unchanged, since the optimal χ_p value was consistent across all 6-second profiles within each 2-minute averaging period.

$$P_{Ray}(r) = P_{hsr}(r) - \chi_p P_{tot,corr}(r)$$

To illustrate both calibration procedures, Fig. 6.5 presents three half-hour averaged profiles comparing the uncorrected (darker lines) and corrected (lighter lines) signals. The top panels show the molecular (HSR) channel in blue, while the bottom panels display the total channel in red. The averaging interval of thirty minutes was chosen arbitrarily to facilitate comparison with the temporal evolution plots presented earlier and does not correspond to any limitation in the instrument's temporal resolution.

In the first time interval (21:00–21:30), both channels capture a low cloud between 300 and 400 m. The prominent peak in the uncorrected molecular profile (darker blue line) indicates substantial Mie crosstalk from the cloud backscatter. After applying the correction, this parasitic contribution is substantially reduced, as seen in the corrected Rayleigh profile (lighter blue line). During the second interval (23:30–00:00), the total channel reveals several aerosol layers extending up to about 1000 m, with no cloud presence. In this case, the crosstalk correction enables the molecular channel to closely follow the expected molecular signal, demonstrating the effectiveness of the procedure for aerosol-dominated conditions. Finally, in the third interval (04:30–05:00), a cloud layer between 800 and 1000 m and two well-defined aerosol layers below are observed in the total channel. After correction, only a weak cloud signature remains in the Rayleigh profile, while the aerosol crosstalk is largely suppressed. These results confirm the reliability of the calibration and correction procedures and their capability to isolate the molecular contribution, even under varying atmospheric conditions.

Across all three examples, the correction effectively reduces Mie crosstalk in the molecular channel for both aerosol layers and cloud regions. Nevertheless, small residual Mie contributions remain, as excessive correction can introduce unphysical negative values in the molecular signal. This occurs because the correction subtracts a fraction of the total signal -—corresponding to the range of strongest backscattering—- from the entire profile, which can locally produce negative values or values smaller than the expected molecular backscatter at other ranges. Further reduction of crosstalk could, in principle, be achieved by increasing the iodine cell's absorption, either by raising its temperature or by extending its optical

path length. However, such adjustments would simultaneously decrease the molecular transmission through the filter, thereby compromising the system's overall spectral performance and reducing the signal-to-noise ratio.

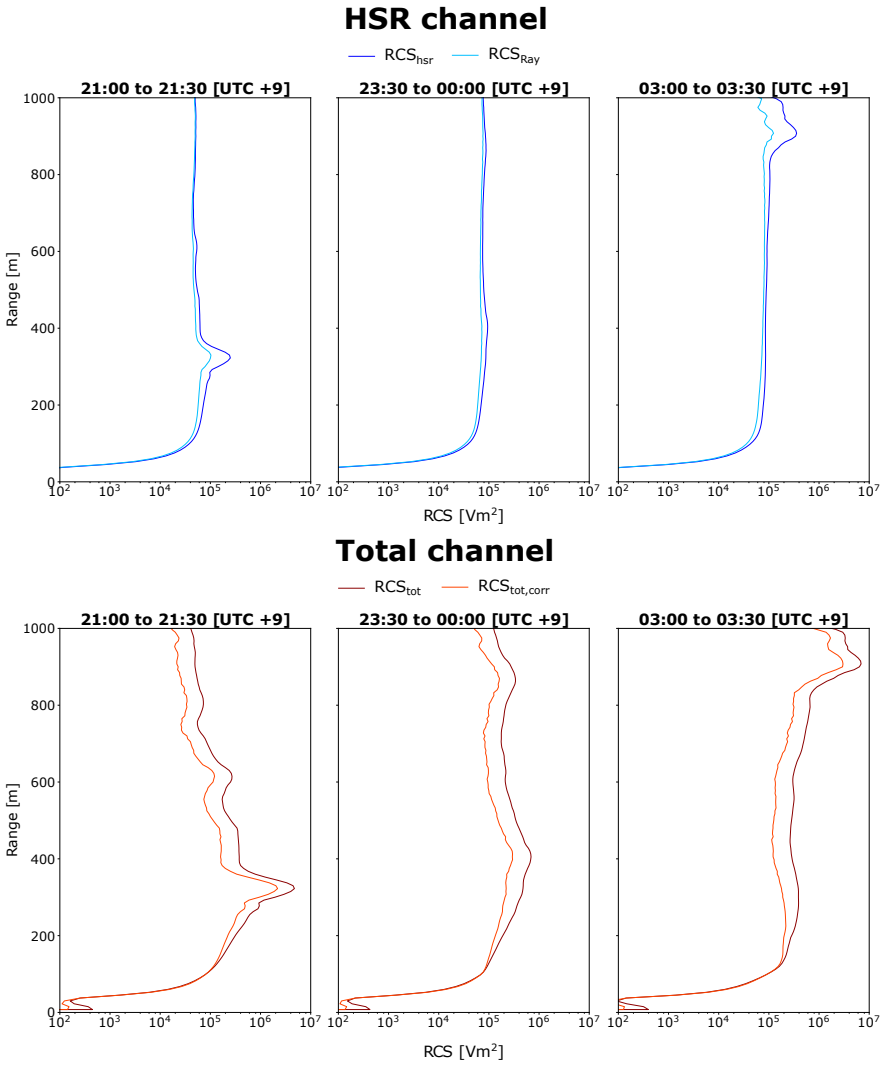

FIGURE 6.5: Half-hour averaged profiles of calibrated (lighter lines) and uncalibrated (darker lines) molecular and total signals.

After determining the crosstalk and interchannel calibration parameters, both channels were corrected as previously described for the entire measurement period. The preprocessed, calibrated signals are shown in Fig. 6.6. The top panel corresponds to the corrected molecular or Rayleigh channel (RCS_{Ray}), while the bottom panel shows the corrected total channel ($RCS_{tot,corr}$). For the total channel, applying the calibration parameter $C(r)$ yields a clearer, more contrasted signal, enabling easier distinction of aerosol layers. Moreover, the correction reduces the overlap height from approximately 150 m to less than 50 m, thereby improving the system's capability to detect aerosols close to the surface.

In the Rayleigh channel, a substantial reduction in Mie crosstalk is observed, as evidenced by the significantly lower intensity of cloud-related signals. Moreover, the calibration process, together with the applied low-pass filtering, significantly attenuated the stripe-like patterns associated with the laser wavelength drift that were visible in the uncorrected data. This effect can be clearly seen in the color-saturated temporal evolution plot in Fig. 6.7, which uses the same color scale as the corresponding uncorrected case shown in Fig. 6.3. This improvement indicates that the applied calibration compensates, at least partially, for spectral fluctuations of the emitted wavelength, leading to a more stable and homogeneous molecular signal. However, as previously discussed, completely removing crosstalk would yield unphysical molecular signals due to overcorrection.

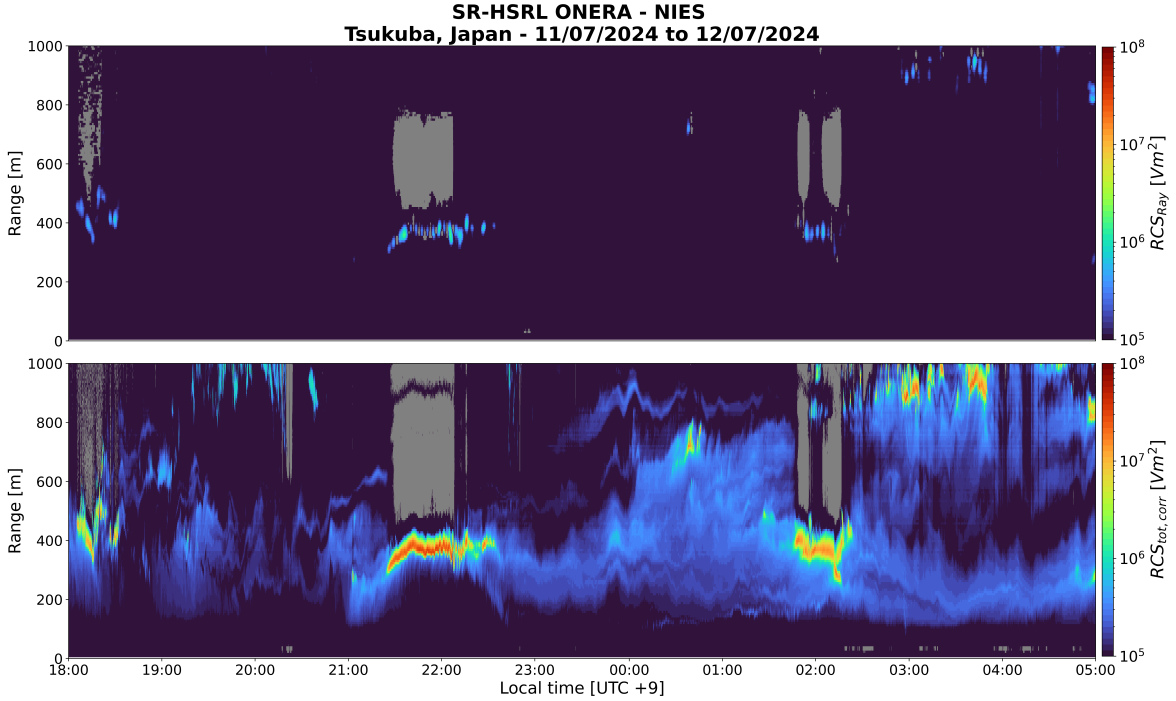

FIGURE 6.6: Temporal evolution of the calibrated signals for the measurement campaign (11/07/2024 to 12/07/2024). The top panel illustrates the Rayleigh channel, and the bottom one represents the corrected total channel.

The calibration and filtering steps produced more stable, physically consistent molecular and total signals, providing a solid foundation for subsequent retrieval of optical properties. The reduction of spectral artifacts and the improved alignment between detection channels ensured that the profiles were suitable for the quantitative analysis of aerosol scattering. As discussed in Section 3.4, in short-range HSRL systems, the overlap function cannot be assumed to be unity. Consequently, the backscatter ratio (BR) cannot be determined directly from the calibrated signals. Instead, it requires computing the attenuated backscatter signals, which in turn involves determining the radiometric constant and the overlap function for

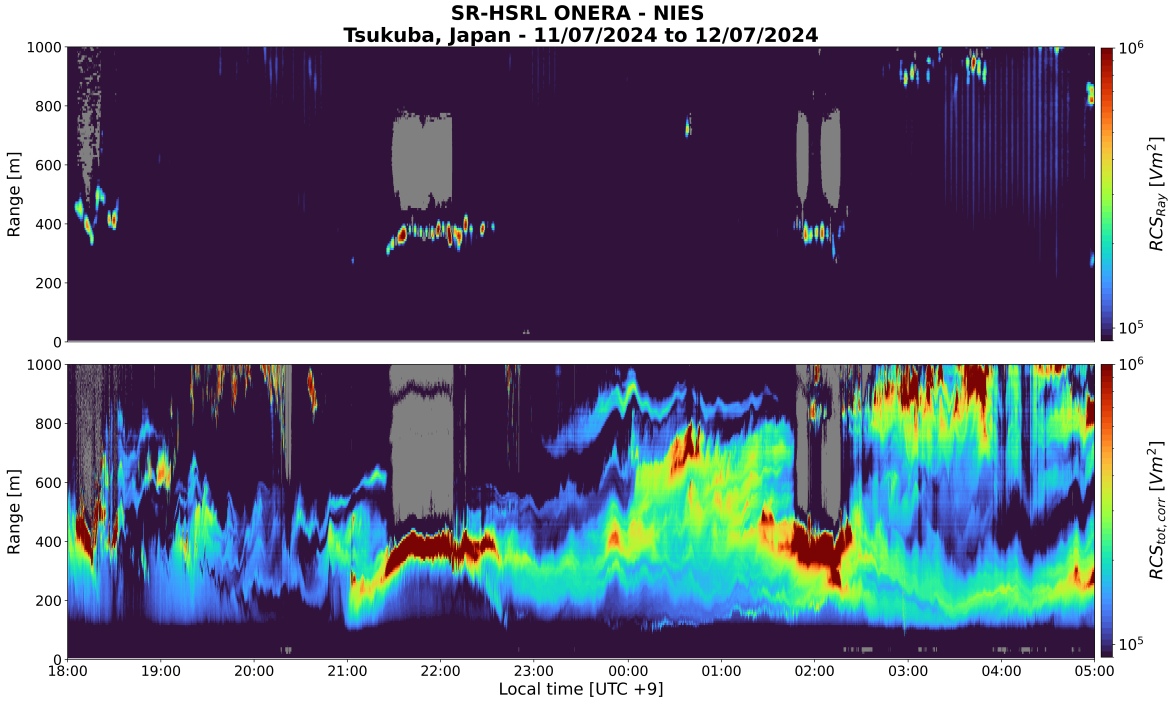

FIGURE 6.7: Color-saturated temporal evolution of the calibrated signals to highlight the reduction in the detected periodic laser wavelength drift in the HSR channel during the validation campaign.

each detection channel. The application of the proposed methodology, based on Rayleigh fits and the interchannel calibration parameter $C(r)$, to the proof-of-concept campaign data is described below.

6.4 Determination of the attenuated backscatter signals

As detailed in Chapter 3, in HSRL retrievals, the calculation of the aerosol backscattering coefficient is based on the determination of the backscatter ratio $BR(r)$. In long-range HSRLs, the overlap is assumed to be unity, and $BR(r)$ is calculated from the ratio of the signals and a calibration constant, itself defined as the ratio of the radiometric constants and calculated from off-line measurements. However, in the short-range HSRL implementation developed in this thesis, where measurements are performed over ranges with overlap ranging from 0 to 1, the computation of $BR(r)$ required the ratio of attenuated backscatter coefficients $U_{Ray,tot}(r)$ rather than the calibrated signals. As defined in Eqs. (3.48) and (3.49), computing the backscatter ratio involves determining the radiometric constant and overlap function for each channel.

In the Rayleigh channel, where the detected signal can be considered mainly molecular, the radiometric constant was determined by performing a Rayleigh fit between the measured

and theoretical molecular profiles. This constant, K_{Ray}, includes all the instrumental parameters that affect the received power, such as the receiver optical efficiency, detector gain, and laser pulse energy. Therefore, its accurate estimation is essential to ensure that the retrieved attenuated backscatter profiles are physically consistent and comparable between the two channels. To obtain K_{Ray}, an iterative fitting procedure was applied in which the measured molecular signal was compared with the theoretical molecular range-corrected signal calculated from local atmospheric conditions. To ensure reliable fitting, we selected an altitude range above 600 m, where the system was expected to have achieved complete overlap. The reference molecular profile was derived using temperature and pressure data from radiosonde observations launched at midnight on July 12th, 2024, at the Tateno meteorological station (36°03'29.2" N, 140°07'32.9" E), located about 1.4 km from the measurement site at the NIES facilities in Tsukuba. This ensured that the radiosonde data closely represented the local atmospheric conditions during the lidar measurements. The optimization minimized the difference between the measured and theoretical molecular signals, and the best-fit value of the radiometric constant was found to be $K_{Ray} = 7 \times 10^{10}$ Vm^{3}sr. This value represents the combined optical and electronic response of the system under the campaign operating conditions. Establishing this constant was a key step in computing attenuated backscatter profiles and, later, in retrieving reliable aerosol backscatter coefficients at short range.

After determining the radiometric constant of the calibrated molecular channel K_{Ray}, the next step to determine the attenuated backscatter signals consisted of estimating the corresponding overlap function $O_{Ray}(r)$. This function describes the effective geometric coupling between the laser beam and the receiver field of view as a function of range. It plays a critical role in accurately retrieving near-field backscatter profiles because this parameter cannot be assumed to be unity, since the laser beam and telescope line of sight only achieve full overlap after a finite distance, typically a few tens to hundreds of meters, depending on the system's geometry. To retrieve $O_{Ray}(r)$, Eq. (3.35) was applied to a time interval with minimal residual aerosol crosstalk in the Rayleigh channel, specifically between 23:00 and 01:00 local time. During this period, the calibrated signals could be considered as primarily molecular. Under these circumstances, it was reasonable to assume that both the aerosol backscatter and extinction coefficients were negligible, i.e., $\beta_{aer}(r) = \alpha_{aer}(r) = 0$. This simplification allowed the overlap function to be determined solely from measurable or known quantities, isolating the geometric contribution of the lidar system. Accordingly, the overlap function can be expressed as:

$$O_{Ray}(r) = \frac{P_{Ray}(r)\, r^2}{K_{Ray} X_m \beta_{mol}(r) \exp\left[-2\int_0^r \alpha_{mol}\left(r'\right) \mathrm{d}r'\right]} \tag{6.1}$$

Where the molecular backscatter and extinction coefficients $\beta_{mol}(r)$ and $\alpha_{mol}(r)$ were calculated from the radiosonde data. Additionally, the effective transmittance of the Rayleigh-Brillouin scattering spectrum throughout the iodine cell $X_m = 5.9 \times 10^{-1}$ was calculated from the cell's characterization measurements. The resulting overlap function is displayed in blue in Fig. 6.8.

After obtaining the radiometric constant K_{Ray} and the overlap function $O_{Ray}(r)$ for the molecular channel, the same procedure was extended to the total channel using the inter-channel calibration parameter $C(r)$ defined in Eq. (3.41). This parameter links both detection paths by accounting for differences in their optical transmission, detector sensitivity, and alignment. By using $C(r)$, it was possible to derive the total channel calibration constants without performing an independent absolute calibration, which would have been difficult to achieve in the field. In a range region where full overlap is reached (above approximately 550 m, as seen in Fig. 6.8), $O_{tot}(r) = O_{Ray}(r) = 1$ and thus the radiometric constant for the total channel was calculated from Eq. (3.41) as displayed in the equation below. This value was obtained assuming a mean $C(r)$ of about 0.45 in the fully overlap range, which agrees with the ratio expected from the receiver optical configuration.

$$K_{tot} = \frac{K_{Ray}}{\tilde{C}\,(r > 550\ \mathrm{m})} = \frac{7 \times 10^{10}\ \mathrm{Vm^3sr}}{0.45} = 1.55 \times 10^{11}\ \mathrm{Vm^3sr} \tag{6.2}$$

Finally, from the previously derived K_{Ray}, K_{tot}, and $O_{Ray}(r)$, Eq. (3.41) was again applied to determine the overlap function of the total channel as shown in the equation below. The retrieved overlap function of the total channel is shown in red in Fig. 6.8. The results obtained emphasize that the overlap function is the most critical parameter to address in short-range lidar measurements, where the assumption of complete overlap cannot be made. As previously discussed by Sassen (1982) [54] and Sicard (2020) [55], even small optical misalignments between the transmitted laser beam and the receiver optical axis can strongly affect the overlap function, especially at short distances where the beam geometry changes rapidly. In the SR-HSRL prototype developed in this thesis, the overlap functions of the molecular and total channels differ in the incomplete overlap region due to differences in optical paths and components used in each detection arm. The first difference comes from the 10:90 beam splitter, which divides the collected atmospheric backscatter between the two channels. This optical element slightly alters the beam profile and divergence, producing a small but measurable channel-dependent variation in the overlap. In addition, the molecular channel includes the narrowband, 40-cm-long iodine cell, which further modifies the optical path and slightly shifts the focal plane relative to the total channel. This difference, combined with the cell's limited aperture, affects both the effective field of view and the

receiver's alignment stability. Furthermore, the detectors in each channel are not positioned at exactly the same distance and their optical axes are not identically positioned relative to the laser beam and the telescope focal plane, introducing small differences in their geometric responses. Finally, the coatings of spectral and interference filters can preferentially transmit specific angular components of incident light, further contributing to variations in the near-field overlap between channels.

$$O_{tot}(r) = \frac{K_{hsr}\, O_{hsr}(r)}{K_{tot}\, C(r)} = 0.45\, \frac{O_{hsr}(r)}{C(r)} \tag{6.3}$$

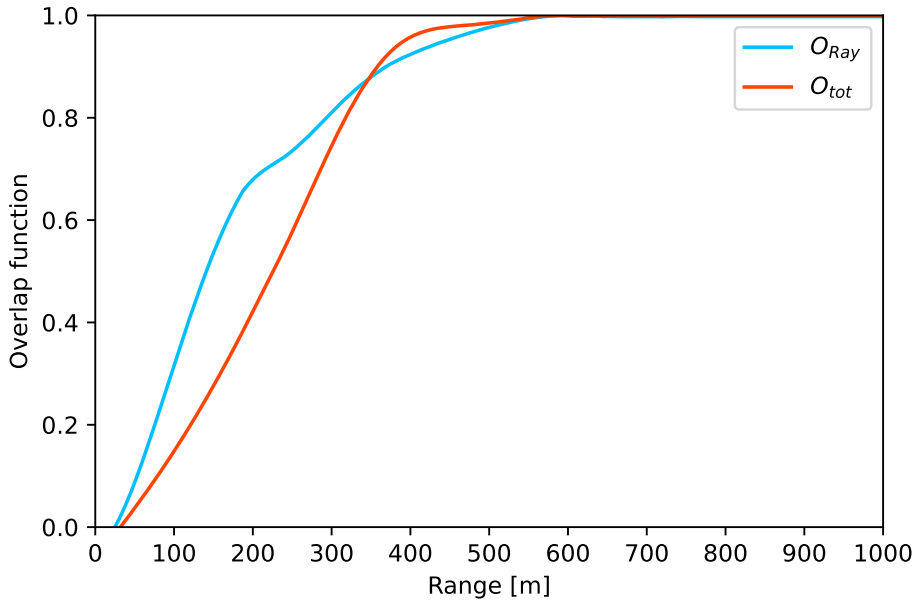

FIGURE 6.8: Overlap function of the Rayleigh (blue) and total (red) channels. Optical path differences between the channels cause the differences seen in the incomplete overlap zone (below 550 m).

As shown in Fig. 6.8, the two curves exhibit the expected behavior for a short-range, bistatic, biaxial lidar configuration. At very short ranges ($r < 50$ m), the overlap values are close to zero since the receiver field of view does not yet intercept the laser beam. Between 50 and 400 m, the overlap increases rapidly with range as the transmitted beam progressively enters the receiver FOV. The total channel (shown in red) reaches full overlap slightly earlier than the molecular channel, around 550 m, while the Rayleigh channel (in blue) reaches unity at about 600 m. This small difference is consistent with the additional optical elements in the molecular channel, mainly the 40 cm iodine cell and its windows, which slightly alter the beam collimation and reduce the FOV in this channel. Beyond the full-overlap height, both functions remain stable, confirming the system's good mechanical and optical alignment during the measurement campaign. In the near-field region below 150 m, small oscillations are observed, likely related to the multi-axial geometry and small residual misalignments

between the laser and telescope axes. These results demonstrate that the full overlap region of the SR-HSRL prototype extends much closer to the instrument compared with typical long-range HSRL systems, where the overlap distance can exceed 1 km. Moreover, because the overlap functions were determined for both channels, the developed instrument was capable of providing reliable aerosol measurements in the lower few hundred meters of the atmosphere, a key objective of this work.

Once the overlap functions and radiometric constants of both channels were determined, the next step was to transform the signals into physically meaningful optical quantities: the attenuated backscatter coefficients U_{Ray} and U_{tot}. These coefficients include both overlap and radiometric effects and serve as the basis for calculating the backscatter ratio. In practice, they provide a first look at the vertical and temporal structure of the atmosphere before any inversion is applied. They allow evaluating the prototypes' capability to capture the spatiotemporal evolution of aerosol and cloud layers in the first kilometer of the atmosphere and to verify the quality of the calibration and overlap correction described earlier. The temporal evolution of the obtained attenuated backscatter profiles is presented in Fig. 6.9. The top panel presents U_{Ray}, and the bottom panel displays U_{tot}. Like in the previous color plots, invalid values are masked in gray.

The figure shows that the Rayleigh channel exhibits a strongly attenuated aerosol component, with close-to-molecular-scattering structures still visible throughout the measurement period due to residual Mie crosstalk. This demonstrates the effective, yet finite, spectral discrimination of the iodine cell used and the prototype's ability to separate the molecular signal even at short ranges. On the other hand, the total channel shows well-defined aerosol layers between 50 and 1000 m, whose altitudes gradually increase after 23:00, consistent with nocturnal boundary-layer evolution and with the results presented before. The presence of intermittent, strong backscattering low-level clouds can also be identified, particularly between 21:30 and 22:30, and around 02:00. In conclusion, the contrast between channels undoubtedly illustrates the performance of the spectral discrimination subsystem. The total channel measures the combined molecular and aerosol backscattering components, being capable of resolving fine vertical and temporal aerosol structures in the PBL with high signal quality, achieving reliable measurements from about 50 m, i.e., within the blind zone of most HSRL systems reported in the literature. On the other hand, the molecular channel efficiently suppresses most aerosol signals, except in regions where cloud backscatter dominates and residual Mie crosstalk persists. These results confirm that the proposed calibration and filtering procedures produce stable and physically consistent attenuated backscatter profiles.

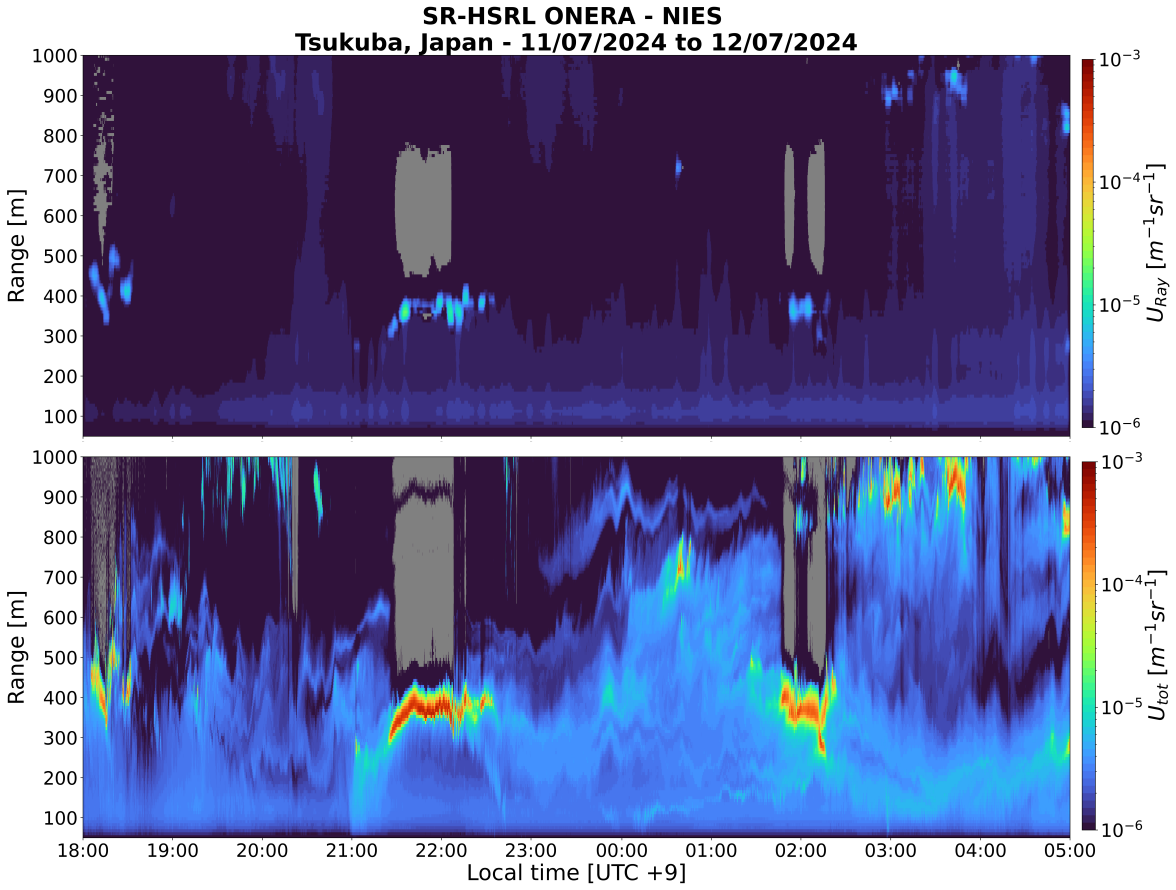

FIGURE 6.9: Temporal evolution of the attenuated backscatter coefficients measured by the SR-HSRL prototype during the field campaign. The top panel presents the molecular channel, and the bottom panel the total channel.

6.5 Estimation of the aerosol backscatter coefficients

As discussed in Section 3.4, one of the advantages of HSRL compared to EBL is the straightforward retrieval of aerosol radiative properties that does not require any assumption or integration methods like classical Klett-Fernald algorithms. Instead, the aerosol backscatter coefficient is retrieved directly from the backscatter ratio *BR*. In long-range lidars, where the overlap can be considered unity, *BR* comes simply from the ratio of the signals multiplied by the calibration constant. For the SR-HSRl developed in this thesis, it was necessary to compute the attenuated backscatter coefficients for both channels. Besides, due to the wide-linewidth laser used, the effective transmittance of Mie signals through the HSR channel could not be neglected. Therefore, it also required laboratory characterization measurements to compute X_p and X_m, getting values of 8.83×10^{-3} and 5.9×10^{-1}, respectively. Based on these values, the backscatter ratio was computed for the proof-of-concept campaign data by applying Eq. (3.50). The temporal evolution of the estimated backscatter ratio is presented as a color plot in Fig. 6.10. The figure clearly shows that the developed SR-HSRL

can distinguish purely molecular and aerosol-loaded atmospheric layers, as evidenced by the zones where the backscatter ratio equals or is very close to 1, indicating a purely molecular atmosphere. It can also sense layers of moderate aerosol loads, where *BR* ranges from 1.5 and <10, as well as dense aerosol layers, where *BR* can reach values up to 20. Finally, it is also clear that the system can measure clouds throughout and above, with values up to 1000.

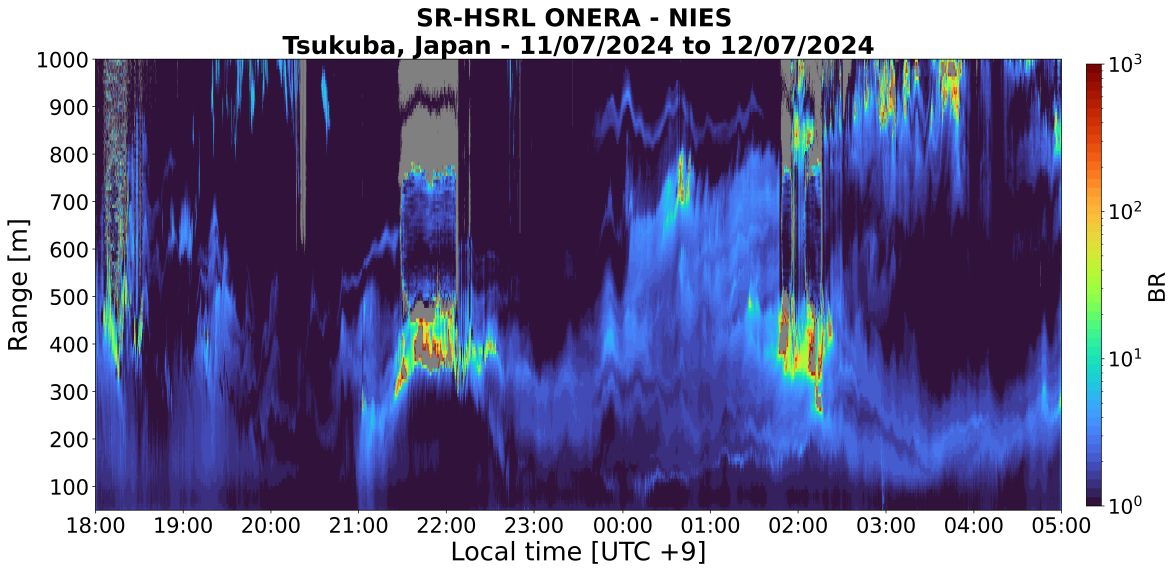

FIGURE 6.10: Temporal evolution of the backscatter ratio measured by the SR-HSRL prototype in the first kilometer of the atmosphere during the field campaign.

After computing the backscatter ratio for the entire campaign period, the aerosol backscatter coefficient was straightforwardly calculated with Eq. (3.44), where the molecular backscatter coefficient β_{mol} was calculated from the corresponding radiosonde data. The retrieval was performed over the full temporal dataset, providing continuous profiles of the aerosol backscatter coefficient throughout the measurement period. Figure 6.11 presents the temporal evolution of the estimated β_{aer}^{HSRL} is shown in Fig. 6.11, which reveals the vertical and temporal evolution of aerosol layers observed during the campaign. The effective retrieval range of the SR-HSRL system extends from approximately 50 to 1000 m, confirming its ability to provide reliable aerosol properties within the blind zone of conventional long-range HSRL systems.

It can be seen in the figure that during the early evening period (18:00–18:30), a thick aerosol layer extended from approximately 300 to 1000 m, with backscattering values ranging from 1.07×10^{-6} to 8.06×10^{-5} $m^{-1}sr^{-1}$. Between 18:30 and 19:00, the aerosol load decreased both below 250 m and above 900 m, leaving a more concentrated layer centered around 440 m, where the aerosol backscatter coefficient reached values between 1.01×10^{-6}

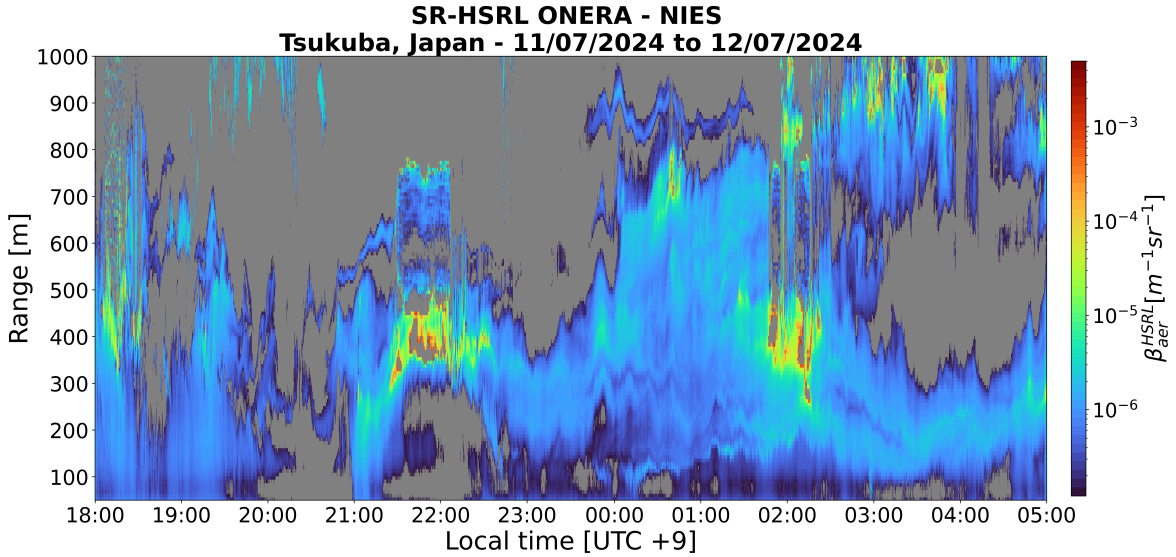

FIGURE 6.11: Temporal evolution of β_{aer}^{HSRL} measured by the SR-HSRL prototype in the first 1000 m. It can be noted that all aerosol layers are preserved, as is the strong backscattering from clouds.

and 1.28×10^{-4} $m^{-1}sr^{-1}$. In the following half hour, aerosol scattering remained significant above 150 m but with lower intensity, varying between 1.32×10^{-6} and 8.77×10^{-6} $m^{-1}sr^{-1}$. Up to 21:00, the atmosphere appeared relatively clean, with weak and fragmented layers observed at 100–200 m, 250–400 m, and 450–550 m, and a slightly stronger layer near 900 m reaching 3.5×10^{-6} $m^{-1}sr^{-1}$.

From 21:00 to 21:30, the aerosol load increased noticeably, forming two distinct layers: one extending from 100 to 450 m with a peak backscatter of 1.77×10^{-4} $m^{-1}sr^{-1}$, and a second, weaker one between 450 and 650 m reaching an intensity of 2.43×10^{-6} $m^{-1}sr^{-1}$. A cloud developed shortly afterward (21:30–22:30) between 300 and 500 m, with very strong backscatter values up to 2.31×10^{-3} $m^{-1}sr^{-1}$. During the next hour and a half, a medium-intensity aerosol layer persisted from near the surface ($\sim$ 50 m) up to about 400 m, with a maximum of 3.05×10^{-5} $m^{-1}sr^{-1}$, while a sparse upper layer (700–900 m) remained visible with a peak intensity of 5.61×10^{-6} $m^{-1}sr^{-1}$.

Between 00:00 and 01:30, the aerosol layers became more complex and extended up to 950 m, with multiple sub-layers forming. The most intense one appeared between 700 and 800 m around 00:30–01:00, where β_{aer}^{HSRL} reached 2.98×10^{-4} $m^{-1}sr^{-1}$. Later, between 01:30 and 02:30, another cloud was detected from 300 to 500 m, showing strong backscattering up to 1.96×10^{-3} $m^{-1}sr^{-1}$ at 450 m. Around 02:00, a layer that developed above this cloud was sensed, extending from about 550 to 1000 m with local maxima at 832 m of(1.09×10^{-4} $m^{-1}sr^{-1}$) and 968 m (5.16×10^{-4} $m^{-1}sr^{-1}$). Afterward, the aerosol distribution

separated into two broad layers: a lower one with moderate backscattering, with peak intensity 4.19×10^{-6} $m^{-1}sr^{-1}$, and an upper one containing clouds that produced the strongest signal of the night (2.75×10^{-3} $m^{-1}sr^{-1}$).

It is important to highlight that the HSRL method can retrieve backscattering values both inside and above clouds, unlike the EBL method. This capability arises because the HSRL retrieval process relies on the calculation of the backscatter ratio, which is derived from the ratio of the attenuated backscatter profiles. As illustrated in Fig. 6.9, U_{tot} is accurately recovered within clouds from the calibrated signals along with the estimated radiometric constant and overlap function. Then, when calculating BR, the ratio U_{tot}/U_{Ray}can become excessively high at the peak cloud intensity, resulting in the denominator of Eq. (3.50) turning negative. Since the backscatter ratio cannot be negative or less than 1, these unphysical values are masked in gray. However, this issue does not impede retrievals in other areas of the cloud or above it. In contrast, numerical integration methods such as the Klett or Fernald algorithms often struggle in conditions of strong extinction because the integrals diverge. This leads to failure in retrieving aerosol backscatter coefficients within and above optically thick layers. The HSRL approach, however, remains stable and allows for successful retrievals both within and above cloud layers, as long as the laser beam is not completely extinguished.

Overall, these results show that the SR-HSRL prototype successfully captured both the diurnal transition and the fine-scale spatiotemporal evolution of aerosol and clouds within the first kilometer of the atmosphere. More importantly, the ability to resolve aerosol layers as close as 50 m from the instrument confirms that the SR-HSRL system effectively bridges the blind zone that limits conventional long-range HSRL systems, thus fulfilling one of the main objectives of this work.

6.5.1 Uncertainty analysis of the retrieved aerosol backscattering coefficients

To accurately interpret the retrieved aerosol backscattering coefficients, it is essential to account for uncertainties arising from the different input parameters –unrelated to the measured signals– used in the HSRL retrieval. In particular, the effective transmittances of the Doppler-broadened Mie and Rayleigh-Brillouin spectra ($X_m = 5.9 \times 10^{-1}$ and $X_p = 8.9 \times 10^{-3}$) and the radiosonde-derived molecular backscattering coefficient (β_{mol}) can introduce non-negligible errors in the estimation of β_{aer}. To evaluate the uncertainty effects, a Monte Carlo (MC) method was implemented in order to simulate uncertainty propagation through the retrieval equation by assessing the impact of introducing noise levels for these variables. In the simulations, synthetic lidar signals were generated and at each range the input variables were

perturbed according to a defined measurement uncertainty, thereby quantifying how random variations in the inputs propagate into the retrieved aerosol backscattering coefficient values.

The relative uncertainties for X_m and X_p were derived from the laboratory characterization measurements of the iodine transmission spectrum in the Keopsys laser wavelength range presented in Section 5.1.1. The results showed variations lower than 1% for X_m and approximately 6.5% for X_p. Concerning the molecular backscattering coefficient, the uncertainties are induced by the atmospheric pressure and temperature measured by the radiosonde. Wang et al. (2022) [92] demonstrated that the influence of atmospheric pressure on β_{mol} is negligible, whereas temperature has a significant impact. For example, an error of only 3 K in the temperature profile can lead to retrieval errors of up to 40% in β_{aer}. Since both the radiosonde data and the validation measurements were performed at nighttime, minimal variations were expected in the temperature and pressure profiles, and therefore their impact on β_{mol} should be minimal. Based on this assumption, a relative temperature uncertainty of 3 K was applied to the temperature profile in the MC simulations, resulting in a 1% variation in β_{mol}.

After determining the uncertainty levels of the three variables, the MC method was applied. The results of the analysis indicate that the induced relative error in the retrieved $\beta_{aer}(r)$ of the combined uncertainties from X_m, X_p, and β_{mol} can reach up to 7.2%. This result confirms that the uncertainty introduced by the iodine cell, laboratory characterization measurements, and radiosonde data remains within an acceptable range for the SR-HSRL prototype. The relatively small combined error of 7.2% in the retrieved β_{aer} values demonstrates that the design choices, especially the spectral filter selection and the wavelength stabilization strategy, were appropriate for achieving stable and reliable short-range HSRL measurements. Furthermore, the low sensitivity of the retrieved values to fluctuations in temperature and filter transmittance of the backscattering components validates the calibration procedures and spectral characterization described in the previous chapters. Overall, this uncertainty assessment supports the robustness of the developed methodology and provides confidence in the system's capability to perform accurate aerosol profiling within the first kilometer of the atmosphere. However, it highlights the importance of conducting a dedicated sensitivity analysis in future work to systematically assess the contribution of each variable to the total retrieval uncertainty, especially the laboratory-derived measurements. This analysis would be particularly useful for refining the calibration strategy of the SR-HSRL and for improving the reliability of aerosol optical property retrievals under different atmospheric conditions.

6.6 Discussion and summary

The novel short-range HSRL developed in this thesis represents a significant advancement in the HSRL field due to its capacity to perform highly detailed lidar measurements and retrieve precise quantitative aerosol backscattering coefficients in the low troposphere, specifically up to the first thousand meters of the atmosphere. The prototype, based on a high-repetition-rate diode-based commercial laser paired with an iodine cell, achieved a high temporal resolution (6 s) and a spatial resolution (7.5 m, limited by the detectors and the signal acquisition system) that is acceptable for the present proof-of-concept study and can be further improved by changing the detection and ADC units.

The SR-HSRL prototype was meticulously designed to minimize the blind zone while optimizing spatial resolution, making it a feasible instrument for studying the lower atmosphere. This was demonstrated in the quicklook presented in Fig. 6.11, as well as in the sample averaged-profile (04:30-05:00) illustrated in the right panel of Fig. 6.12. This profile demonstrates that the effective retrieval range of aerosol backscatter coefficient is from 50 to 1000 meters above ground level, the blind zone of the majority of HSRLs reported in the literature review (Chapter 4).

Another advantage of the SR-HSRL prototype conceived in this thesis is that it enables accurate data retrieval even within and above optically dense cloud layers, provided the laser beam does not experience complete extinction. This is because the inversion method relies on the direct computation of the backscatter ratio rather than on traditional numerical integration methods such as the Klett or Fernald algorithms frequently employed in EBL systems. Since integrals diverge in the presence of strong extinction, these methods often fail within optically thick layers, preventing the retrieval of information above clouds. In contrast, the HSRL approach remains stable except for peak cloud intensity, allowing for accurate data retrieval even within and above optically dense cloud layers, provided the laser beam does not face complete extinction. This unique capability positions HSRLs as worthy instruments for examining cloud formations and aerosol-cloud interaction processes. For instance, the left panel of Fig. 6.12 depicts a cloud extending from 300 to 550 meters, where the retrieved backscattering values soar to approximately 10^{-3} $m^{-1}sr^{-1}$. This measurement not only identifies the cloud but also reveals the presence of an overlying aerosol layer, together with an additional cloud situated above the primary cloud. This highlights the HSRL's efficacy in studying atmospheric phenomena.

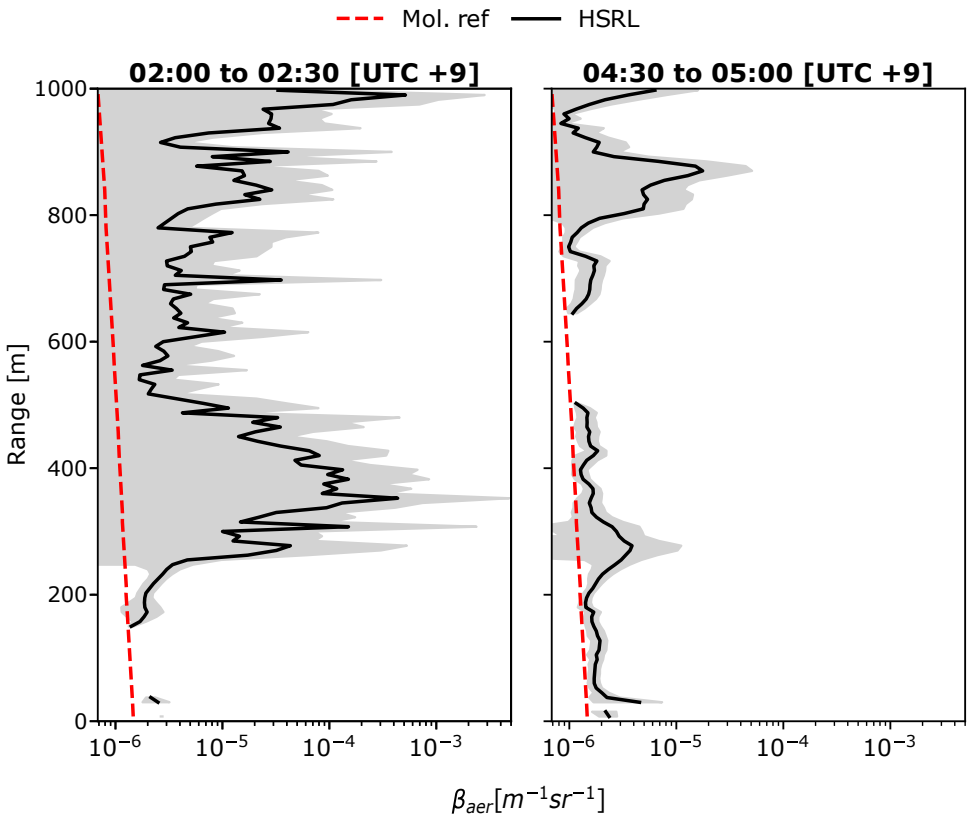

FIGURE 6.12: Averaged profiles of the backscatter coefficients retrieved in the short range (from 50 m) for aerosol layers and clouds. The gray shadow represents the standard deviation of the averaged profile, with variations due to atmospheric changes over the 30-minute integration time.

Compared with the only short-range HSRL reported in the literature, i.e., the HSR-SLidar developed by Chang et al. [27], the pulsed short-range HSRL presented in this thesis is instrumentally more complex but offers several key advantages. Both systems achieve a comparable blind-zone height (30 m for the HSR-SLidar and 50 m for the SR-HSRL). However, the present prototype overcomes all the intrinsic limitations of Scheimpflug-based lidar systems. First, the spatial resolution of the SR-HSRL is constant along the range, whereas in the HSR-SLidar, it depends on the imaging geometry and pixel projection and thus varies with distance. Second, the SR-HSRL, as a time-of-flight instrument, does not require range calibration or geometric reconstruction, simplifying the data processing pipeline and minimizing range-dependent systematic errors. Third, the system developed in this thesis enables continuous, synchronized acquisition of molecular and total backscatter signals without alternating between on- and off-resonance wavelengths, avoiding temporal discontinuities and ensuring high temporal resolution (6 s per profile). Finally, operating around 532 nm allows for a direct comparison of the aerosol optical properties retrieved by the SR-HSRL with those from reference HSRL systems.

Although the HSR-SLidar achieves a higher spectral discrimination ratio owing to the extremely narrow rubidium absorption line, the SR-HSRL provides direct, simultaneous measurements of both molecular and particulate backscattering with greater flexibility in wavelength selection and modular filter replacement. In summary, the system developed in this work complements and extends the capabilities of the HSR-SLidar, providing a more versatile lidar system for near-source aerosol characterization and for future mobile or airborne applications.

6.7 Current limitations of the SR-HSRL technique

While the results obtained in this thesis demonstrate the feasibility of short-range implementation of the HSRL technique, several limitations remain that constrain the system's current performance and prevent the retrieval of aerosol extinction coefficients. These limitations, associated with instrumental and methodological factors, are discussed below.

6.7.1 Instrumental limitations

The instrumental limitations were identified during the state-of-the-art review and numerical simulations. The first, and most important, comes from the laser spectral characteristics. The prototype used a diode-based laser with a linewidth of 300 MHz, broader than any reported for long-range HSRL systems (typically around 100 MHz). This wide linewidth reduces the spectral contrast between the Doppler-broadened molecular and aerosol backscattering, decreasing the effective discrimination ratio of the iodine filter. As a consequence, the separation between the Rayleigh and Mie components is less precise and effective, increasing the uncertainty in the retrieved backscatter ratio. Since HSRL aerosol extinction coefficient retrievals rely on spectral discrimination, even small Mie crosstalk can prevent proper extinction assessments.

The spectral filter itself also introduces limitations. The 40-cm-long iodine cell used in the prototype provided a rather moderate spectral discrimination ratio (~ 300), which proved sufficient for retrieving aerosol backscattering coefficients. However, it appears insufficient to resolve the minor atmospheric transmission differences required for HSRL extinction retrieval. In addition to the finite spectral performance, stripe-like laser wavelength shifts were observed for laser temperature fluctuations as small as $\pm 0.01°$C. These small drifts shifted the laser central frequency relative to the iodine absorption line center, thereby altering the cell's transmittance and, in turn, the differential molecular-to-particulate transmission required for computing the extinction. These effects are negligible for backscattering retrieval

but become critical for extinction since the HSRL inversion method relies on logarithmic differentiation.

The final instrumental limitation that possibly prevented the retrieval of aerosol extinction coefficients concerned the characterization of the overlap functions. Although the proposed method, based on the interchannel calibration parameter, allowed retrieving the overlap functions for both channels, minor residual uncertainties in the near-field region (below full overlap) can bias the ratio between the total and Rayleigh signals. Because extinction is derived from this ratio's derivative, even slight geometric errors or noise can lead to significant, unphysical variations in the estimated values.

6.7.2 Methodological and signal-related limitations

From a methodological standpoint, the main constraint arises from the signal-to-noise ratio (SNR). Despite achieving acceptable SNR values during the campaign ($\sim$470 for the total channel and 200 for the molecular channel), extinction retrieval requires extremely low noise levels because it depends on the slope of the signal ratio rather than its absolute value. The differentiation of noisy signals amplifies random fluctuations, leading to unstable or negative extinction values, especially in regions with weak aerosol load. Calibration uncertainties also contribute to this issue. The extinction retrieval depends on the accuracy of the interchannel calibration parameter $C(r)$ and the crosstalk coefficient χ_p. While these parameters were well constrained for backscatter retrieval, extinction estimation is a second-order process involving derivatives of these quantities with respect to range. Even minor residual errors or interpolation noise in $C(r)$ can translate into significant systematic errors in the computed extinction.

Furthermore, the intrinsic sensitivity of the HSRL extinction retrieval equation exacerbates these effects. Because the extinction coefficient is calculated from the range derivative of the logarithm of the molecular-to-total signal ratio, any residual noise, drift, or calibration bias is greatly magnified. Under real atmospheric conditions, especially in clean air, this leads to unstable results that cannot be physically interpreted.

6.7.3 Future improvements

Future improvements should focus on increasing spectral discrimination and system stability. Using a laser with a narrower linewidth ($<$ 150 MHz) would significantly improve molecular–aerosol separation, as demonstrated by the numerical simulations results. Implementing a dual-cell or dual-pass iodine configuration (like the spectral system configuration

of the HSRL developed by Liu et al. (2009) [98]) or increasing the cell optical path or pressure/temperature could enhance the spectral contrast without major hardware changes. In parallel, a more precise temperature-control system (stability of $< \pm 0.01^{\circ}$C) for both the laser and the iodine cell would reduce the observed wavelength drift. Improvements in the overlap characterization, for instance, through dedicated near-field calibration, as proposed by Ceolato et al. [21], or geometric modeling, would also help constrain the short-range uncertainty. Finally, integrating auxiliary instruments such as a Raman channel or a co-located sunphotometer would enable cross-validation and extinction calibration. By implementing these technical improvements, the SR-HSRL concept could be extended to new configurations, including scanning or airborne platforms, to study aerosol radiative properties close to emission sources. With further optimization, the instrument could serve as a reference tool for assumption-free, highly accurate aerosol and cloud measurements at short and ultra-short ranges, bridging the gap between short-range elastic lidars and long-range HSRL systems.

Chapter 7

Conclusions and perspectives

7.1 General overview

Over the last few decades, several climate, air quality, and aeronautical applications have stimulated the development of short-range lidars to assess aerosol particles over short distances. However, these instruments are inherently limited in accuracy, particularly for assessing ultrafine particles. On the other hand, HSRLs offer assumption-free, accurate aerosol retrievals. Yet, existing HSRLs have been primarily designed for long-range measurements. A comprehensive literature review found that no pulsed HSRL has been reported for short-range aerosol studies. In this context, this thesis proposed and demonstrated a novel short-range, time-of-flight-based HSRL (SR-HSRL) prototype that combines the strengths of SR-EBLs (e.g., low blind zone, high spatiotemporal resolution) and HSRLs (e.g., assumption-free, highly accurate calibrated aerosol radiative properties). The developed prototype, specifically designed for the near-field region where traditional HSRLs cannot operate, achieves calibrated aerosol retrievals overcoming the limitations of the HSR-SLidar: constant spatial resolution and continuous, synchronized, high-repetition-rate operation. To achieve the main thesis goal, three specific objectives were established.

- The first objective focused on the simulation-based design and performance estimation of the instrument. Two spectral filters (iodine cells and scanning FWMIs) were chosen from a comprehensive review of the state of the art. Then, an end-to-end numerical model was developed to estimate the performance of the filters for different configurations and laser linewidths. The results enabled optimization of their optical and spectral design.

- The second objective aimed at the laboratory characterization and validation of the performance. A dedicated methodology was established to measure the temporal and spectral properties of commercial laser sources, identifying two that were well-suited for the SR-HSRL prototype. Laboratory tests were then conducted to validate the

spectral performance of the two filters using the selected lasers. Based on these results, a first prototype was assembled, and its spectral performance was verified under controlled conditions before being validated during a collaborative measurement campaign at the National Institute for Environmental Studies (NIES) in Tsukuba, Japan.

- Finally, the third objective addressed the retrieval and analysis of calibrated backscattering profiles. A novel overlap- and radiometric-calibration methodology was proposed. Then, an inversion methodology based on the computation of the backscatter ratio from attenuated backscatter profiles was proposed and implemented to retrieve assumption-free aerosol backscattering coefficients from the field campaign data. The results demonstrated the prototype's ability to perform accurate, autocalibrated aerosol and cloud retrievals in the near-field region, where conventional HSRL systems are typically blind.

Having defined and met the thesis objectives, this manuscript followed a logical progression from theoretical foundations to experimental validation and data analysis. Each chapter contributed to one or more of the objectives described above, together forming a coherent workflow that led from the conceptual design of the SR-HSRL prototype to its successful experimental validation and first retrievals of near-field aerosol properties. The content and results of each chapter are briefly summarized below.

A dedicated SR-HSRL inversion method was proposed in Chapter 3. After discussing the theoretical bases of absorption and scattering –the physical principles of the lidar technique–, the operating principle of HSRLs was presented. Then, since short-range operation requires assessing the system's overlap function, a dedicated SR-HSRL inversion method was proposed. It is based on the absolute calibration of the system via the interchannel calibration parameter, obtained from offline measurements. From this parameter, the total signal is corrected. Then, Mie crosstalk is assessed and removed from the HSR channel, yielding a purely molecular signal. This allows determining the overlap functions and radiometric constants of both channels, from which the attenuated backscatter is calculated. Then, the backscatter ratio is estimated, enabling the retrieval of the aerosol backscatter coefficient without assumptions.

A comprehensive analysis of the state of the art in short-range lidar and high spectral resolution lidar was performed in Chapter 4. The objective was to identify the novelty, challenges, and potential technological limitations of developing an SR-HSRL for aerosol studies. The analysis of the operating principles, design strategies, and performance of both lidar categories provided the conceptual and technological context for the design and implementation of the SR-HSRL proposed in this work. The literature review indicated that no

time-of-flight-based, short-range, high-spectral-resolution lidar systems have been reported to date. Only one short-range HSRL was found. It is a CW near-infrared, Scheimpflug-based HSRL. Being a SLidar, it inherits the advantages and disadvantages of this operating principle. The literature review indicated that developing a time-of-flight-based SR-HSRL was a significant contribution to lidar remote sensing. Our prototype helps close the gap in highly accurate, high-spatiotemporal-resolution aerosol characterization at short ranges (the blind zone of long-range elastic and high-spectral-resolution lidars).

The design and development methodology of the SR-HSRL prototype was described in Chapter 5, laying the foundation for its implementation and ensuring that the transmitter and spectral filtering units meet the performance requirements for optimal operation. It began with the description of the comprehensive characterization of the customized commercial laser sources identified as suitable candidates for the SR-HSRL implementation. Subsequently, numerical simulations were carried out to predict the spectral performance and limitations of two candidate spectral filters identified from the state-of-the-art review –a scanning FWMI and an iodine vapor cell–. These simulations guided the optimization of design parameters to maximize the spectral discrimination performance for different laser linewidths. Thereafter, the laboratory validation of the spectral performance of the combined laser–filter configurations was presented. Finally, based on the laboratory characterization and validation measurements, the most appropriate laser/spectral filter combinations for different operational conditions were identified and discussed.

Finally, the results of a field campaign to validate the SR-HSRL concept were presented in Chapter 6. Building upon the design and characterization of the transmitter and spectral units, a fully operational SR-HSRL prototype based on the selected laser and a 40-cm-long iodine cell was developed in collaboration between ONERA and NIES, the National Institute of Environmental Studies of Japan. Its performance was evaluated under real atmospheric conditions during a field validation campaign conducted in Tsukuba, Japan, in July 2024. Applying the proposed signal calibration and data inversion methodology, it was possible to retrieve calibrated aerosol backscatter coefficients from 50 to 1000 m with a high temporal resolution (6 s), and an acceptable spatial resolution (7.5 m, limited by the detectors and the signal acquisition system). It was demonstrated that the SR-HSRL prototype enabled accurate data retrieval within and above optically dense cloud layers, provided the laser beam does not experience complete extinction. The advantages and disadvantages of the pulsed SR-HSRL prototype vs the reported HSR-SLidar were discussed.

7.2 Synthesis of the main results

The feasibility of applying the high spectral resolution lidar technique to short-range operation was demonstrated through the development and evaluation of a compact SR-HSRL prototype integrating an iodine absorption cell and a non-conventional, high-repetition-rate diode-based laser with a 300 MHz linewidth and a 4.96 ns pulse duration. Developing this instrument represented a major scientific and technical challenge. One of the key technological challenges was identifying a spectrally narrow and stable commercial laser source with nanosecond pulse duration to support short-range and high spectral resolution measurements with high spatiotemporal precision. This required establishing a complete characterization methodology for commercial lasers, since manufacturers generally do not provide full spectral specifications. Furthermore, the laser needed to be affordable, compact, wavelength-tunable, and operate at a high repetition rate –features opposite to those of the lasers typically used for long-range HSRL systems, except for the diode-laser-based HSRL developed by Hayman and Spuler [93], which, however, is a long-range lidar with a 150 m resolution–. The developed prototype was validated through a proof-of-concept field campaign, confirming its operational feasibility.

From a data-analysis perspective, thanks to its optimized configuration with a low blind zone (50 m to full overlap at 550 m) and high spatial resolution, the developed SR-HSRL prototype proved to be suitable for characterizing aerosols in the lower atmosphere. The retrieved profiles revealed several aerosol layers between 50 and 1000 m with aerosol backscattering coefficients values ranging from close-to-moleular values (10^{-6} $m^{-1}sr^{-1}$) to cloud values (10^{-3} m^{-1}), consistent with typical PBL values. A further advantage of this system lies in its retrieval method, which produces radiometric- and overlap-calibrated, physically meaningful signals (i.e., attenuated backscatter profiles) for both detection channels. This allows for measurements within and above clouds, provided the laser beam is not completely extinguished. The Monte Carlo simulation-based uncertainty analysis estimated a total uncertainty of 7.2% in the retrieved $\beta_{aer}(r)$, confirming the reliability of the developed SR-HSRL inversion method. This capability makes the instrument particularly valuable for investigating cloud formation and aerosol–cloud interactions, such as contrail-induced cirrus clouds.

From an instrumental standpoint, the prototype is compact and cost-effective. Unlike conventional long-range HSRLs based on high-energy, low-repetition-rate, injection-seeded Q-switched Nd:YAG lasers, the system developed in this thesis employed an amplified fiber laser at 532 nm with low-energy pulses ($\sim$1-11 μJ) and a high repetition rate (50–65 kHz). Performing HSRL measurements at short ranges and with high spatial resolution required a compromise between pulse width (4.96 ns), linewidth (300 MHz), and overlap distance

(50–1000 m), which is defined by the optomechanical alignment of the receiver optics. While long-range HSRLs generally prioritize narrow linewidths to maximize spectral discrimination –from NASA's HSRL-2 38 MHz [49] laser to DLR's <150 MHz laser [110]–, this work demonstrated that accurate spectral separation is achievable with broader linewidths when supported by careful system optimization. A spectral discrimination ratio of about 300 was obtained—sufficient to resolve multiple aerosol layers while maintaining high range (7.5 m) and temporal (6 s) resolution.

Compared with the only other short-range HSRL reported in the literature, i.e., the HSR-SLidar developed by Chang et al. [27], the pulsed SR-HSRL presented in this thesis is instrumentally more complex but offers several key advantages. Both systems achieve comparable blind-zone heights (30 m for the HSR-SLidar and 50 m for the SR-HSRL), but the present prototype overcomes the main limitations of Scheimpflug-based lidar systems. First, the spatial resolution of the SR-HSRL is constant with range, whereas in the HSR-SLidar, it depends on imaging geometry and varies with distance. Second, the SR-HSRL, as a time-of-flight system, does not require range calibration or geometric reconstruction, simplifying data processing and minimizing systematic errors. Third, the SR-HSRL allows continuous, synchronized acquisition of molecular and total backscatter signals without wavelength switching, thereby avoiding temporal discontinuities and ensuring consistent 6-second temporal resolution. Operating at 532 nm also facilitates direct comparison with standard atmospheric lidars. Although the HSR-SLidar achieves a higher spectral discrimination ratio due to the narrow rubidium absorption line, the SR-HSRL provides direct, simultaneous retrievals with greater flexibility in wavelength selection and modular filter replacement. Overall, the SR-HSRL complements and extends the capabilities of the HSR-SLidar, offering a more versatile and adaptable platform for near-source aerosol characterization and potential airborne applications.

Short-range elastic backscatter lidars have already proven to be powerful instruments for detecting particles close to their sources with high spatiotemporal resolution [19–22, 26, 71]. These systems have introduced new diagnostic capabilities for both aeronautical and environmental studies, such as monitoring aircraft engine emissions and characterizing the atmosphere in the lower planetary boundary layer, where long-range lidars are blind. However, the inherently ill-posed nature of the EBL inversion problem limits the accuracy of SR-EBLs. In ultra-short-range measurements, the absence of a molecular reference zone complicates the inversion process, requiring additional calibrations and dedicated forward models [22]. Consequently, quantifying ultrafine particles, such as freshly emitted soot, remains particularly challenging for EBLs. The SR-HSRL developed in this work bridges this

gap by enabling accurate characterization of coarse-to-ultrafine aerosols over short ranges without any assumptions about the lidar ratio. Since HSRL is a well-posed problem, the proposed method enables direct and assumption-free retrieval of aerosol optical properties. With its enhanced precision, the SR-HSRL combines the near-field capability of EBLs with the accuracy of HSRL techniques, opening the door to a new generation of compact, high-performance lidars for near-ground aerosol research.

7.3 Scientific and technical contributions

7.3.1 General contributions

The main contribution of this work was to extend the HSRL technique to short-range operation, enabling assumption-free aerosol retrievals in regions where conventional HSRLs cannot operate. This major achievement is based on several smaller contributions. First, a complete methodology was developed for laser characterization and spectral filter optimization, establishing a systematic framework for designing short-range high spectral resolution lidars. Second, an original calibration approach was proposed that integrates interchannel calibration, Mie crosstalk correction, overlap retrieval, and radiometric calibration into a unified framework. Third, successful field implementation confirmed the system's ability to produce stable, temporally resolved aerosol backscatter coefficient profiles under real atmospheric conditions. Finally, a Monte Carlo sensitivity analysis quantified the impact of spectral and atmospheric uncertainties on retrieval accuracy, highlighting the method's robustness and identifying key parameters for future optimization. In summary, this work demonstrates the feasibility of performing high spectral resolution lidar measurements at short ranges while maintaining high spatiotemporal resolution and acceptable uncertainty levels (7.2%). The SR-HSRL developed in this thesis thus represents a significant step toward compact, accurate, and assumption-free lidar systems for near-field aerosol and cloud research.

7.3.2 Contribution to ONERA's methodological competence in short-range aerosol lidar

As mentioned above, the Colibri Aerosol Lidars (CALs) developed by ONERA have proven to be novel and outstanding tools for measuring particles near the source with very high spatiotemporal resolution [21, 22, 25, 26]. They have introduced new diagnostic capabilities for several aeronautics and environmental applications, such as measuring the pollution emitted by airplane engines and characterizing the atmosphere in the lower planetary boundary layer, where long-range atmospheric lidars are blind. However, the inherently ill-posed EBL

problem limits the accuracy of these instruments. Furthermore, the inversion of the signals requires geometric and radiometric calibrations, as well as a dedicated forward inversion method that does not require knowledge of boundary conditions or a reference zone.

Assessing ultrafine particles, such as freshly emitted soot, still poses a significant challenge for elastic Colibri lidars. These shortcomings motivated the development of the next generation of ONERA's Colibri aerosol lidars: the SR-HSRL prototype developed in this thesis. This novel instrument offers greater accuracy since the HSRL is a well-posed problem that can be solved without assumptions. This allows for a more straightforward inversion of the particles' radiometric and microphysical properties. With enhanced accuracy, the SR-HSRL will be able to measure smaller particles, such as soot and volatile particulate matter, while maintaining the short-range capabilities characteristic of the Colibri instruments. This is particularly important for the aviation industry because the evolution of regulatory standards is driving the industry's efforts to reduce non-volatile and volatile particulate matter emissions from aircraft engines. The actions towards lower-emission engines focus on technological advances in engine design, the use of low-sulfur jet fuel, and improved combustion efficiency [25]. Since soot is primarily produced during fuel-rich combustion, particular efforts have been made to develop lean-burn engines, which promise lower soot and volatile PM emissions due to lower temperatures and the absence of fuel-rich zones [132]. Thus, the development of the high-spectral-resolution CAL will enable certification procedures for new lean-burn aircraft engines by allowing a more accurate assessment of lower concentrations of soot and non-volatile particles.

7.4 Perspectives

The SR-HSRL developed in this thesis represents a significant technological advance for lidar remote sensing, allowing assumption-free and calibrated retrievals of aerosol and cloud backscatter coefficients within the blind zone of conventional HSRL systems. However, several instrumental and methodological limitations constrained its full potential, particularly preventing the retrieval of aerosol extinction coefficients. These limitations emerged during both the prototype characterization and the field measurements, highlighting areas for improvement in future system developments. Instrumentally, the main constraints were the laser source's broad linewidth, which limited the iodine cell's spectral discrimination capability, and small wavelength drifts observed during operation. Methodologically, residual uncertainties in the determination of the overlap function, low signal-to-noise ratio, calibration errors, and partial Mie crosstalk contributed to unstable or biased extinction retrievals.

The perspectives and future work of this thesis begin by addressing the limitations of the SR-HSRL for achieving full aerosol optical property retrievals. Building on the SR-HSRL concept developed in this thesis, current efforts focus on developing ONERA's next-generation Colibri aerosol lidar (CAL): an ultra-short-range HSRL (CAL-HSR). The new configuration aims to implement the HSRL technique within the first hundred meters, enabling horizontal-to-vertical measurements. Inheriting the capabilities of elastic CALs (direct overlap function and radiometric constant measurement), this new implementation will avoid their disadvantages (lidar ratio assumption, dedicated forward inversion method). The experience gained from the design, calibration, and validation of the SR-HSRL prototype provided a solid foundation for this next step. The ultra-short-range implementation focuses on optimizing the design to achieve a more compact instrument, improving spatial resolution to the centimeter scale, optimizing the overlap geometry, and enhancing spectral discrimination using a narrower-linewidth laser source. The aim of the CAL-HSR is to enable the direct, accurate, assumption-free measurement of aerosol optical properties of ultrafine particles such as soot and other volatile particulate matter emitted by aeronautical engines, bridging the final gap between laboratory diagnostics and atmospheric lidar remote sensing.

The novel CAL-HSR has been designed and is currently in the test phase. It employs the Teem Photonics laser and an iodine vapor cell. A first laboratory proof-of-concept test was performed to determine whether it could suppress Mie signals at ultra-short ranges (<6 m). It used the laser v0 and the Thorlabs iodine cell. This first version is mounted in a 60 cm x 45 cm optical table, compact enough to be easily transported. Like the SR-HSRL prototype, this ultra-short-range implementation is in a bistatic, multi-axial configuration, with the full overlap range below 4 m. The transmitter subsystem consists of the laser v0, two mirrors to adjust the overlap function, and a lens to reduce the laser divergence. The receiver unit comprises a compact telescope, beam-collimation lenses, interference and neutral-density filters, and a 90:10 NPBS that transmits 10% of the signal to the channel's PMT. The other 90% of the received radiation is reflected towards the spectral filter subsystem. It is composed of Thorlabs' 10-cm-long, 19-mm-diameter iodine cell, an additional interference filter to suppress possible iodine fluorescence, a focusing lens, a neutral density filter, and a PMT.

To perform the first validation test, water droplets were produced using a commercial nebulizer at a range $r = 4.5$ m. The 30-second measurement aimed to verify Mie crosstalk in the HSR channel. The temporal evolution of the water droplets spray is displayed in Fig. 8.1. The spatial resolution is <56 cm, with a maximum measurement range determined by the laboratory's wall at 6 m. The temporal resolution is 4 ms. Regarding spectral performance, the water-droplet spray is negligible in the HSR channel; it is of the same order of magnitude

as the molecular signal below. There is no Mie crosstalk, as the transmission of water-droplet signals is the same order of magnitude (10^{-4}) as the cell characterization measurements presented in Section 5.4.1.

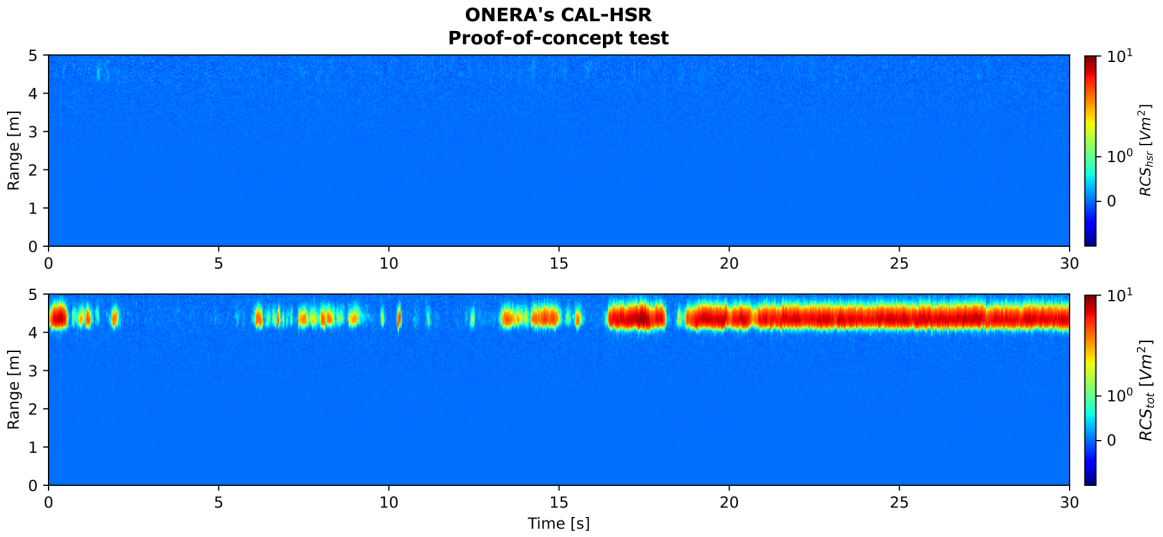

FIGURE 7.1: CAL-HSR proof-of-concept test to verify Mie suppression in the HSR channel. The top panel displays the HSR channel's RCS, indicating no water-droplet signals. The bottom panel shows the total channel's RCS, where the evolution of the water droplets spray is evident.

Further tests have been performed with the current version of the system. The aim is to validate the system's complete performance under field conditions. To this end, a measurement campaign was conducted at ONERA Toulouse, where an aerosol chamber has been developed to test CALs by producing different types of aerosols under controlled conditions. The second CAL-HSR prototype used Teem Photonics laser v1 and the 10-cm-long iodine cell. Some tests were performed with the designed 20-cm-long iodine cell; however, the laser divergence in the first meters was excessive, leading to geometric truncation within the cell. Thus, to avoid signal loss, the 10-cm-long was preferred. The test consisted of producing fog-oil aerosols inside the chamber, 30 to 35 meters away from the lidar. The measurements were performed on-line and off-line at the iodine absorption line to apply the proposed inversion method. The temporal evolution of the offline measurements is presented in the left panels of Fig. 8.2, while the standard (online) measurements are displayed on the right panels.

In general, the results show the high spatiotemporal resolution achieved with the system (<60 cm-scale spatial resolution, 4 ms temporal resolution). The offline measurements show that, outside the iodine absorption line, both channels detect the fog-oil plume between 27

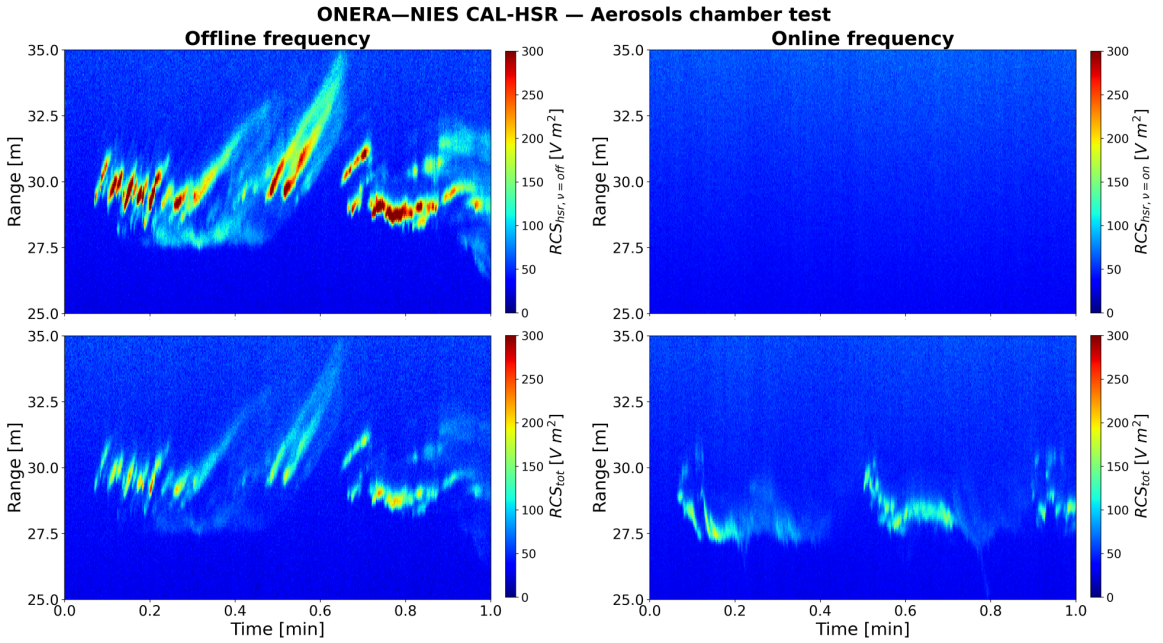

FIGURE 7.2: CAL-HSR validation test. The panels on the left represent the measurements at $\nu = \nu_{off}$, where the aerosol signals are passed through the iodine cell. The panels on the right show the standard measurements, where the HSR channel clearly shows that the aerosol signals were suppressed.

and 35 meters. It is also clear that the intensity is greater (about 10 times) in the HSR channel, which was expected since it receives 90% of the backscattered radiation. This confirms there is no beam truncation inside the cell. The online measurements show that the 10-cm-long iodine cell effectively suppresses all aerosol signals, as no fog-oil signals are detected when the laser wavelength matches the center of iodine's absorption line. The estimated Mie transmission is in the order of 10^{-3}. The mean RCS of the online measurement are presented in Fig. 8.3. The total channel, displayed in blue, shows the fog-oil plume detected between 25 and 30 m. In contrast, the HSR signal shows that the iodine cell effectively suppresses the Mie component, as the signal remains approximately constant in this zone.

The primary current limitation of the ultra-short-range CAL-HSR implementation is the inability to detect the molecular decay in the HSR channel. To address this problem, future work includes replacing the detectors with photo-counting sensors to improve sensitivity as well as increasing the telescope diameter and the laser pulse energy to augment the amount of collected signals. After improvements, a new field validation campaign will be performed at ONERA. Several calibrated aerosols –such as calibrated water droplets as well as latex and dust particles– will be measured, and the retrieved aerosol backscattering values will be compared to theoretical or simulated values. Moreover, the radiometric constant and the overlap function will be experimentally determined and compared to the method developed

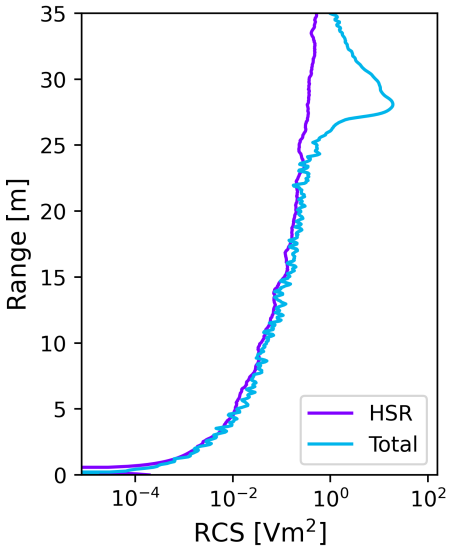

FIGURE 7.3: Mean range-corrected signals measured at the online frequency. It is clear that the Mie component is effectively suppressed in the HSR channel.

in this thesis for the SR-HSRL prototype. With improved calibration and instrumentation, it is expected to retrieve aerosol extinction coefficients and lidar ratios, thereby bridging CAL's current gap in the assumption-free, accurate characterization of ultrafine particles such as soot or volatile particulate matter.

In conclusion, this thesis marks an important step forward in the development of short-range high spectral resolution lidars, paving the way for a new generation of CALs capable of accurately characterizing aerosols and clouds in the lower atmosphere. By combining scientific rigor, technological innovation, and practical relevance, this research strengthens ONERA's remote-sensing capabilities and contributes more broadly to advancing the understanding of near-field atmospheric processes. The progress achieved provides a solid foundation for the future development of the CAL-HSR and for the expansion of increasingly precise and sustainable environmental and aeronautical applications.

Chapter 8

Conclusions et perspectives

8.1 Aperçu général

Au cours des dernières décennies, de nombreuses applications dans les domaines du climat, de la qualité de l'air et de l'aéronautique ont stimulé le développement de lidars à courte portée destinés à l'étude des particules d'aérosols à de faibles distances. Toutefois, ces instruments présentent des limitations intrinsèques en matière de précision, notamment pour la caractérisation des particules ultrafines. À l'inverse, les lidars à haute résolution spectrale (HSRL) permettent une restitution précise et sans hypothèse des propriétés des aérosols, mais les systèmes existants ont principalement été conçus pour des mesures à longue portée. Une analyse approfondie de la littérature a montré qu'aucun lidar HSRL pulsé n'avait encore été développé pour des études d'aérosols à courte portée. Dans ce contexte, cette thèse a proposé et démontré un prototype innovant de lidar HSRL à courte portée (SR-HSRL), fondé sur le principe du temps de vol, combinant les atouts des SR-EBL (zone aveugle réduite, haute résolution spatio-temporelle) et des HSRL (mesures calibrées, précises et sans hypothèses sur les propriétés radiatives des aérosols). Conçu spécifiquement pour la région de proche champ où les HSRL conventionnels ne peuvent pas opérer, le prototype développé permet la restitution calibrée des aérosols tout en surmontant les limitations du HSR-SLidar : résolution spatiale constante et acquisition continue, synchronisée et à haute cadence. Afin d'atteindre l'objectif principal de la thèse, trois objectifs spécifiques ont été définis.

- Le premier objectif portait sur la conception et l'estimation des performances de l'instrument à partir de simulations numériques. Deux filtres spectraux (cellules d'iode et interféromètres de Michelson à élargissement de champ et balayage, FWMIs) ont été sélectionnés à partir d'une revue complète de l'état de l'art. Un modèle numérique de bout en bout a ensuite été développé pour évaluer leurs performances selon différentes configurations et différentes largeurs de raie laser, permettant ainsi d'optimiser leur conception optique et spectrale.

- Le deuxième objectif concernait la caractérisation en laboratoire et la validation expérimentale des performances. Une méthodologie dédiée a été élaborée pour mesurer les propriétés temporelles et spectrales de lasers commerciaux, ce qui a permis d'en

identifier deux particulièrement adaptés au prototype SR-HSRL. Des essais en laboratoire ont ensuite été menés afin de valider les performances spectrales des deux filtres à l'aide des lasers sélectionnés. Sur la base de ces résultats, un premier prototype a été assemblé et ses performances spectrales ont été vérifiées dans des conditions contrôlées, avant d'être validées lors d'une campagne de mesures collaborative menée à l'Institut National d'Études Environnementales (NIES) à Tsukuba, au Japon.

- Enfin, le troisième objectif portait sur la restitution et l'analyse des profils de rétrodiffusion calibrés. Une méthodologie originale de calibration du recouvrement et de la réponse radiométrique a été développée. Une méthode d'inversion, basée sur le calcul du rapport de rétrodiffusion à partir des profils de rétrodiffusion atténuée, a ensuite été proposée et appliquée afin d'obtenir les coefficients de rétrodiffusion des aérosols sans recourir à des hypothèses. Les résultats ont démontré la capacité du prototype à réaliser des mesures précises et auto-étalonnées des aérosols et des nuages dans la région de proche champ, là où les systèmes HSRL conventionnels sont généralement aveugles.

Après avoir défini et atteint les objectifs de la thèse, le manuscrit a suivi une progression logique, allant des fondements théoriques à la validation expérimentale et à l'analyse des données. Chaque chapitre a contribué à un ou plusieurs des objectifs mentionnés ci-dessus, formant ainsi un ensemble cohérent menant de la conception du prototype SR-HSRL à sa validation expérimentale et aux premières restitutions des propriétés des aérosols de proche champ. Le contenu et les résultats de chaque chapitre sont brièvement résumés ci-dessous.

Une méthode d'inversion dédiée au SR-HSRL a été présentée dans le Chapitre 3. Après avoir rappelé les bases théoriques de l'absorption et de la diffusion – principes physiques sous-jacents à la technique lidar –, le principe de fonctionnement des HSRL a été décrit. Puis, dans la mesure où les mesures à courte portée nécessitent l'évaluation de la fonction de recouvrement du système, une méthode d'inversion spécifique au SR-HSRL a été proposée. Elle repose sur la calibration absolue du système par un paramètre d'intercalibration des canaux, dérivé de mesures hors ligne. À partir de ce paramètre, le signal total est corrigé. La diaphonie Mie est ensuite évaluée et supprimée du canal HSR, ce qui produit un signal purement moléculaire. Cela permet de déterminer les fonctions de recouvrement et les constantes radiométriques des deux canaux, à partir desquelles la rétrodiffusion atténuée est calculée. Le rapport de rétrodiffusion peut alors être estimé, ce qui permet de reconstituer le coefficient de rétrodiffusion des aérosols sans hypothèses.

Une analyse approfondie de l'état de l'art en matière de lidars à courte portée et de lidars à haute résolution spectrale a été menée dans le Chapitre 4. L'objectif était d'identifier

les éléments de nouveauté, les défis et les limitations technologiques potentielles associés au développement d'un SR-HSRL destiné à l'étude des aérosols. L'analyse des principes de fonctionnement, des stratégies de conception et des performances des deux catégories de lidars a fourni le cadre conceptuel et technologique pour la conception et la mise en œuvre du SR-HSRL présenté dans ce travail. La revue de la littérature a montré qu'aucun système lidar à haute résolution spectrale et à courte portée, fondé sur le principe du temps de vol, n'avait été rapporté à ce jour. Un seul HSRL à courte portée a été identifié : un lidar continu (CW) à proche infrarouge basé sur le principe de Scheimpflug. En tant que SLidar, il présente les avantages et les inconvénients propres à ce principe de fonctionnement. La revue bibliographique a donc mis en évidence que le développement d'un SR-HSRL pulsé représentait une contribution significative au domaine de la télédétection lidar. Le prototype proposé dans cette thèse comble ainsi le fossé existant dans la caractérisation précise et à haute résolution spatio-temporelle des aérosols à courte portée – la zone aveugle des lidars élastiques et à haute résolution spectrale de longue portée –.

La méthodologie de conception et de développement du prototype SR-HSRL a été décrite dans le Chapitre 5, posant les bases de sa mise en œuvre et garantissant que les unités émettrice et de filtrage spectral satisfassent aux exigences de performance nécessaires à un fonctionnement optimal. Le chapitre débute par la description de la caractérisation approfondie des sources laser commerciales personnalisées identifiées comme candidates au développement du SR-HSRL. Des simulations numériques ont ensuite été réalisées pour prédire la performance spectrale et les limitations de deux filtres spectraux candidats issus de la revue de la littérature — un interféromètre de Michelson à élargissement de champ et balayage et une cellule à vapeur d'iode. Ces simulations ont orienté l'optimisation des paramètres de conception afin de maximiser la discrimination spectrale pour différentes largeurs de raie laser. Puis, la validation expérimentale en laboratoire des performances spectrales des configurations laser–filtre a été présentée. Enfin, sur la base de ces résultats, les combinaisons laser/filtres les plus adaptées à différentes conditions opérationnelles ont été identifiées et discutées.

Enfin, les résultats de la campagne de terrain destinée à valider le concept SR-HSRL ont été présentés dans le Chapitre 6. S'appuyant sur la conception et la caractérisation des unités d'émission et de filtrage spectral, un prototype SR-HSRL pleinement opérationnel, intégrant le laser sélectionné et une cellule d'iode de 40 cm, a été développé en collaboration entre l'ONERA et le NIES (National Institute for Environmental Studies, Japon). Ses performances ont été évaluées dans des conditions atmosphériques réelles lors d'une campagne de validation menée à Tsukuba, au Japon, en juillet 2024. En appliquant la méthodologie de

calibration et d'inversion des signaux proposée, il a été possible de restituer des coefficients de rétrodiffusion calibrés des aérosols entre 50 et 1000 m, avec une résolution temporelle élevée (6 s) et une résolution spatiale acceptable (7,5 m, limitée par les détecteurs et le système d'acquisition). Il a été démontré que le prototype SR-HSRL permettait la restitution précise de données au sein et au-dessus de couches nuageuses optiquement denses, à condition que le faisceau laser ne soit pas totalement atténué. Les avantages et les limites du prototype SR-HSRL pulsé ont été comparés à ceux du HSR-SLidar décrit dans la littérature.

8.2 Synthèse des principaux résultats

La faisabilité de l'application de la technique lidar à haute résolution spectrale à des mesures à courte portée a été démontrée à travers le développement et l'évaluation d'un prototype compact de SR-HSRL intégrant une cellule d'absorption à l'iode et un laser à diode amplifié, non conventionnel, à haute fréquence de répétition, présentant une largeur de raie de 300 MHz et une durée d'impulsion de 4,96 ns. Le développement de cet instrument a représenté un défi scientifique et technique majeur. L'un des principaux enjeux technologiques consistait à identifier une source laser commerciale à la fois spectralement fine et stable, avec une durée d'impulsion de l'ordre de la nanoseconde, afin de permettre des mesures à courte portée et à haute résolution spectrale, avec une grande précision spatio-temporelle. Cela a nécessité l'élaboration d'une méthodologie complète de caractérisation des lasers commerciaux, les fabricants ne fournissant généralement pas de spécifications spectrales détaillées. De plus, le laser devait être économique, compact, accordable en longueur d'onde et fonctionner à haute cadence — des caractéristiques souvent opposées à celles des lasers habituellement utilisés dans les HSRL longue portée, à l'exception du système à laser à diode développé par Hayman et Spuler [93], qui demeure toutefois un lidar de longue portée avec une résolution de 150 m. Le prototype développé a été validé lors d'une campagne de terrain de démonstration, confirmant sa faisabilité opérationnelle.

D'un point de vue analytique, grâce à sa configuration optimisée avec une zone aveugle réduite (50 m jusqu'au recouvrement complet à 550 m) et une haute résolution spatiale, le prototype SR-HSRL développé s'est révélé adapté à la caractérisation des aérosols dans les basses couches de l'atmosphère. Les profils obtenus ont mis en évidence plusieurs couches d'aérosols entre 50 et 1000 m, avec des coefficients de rétrodiffusion des aérosols variant de valeurs proches de la diffusion moléculaire (10^{-6} $m^{-1}sr^{-1}$) à des valeurs caractéristiques des nuages (10^{-3} m^{-1}), cohérentes avec celles typiquement observées dans la couche limite planétaire (PBL). Un autre avantage de ce système réside dans sa méthode de restitution, qui produit des signaux calibrés radiométriquement et en recouvrement, physiquement

cohérents (profils de rétrodiffusion atténuée) pour les deux canaux de détection. Cela permet d'effectuer des mesures à l'intérieur et au-dessus des nuages, tant que le faisceau laser n'est pas complètement atténué. L'analyse d'incertitude, fondée sur des simulations Monte Carlo, a estimé une incertitude totale de 7,2 % sur le coefficient de rétrodiffusion des aérosols $\beta_{aer}(r)$, confirmant la fiabilité de la méthode d'inversion développée pour le SR-HSRL. Cette capacité rend l'instrument particulièrement pertinent pour l'étude de la formation des nuages et des interactions aérosols–nuages, notamment dans le cas des cirrus induits par les traînées de condensation.

Sur le plan instrumental, le prototype est à la fois compact et économique. Contrairement aux HSRL longue portée conventionnels, fondés sur des lasers Nd:YAG à commutation Q, à forte énergie et faible fréquence de répétition, le système développé dans cette thèse utilise un laser à fibre amplifiée émettant à 532 nm, avec des impulsions de faible énergie ($\sim$1–11 µJ) et une cadence élevée (50–65 kHz). La réalisation de mesures HSRL à courte portée et à haute résolution spatiale a nécessité un compromis entre la durée d'impulsion (4,96 ns), la largeur de raie (300 MHz) et la distance de recouvrement (50–1000 m), cette dernière étant définie par l'alignement opto-mécanique du récepteur. Alors que les HSRL longue portée privilégient généralement des largeurs de raie très étroites afin de maximiser la discrimination spectrale — allant du laser à 38 MHz du HSRL-2 de la NASA [49] au laser de moins de 150 MHz du DLR [110] —, ce travail a démontré qu'une séparation spectrale précise reste réalisable avec des largeurs de raie plus larges, à condition d'une optimisation rigoureuse du système. Un rapport de discrimination spectrale d'environ 300 a été obtenu, suffisant pour résoudre plusieurs couches d'aérosols tout en maintenant une résolution spatiale (7,5 m) et temporelle (6 s) élevées.

Comparé au seul autre HSRL à courte portée décrit dans la littérature — le HSR-SLidar développé par Chang et al. [27] —, le SR-HSRL pulsé présenté dans cette thèse est plus complexe sur le plan instrumental, mais offre plusieurs avantages déterminants. Les deux systèmes atteignent des hauteurs de zone aveugle comparables (30 m pour le HSR-SLidar et 50 m pour le SR-HSRL), mais le prototype développé surmonte les principales limites des lidars basés sur le principe de Scheimpflug. Premièrement, la résolution spatiale du SR-HSRL est constante en fonction de la distance, alors que celle du HSR-SLidar dépend de la géométrie d'imagerie et varie avec la portée. Deuxièmement, en tant que système fondé sur le principe du temps de vol, le SR-HSRL ne nécessite ni la calibration de distance ni la reconstruction géométrique, ce qui simplifie le traitement des données et réduit les erreurs systématiques. Troisièmement, le SR-HSRL permet l'acquisition continue et synchronisée des signaux de rétrodiffusion moléculaire et totale sans commutation de longueur d'onde,

évitant ainsi les discontinuités temporelles et garantissant une résolution temporelle constante de 6 s. Son fonctionnement à 532 nm facilite en outre la comparaison directe avec les lidars atmosphériques standards. Bien que le HSR-SLidar atteigne un rapport de discrimination spectrale plus élevé grâce à la raie d'absorption étroite du rubidium, le SR-HSRL permet des mesures directes et simultanées, avec une plus grande flexibilité quant au choix de la longueur d'onde et au remplacement modulaire des filtres. Globalement, le SR-HSRL complète et étend les capacités du HSR-SLidar, offrant une plateforme plus polyvalente et adaptable pour la caractérisation des aérosols à proximité de leur source et pour de potentielles applications aéroportées.

Les lidars à rétrodiffusion élastique à courte portée ont déjà démontré leur efficacité pour la détection de particules proches de leur source avec une très haute résolution spatio-temporelle [19–22, 26, 71]. Ces systèmes ont ouvert de nouvelles perspectives diagnostiques pour les études aéronautiques et environnementales, notamment pour la surveillance des émissions des moteurs d'avions et la caractérisation de l'atmosphère dans la basse couche limite planétaire, où les lidars longue portée sont aveugles. Cependant, la nature intrinsèquement mal posée du problème d'inversion des EBL limite la précision des SR-EBL. Dans les mesures à ultra-courte portée, l'absence de zone de référence moléculaire complique le processus d'inversion, nécessitant des calibrations supplémentaires et des modèles directs dédiés [22]. Par conséquent, la quantification des particules ultrafines, telles que la suie fraîchement émise, demeure particulièrement difficile pour les EBL. Le SR-HSRL développé dans cette thèse comble cette lacune en permettant la caractérisation précise des aérosols, des plus grossiers aux plus ultrafins, sur de courtes distances, sans recourir à des hypothèses sur le rapport lidar. Comme le problème HSRL est bien posé, la méthode proposée permet de reconstituer directement et sans hypothèses les propriétés optiques des aérosols. Grâce à sa précision accrue, le SR-HSRL combine la capacité de proximité des EBL avec la rigueur et l'exactitude des techniques HSRL, ouvrant ainsi la voie à une nouvelle génération de lidars compacts et performants dédiés à la recherche sur les aérosols de la basse atmosphère.

8.3 Contributions scientifiques et techniques

8.3.1 Contributions générales

La principale contribution de ce travail a consisté à étendre la technique HSRL à des mesures à courte portée, permettant ainsi la restitution des propriétés des aérosols sans hypothèses, dans des régions où les HSRL conventionnels ne peuvent pas opérer. Ce résultat majeur repose sur plusieurs avancées complémentaires. Tout d'abord, une méthodologie complète de caractérisation laser et d'optimisation des filtres spectraux a été développée, établissant un

cadre systématique pour la conception de lidars à haute résolution spectrale à courte portée. Ensuite, une approche de calibration originale a été proposée, intégrant dans un cadre unifié la calibration intercanaux, la correction de la diaphonie Mie, la restitution de la fonction de recouvrement et la calibration radiométrique. Par ailleurs, la mise en œuvre sur le terrain a démontré la capacité du système à produire des profils stables et temporellement résolus du coefficient de rétrodiffusion des aérosols dans des conditions atmosphériques réelles. Enfin, une analyse de sensibilité de type Monte Carlo a permis de quantifier l'impact des incertitudes spectrales et atmosphériques sur la précision des restitutions, mettant en évidence la robustesse de la méthode et identifiant les paramètres clés pour de futures optimisations. En résumé, ce travail démontre la faisabilité de mesures lidar à haute résolution spectrale à courte portée tout en maintenant une haute résolution spatio-temporelle et un niveau d'incertitude acceptable (7,2 %). Le SR-HSRL développé dans le cadre de cette thèse constitue ainsi une avancée significative vers des systèmes lidar compacts, précis et sans hypothèses, dédiés à l'étude des aérosols et des nuages à courte portée.

8.3.2 Contribution à la compétence méthodologique de l'ONERA en lidar d'aérosols à courte portée

Comme mentionné précédemment, les Colibri Aerosol Lidars (CALs) développés à l'ONERA se sont révélés des outils innovants et performants pour la mesure des particules à proximité de leur source, avec une très haute résolution spatio-temporelle [21, 22, 25, 26]. Ils ont introduit de nouvelles capacités diagnostiques pour de nombreuses applications aéronautiques et environnementales, telles que la mesure de la pollution émise par les moteurs d'avion et la caractérisation de l'atmosphère dans la basse couche limite planétaire, là où les lidars atmosphériques à longue portée sont aveugles. Cependant, la nature intrinsèquement mal posée du problème EBL limite la précision de ces instruments. De plus, l'inversion des signaux nécessite des calibrations géométriques et radiométriques, ainsi qu'une méthode d'inversion directe spécifique, ne requérant ni conditions aux limites ni une zone de référence.

La mesure des particules ultrafines, telles que la suie fraîchement émise, demeure un défi majeur pour les lidars élastiques Colibri. Ces limitations ont motivé le développement de la nouvelle génération des lidars d'aérosols Colibri de l'ONERA : le prototype SR-HSRL élaboré dans le cadre de cette thèse. Cet instrument innovant offre une précision accrue, le problème HSRL étant bien posé et pouvant être résolu sans hypothèses. Cela permet une inversion plus directe et plus rigoureuse des propriétés radiométriques et microphysiques des particules. Grâce à cette amélioration de la précision, le SR-HSRL pourra mesurer des particules plus petites, telles que la suie et les particules volatiles, tout en conservant les capacités à courte portée propres aux instruments Colibri. Cet aspect revêt une importance

particulière pour l'industrie aéronautique, car l'évolution des normes réglementaires incite le secteur à réduire les émissions de particules volatiles et non volatiles émises par les moteurs d'avion. Les efforts engagés pour développer des moteurs à faibles émissions reposent sur des avancées technologiques en conception, sur l'utilisation de carburants à faible teneur en soufre et sur l'amélioration de l'efficacité de la combustion [25]. Comme la suie est principalement produite lors de combustions riches en carburant, des efforts considérables ont été consacrés au développement de moteurs à combustion pauvre (*lean-burn*), qui promettent une réduction des émissions de suie et de particules volatiles grâce à des températures plus basses et à l'absence de zones riches en carburant [132]. Ainsi, le développement d'un lidar Colibri à haute résolution spectrale ouvrira la voie à des procédures de certification pour les nouveaux moteurs à combustion pauvre, en permettant une évaluation plus précise des faibles concentrations de suie et de particules non volatiles.

8.4 Perspectives

Le SR-HSRL développé dans le cadre de cette thèse représente une avancée technologique majeure pour la télédétection lidar, en permettant la restitution calibrée et sans hypothèses des coefficients de rétrodiffusion des aérosols et des nuages dans la zone aveugle des systèmes HSRL conventionnels. Cependant, plusieurs limitations instrumentales et méthodologiques ont restreint son plein potentiel, notamment en empêchant la restitution des coefficients d'extinction des aérosols. Ces limitations, identifiées tant lors de la caractérisation du prototype que lors des mesures de terrain, ont permis de mettre en évidence les axes d'amélioration à envisager pour les futurs développements. D'un point de vue instrumental, les principales contraintes concernent la largeur de raie du laser, qui limite la capacité de discrimination spectrale de la cellule d'iode, ainsi que de légères dérives de longueur d'onde observées en fonctionnement. D'un point de vue méthodologique, des incertitudes résiduelles dans la détermination de la fonction de recouvrement, un faible rapport signal/bruit, des erreurs de calibration et une diaphonie Mie partielle ont contribué à des restitutions d'extinction instables ou biaisées.

Les perspectives et les travaux futurs de cette thèse débutent par la prise en compte de ces limitations, dans le but d'atteindre une restitution complète des propriétés optiques des aérosols. En s'appuyant sur le concept de SR-HSRL développé ici, les efforts actuels portent sur la conception de la nouvelle génération des lidars d'aérosols Colibri de l'ONERA : un lidar à haute résolution spectrale et à ultra-courte portée, dénommé CAL-HSR. Cette nouvelle configuration vise à mettre en œuvre la technique HSRL dans les tout premiers centaines de mètres, permettant des mesures tant horizontales que verticales. En héritant des capacités des lidars élastiques Colibri – notamment la mesure directe de la fonction de

recouvrement et de la constante radiométrique –, cette nouvelle approche éliminera leurs principaux inconvénients, tels que la nécessité de supposer un rapport lidar ou de recourir à une méthode d'inversion directe spécifique. L'expérience acquise lors de la conception, de la calibration et de la validation du prototype SR-HSRL constitue une base solide pour cette évolution. L'implémentation à ultra-courte portée vise à optimiser le design de l'instrument afin d'obtenir un système plus compact, une résolution spatiale améliorée à l'échelle centimétrique, une géométrie de recouvrement optimisée et une discrimination spectrale renforcée grâce à une source laser à largeur de raie plus étroite. L'objectif du CAL-HSR est de permettre la mesure directe, précise et sans hypothèses des propriétés optiques des particules ultrafines — telles que la suie et les particules volatiles issues des moteurs aéronautiques —, comblant ainsi le dernier fossé entre les diagnostics de laboratoire et la télédétection lidar atmosphérique.

Le nouveau CAL-HSR a été conçu et est actuellement en phase de test. Il utilise un laser Teem Photonics associé à une cellule à vapeur d'iode. Un premier essai de validation en laboratoire a été réalisé afin de vérifier la suppression du signal Mie à des distances ultra-courtes (<6 m). Ce test a été mené avec le laser v0 et la cellule d'iode Thorlabs. Cette première version est montée sur une table optique de 60 cm $\times$ 45 cm, suffisamment compacte pour être facilement transportée. Comme pour le prototype SR-HSRL, cette version à ultra-courte portée adopte une configuration bistatique et multi-axiale, avec une portée de recouvrement complète inférieure à 4 m. Le sous-système émetteur comprend le laser v0, deux miroirs pour ajuster la fonction de recouvrement et une lentille pour réduire la divergence du faisceau laser. L'unité de réception est constituée d'un télescope compact, de lentilles de collimation, de filtres interférentiels et neutres, ainsi que d'un séparateur de faisceau non polarisant (NPBS) 90:10 transmettant 10 % du signal vers le PMT du canal. Les 90 % restants du rayonnement reçu sont réfléchis vers le sous-système de filtrage spectral, composé d'une cellule d'iode Thorlabs de 10 cm de long et 19 mm de diamètre, d'un filtre interférentiel supplémentaire pour supprimer toute fluorescence éventuelle de l'iode, d'une lentille de focalisation, d'un filtre neutre et d'un PMT.

Pour la première validation expérimentale, des gouttelettes d'eau ont été générées à l'aide d'un nébuliseur commercial à une distance de $r = 4.5$ m. La mesure, d'une durée de 30 s, visait à vérifier la présence éventuelle de diaphonie Mie dans le canal HSR. L'évolution temporelle du jet de gouttelettes d'eau est illustrée à la Figure 8.1. La résolution spatiale est inférieure à 56 cm, la portée maximale étant limitée à 6 m par le mur du laboratoire. La résolution temporelle est de 4 ms. En ce qui concerne les performances spectrales, le signal

des gouttelettes d'eau est négligeable dans le canal HSR : il est d'un ordre de grandeur comparable à celui du signal moléculaire sous-jacent. Aucune diaphonie Mie n'a été observée, la transmission des signaux de gouttelettes étant du même ordre de grandeur (10^{-4}) que celle mesurée lors de la caractérisation de la cellule d'iode (Section 5.4.1).

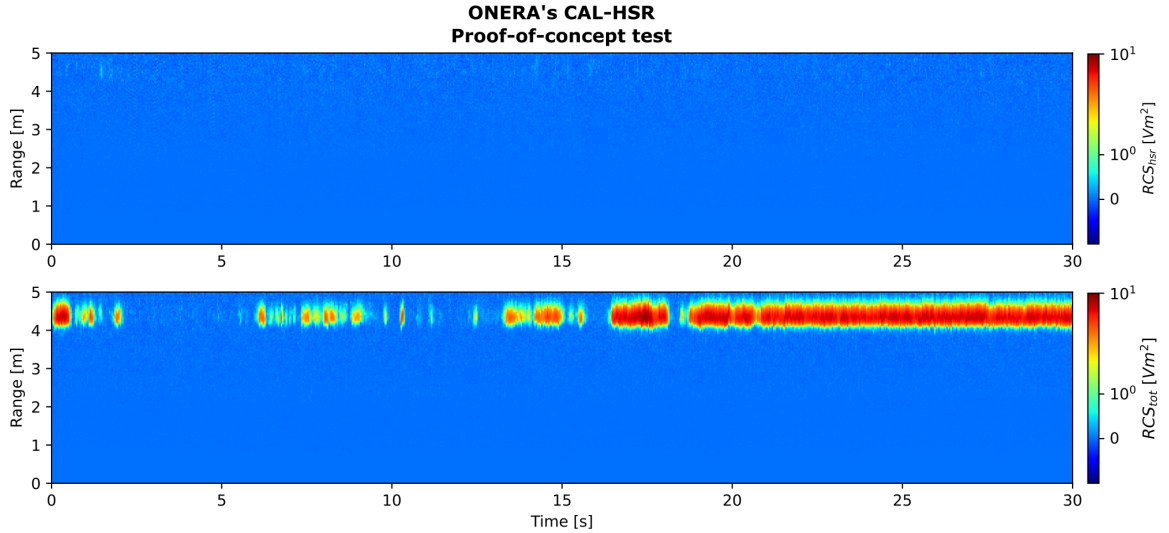

FIGURE 8.1: Essai de validation du CAL-HSR visant à vérifier la suppression du signal Mie dans le canal HSR. Le panneau supérieur indique le RCS du canal HSR, qui ne présente aucun signal de gouttelettes d'eau. Le panneau inférieur illustre le RCS du canal total, où l'évolution du jet de gouttelettes est clairement visible.

Des essais complémentaires ont été réalisés avec la version actuelle du système afin de valider ses performances en conditions réelles. À cette fin, une campagne de mesures a été menée à l'ONERA Toulouse, où une chambre à aérosols a été développée pour tester les CAL en produisant différents types d'aérosols dans des conditions contrôlées. La seconde version du CAL-HSR utilisait le laser Teem Photonics v1 et la cellule d'iode de 10 cm de long. Certains essais ont été effectués avec la cellule d'iode de 20 cm, mais la divergence du laser dans les premiers mètres s'est révélée trop importante, entraînant une troncature géométrique à l'intérieur de la cellule. Pour éviter toute perte de signal, la cellule de 10 cm a donc été privilégiée. Le test consistait à produire des aérosols d'huile de brouillard (*fog-oil*) dans la chambre, à une distance comprise entre 30 et 35 m du lidar. Les mesures ont été effectuées en ligne et hors ligne à la raie d'absorption de l'iode, afin d'appliquer la méthode d'inversion proposée. L'évolution temporelle des mesures hors ligne est présentée dans les panneaux de gauche de la Figure 8.2, tandis que les mesures standard (en ligne) sont illustrées dans les panneaux de droite.

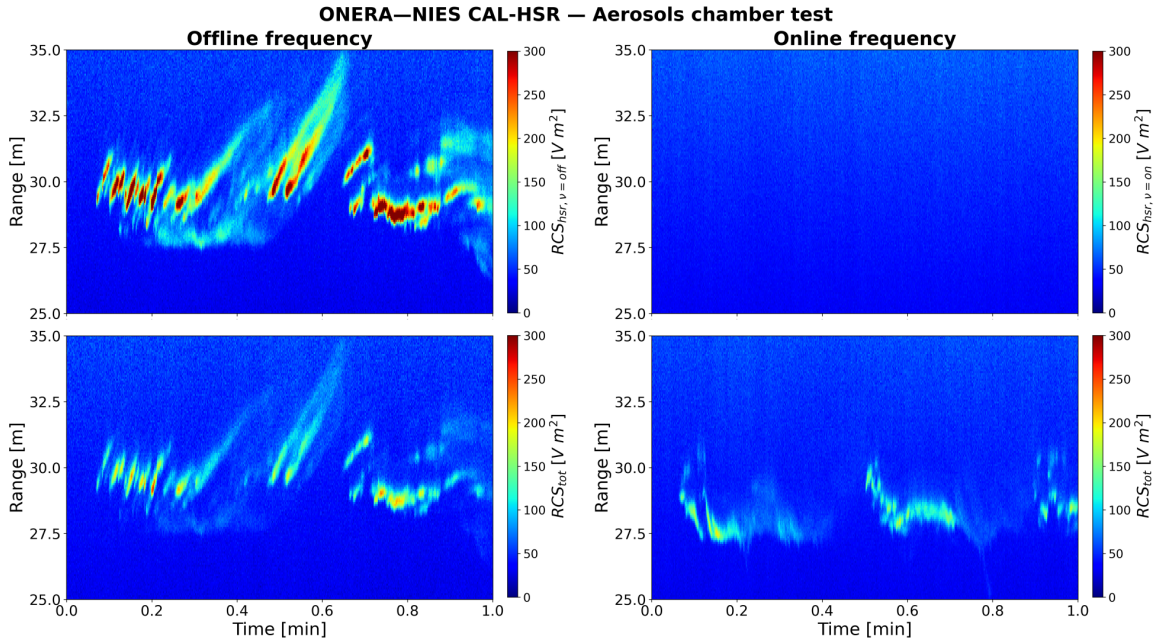

FIGURE 8.2: Essai de validation du CAL-HSR. Les panneaux de gauche représentent les mesures à $\nu = \nu_{off}$, où les signaux d'aérosols traversent la cellule d'iode. Les panneaux de droite montrent les mesures standard, où le canal HSR révèle clairement la suppression des signaux d'aérosols.

De manière générale, les résultats obtenus démontrent la haute résolution spatio-temporelle du système (résolution spatiale <60 cm et temporelle de 4 ms). Les mesures hors ligne montrent qu'en dehors de la raie d'absorption de l'iode, les deux canaux détectent le panache d'huile de brouillard entre 27 et 35 m. On observe également que l'intensité est environ dix fois plus élevée dans le canal HSR, ce qui était attendu puisqu'il reçoit 90 % du rayonnement rétrodiffusé. Cela confirme l'absence de troncature du faisceau au sein de la cellule. Les mesures en ligne montrent que la cellule d'iode de 10 cm supprime efficacement tous les signaux d'aérosols, aucun signal d'huile de brouillard n'étant détecté lorsque la longueur d'onde du laser correspond au centre de la raie d'absorption de l'iode. La transmission Mie estimée est de l'ordre de 10^{-3}. La Figure 8.3 présente les signaux moyens corrigés de la portée pour la mesure en ligne : le canal total (en bleu) montre le panache d'huile de brouillard détecté entre 25 et 30 m, tandis que le canal HSR indique que la cellule d'iode supprime efficacement la composante Mie, le signal restant quasi constant dans cette zone.

La principale limitation actuelle du CAL-HSR à ultra-courte portée réside dans l'impossibilité de détecter la décroissance moléculaire au sein du canal HSR. Pour surmonter cette contrainte, les travaux futurs incluront le remplacement des détecteurs par des capteurs à comptage de photons afin d'améliorer la sensibilité, ainsi que l'augmentation du diamètre

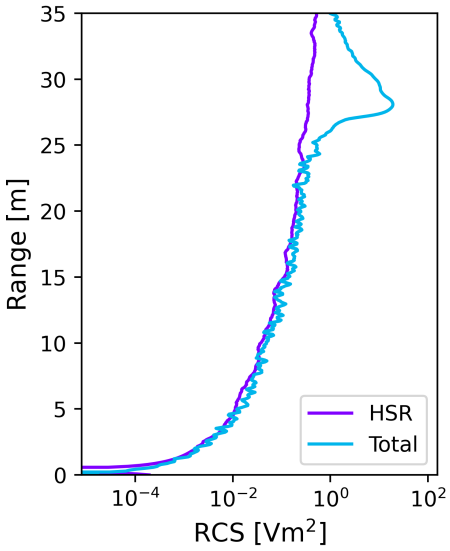

FIGURE 8.3: Signaux moyens corrigés de la portée mesurés à la fréquence en ligne. La suppression de la composante Mie dans le canal HSR est clairement visible.

du télescope et de l'énergie des impulsions laser afin d'accroître la quantité de signal collectée. Après ces améliorations, une nouvelle campagne de validation sur le terrain sera menée à l'ONERA. Plusieurs types d'aérosols calibrés — tels que des gouttelettes d'eau ou des particules de latex — seront mesurés, et les coefficients de rétrodiffusion obtenus seront comparés aux valeurs théoriques ou simulées. Par ailleurs, la constante radiométrique et la fonction de recouvrement seront déterminées expérimentalement et comparées à la méthode développée dans cette thèse pour le prototype SR-HSRL. Grâce à une meilleure calibration et à une instrumentation optimisée, il sera alors possible de restituer les coefficients d'extinction et les rapports lidar, comblant ainsi la lacune actuelle des CAL dans la caractérisation précise et sans hypothèses des particules ultrafines telles que la suie ou les particules volatiles.

En conclusion, les travaux présentés dans cette thèse ont permis de franchir une étape importante dans le développement de lidars à haute résolution spectrale à courte portée, ouvrant la voie à une nouvelle génération d'instruments CAL capables de caractériser avec précision les aérosols et les nuages dans la basse atmosphère. En conciliant rigueur scientifique, innovation technologique et pertinence applicative, ce travail contribue au renforcement des capacités de télédétection de l'ONERA et, plus largement, à une meilleure compréhension des processus atmosphériques de proximité. Les avancées obtenues constituent un socle solide pour les développements futurs du lidar CAL-HSR et pour l'essor d'applications environnementales et aéronautiques toujours plus précises et durables.

Bibliography

[1] J. M. Wallace and P. V. Hobbs. *Atmospheric Science: An Introductory Survey*. 2nd ed. Elsevier, 2006.

[2] O. Boucher. *Atmospheric Aerosols: Properties and Climate Impacts*. New York: Springer, 2015.

[3] CRANA. Fundación Centro de Recursos Ambientales de Navarra. *Aerosoles o materia particulada (MPA)*. https://goo.gl/qrCdBw.

[4] J. L. Guerrero-Rascado. "Técnica LIDAR para la caracterización atmosférica mediante dispersión elástica y Raman". PhD thesis. Universidad de Granada, 2008.

[5] G. Myhre et al. "Aerosols and their Relation to Global Climate and Climate Sensitivity". In: *Nature Education Knowledge* 4.5 (2013), p. 7.

[6] M.O. Andreae and D. Rosenfeld. "Aerosol–cloud–precipitation interactions. Part 1. The nature and sources of cloud-active aerosols". In: *Earth-Science Reviews* 89.1 (2008), pp. 13–41.

[7] D. S. Lee et al. "The contribution of global aviation to anthropogenic climate forcing for 2000 to 2018". In: *Atmospheric Environment* 244 (2021), p. 117834. DOI: 10.1016/j.atmosenv.2020.117834.

[8] Qin M. Fang W. Liao Z. Gui H. Shi Z. Yang H. Meng F. Shao D. Hu J. Han B. Xie P. Duan J. and W. Liu. "Detection of Aircraft Emissions Using Long-Path Differential Optical Absorption Spectroscopy at Hefei Xinqiao International Airport". In: *Remote Sensing* 14.16 (2022). DOI: 10.3390/rs14163927.

[9] M Klower et al. "Quantifying aviation's contribution to global warming". In: *Environmental Research Letters* 16.10 (2021), p. 104027. DOI: 10.1088/1748-9326/ac286e.

[10] F. Yu, B. Karcher, and B. E. Anderson. "Revisiting Contrail Ice Formation: Impact of Primary Soot Particle Sizes and Contribution of Volatile Particles". In: *Environmental Science & Technology* 58.40 (2024), pp. 17650–17660. DOI: 10.1021/acs.est.4c04340.

[11] J. A. Bravo-Aranda. "Lidar depolarization technique: Assessment of the hardware polarizing sensitivity and applications". PhD thesis. Universidad de Granada, 2014.

[12] M. Haarig et al. “First triple-wavelength lidar observations of depolarization and extinction-to-backscatter ratios of Saharan dust”. In: *Atmospheric Chemistry and Physics* 22.1 (2022), pp. 355–369. DOI: 10.5194/acp-22-355-2022.

[13] Siqi Qi et al. “Classification of atmospheric aerosols and clouds by use of dual-polarization lidar measurements”. In: *Optics Express* 29.15 (2021), pp. 23461–23476. DOI: 10.1364/OE.430456.

[14] Andres Bedoya-Velásquez et al. “Estimation of the Mass Concentration of Volcanic Ash Using Ceilometers: Study of Fresh and Transported Plumes from La Palma Volcano”. In: *Remote Sensing* 14 (Nov. 2022), p. 5680. DOI: 10.3390/rs14225680.

[15] R. Ceolato and M. J. Berg. “Aerosol light extinction and backscattering: A review with a lidar perspective”. In: *Journal of Quantitative Spectroscopy and Radiative Transfer* 262 (2021), p. 107492. DOI: 10.1016/j.jqsrt.2020.107492.

[16] E. E. Eloranta. *High Spectral Resolution Lidar. In: Lidar*. Edited by: Weitkamp, C. New York: Springer, 2005, 143–163.

[17] J. W. Hair et al. “High-spectral-resolution lidar with iodine-vapor filters: measurement of atmospheric-state and aerosol profiles”. In: *Applied Optics* 40 (30 2001), pp. 5280–5294. DOI: 10.1364/AO.40.005280.

[18] Y. Jin et al. “Development of a 355-nm high-spectral-resolution lidar using a scanning Michelson interferometer for aerosol profile measurement”. In: *Optics Express* 28 (16 2020), pp. 23209–23222. DOI: 10.1364/oe.390987.

[19] C. Chen et al. “Observations of Atmospheric Aerosol and Cloud Using a Polarized Micropulse Lidar in Xi’an, China”. In: *Atmosphere* 12.6 (2021). DOI: 10.3390/atmos12060796.

[20] P. M. Ong et al. “Surface Aerosol Properties Studied Using a Near-Horizontal Lidar”. In: *Atmosphere* 11.1 (2020). DOI: 10.3390/atmos11010036.

[21] R. Ceolato, A.E. Bedoya-Velásquez, and V. Mouysset. “Short-Range Elastic Backscatter Micro-Lidar for Quantitative Aerosol Profiling with High Range and Temporal Resolution”. In: *Remote Sensing* 12.20 (2020). DOI: 10.3390/rs12203286.

[22] R. Ceolato et al. “Black carbon aerosol number and mass concentration measurements by picosecond short-range elastic backscatter lidar”. In: *Scientific Reports* 12 (2022), p. 8443. DOI: 10.1038/s41598-022-11954-7.

[23] M. Queißer, M. Harris, and S. Knoop. “Atmospheric visibility inferred from continuous-wave Doppler wind lidar”. In: *Atmospheric Measurement Techniques* 15.18 (2022), pp. 5527–5544. DOI: 10.5194/amt-15-5527-2022.

[24] Tianwen Wei et al. "Retrieving aerosol backscatter coefficient using coherent Doppler wind lidar". In: *Optics Express* 33.4 (2025), pp. 6832–6849. DOI: 10.1364/OE.551730.

[25] R. Ceolato et al. "Non-Invasive Assessment of Aircraft Engine Particulate Matter Emissions with Lidar". In: *EGUsphere* 2025 (2025), pp. 1–19. DOI: 10.5194/egusphere-2025-2612.

[26] Andres Esteban Bedoya-Velásquez et al. "Synergy between Short-Range Lidar and In Situ Instruments for Determining the Atmospheric Boundary Layer Lidar Ratio". In: *Remote Sensing* 16.9 (2024), p. 1583. DOI: 10.3390/rs16091583.

[27] Y. Chang et al. "High Spectral Resolution Scheimpflug Lidar for Atmospheric Aerosol Sensing". In: *Laser & Photonics Reviews* (2025), e00897. DOI: 10.1002/lpor.202500897.

[28] Manuela Hoyos-Restrepo et al. "Short-Range High Spectral Resolution Lidar for Aerosol Sensing Using a Compact High-Repetition-Rate Fiber Laser". In: *Remote Sensing* 17.17 (2025). DOI: 10.3390/rs17173084.

[29] Gulev, S.K., P.W. Thorne, J. Ahn, F.J. Dentener, C.M. Domingues, S. Gerland, D. Gong, D.S. Kaufman, H.C. Nnamchi, J. Quaas, J.A. Rivera, S. Sathyendranath, S.L. Smith, B. Trewin, K. von Schuckmann, and R.S. Vose, 2021: Changing State of the Climate System. In Climate Change 2021: The Physical Science Basis. Contribution of Working Group I to the Sixth Assessment Report of the Intergovernmental Panel on Climate Change [Masson-Delmotte, V., P. Zhai, A. Pirani, S.L. Connors, C. Péan, S. Berger, N. Caud, Y. Chen, L. Goldfarb, M.I. Gomis, M. Huang, K. Leitzell, E. Lonnoy, J.B.R. Matthews, T.K. Maycock, T. Waterfield, O. Yelekçi, R. Yu, and B. Zhou (eds.)].Cambridge University Press. In Press. https://www.ipcc.ch/report/ar6/wg1/downloads/report/IPCC_AR6_WGI_Full_Report.pdf.

[30] Forster, P., T. Storelvmo, K. Armour, W. Collins, J.-L. Dufresne, D. Frame, D.J. Lunt, T. Mauritsen, M.D. Palmer, M. Watanabe, M. Wild, and H. Zhang: 2021, The Earth's Energy Budget, Climate Feedbacks, and Climate Sensitivity. In Climate Change 2021: The Physical Science Basis. Contribution of Working Group I to the Sixth Assessment Report of the Intergovernmental Panel on Climate Change [Masson-Delmotte, V., P. Zhai, A. Pirani, S.L. Connors, C. Péan, S. Berger, N. Caud, Y. Chen, L. Goldfarb, M.I. Gomis, M. Huang, K. Leitzell, E. Lonnoy, J.B.R. Matthews, T.K. Maycock, T. Waterfield, O. Yelekçi, R. Yu, and B. Zhou (eds.)]. Cambridge University Press. In Press. https://www.ipcc.ch/report/ar6/wg1/downloads/report/IPCC_AR6_WGI_Full_Report.pdf.

[31] Air Quality Expert Group (AQEG). *Particulate Matter in the United Kingdom. Chaper 2: What is particulate matter?* Defra, London, 2005.

[32] J. Davies. *Aerosol in the Atmosphere*. https://allaboutaerosol.com/aerosol-in-the-atmosphere/.

[33] C. E. Junge. "The size distribution and aging of natural aerosols as determined from electrical and optical data on the atmosphere". In: *Journal of Meteorology* 12.1 (1955), pp. 13–25. DOI: 10.1175/1520-0469(1955)012<0013:TSDAAO>2.0.CO;2.

[34] J. H. Seinfeld and S. N. Pandis. *Atmospheric Chemistry and Physics*. Hoboken, New Jersey: John Wiley & Sons, Inc., 2006.

[35] A.A. Kokhanovsky. *Light Absorption and Scattering by Particles in the Atmosphere*. Springer–Praxis, Berlin, 2008.

[36] C. F. Bohren and D. R. Huffman. *Absorption and Scattering of Light by Small Particles*. Wiley-VCH, 1983.

[37] H. Horvath. "Atmospheric light absorption – A review". In: *Atmos. Environ.* 27 (1993), 293–317.

[38] O. Dubovik, B.N. Holben, and T.F. et al. Eck. "Variability of absorption and optical properties of key aerosol types observed in worldwide locations". In: *Journal of Atmospheric Sciences* 59 (2002), 590–608.

[39] K.S. Shifrin. *Light Scattering in a Turbid Medium*. Gostekhteoriz Dat, Moscow, 1951.

[40] Rudolf Penndorf. "Angular Mie Scattering∗". In: *Journal of the Optical Society of America* 52.4 (1962), pp. 402–408. DOI: 10.1364/JOSA.52.000402.

[41] A. J. Cox, A. J. DeWeerd, and J. Linden. "An experiment to measure Mie and Rayleigh total scattering cross sections". In: *Amer. J. Phys.* 70.6 (2002), 620–625.

[42] R. Thalman et al. "Rayleigh scattering cross-section measurements of nitrogen, argon, oxygen and air". In: *J. Quant. Spec. Rad. Tran.* 147 (2014), 171–177.

[43] G. Mie. "Beiträge zur Optik trüber Medien, speziell kolloidaler Metallösungen". In: *Annalen der Physik, Vierte Folge* 25.3 (1908), 377–445.

[44] C.F. Bohren. *Scattering by particles. In: Handbook of Optics*. 3rd ed. Vol. 1. Chapter 7. McGraw-Hill, 2009.

[45] H.C. van de Hulst. *Light Scattering By Small Particles*. Vol. 10. New York, 1981.

[46] M. Mishchenko, L. Travis, and A. Lacis. *Scattering, absorption, and emission of light by small particles*. Cambridge University Press, 2000.

[47] L. Deák and T. Fülöp. "Reciprocity in quantum, electromagnetic and other wave scattering". In: *Annals of Physics* 327.4 (2012), pp. 1050–1077.

[48] S. T. Shipley et al. "High spectral resolution lidar to measure optical scattering properties of atmospheric aerosols. 1: Theory and instrumentation". In: *Applied Optics* 22 (23 1983), pp. 3716–3724. DOI: 10.1364/AO.22.003716.

[49] J. W. Hair et al. "Airborne High Spectral Resolution Lidar for profiling aerosol optical properties". In: *Applied Optics* 47 (36 2008), pp. 6734–6752. DOI: 10.1364/AO.47.006734.

[50] The Leibniz Institute for Tropospheric Research. HSRL. Technology at TROPOS - Remote Sensing. Accessed December 6, 2022. Available at: https://www.tropos.de/en/research/projects-infrastructures-technology/technology-at-tropos/remote-sensing/hsrl.

[51] Y. Xiao et al. "Simulating return signals of a spaceborne high-spectral resolution lidar channel at 532 nm". In: *Optics Communications* 417 (2018), pp. 89–96. DOI: 10.1016/j.optcom.2018.02.046.

[52] A. Bucholtz. "Rayleigh-scattering calculations for the terrestrial atmosphere". In: *Applied Optics* 34.15 (1995), pp. 2765–2773. DOI: 10.1364/AO.34.002765.

[53] B.A. Bodhaine et al. "On Rayleigh Optical Depth Calculations". In: *Journal of Atmospheric and Oceanic Technology* 16.11 (1999), pp. 1854–1861. DOI: 10.1175/1520-0426(1999)016<1854:ORODC>2.0.CO;2.

[54] K. Sassen and G. C. Dodd. "Lidar crossover function and misalignment effects". In: *Applied Optics* 21.17 (1982), pp. 3162–3165. DOI: 10.1364/AO.21.003162.

[55] M. Sicard et al. "Calculation of the Overlap Function and Associated Error of an Elastic Lidar or a Ceilometer: Cross-Comparison with a Cooperative Overlap-Corrected System". In: *Sensors* 20.21 (2020). DOI: 10.3390/s20216312.

[56] K. Stelmaszczyk et al. "Analytical function for lidar geometrical compression form-factor calculations". In: *Applied Optics* 44.7 (2005), pp. 1323–1331. DOI: 10.1364/AO.44.001323.

[57] A. Comerón et al. "An explicit formulation for the retrieval of the overlap function in an elastic and Raman aerosol lidar". In: *Atmospheric Measurement Techniques* 16.11 (2023), pp. 3015–3025. DOI: 10.5194/amt-16-3015-2023.

[58] N. Wang et al. "Experimental Determination of Lidar Overlap Profile Based on Dual Field-of-View High Spectral Resolution Lidar". In: *EPJ Web of Conferences* 237 (2020), p. 07014. DOI: 10.1051/epjconf/202023707014.

[59] E. Eloranta. “High Spectral Resolution lidar measurements of atmospheric extinction: Progress and challenges”. In: *2014 IEEE Aerospace Conference*. 2014, pp. 1–6. DOI: 10.1109/AERO.2014.6836214.

[60] T. Halldórsson and J. Langerholc. “Geometrical form factors for the lidar function”. In: *Applied Optics* 17.2 (1978), pp. 240–244. DOI: 10.1364/AO.17.000240.

[61] A. C. Povey et al. “Estimation of a lidar’s overlap function and its calibration by nonlinear regression”. In: *Applied Optics* 51.21 (2012), pp. 5130–5143. DOI: 10.1364/AO.51.005130.

[62] X. Shen et al. “Development of ZJU high-spectral-resolution lidar for aerosol and cloud: Calibration of overlap function”. In: *Journal of Quantitative Spectroscopy and Radiative Transfer* 257 (2020), p. 107338. DOI: 10.1016/j.jqsrt.2020.107338.

[63] L. Mei et al. “Experimental Calibration of the Overlap Factor for the Pulsed Atmospheric Lidar by Employing a Collocated Scheimpflug Lidar”. In: *Remote Sensing* 12.7 (2020). DOI: 10.3390/rs12071227.

[64] C. J. Grund and E. W. Eloranta. “University of Wisconsin High Spectral Resolution Lidar”. In: *Optical Engineering* 30 (1 1991), pp. 6–12. DOI: 10.1117/12.55766.

[65] R. Chen, Yuesong Jiang, and Haiyang Wang. “Calculation method of the overlap factor and its enhancement for airborne lidar”. In: *Optics Communications* 331 (2014), pp. 181–188. DOI: 10.1016/j.optcom.2014.05.063.

[66] D. Liu et al. “Performance estimation of space-borne high-spectral-resolution lidar for cloud and aerosol optical properties at 532 nm”. In: *Optics Express* 27 (8 2019), A481–A494. DOI: 10.1364/oe.27.00a481.

[67] H. Zhang et al. “Comparison of scanning aerosol lidar and in situ measurements of aerosol physical properties and boundary layer heights”. In: *Aerosol Research* 2.1 (2024), pp. 135–151. DOI: 10.5194/ar-2-135-2024.

[68] L. Mei, Z. Kong, and T. Ma. “Dual-wavelength Mie-scattering Scheimpflug lidar system developed for the studies of the aerosol extinction coefficient and the Ångström exponent”. In: *Optics Express* 26.24 (2018), pp. 31942–31956. DOI: 10.1364/OE.26.031942.

[69] L. Mei et al. “Comparison studies of the Scheimpflug lidar technique and the pulsed lidar technique for atmospheric aerosol sensing”. In: *Applied Optics* 58.32 (2019), pp. 8981–8992. DOI: 10.1364/AO.58.008981.

[70] X. Wang et al. “Fusion of the pulsed lidar and the Scheimpflug lidar for full tropospheric aerosol sensing”. In: *Optics Laser Technology* 190 (2025), p. 113252. DOI: 10.1016/j.optlastec.2025.113252.

[71] O.O. Osibanjo et al. “Intercomparison of planetary boundary-layer height in Mexico City as retrieved by microwave radiometer, micro-pulse lidar and radiosondes”. In: *Atmospheric Research* 271 (2022), p. 106088. DOI: 10.1016/j.atmosres.2022.106088.

[72] G. Fiocco and J. B. DeWolf. “Frequency spectrum of laser echoes from atmospheric constituents and determination of the aerosol content of air”. In: *Journal of the Atmospheric Sciences* 25 (1968), pp. 488–496. DOI: 10.1175/1520-0469(1968)025<0488:FSOLEF>2.0.CO;2.

[73] E. W. Eloranta, F. L. Roesler and J. T. Sroga. The High Spectral Resolution Lidar. In Technical Digest, Workshop on Optical and Laser Remote Sensing, Monterey, Calif., Feb. 9-11 1982, (unpublished report, 1982), paper I3.

[74] C. J. Grund. “Application of the HSRL model II to measurements of the aerosol backscatter phase function and cross section”. MA thesis. University of Wisconsin-Madison, Department of Meteorology, 1984.

[75] C. J. Grund. “Measurement of cirrus cloud optical properties by high spectral resolution lidar”. PhD thesis. University of Wisconsin-Madison, Department of Meteorology, 1987.

[76] C. J. Grund and E. W. Eloranta. “The 27–28 October 1986 FIRE IFO Cirrus Case Study: Cloud Optical Properties Determined by High Spectral Resolution Lidar”. In: *Monthly Weather Review* 118.11 (1990), pp. 2344 –2355. DOI: 10.1175/1520-0493(1990)118<2344:TOFICC>2.0.CO;2.

[77] R. L. Schwiesow and L. Lading. “Temperature profiling by Rayleigh-scattering lidar”. In: *Applied Optics* 20.11 (1981), pp. 1972–1979. DOI: 10.1364/AO.20.001972.

[78] H. Shimizu and C.-Y. She. Atomic and Molecular Blocking Filters for High-Resolution Lidar: A Proposed Method for Measuring Atmospheric Visibility Temperature and Pressure. In Eleventh International Laser Radar Conference, NASA Conference Publication 2228 (June 1982), paper D9, pp. 117-119.

[79] H. Shimizu, S. A. Lee, and C.-Y. She. “High spectral resolution lidar system with atomic blocking filters for measuring atmospheric parameters”. In: *Applied Optics* 22 (9 1983), pp. 1373–1381. DOI: 10.1364/AO.22.001373.

[80] C.-Y. She et al. “High-spectral-resolution Rayleigh-Mie lidar measurement of aerosol and atmospheric profiles”. In: *Optics Letters* 17 (7 1992), pp. 541–543. DOI: 10.1364/OL.17.000541.

[81] P. Piironen and E. W. Eloranta. "Demonstration of a high-spectral-resolution lidar based on an iodine absorption filter". In: *Optics Letters* 19 (3 1994), pp. 234–236. DOI: 10.1364/OL.19.000234.

[82] H. Xia et al. "Stratospheric temperature measurement with scanning Fabry-Perot interferometer for wind retrieval from mobile Rayleigh Doppler lidar". In: *Optics Express* 22 (18 2014), p. 21775. DOI: 10.1364/oe.22.021775.

[83] J. Xu et al. "High-spectral-resolution lidar for measuring tropospheric temperature profiles by means of Rayleigh–Brillouin scattering". In: *Optics Letters* 46 (13 2021), pp. 3320–3323. DOI: 10.1364/ol.424526.

[84] D. Bruneau et al. "355-nm high spectral resolution airborne lidar LNG: system description and first results". In: *Applied Optics* 54 (29 Oct. 2015), pp. 8776–8785. DOI: 10.1364/ao.54.008776.

[85] S. P. Burton et al. "Aerosol classification using airborne High Spectral Resolution Lidar measurements – methodology and examples". In: *Atmospheric Measurement Techniques* 5 (2012), 73–98.

[86] S. P. Burton et al. "Aerosol classification from airborne HSRL and comparisons with the CALIPSO vertical feature mask". In: *Atmospheric Measurement Techniques* 6 (5 2013), pp. 1397–1412. DOI: 10.5194/amt-6-1397-2013.

[87] Z. Li et al. "Research on characters of the marine atmospheric boundary layer structure and aerosol profiles by high spectral resolution lidar". In: *Optical Engineering* 47 (8 Aug. 2008), p. 086001. DOI: 10.1117/1.2969122.

[88] Y. Zhou et al. "Retrieving the seawater volume scattering function at the 180° scattering angle with a high-spectral-resolution lidar". In: *Optics Express* 25 (10 2017), p. 11813. DOI: 10.1364/oe.25.011813.

[89] Y. Zhou et al. "Shipborne oceanic high-spectral-resolution lidar for accurate estimation of seawater depth-resolved optical properties". In: *Light: Science and Applications* 11 (1 2022), p. 261. DOI: 10.1038/s41377-022-00951-0.

[90] Y. Jin et al. "Measurement method of high spectral resolution lidar with a multimode laser and a scanning Mach–Zehnder interferometer". In: *Applied Optics* 56 (21 2017), pp. 5990–5995. DOI: 10.1364/ao.56.005990.

[91] Z. Cheng et al. "Generalized high-spectral-resolution lidar technique with a multimode laser for aerosol remote sensing". In: *Optics Express* 25 (2 Jan. 2017), p. 979. DOI: 10.1364/oe.25.000979.

[92] B. Wang et al. “High-spectral-resolution LIDAR based on a few-longitudinal mode laser for aerosol and cloud characteristics detection”. In: *Optics Letters* 47 (19 2022), p. 5028. DOI: 10.1364/ol.471927.

[93] M. Hayman and S. Spuler. “Demonstration of a diode-laser-based high spectral resolution lidar (HSRL) for quantitative profiling of clouds and aerosols”. In: *Optics Express* 25 (24 2017), A1096–A1110. DOI: 10.1364/oe.25.0a1096.

[94] Y. Chen et al. “Fiber laser based high-spectral resolution lidar for earth science measurements”. In: vol. 8601. SPIE, 2013, 86011R. ISBN: 9780819493705. DOI: 10.1117/12.2005915.

[95] F. Gao et al. “Accurate measurement of aerosol optical properties using the multi-longitudinal mode high-spectral-resolution lidar with self-tuning Mach–Zehnder interferometer”. In: *Chinese Optics Letters* 21 (3 2023), p. 030101. DOI: 10.3788/col202321.030101.

[96] Z. Liu, I. Matsui, and N. Sugimoto. “High-spectral-resolution lidar using an iodine absorption filter for atmospheric measurements”. In: *Optical Engineering* 38 (10 1999), pp. 1661–1670. DOI: 10.1117/1.602218.

[97] Y. Jin et al. “Demonstration of aerosol profile measurement with a dual-wavelength high-spectral-resolution lidar using a scanning interferometer”. In: *Applied Optics* 61 (13 2022), pp. 3523–3532. DOI: 10.1364/ao.451707.

[98] Z.-S. Liu et al. “Iodine-filter-based high spectral resolution lidar for atmospheric temperature measurements”. In: *Optics Letters* 34 (18 2009), pp. 2712–2714. DOI: 10.1364/OL.34.002712.

[99] M. Zhao et al. “Development of high spectral resolution lidar system for measuring aerosol and cloud”. In: *Journal of the Optical Society of Korea* 19 (6 2015), pp. 695–699. DOI: 10.3807/JOSK.2015.19.6.695.

[100] D. Liu et al. “Polarized high-spectral-resolution lidar based on field-widened Michelson interferometer”. In: vol. 9832. SPIE, 2016, 98320Z. DOI: 10.1117/12.2223735.

[101] N. Wang et al. “Development of ZJU high-spectral-resolution lidar for aerosol and cloud: Feature detection and classification”. In: *Journal of Quantitative Spectroscopy and Radiative Transfer* 261 (2021). DOI: 10.1016/j.jqsrt.2021.107513.

[102] J. Ke et al. “Development of China’s first space-borne aerosol-cloud high-spectral-resolution lidar: retrieval algorithm and airborne demonstration”. In: *PhotoniX* 3 (17 2022). DOI: 10.1186/s43074-022-00063-3.

[103] J. Liu, D. X. Hua, and Y. Li. "Development of a high-spectral-resolution lidar for accurate profiling of the urban aerosol spatial variations". In: *Journal of Physics: Conference Series* 48 (1 2006), pp. 745–749. DOI: 10.1088/1742-6596/48/1/141.

[104] F. Shen et al. "Fabry–Perot etalon-based ultraviolet trifrequency high-spectral-resolution lidar for wind, temperature, and aerosol measurements from 02 to 35 km altitude". In: *Applied Optics* 57 (31 2018), p. 9328. DOI: 10.1364/ao.57.009328.

[105] A. Sannino et al. "Development of a High Spectral Resolution Lidar for day-time measurements of aerosol extinction". In: vol. 197. EDP Sciences, 2019, p. 02009. DOI: 10.1051/epjconf/201919702009.

[106] M. Esselborn et al. "Airborne high spectral resolution lidar for measuring aerosol extinction and backscatter coefficients". In: *Applied Optics* 47 (3 2008), pp. 346–358. DOI: 10.1364/AO.47.000346.

[107] M. Wirth et al. "The airborne multi-wavelength water vapor differential absorption lidar WALES: System design and performance". In: *Applied Physics B: Lasers and Optics* 96 (1 2009), pp. 201–213. DOI: 10.1007/s00340-009-3365-7.

[108] S. P. Burton et al. "Observations of the spectral dependence of linear particle depolarization ratio of aerosols using NASA Langley airborne High Spectral Resolution Lidar". In: *Atmospheric Chemistry and Physics* 15.23 (2015), pp. 13453–13473. DOI: 10.5194/acp-15-13453-2015.

[109] S. P. Burton et al. "Calibration of a high spectral resolution lidar using a Michelson interferometer, with data examples from ORACLES". In: *Applied Optics* 57 (21 2018), pp. 6061–6075. DOI: 10.1364/ao.57.006061.

[110] D. S. Hoffman et al. "Development of a high spectral resolution lidar based on confocal Fabry-Perot spectral filters". In: *Applied Optics* 51 (25 2012), pp. 6233–6244. DOI: 10.1364/AO.51.006233.

[111] I. I. Razenkov and E. W. Eloranta. "High spectral resolution lidar at the University of Wisconsin-Madison". In: vol. 176. EDP Sciences, 2018. DOI: 10.1051/epjconf/201817601024.

[112] J.C. Diels and W. Rudolph. "1 - Fundamentals". In: *Ultrashort Laser Pulse Phenomena (2nd Edition)*. Ed. by J.C. Diels and W. Rudolph. Burlington: Academic Press, 2006, pp. 1–60. ISBN: 978-0-12-215493-5. DOI: 10.1016/B978-012215493-5/50002-1.

[113] E. Hecht. *Optics*. 5; global. Pearson Education, 2016.

[114] Thorlabs, Inc. Fabry-Perot Interferometer Tutorial. Accessed 14 July 2023, https://www.thorlabs.com/newgrouppage9.cfm?objectgroup_id=9021.

[115] Z. Cheng et al. “Interferometric filters for spectral discrimination in high-spectral-resolution lidar: Performance comparisons between Fabry-Perot interferometer and field-widened Michelson interferometer”. In: *Applied Optics* 52 (32 2013), pp. 7838–7850. DOI: 10.1364/AO.52.007838.

[116] D. Liu et al. “System analysis of a tilted field-widened Michelson interferometer for high spectral resolution lidar”. In: *Optics Express* 20 (2 2012), pp. 1406–1420. DOI: 10.1364/OE.20.001406.

[117] Z. Cheng et al. “Field-widened Michelson interferometer system as the spectroscopic filter of high-spectral-resolution lidar”. In: *Laser Radar Technology and Applications XXI*. Ed. by Monte D. Turner and Gary W. Kamerman. Vol. 9832. International Society for Optics and Photonics. SPIE, 2016, 98320Y. DOI: 10.1117/12.2223715.

[118] Y. Zhang et al. “Design of iodine absorption cell for high-spectral-resolution lidar”. In: *Optics Express* 25 (14 2017), p. 15913. DOI: 10.1364/oe.25.015913.

[119] J. Dong et al. “Optimal iodine absorption line applied for spaceborne high spectral resolution lidar”. In: *Applied Optics* 57 (19 2018), p. 5413. DOI: 10.1364/ao.57.005413.

[120] B. Witschas. “Analytical model for Rayleigh–Brillouin line shapes in air”. In: *Applied Optics* 50.3 (2011), pp. 267–270. DOI: 10.1364/AO.50.000267.

[121] D. Bruneau and J. Pelon. “Simultaneous measurements of particle backscattering and extinction coefficients and wind velocity by lidar with a Mach–Zehnder interferometer: principle of operation and performance assessment”. In: *Applied Optics* 42.6 (2003), pp. 1101–1114. DOI: 10.1364/AO.42.001101.

[122] J. N. Forkey, W. R. Lempert, and R. B. Miles. “Corrected and calibrated I2 absorption model at frequency-doubled Nd:YAG laser wavelengths”. In: *Applied Optics* 36.27 (1997), pp. 6729–6738. DOI: 10.1364/AO.36.006729.

[123] F. Krause et al. “Simple and compact diode laser system stabilized to Doppler-broadened iodine lines at 633 nm”. In: *Applied Optics* 59.34 (2020), pp. 10808–10812. DOI: 10.1364/AO.409308.

[124] D.R. Stull. “Vapor Pressure of Pure Substances. Organic and Inorganic Compounds”. In: *Industrial & Engineering Chemistry* 39.4 (1947), pp. 517–550. DOI: 10.1021/ie50448a022.

[125] U. Wandiger. *Introduction to Lidar. In: Lidar*. Edited by: Weitkamp, C. New York: Springer, 2005, pp. 1–18.

[126] R. M. Measures. *Laser Remote Sensing: Fundamentals and Applications*. Krieger Publishing Company, 1992.

[127] J.Turunen et al. “Measurement of spatial coherence of light [Invited]”. In: *Journal of the Optical Society of America A* 39.12 (2022), pp. C214–C239. DOI: 10.1364/JOSAA.475374.

[128] RP Photonics Encyclopedia. *Beam divergence*. Available at: https://www.rp-photonics.com/beam_divergence.html. 2024.

[129] J. E. Greivenkamp. *Interference. In: Handbook of Optics*. 3rd ed. Vol. 1. Chapter 2. McGraw-Hill, 2009.

[130] Keopsys by Lumibird (2025). Pulsed green laser transmitter for underwater-telemetry and environment applications. Available at: https://www.keopsys.com/portfolio/underwater-telemetry-pgfl-series/ (Accessed: 18 August 2025).

[131] W. Sun et al. “Technique to separate lidar signal and sunlight”. In: *Optics Express* 24.12 (2016), pp. 12949–12954. DOI: 10.1364/OE.24.012949.

[132] U. Trivanovic and S. E. Pratsinis. “Opinion: Eliminating aircraft soot emissions”. In: *Aerosol Research* 2.2 (2024), pp. 207–223. DOI: 10.5194/ar-2-207-2024.